STUDY OF TEMPERATURE, SALINITY, AND CIRCULATION OVER COASTAL AND SHELF WATERS USING NESTED-GRID CIRCULATION MODELS

by

Yi Sui

Submitted in partial fulfilment of the requirements
for the degree of Doctor of Philosophy

at

Dalhousie University
Halifax, Nova Scotia
May 2023

TABLE OF CONTENTS

LIST OF TABLES

LIST OF FIGURES

ABSTRACT

The coastal and shelf waters (CSWs) support a wide range of human activities including tourism, recreation, transportation, and fisheries. Reliable knowledge of dynamics and temperature/salinity over the CSWs are of great importance to both human socio-economic concerns and the marine environment. In this thesis, three numerical modelling systems with different complexity are used to investigate the marine environmental conditions and important physical processes affecting their variability over the CSWs. Firstly, a Lagrangian particle tracking model is used to study retention and hydrodynamic connectivity of surface waters over the Scotian Shelf and its adjacent waters. The three-dimensional (3D) currents produced by the Princeton Ocean Model (POM) are used. The calculated near-surface retention is relatively low over western Cabot Strait, the inner Scotian Shelf, and the shelf break. The retention is relatively high in Northumberland Strait. Secondly, a four-level nested-grid coupled circulation-ice modelling system based on the Regional Ocean Modelling System (ROMS) and the Sea Ice Model (CICE) is used to investigate the 3D circulation and temperature/salinity in Halifax Harbour (HH), and landward intrusion of offshore sub-surface waters into Bedford Basin. Model results demonstrate that the persistent northwesterly winds are the most effective in triggering the intense landward intrusion than winds from other directions. Model results are also used in quantifying the cumulative effects of winds and tides on the time-mean currents and temperature/salinity in HH. Thirdly, a shelf circulation modelling system based on ROMS is used to examine the hydrodynamic responses of the northern South China Sea to Typhoon Linfa. Analysis of model results demonstrates the importance of storm-induced upwelling and vertical mixing in different stages of the typhoon, depending on the translational speeds, wind intensity and structure of the storm, and vertical stratification. Furthermore, the peak frequency of the storm-induced near-inertial oscillations (NIOs) is modified by the background large-scale circulation.

LIST OF ABBREVIATIONS AND SYMBOLS USED

Abbreviation	Definition
1D	One-Dimensional
2D	Two-Dimensional
3D	Three-Dimensional
AADL	Area Affected Directly by Linfa
ADCP	Acoustic Doppler Current Profiler
ADV	Advection
AZMP	Atlantic Zone Monitoring Program
BBMP	Bedford Basin Monitoring Program
BoF	Bay of Fundy
CANDIE	Canadian Version of Diecast
CBI	Cape Breton Island
CFSR	Climate Forecast System Reanalysis
CFSv2	Climate Forecast System reanalysis version 2
Chl	Chlorophyll Concentration
CICE	Los Alamos Community Ice Code
CoM	Center of Mass
CORR	Correlation Coefficients
CPD	Cycles Per Day
CR	Control Run
CTD	Conductivity, Temperature and Depth Probe
cScS	Central Scotian shelf
CSWs	Coastal and Shelf Waters
DO	Dissolved Oxygen
DRAC	Digital Research Alliance Compute Canada
ECS	Eastern Canadian Shelf
eScS	Eastern Scotian Shelf
GeB	Georges Bank
GEBCO	General Bathymetric Chart of the Oceans
GHRSST	Group for High-Resolution SST dataset

Abbreviation	Definition
GLORYS	Global Ocean Reanalysis and Simulation Dataset
GoM	Gulf of Maine
GSL	Gulf of St. Lawrence
Hadv	Horizontal Advection
Hmix	Horizontal Mixing
HYCOM	Hybrid Coordinate Ocean Model
IH	Inner Harbour
LAL	Looping Area of Linfa
LCS	Lagrangian Coherent Structures
LS	Labrador Shelf
MODIS	Moderate Resolution Imaging Spectroradiometer
MOM	Modular Ocean Model
MLD	Mixed Layer Depth
MSL	Mean Sea Level
MSW	Maximum Sustained Wind
NARR	North American Regional Reanalysis
NCODA	Navy Coupled Ocean Data Assimilation
NIOs	Near-inertial Oscillations
NHF	Net Heat Flux at the Sea Surface
NL	Newfoundland
NFS	Newfoundland Shelf
NoAdv	Advection terms for model temperature and salinity are turned off
NH	Northern Hemisphere
nSCS	Northern South China Sea
NT	No Tides Run
NW	No Wind Run
nwLCC	Northwest Luzon Coastal Current
OH	Outer Harbour
OTIS	Oregon State University Tidal Inversion System
PEI	Prince Edward Island
PRE	Pearl River Estuary
PSU	Practical Salinity Unit
POM	Princeton Ocean Model

Abbreviation	Definition
RB	Relative Bias
ROMS	Regional Ocean Modeling System
RMSE	Root Mean Square Error
ScS	Scotian Shelf
SCS	South China Sea
seCS	Southeastern Canadian Shelf
SI	Scatter Index
SLGO	St. Lawrence Global Observatory
SLP	Atmospheric Pressure at the Mean Sea Level
Smooth	Smooth Run
SOCs	Sediment Oxygen Consumptions
SST	Sea Surface Temperature
SSS	Sea Surface Salinity
SLDMB	Self-Locating Datum Marker Buoy
TC	Tropical Cyclone
TW	Taiwan
UTC	Coordinated Universal Time
Vadv	Vertical Advection
Vmix	Vertical Mixing
VOC	Vietnam Offshore Current
wnLCC	Northwest Luzon Coastal Current
wScS	Western Scotian Shelf

Symbol	Description	Unit
A_1, A_2	Intense SST cooling areas due to Linfa	m^2
B	Hurricane shape parameter	
DA	Downstream area	m^2
F	Form factor of tides	
K_h	Horizontal eddy diffusivity coefficient	$m^2\ s^{-1}$
K_z	Vertical eddy diffusivity coefficient	$m^2\ s^{-1}$
N	Number of particles	
R	Retention index	mmol m^{-3}
R_m	Radius of maximum wind	
S_{A1}	Total mass of the salt of the salty water in Bedford Basin	m
S_{A2}	Total mass of salt of the salty water in Outer Halifax Harbour	kg
$\Delta\bar{S}_0^{CR-NT}$	Differences in surface salinity between cases CR (Control Run) and NT (NO Tides)	kg
$\Delta\bar{S}_{12}^{CR-NT}$	Differences in salinity at 12 m between cases CR (Control Run) and NT (NO Tides)	
$\Delta\bar{S}_0^{CR-NW}$	Differences in surface salinity between cases CR (Control Run) and NW (NO Winds)	
$\Delta\bar{S}_{12}^{CR-NW}$	Differences in salinity at 12 m between cases CR (Control Run) and NW (NO Winds)	
T	Temperature	
$\Delta\bar{T}_0^{CR-NT}$	Differences in surface temperature between cases CR (Control Run) and NT (NO Tides)	°C
$\Delta\bar{T}_{12}^{CR-NT}$	Differences in temperature at 12 m between cases CR (Control Run) and NT (NO Tides)	°C
$\Delta\bar{T}_0^{CR-NW}$	Differences in surface temperature between cases CR (Control Run) and NW (NO Winds)	°C
$\Delta\bar{T}_{12}^{CR-NW}$	Differences in temperature at 12 m between cases CR (Control Run) and NW (NO Winds)	°C
UA	Upstream area	°C
$\Delta\bar{U}_0^{CR-NT}$	Differences in surface currents between cases CR (Control Run) and NT (NO Tides)	
$\Delta\bar{U}_{12}^{CR-NT}$	Differences in currents at 12 m between cases CR (Control Run) and NT (NO Tides)	$m\ s^{-1}$
$\Delta\bar{U}_0^{CR-NW}$	Differences in surface currents between cases CR (Control Run) and NW (NO Winds)	$m\ s^{-1}$

Symbol	Description	Unit
$\Delta\overline{U}_{12}^{CR-NW}$	Differences in currents at 12 mbetween cases CR (Control Run) and NW (NO Winds)	m s^{-1}
$\Delta\overline{U}_{12}^{CR-NW}$	Differences in currents at 12 m between cases CR (Control Run) and NW (NO Winds)	m s^{-1}
a, b	Coefficient for the linear dependence	
f	Coriolis parameter	rad s^{-1}
f_{p}	Peak frequency	cpd
$p(r)$	Ambient atmospheric pressure	Pa
$p(c)$	Central pressure	Pa
Δr	Separation distance	m
Δt	Time step	s
$\vec{\mathrm{u}}$	Velocity vector	m s^{-1}
t	Time	s
α	Wind transfer coefficient	
β	Coefficient of the semi-prognostic method	
ρ	Water density	kg m^{-3}
ρ_a	Air density	kg m^{-3}
φ	Phases of tides	deg
φ_{CR}	Model results in the case CR (Control Run)	
φ_{NT}	Model results in the case NT (No Tides)	
φ_{NW}	Model results in the case NW (NO Winds)	
$\Delta\varphi_{tide}$	Roles of tides	
$\Delta\varphi_{wind}$	Roles of winds	
γ^2	Relative variance	
$\vec{\delta}$	Random displacement	m
η	Surface elevation	m
τ	Wind stress	kg m^{-1} s^{-2}

ACKNOWLEDGEMENTS

Firstly, I would like to express my sincere gratitude to my supervisor Dr. Jinyu Sheng for giving me the opportunity to work on my doctoral research. Throughout my doctoral research, Dr. Jinyu Sheng has provided me much constructive and invaluable guidance for conducting my research work. He also gave me a lot of advice about how to make good oral presentations and about scientific writing. Without his patient guidance and encouragement, I could not have completed this thesis. His enthusiasm, motivation, hardworking, and profound knowledge gave me a good example about how to be a good researcher. It was a great honor to work and study under his guidance.

Secondly, I would also thank other thesis committee members, including Drs. Katja Fennel, Youyu Lu, Yongsheng Wu, and Marlon Lewis, for their insightful comments, encouragement, and contributions to my thesis research. I would also like to thank my external examiner Dr. Marek Stastna for taking the time to read my thesis and providing constructive comments.

Thirdly, I would like to thank team members in our research group, including Drs. Pengcheng Wang, Shengmu Yang, Shangfei Lin, and Yuan Wang, for their suggestions and help during my doctoral study. I appreciate the great help from Dr. Kyoko Ohashi for sharing the source codes used in this study. I also thank Dr. Rod Johnson for providing a research cruise opportunity at Bermuda to fulfill one of my PhD program requirements. Thanks also go to the many other faculty members and other fellow graduate students in the Department of oceanography for their help.

CHAPTER 1

INTRODUCTION

1.1 Background

The coastal and shelf waters (CSWs) extend from the coastline (including bays and estuaries) to the edge of the abyssal plain of the adjoining basin, and encompass both the continental shelf and the slope (*Kantha and Clayson*, 2000). As an important link between the land and deep ocean and also between the atmosphere and sea, the CSWs are strongly influenced by winds, tides, buoyancy forcing (including the net heat and freshwater fluxes at the sea surface and freshwater discharges from rivers or ice melt), and indirectly by large-scale ocean circulations. Circulation and temperature/salinity over the CSWs play an important role in local fisheries, aquaculture, offshore hydrocarbon production, shipping and transportation, marine recreation and tourism. Reliable knowledge of oceanographic processes over the CSWs is important to many social and economic activities.

1.1.1 Main Driving Forcings over Coastal and Shelf Waters

Winds (and to a lesser extent, the atmospheric pressure fluctuations) play a very important role in the three-dimensional (3D) ocean circulation and temperature/salinity over the CSWs (*Loder et al.*, 1988; *Urrego-Blanco and Sheng*, 2014a). Over these regions, winds have synoptic, seasonal and decadal timescales from hours to months (i.e., breeze, monsoon) and have spatial scales from tens of meters to thousands of kilometers. Therefore, there is a variety of wind-induced oceanic processes operating on the CSWs. Based on the classical Ekman theory (*Ekman*, 1905), the steady winds induce significant wind-driven currents in the surface Ekman layer. Due to the Earth's rotation (i.e. Coriolis effect), the surface waters flow in a direction about 45° to the right of the wind direction on the Northern Hemisphere (NH). Below the sea surface, the Ekman current runs in directions slightly to the right of the current at the layer above it (*Ekman*, 1905). The net transport of the Ekman current in the surface Ekman layer (known as "the Ekman transport") deflects 90° to the right of the wind direction in the NH. For the steady winds

blowing alongshore with the coast on the left side of the wind direction in the NH, the upper layer Ekman transport is in the offshore direction. The surface waters near the coast are replaced by the cool and nutrient-rich waters from the below (*Ekman*, 1905; *Shan and Sheng*, 2022). This process is known as the "wind-driven coastal upwelling", which is one of important oceanographic processes affecting many fisheries and marine ecosystems over the CSWs. Wind-driven coastal upwelling also transports nutrient and material (pollutants, fresh water) from the coastal waters to the deep sea (*Kantha and Clayson*, 2000). The reverse process known as the "wind-driven coastal downwelling" occurs for the steady winds blowing in parallel to the shore with the coast on the right in the NH. When the downwelling occurs over the CSWs, the light surface waters sink to deep layers. This process leads to vertical convection, which substantially increases the mixing and decreases the stratification (*Havik and Vage*, 2018). Due to their importance, wind-driven dynamic processes over the Eastern Canadian Shelf (ECS) were extensively studied. For example, *Yang and Sheng* (2008) demonstrated local winds strongly affected 3D circulation and caused upwelling/downwelling in Lunenburg Bay. *Zhai* et al. (2008) further revealed that the wind-driven dynamics played a dominant role in affecting the spatial and temporal variability of temperature and salinity in Lunenburg Bay. One of the important scientific questions to be addressed in this thesis is the quantitative roles of the local winds and their seasonal variability on the 3D circulation and hydrographic conditions over different areas of the CSWs.

The CSWs such as the ECS and the northern South China Sea (nSCS) are also affected by winter storms and tropical cyclones or hurricanes (typhoons). Strong winds during extreme weather events can generate large variations in the surface elevation (i.e., storm surge) over the CSWs, which can cause extensive property losses, erosion of beaches, damage to coastal habitats, and undermine foundations of marine infrastructure. The storm surges generated by winter storms and tropical cyclones have different variability in spatial and temporal scales. Tropical storms typically generate intensive but localized surges extending over a few tens of kilometers around its storm center (*Needham et al.,* 2015). Tropical cyclones usually move relatively fast and hence their effects on the surface elevations are localized. In comparison, winter storms usually generate less

intensive but widespread storm surges over hundreds of kilometers over the regions affected directly by strong winds (*Provan et al.,* 2022).

The 3D circulation and temperature/salinity affected by tropical cyclones and winter storms over the ECS were also studied in the past. *Sheng* et al. (2006) investigated the upper ocean responses to Hurricane Juan in September 2003 over the Scotian Shelf (ScS) and the adjacent slope waters. Their results showed that the intense storm-induced currents and the storm-induced vertical mixing played a dominant role in SST cooling over the ScS. *Wang and Sheng* (2016) also studied the ocean responses to three extreme weather events and showed that the SST cooling during these events were biased to the right of the storm tracks and strong near-inertial currents occurred over the areas behind the storm.

The 3D circulation and temperature/salinity over the CSWs are also affected by tides (*Wu et al*., 2011; *Wang et al.,* 2022). Tidal currents and elevations are significantly large over several areas of the ECS, such as the Bay of Fundy (BoF). Many man-made infrastructures, such as offshore oil/gas platforms and nearshore aquaculture facilities require good knowledge on tidal currents and tidal elevations. Previous studies showed that tides significantly affect the general mean currents over some shallow areas in the ScS (*Yang and Sheng*, 2008; *Ohashi* et al., 2009a). Furthermore, tidal currents also induce shoreward non-tidal currents and associated coastal upwelling over the CSWs (*Chegini et al*., 2018). Tidal currents also affect the water transport, which is important for the movement of pollutants over the CSWs (e.g., *Cai et al.,* 2014; *Feng et al.,* 2008; *Lin et al.,* 2015). *Shan* (2010) demonstrated that strong tidal currents significantly affect the general mean circulation and hydrographic conditions in fjords like Halifax Harbour. *Feng et al.* (2022) showed that the tides have a clear influence on seasonal circulation and hydrographic variability over the CSWS in the ScS.

Buoyancy forcing is defined as the upward forcing exerted on the water parcel associated with the density gradients in the ocean (*Wirth and Negretti*, 2022). The density gradients over the CSWs are affected by the net heat fluxes and freshwater fluxes at the sea surface and freshwater discharges from rivers or ice melt. The ocean currents driven by density

gradients of seawater are known as the buoyancy-driven current (*Treguier et al.,* 2012). The buoyancy-driven coastal currents over the ECS and nSCS generally occur over the CSWs with large freshwater discharges (e.g., river, estuaries, and fjords). Due to the large freshwater discharges from rivers and the Earth's rotation (i.e. the Coriolis term), the coastal currents (or estuarine plumes) are generated over the mouth of the river and adjacent coastal waters. Due to the Coriolis term, the coastal currents veer cyclonically in the NH and propagate along the coast with the coastline on the right hand side of the currents (*Pritchard,* 1952*; Griffiths and Linden*, 1981). Previous studies suggested that the buoyancy forcing is one of the main driving mechanisms for the coastal currents over many areas of CSWs, including the western Gulf of St. Lawrence (GSL), the Gulf of Maine (GoM), ScS, and Norwegian Shelf (*Mork*, 1981; *Munchow and Garvine,* 1993; *Fong and Geyer*, 2001; *Sheng*, 2001; *Yankovsky et al.,* 2001).

1.1.2 Observations

Sustained and systematic oceanographic observations are key for understanding and quantifying the 3D and time-variable circulations and temperature/salinity over the CSWs. Observations have been extensively used for supporting the decision making, providing important information for the coastal zone management, and improving our understanding of the physical and biological processes over the CSWs.

Sea level is one of the important oceanographic variables to be observed. Sea level measurements made by tide gauges have widely been used in studying the tides and sea level fluctuations over the CSWs. In-situ measurements of water temperature and salinity by the conductivity, temperature and depth (CTD) probe have a long history in the oceanographic observations. A CTD is typically deployed from a ship to measure both the temperature and salinity vertical profiles simultaneously (*Paradis and Wood*, *2013*). Other sensors can be added to the conventional CTD to measure different oceanographic variables such as the fluorescence, dissolved oxygen concentration, and nitrate concentration. The ocean currents can be measured by the Acoustic Doppler Current Profiler (ADCP), high-frequency radar and other advanced sensors.

Remote sensing (typically from satellite) is another widely used observational technique in oceanography (*Robinson*, 1985; *Blondeau-Patissier et al.,* 2014). Satellite remote sensing allows for collections of oceanographic variables over large surface areas during a short duration, and having observations over regions not adequately sampled by in-situ observations (*Robinson*, 1985; *Dever et al.,* 2016). Recent developments in remote sensing allow us to have high-resolution, reliable and accurate surface data over the CSWs (*Lacava and Ciancia*, 2020). The most routinely available near real-time and archival products inferred from the satellite remote sensing data include the sea surface temperature (SST), sea surface salinity (SSS), sea surface winds, chlorophyll, optical clarity and other variables.

In this thesis, various ocean observations are used to study the oceanic processes and also to validate the performance of our numerical models.

1.1.3 Ocean circulation Models

Due to the limitation in the spatial and temporal coverage of the in-situ observations and satellite remote sensing data, numerical models have become a very important tool in oceanographic research. Most ocean circulation models are based on the Reynolds-averaged Navier-Stokes equations and continuity equation with several major approximations justified by scaling analysis. Different ocean circulation models have different advantages in the treatments of the local topography, vertical coordinates, and the space/time discretization of the equations.

Three vertical coordinates are applied in the widely-used ocean circulation models: the z-coordinate (geopotential levels), σ-coordinate (topography-following layers), and ρ-coordinate (isopycnal layers) (*Ezer and Mellor,* 2004). The z-coordinate is the simplest vertical coordinate, which is set to be a monotonic function of depth. The z-coordinate usually represents the vertical distance from ocean surface at $z=0$ to the ocean topography at $z=-H(x, y)$, with the upward positive direction. Here, $H(x, y)$ is the local water depth. The first well-known z-coordinate model is the Modular Ocean Model (MOM), which was initially developed in the 1960's-1980's by *Bryan* (1969a). DieCAST (Dietrich/Center for Air–Sea Technology; *Dietrich et al.,* 1987) also uses the z-

coordinate, which was applied to study the wind-driven circulation in Lake Neuchatel, Switzerland (*Zuur and Dietrich*, 1990) and the Loop Current and associated eddies in the Gulf of Mexico (*Dietrich and Lin,* 1994). CANDIE (Canadian Version of Diecast), which was developed based on DieCAST (*Sheng et al.,* 1998), was used to study the 3D circulation and temperature/salinity of Lake Huron, Georgian Bay, and other areas of CSWs (*Sheng and Rao*, 2006). The z-coordinate models are easy to implement. One of the major drawbacks of the conventional z-coordinate models, however, is the crude representation of topography in the model, which may lead to large truncation errors over steep topography (*Sheng et al.,* 1998). The other drawback is the poor representation of currents in the bottom boundary layers of the CSWs.

The σ-coordinate used in the ocean circulation model is usually defined as $\sigma = \frac{z-\eta}{H+\eta}$, where z is the Cartesian vertical coordinate, with $z = 0$ for the equilibrium position of the sea surface (*Ezer and Mellor,* 2004). Here, $\eta(x, y, t)$ is the displacement of the sea surface from its equilibrium position ($z = 0$). This vertical coordinate system follows the ocean bottom and therefore better resolves the hydrodynamics in the bottom boundary layer. Therefore, the σ-coordinate models have been widely used in the CSWs where the top and bottom boundary layers are thought to be important (*Haidvogel et al.,* 2008). The Princeton Ocean Model (POM, *Blumberg and Mellor,* 1987) is one of the first-generation σ-coordinate models and was extensively used in the past. *Blumberg and Goodrich* (1990) used POM to study the wind-induced destratification in Chesapeake Bay. The Regional Ocean Modeling System (ROMS, *Shchepetkin and McWilliams,* 2005; *Haidvogel et al.,* 2008) also uses the σ-coordinate, which has widely been used for simulating the 3D currents over the CSWs (e.g. *Fennel et al.,* 2006; *Gruber et al.,* 2006; *Lachkar and Gruber*, 2013; *Brennan et al*., 2016; *Turi et al.,* 2014; *Frischknecht et al.,* 2015, *Rutherford and Fennel*, 2018). ROMS has a highly flexible modular design, which allows it to be readily modified for use in a number of applications including the model simulations of sediment transport, biology, waves, and sea ice.

The ρ-coordinate uses the potential density referenced to a given pressure in the vertical coordinate. The ρ-coordinate ocean circulation models divide the water column into distinct homogeneous layers, of which thicknesses vary from place to place and from one

time step to the next (*Fox-Kemper et al.*, 2019). By using the ρ-coordinate, ocean circulation models have the ability to efficiently resolve baroclinic structure with relatively few vertical coordinates (*Halliwell*, 1988). As one of the ρ-coordinate models, Miami Isopycnic-Coordinate Ocean Model (MICOM) has been widely used in many different studies (e.g. *Chassignet et al.,* 1996; *Bleck,* 2002; *Paiva et al.,* 2000). The HYbrid Coordinate Ocean Model (HYCOM) uses the hybrid layer structures that evolved from the MICOM (*Halliwell et al.,* 1998). *Kara et al.* (2008) used multiple statistical metrics to evaluate the performance of the HYCOM and demonstrated that the reanalysis has the ability to reproduce the past SST events in climatological and interannual simulations. Based on the global HYCOM simulation, *Metzger et al.* (2010) reported high correlations between the simulated and observed Indonesian Throughflow.

In this thesis, three numerical ocean circulation models with the different levels of complexity are used to study the dynamics and temperature/salinity over three different areas of the CSWs. They are:

- A nested-grid ocean circulation modelling system (DalCoast) for the GSL-ScS-GOM region based on POM. The 3D currents produced by the DalCoast are used to drive a Lagrangian particle tracking model. The simulated particle movements are used to examine the circulation and retention of surface waters over the ScS and its adjacent coastal waters.

- A nested-grid coupled circulation-ice modelling system for the southeastern Canadian Shelf (NGMS-seCS) based on ROMS. The NGMS-seCS is used to study the 3D circulation and hydrography in Halifax Harbour (HH) and physical processes affecting landward intrusion of offshore sub-surface waters into Bedford Basin (BB).

- A circulation modelling system for the nSCS (ROMS-nSCS) based on ROMS. The ROMS-nSCS is used to study the storm-induced changes in the 3D circulation and temperature/salinity during a typhoon event over the nSCS.

There are two major reasons for using three different circulation model systems in my thesis. Firstly, it usually takes a long time to develop and validate a modelling system. Therefore an incremental approach has been taken in my doctorial research by using different but fully developed and calibrated modelling systems in each of Chapters 2-4. Secondly, different modelling systems are used to address specific research questions.

These three numerical ocean circulation models run on the high-performance computing platform provided by the "Digital Research Alliance Compute Canada (DRAC)". DRAC is a national organization supported by universities, research organizations, and industry partners (https://alliancecan.ca/en). The high-performance computing platform uses use the latest high-performance computing technology, including powerful CPUs, fast interconnects, and large-scale storage, to enable researchers to conduct complex calculations and numerical simulations. In my research, 64-core MPI parallel computing was utilized to accelerate the computing of the numerical ocean circulation models.

1.2 Objectives of the Thesis

The overall objective of my doctoral research is to improve our understanding of main processes affecting the 3D circulations and temperature/salinity over the CSWs, with a special focus on the ECS and nSCS. Extensive studies were made in the past on the 3D ocean currents, temperature/salinity and associated variability over the CSWs. Many important scientific questions, however, remain to be addressed. For example, how do winds and tides affect the hydrodynamic connectivity over the ECS? What are the main processes affecting the landward intrusion of offshore deep waters into BB? What are the physical processes affecting the 3D circulations and temperature/salinity over the nSCS during extreme weather events? My doctoral research focuses on the following three research initiatives. The first initiative is to investigate the 3D circulation, particle movements, retention and connectivity over the ScS and adjacent waters. The second initiative is to study the 3D circulations and physical processes of landward intrusion of offshore deep waters into Bedford Basin. The third initiative is to investigate the storm-induced circulations and temperature/salinity variabilities over the nSCS during extreme weather events.

1.3 Outline of the Thesis

The structure of this thesis is as follows.

In Chapter 2, the 3D circulation, particle movements, retention and connectivity over the ScS and the adjacent deep ocean waters are studied using a Lagrangian particle tracking model based on the simulated currents provided by the DalCoast. The effects of local winds and tides on the retention are investigated. The research results of Chapter 2 are documented in *Sui et al.* (2017).

In Chapter 3, the 3D circulation and temperature/salinity in HH are studied using the NGMS-seCS. This is motivated by our finding in Chapter 2 that the 3D circulation and temperature/salinity are strongly affected by winds, tides, topography and other physical proceses over the ScS. The NGMS-seCS is also used in examining the role of persistent winds from four specific directions (i.e., northwesterly, southwesterly, southeasterly and northeasterly winds) in generating the intense landward intrusion of offshore sub-surface waters into BB. The accumulative effects of winds and tides on the 3D time-mean circulation and hydrography in HH are also quantified based on model results. The research results in this Chapter will be used in a manuscript to be submitted shortly.

In Chapter 4, the storm-induced 3D circulation and temperature/salinity over the nSCS during Typhoon Linfa in June 2009 are examined using ROMS-nSCS. This study is based on the important scientific question not fully addressed in Chapters 2 and 3 which is the ocean response to extreme weather events. The research results of Chapter 4 are documented in *Sui et al.,* (2022).

An overall summary and discussions of future work are given in Chapter 5.

CHAPTER 2

CIRULATION, RETENTION AND HYDRODYNAMIC CONNECTIVITY OVER THE SCOTIAN SHELF AND ADJACENT WATERS

2.1 Introduction

The Eastern Canadian Shelf (ECS) over the northwest Atlantic Ocean supports many ocean use sectors including commercial fisheries, aquaculture, offshore hydrocarbon production, shipping and transportation, marine recreation and tourism, and other economic activities that directly contribute to the Canadian economy (*Rutherford et al.,* 2005). This region also consists of several highly productive marine ecosystems such as rich commercial fishing grounds over the Grand Banks, Gulf of St. Lawrence (GSL), Scotian Shelf (ScS) and Gulf of Maine (GoM).

Marine ecosystems are strongly influenced by physical environmental conditions such as ocean currents, temperature and salinity. Ocean currents and turbulent mixing, for example, affect the availability of nutrients for plant growth and availability of food for marine animals. Eggs and larvae of fish and other animals, on the other hand, can drift with ocean currents from their spawning grounds to nursery areas where they feed and grow (*Lechner et al,* 2016).

Significant efforts have been made in the past to determine the general circulation and associated seasonal and interannual variability over the ECS (*Sheng and Thompson,* 1996; *Lynch et al.,* 1996; *Loder et al.,* 1998; *Wu et al.,* 2012; *Urrego-Blanco and Sheng,* 2014a,b). The large-scale circulation over the ECS is predominantly influenced by the North Atlantic subpolar gyre and its western boundary current, the Labrador Current (*Loder et al.,* 1998). The general circulation and temperature/salinity over the ECS, particularly over the outer shelf and slope regions of the ScS and GoM, are also strongly affected by the western boundary current of the North Atlantic subtropical gyre, namely the Gulf Stream and its northern extension, the North Atlantic Current.

The three-dimensional (3D) currents, hydrographic conditions and particle movements on the ECS have significant temporal and spatial variability, which are affected by the local irregular bathymetry, tidal forcing, atmospheric forcing, and river discharges (*Urrego-Blanco and Sheng,* 2012). *Cong et al.* (1996) calculated retention indices for offshore banks on the Scotian Shelf based on wind-driven currents produced by a barotropic circulation model. The particle movements over coastal embayments such as Halifax Harbour and Lunenburg Bay of the Scotian Shelf were calculated from 3D ocean currents produced by primitive-equation ocean circulation models (*Sheng et al.,* 2009; *Shan et al.,* 2012). *Shan et al.* (2014) examined the 3D circulation and particle movement over Sable Gully of the Scotian Shelf. *Rutherford and Fennel* (2018) calculated the retention times, transport pathways, and transit times over the northwestern Atlantic Ocean using a high-resolution circulation model. The main objective of this study is to examine the retention and hydrodynamic connectivity of passive particles in near-surface waters over the Scotian Shelf and its adjacent waters including the southern Gulf of St. Lawrence and inner Gulf of Maine using a Lagrangian particle tracking model with simulated 3D ocean currents.

The structure of this chapter is as follows. Section 2.2 discusses the nested-grid coastal circulation modelling system and the Lagrangian particle tracking model. Section 2.3 discusses the performance of the circulation modelling system and the particle tracking model using three types of oceanographic observations. Section 2.4 discusses the calculated retention of passive particles over the Scotian Shelf and adjacent waters. This section also examines the main physical processes affecting the surface retention. The last section 2.5 presents the summary and conclusions.

2.2 Nested Grid Ocean Circulation Modelling System

2.2.1 Ocean Circulation Model

The ocean circulation model used in this study is a nested-grid ocean circulation modelling system known as DalCoast. The circulation modelling system is constructed from the Princeton Ocean Model (POM*; Mellor,* 2004), which is a 3D, σ-coordinate, primitive-equation ocean circulation model. Different versions of DalCoast were

developed in the past for different scientific applications (*Sheng et al.,* 2009; *Ohashi et al.,* 2013; *Shan et al.,* 2012, 2014).

The version of DalCoast used in this study is similar to that used by *Ohashi and Sheng* (2013, 2015) and has a nested two-level structure with a fine-resolution inner model nested inside a coarse-resolution outer model. The outer model domain covers the ECS from the Labrador Shelf (LS) to the Gulf of Maine (GoM) (72°W-42°W and 38°N-60°N) (Fig. 2.1a). The inner model domain covers the GSL, the ScS, the GoM, and adjacent deep waters (71.5°W-56°W and 38.5°N-52°N) (Fig. 2.1b). The outer model is two-dimensional and barotropic with a horizontal resolution of 1/12°. The inner model is baroclinic and three-dimensional with a horizontal resolution of 1/16°. The inner model has 40 σ (terrain-following) levels in the vertical that are concentrated near the surface and bottom. The model bathymetry is based on the General Bathymetric Chart of the Oceans (GEBCO) data with a resolution of 30 arc-seconds (*Weatherall et al.,* 2015).

The outer model is driven by atmospheric forcing. The inner model external forcing includes tidal forcing, atmospheric forcing, surface heat fluxes, and river discharge. The atmospheric forcing used to drive both models includes three-hourly fields of sea-level atmospheric pressure and surface wind fields extracted from the North American Regional Reanalysis dataset (NARR; *Mesinger al.,* 2006). The surface wind speed is converted to wind stress using the bulk formula of *Large and Pond* (1981). Hourly tidal forcing for eight major tidal constituents (M_2, S_2, N_2, K_2, K_1, O_1, P_1, and O_1), in the form of tidal elevations and tidal currents specified at the lateral open boundaries of inner model, are produced by a tidal prediction system known as OTIS (*Egbert and Erofeeva,* 2002). In addition, the hourly wind-driven surface elevations and depth-averaged currents produced by the outer model are added to the open boundary conditions of the inner model (one-way nesting).

The surface heat flux for the inner model is calculated based on the model-calculated sea surface temperature in combination with three-hourly NARR fields of wind speed, air pressure, air temperature, cloud cover, downward shortwave radiation flux, and precipitation (*Mellor,* 2004). The subgrid scale horizontal mixing is calculated using the velocity shear and grid size dependent scheme of *Smagorinsky* (1963). The vertical

mixing is parameterized using the *Mellor and Yamada* (1982) level-2.5 turbulent closure scheme. Temperature and salinity fields of inner model are initialized by a gridded (1/6 ^{o} by 1/6 ^{o}) monthly mean climatology generated by *Geshelin et al.* (1999). To reduce model bias and drift from the seasonal cycle of temperature/salinity in the model, the spectral nudging technique (*Thompson et al.,* 2007) and the semi-prognostic method (*Sheng et al.,* 2001) with the same climatology of *Geshelin et al.* (1999) are applied in the inner model of DalCoast. More details on the semi-prognostic method and spectral nudging method are given in Appendices A and B.

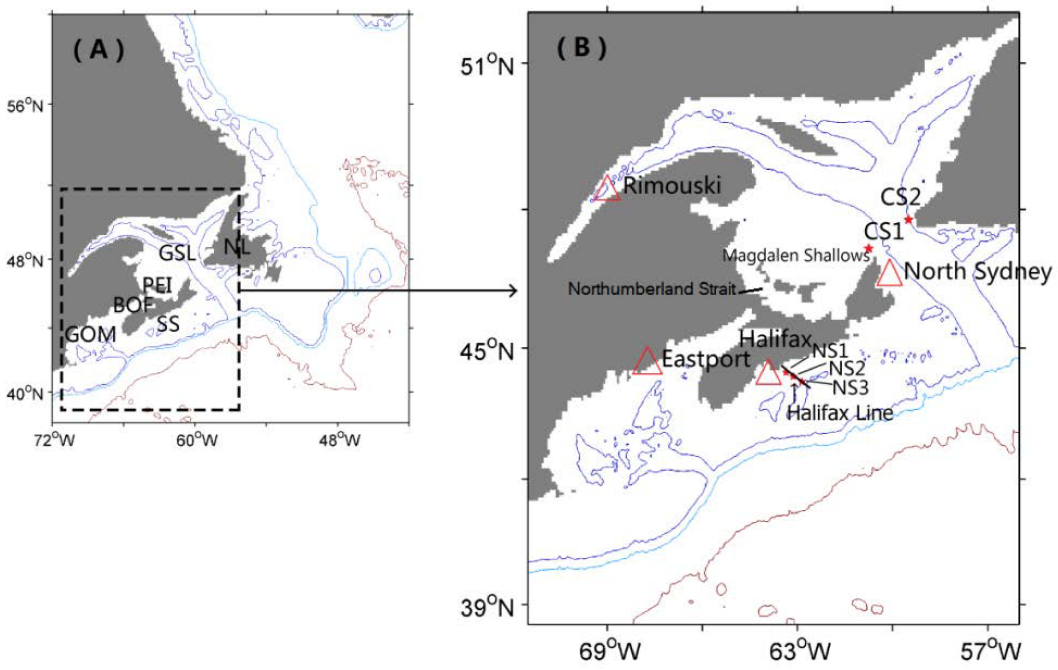

Figure 2.1：Domain and bathymetry of (a) the coarse-resolution outer model and (b) fine-resolution inner model of DalCoast. The 200, 1000, and 4000 meter depth contours of the model bathymetry are shown. Abbreviations are used for the Gulf of Maine (GoM), the Bay of Fundy (BoF), the Scotian Shelf (ScS), Prince Edward Island (PEI), the Gulf of St. Lawrence (GSL), and Newfoundland (NL). The red triangles in (b) mark the positions of four tide gauges (Rimouski, North Sydney, Halifax, and Eastport). The red stars in (b) represent the approximate release locations for near-surface drifters along the Halifax line and drifters on Cabot Strait. In (b) three bottom-mounted ADCPs were located at the positions marked by red stars and labelled NS1, NS2 and NS3 over the central Scotian Shelf.

The nested-grid circulation modelling system is initialized from a state of rest with the model initial temperature/salinity set to be the December mean hydrographic climatology. The modelling system is integrated for 25 months from the beginning of December 2006 to the end of December 2008. The model results after September 2007 are used for model validation and analysis.

2.2.2 Particle Tracking Model

Lagrangian trajectories of virtual particles (v-particles) carried passively or actively by ocean currents are very useful for estimating the fate of oil spills (*Soomere et al.,* 2010) or living organisms (*Corell,* 2012; *Ohashi and Sheng,* 2015), as well as for planning rescue operations or finding lost goods. In large enough quantities, Lagrangian trajectories of v-particles can be used to track entire water masses, or to map the mean flow (*Richardson,* 1983).

The particle tracking scheme used in this study is the one developed by *Ohashi and Sheng* (2015). The 3D movement of a v-particle carried by time-varying 3D ocean currents can be calculated as:

$$\vec{x}^{t+\Delta t} = \vec{x}^{t} + \int_{t}^{t+\Delta t} \vec{u}(\vec{x}, t)dt + \vec{\delta} \tag{2.1}$$

where $\vec{x}^{t+\Delta t}$ and $\vec{x}^{t}$ are position vectors of a passive particle at time $t + \Delta t$ and previous time t respectively, $\vec{u}(\vec{x}, t)$ is the velocity vector of model currents, and $\vec{\delta}$ is the 3D random walk component to account for the subgrid-scale turbulence and other local processes that are not resolved by the inner model. The 3D random walk component $\vec{\delta}(\delta x, \delta y, \delta z)$ in the x, y, and z directions can be expressed as (*Taylor,* 1922): $\delta x = \xi\sqrt{2K_h\Delta t}$, $\delta y = \xi\sqrt{2K_h\Delta t}$, $\delta z = \xi\sqrt{2K_z\Delta t}$. Here, ξ is a Gaussian random number in the range of [-1, 1], K_h and K_z are the horizontal and vertical eddy diffusivity coefficients, and Δt is the time step (which is one hour in this study) used for time integration in Eq (2.1). Eddy diffusivity coefficients (K_h and K_z) can vary in space and time. Past studies using drifters and numerical particle-tracking experiments (*Tseng,* 2002; *Thompson et al.,* 2002) suggested that the horizontal and vertical eddy diffusive coefficients in the coastal ocean vary from 10^{-1} to 10 m^2 s^{-1} and from 10^{-4} to 10^{-2} m^2 s^{-1}, respectively. In this

study, the hourly inner model currents are used to drive this particle tracking scheme. We follow *Shan and Sheng* (2012), set the horizontal diffusivity coefficient for the random walk (K_h) to be 1.0 $m^2\ s^{-1}$, and set the vertical diffusivity (K_z) to be $10^{-3}\ m^2\ s^{-1}$. According to *Shan and Sheng* (2012), the effects of random walk with these diffusivity coefficients are small on affecting the movements of the numerical particles in ocean, which means that the advection is the dominant process to driver the numerical particles. The fourth-order Runge-Kutta scheme (*Carpenter et al.,* 2005) is used to track the passive particles.

2.3 Model Validation

DalCoast has been validated extensively using various oceanographic observations in the past (*Thompson et al.,* 2007; *Ohashi et al.,* 2009a,b; *Ohashi and Sheng,* 2013, 2015). Previous studies show that DalCoast has good skill in simulating the vertical distribution of temperature and salinity fields over the model domain. In this study, the performances of the inner model of DalCoast and the particle tracking model are further validated using three types of oceanographic observations. The first type of observations is the sea level observations at four tide gauge sites: (a) Rimouski on the northwestern GSL, (b) North Sydney on western Cabot Strait, (c) Halifax on the central Scotian Shelf, and (d) Eastport on the inner GoM. The tide gauge data were taken from the website of Department of Fisheries and Oceans, Canada. Locations of these four sites are shown in Fig. 2.1b. The second type is the sub-surface current measurements made by three Acoustic Doppler Current Profilers (ADCPs) moored at locations NS1, NS2, and NS3 along the Halifax Line over the Scotian Shelf (Fig. 2.1b, *van der Baaren and Tang,* 2009).

The third type of oceanographic measurements is the observed trajectories of near-surface drifters collected during the satellite-tracked surface drifter program by *van der Baaren and Tang* (2009). As part of this drift program, two drifter experiments were conducted respectively in October 2007 and October 2008. In October 2007, seven near-surface drifters were deployed at the 5-m depth along the Halifax line at three different sites (NS1, NS2, and NS3) during the fall cruise of Fisheries and Oceans Canada's Atlantic Zone Monitoring Program (AZMP) (Fig. 2.1b). In October 2008, four near-

surface drifters were deployed at 5 m over western Cabot Strait (CS1) and eastern Cabot Strait (CS2) respectively (Fig. 2.1b). Two types of near-surface drifters were used respectively in the two drifter experiments. The first type of the drifters (Type 1), which was used for the first drifter experiment along the Halifax Line in October 2007, is the Self-Locating Datum Marker Buoy (SLDMB) manufactured by Seimac Ltd. The Seimac drifter has a pyramid-shaped float above the water line, with an electronic unit underneath and a fishnet-type surface drogue tethered to the electronic unit. The second type of drifters (Type 2), which was deployed over the Cabot Strait in October 2008 in the second drifter experiment, is also the SLDMB but manufactured by MetOcean Data Systems. The MetOcean drifter has a cylindrical hull for the electronics and four vanes with a foam float attached to it and an antenna above the hull. Position information of these drifters, including longitude, latitude and time, was collected half-hourly for the Seimac drifters and hourly for the MetOcean drifters. The data of the position information are transmitted to Argos satellites. Similar types of drifters were used to track ice drift previously by *van der Baaren and Prinsenberg* (2000 a,b; 2001; 2006).

To quantify the model performance, we use the γ^2 index suggested by *Thompson and Sheng* (1997):

$$\gamma^2 = \frac{Var(O-M)}{Var(O)} \tag{2.2}$$

where *Var* represents the variance operator, and *O* and *M* denote the observed and model simulated variables respectively. Physically, the γ^2 index represents the ratio between the variance of the model hindcast errors and the variance of the observations. The smaller γ^2 is, the better is the model performance. In this study, $\gamma^2 = 1$ is chosen as a threshold value to assess the model performance.

2.3.1 Surface Elevations

Figure 2.2 presents time series of the observed and simulated surface elevations at four tidal gauge sites (Rimouski, North Sydney, Halifax, and Eastport) during a 11-day period (1-12 October 2007). During this period, normal weather without any severe storms prevailed over the study region. Therefore, temporal variability of the surface elevations

shown in Fig. 2 is mostly associated with tidal elevations. The γ^2 values are about 0.089 at Rimouski, 0.105 at North Sydney, 0.057 at Halifax, and 0.035 at Eastport (Fig. 2.2). These small γ^2 values indicate that about 89-96% of the total variance of the observed surface elevations at these four sites are accounted for by the model results. These small small γ^2 values also indicate that the inner model of DalCoast has satisfactory hindcast skill in reconstructing the time evolution of surface elevations at these four sites.

To assess the model skill in simulating individual tidal constituents in the study region, a tidal harmonic analysis was conducted to estimate amplitudes and phases of four major tidal constituents (M_2, S_2, K_1, and O_1) from time series of observed and simulated surface elevations at the four sites for October 2007. As shown in Table 2.1, the M_2 constituent estimated from observations at the four sites has amplitudes ranging from ~37 cm at North Sydney on Cabot Strait to ~261 cm at Eastport on the inner GoM. The S_2 constituent at the four sites has amplitudes ranging from ~8 cm at North Sydney to ~50 cm at Rimouski in the northwest GSL. By comparison, the K_1 constituent has relatively small amplitudes of about 7-17 cm at all four sites. The O_1 constituent has also relatively small amplitudes of about 5.1-10.6 cm at all four sites.

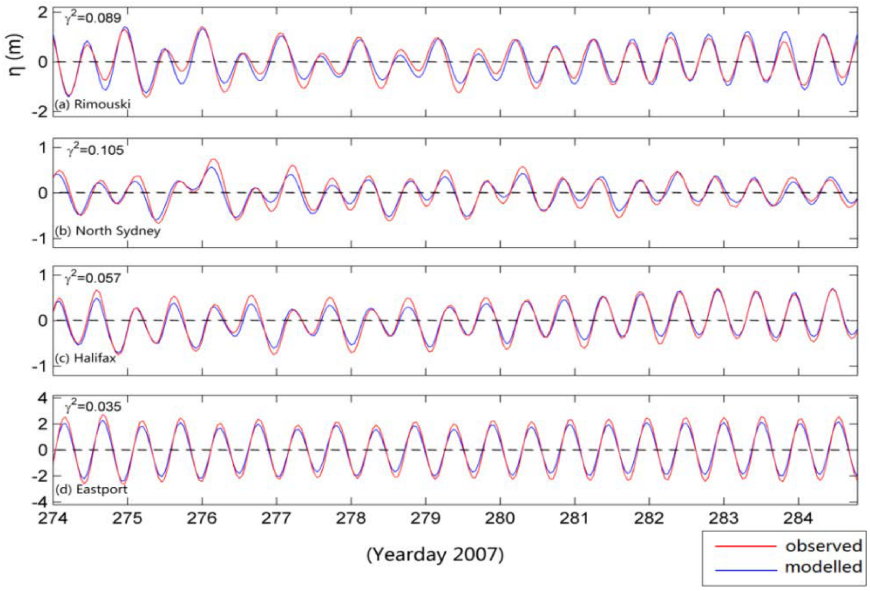

Figure 2.2: Time series of observed and simulated sea surface elevations at four sites of (a) Rimouski, (b) North Sydney, (c) Halifax, and (d) Eastport. These four sites are marked in Fig. 1b. The simulated sea surface elevations are produced by the inner

model of DalCoast. Table 2.1: Amplitudes and phases of four major tidal constituents calculated from observed and simulated sea surface elevations in October 2007 at Rimouski, North Sydney, Halifax, and Eastport.

	Amplitude (cm)			Phase (deg)		
Station	Observed	Modeled	△H	Observed	Modeled	△φ
			M_2			
Rimouski	131.52	123.81	7.71	347.17	345.93	1.24
North Sydney	37.33	35.04	2.29	104.86	98.50	6.36
Halifax	64.28	58.46	5.52	80.04	78.91	1.07
Eastport	261.44	252.19	9.25	131.83	140.23	-8.4
			S_2			
Rimouski	49.67	48.06	1.61	300.77	300.18	0.59
North Sydney	8.25	7.70	0.55	251.57	251.99	-0.42
Halifax	15.89	14.79	1.10	22.87	20.06	2.81
Eastport	47.13	45.92	2.21	86.76	89.75	-2.99
			K_1			
Rimouski	16.69	18.21	-1.52	296.92	284.41	12.51
North Sydney	10.81	9.67	1.14	347.20	330.37	16.83
Halifax	6.87	8.96	-2.09	124.45	140.25	-15.8
Eastport	10.74	8.08	2.65	195.82	188.61	-12.79
			O_1			
Rimouski	27.92	29.70	-1.79	318.06	321.74	-3.68
North Sydney	8.19	10.60	-2.41	341.76	353.80	-12.04
Halifax	5.11	6.13	-1.02	170.68	185.63	-14.95
Eastport	11.97	8.43	3.33	329.32	306.45	22.87

Table 2.1 also demonstrates that the inner model of DalCoast reproduces reasonably well the observed amplitudes and phases of M_2 at the four sites, with the absolute model errors (differences between observations and model results) of about 2.3-9.5 cm in amplitude and between -8.4^o and 6.4^o in phase at the four sites. For S_2, the model errors are about

0.6-2.2 cm in amplitude and between -3^{o} and 2.8^{o} in phase. The absolute model errors in amplitude and phase for these two major semidiurnal tidal constituents are small.

For K_1, the model errors are between -2.1 and 2.7 cm in amplitude and between -13^{o} and 17^{o} in phase. It should be noted that the relative model errors in amplitude are small and about 3-9% for the two major semi-diurnal tides (M_2 and S_2), but relatively large and about 6-30% for the two diurnal tides (K_1 and O_1). Further studies are needed to examine the main physical processes affecting the performance of DalCoast in simulating these two diurnal tides.

We follow *Pugh* (2004) and quantify the type of tides at these four sites based on estimations of tidal amplitudes in Table 2.1 using the form factor (*F*) defined as

$$F = \frac{H_{O1}+H_{K1}}{H_{M2}+H_{S2}} \tag{2.3}$$

where H_{O1}, H_{K1}, H_{OM2}, and H_{S2} are respectively the amplitudes of diurnal tides K_1 and O_1 and semi-diurnal tides M_2 and S_2 based on observed or simulated values listed in Table 2.1. The tides are considered to be (a) semidiurnal for *F* values less than 0.25; (b) mixed and mainly semidiurnal for *F* values of 0.25-1.5, (c) mixed for *F* values of 1.5-3.0, and (d) mainly diurnal for *F*>3. The form factor at Rimouski and North Sydney is about 0.25 and 0.42 respectively, indicating that the tides at these two sites are mixed and mainly semidiurnal (Fig. 2.2a,b). The tides at Rimouski are more semidiurnal than those at North Sydney. The form factor is about 0.15 at Halifax and 0.07 at Eastport, indicating that tides at these sites are mainly semidiurnal (Fig. 2.2c,d). The tides at Eastport are more purely semidiurnal than those at Halifax.

2.3.2 Sub-Surface Currents

Figure 2.3 presents time series of observed and simulated currents at NS1, NS2, and NS3 for the 11-day period of 1-12 October 2007. These three sites were located inside the main pathway of the Nova Scotia Current (*Dever et al.,* 2016). The Nova Scotia Current is a coastal current flowing southwestward over the inner Scotian Shelf (*Petrie,* 1987). This Current originates from the northwestern GSL, where a large-scale estuarine plume

and an intense coastal jet known as the Gaspé Current are developed due to a large amount of freshwater discharges from the St. Lawrence River (*El-Sabh,* 1976; *Tang,* 1980; *Sheng,* 2001). The Gaspé Current spreads over the southwestern GSL and exits through western Cabot Strait. After emanating from the western Cabot Strait, the low-salinity waters flow onto the eastern Scotian Shelf (eScS) to form the Nova Scotia Current (*Petrie,* 1987; *Urrego-Blanco and Sheng,* 2012).

The observed sub-surface currents shown in Figs. 2.3a,b and 3g,f demonstrate that both the eastward and northward components of observed sub-surface currents at 15 m and 30 m at site NS1 have time-mean values of about -0.2 m/s during this 11-day period. These time-mean sub-surface currents represent the southwestward Nova Scotia Current. The observed sub-surface currents at site NS1 also have tidal currents and large synoptic (i.e., mainly wind-driven) variabilities and significant sub-synoptic and seasonal variabilities. Tidal analysis indicates that the barotropic tides (not shown) account for small portions of observed temporal variabilities at these two depths at NS1. At sites NS2 and NS3, by comparison, the observed sub-surface currents at 15 m and 30 m (Figs 2.3c-f and 2.3i-l) have similar temporal variabilities as those at site NS1, but with much weaker time-mean sub-surface currents at these two sites than at site NS1. Furthermore, the barotropic tidal currents (not shown) account for relatively large portions of the observed temporal variabilities of sub-surface currents at NS2 and NS3. It should be noted that the core of the Nova Scotia Current was located near site NS2 (see Fig. 2.6 of *Dever et al.,* 2016) in the period 2011-2014. The sub-surface current observations shown in Fig. 2.3, however, indicate that the core of the Nova Scotia Current was located near site NS1 during the 11-day period in October 2007. Further studies are needed to explain the main physical processes affecting the onshore shift of this Current in October 2007.

Figure 2.3 also demonstrates that the simulated sub-surface currents produced by the inner model of DalCoast agree reasonably well with the current observations at depths of 15 m and 30 m of these three sites. The γ^2 values are about 0.41-0.45 (0.47-0.52) for the eastward (northward) components of simulated currents at site NS1, 0.46-0.62 (0.42-0.57) for the eastward (northward) component at site NS2, and about 0.41-0.52 (0.32-0.46) for the eastward (northward) components at sites NS3. In comparison with the γ^2

values for the simulated surface elevations, the inner model of DalCoast reproduces less well the observed currents than the observed sea surface elevations. This could be explained by the fact that the ocean currents are more sensitive to the small-scale features of topography than sea surface elevations.

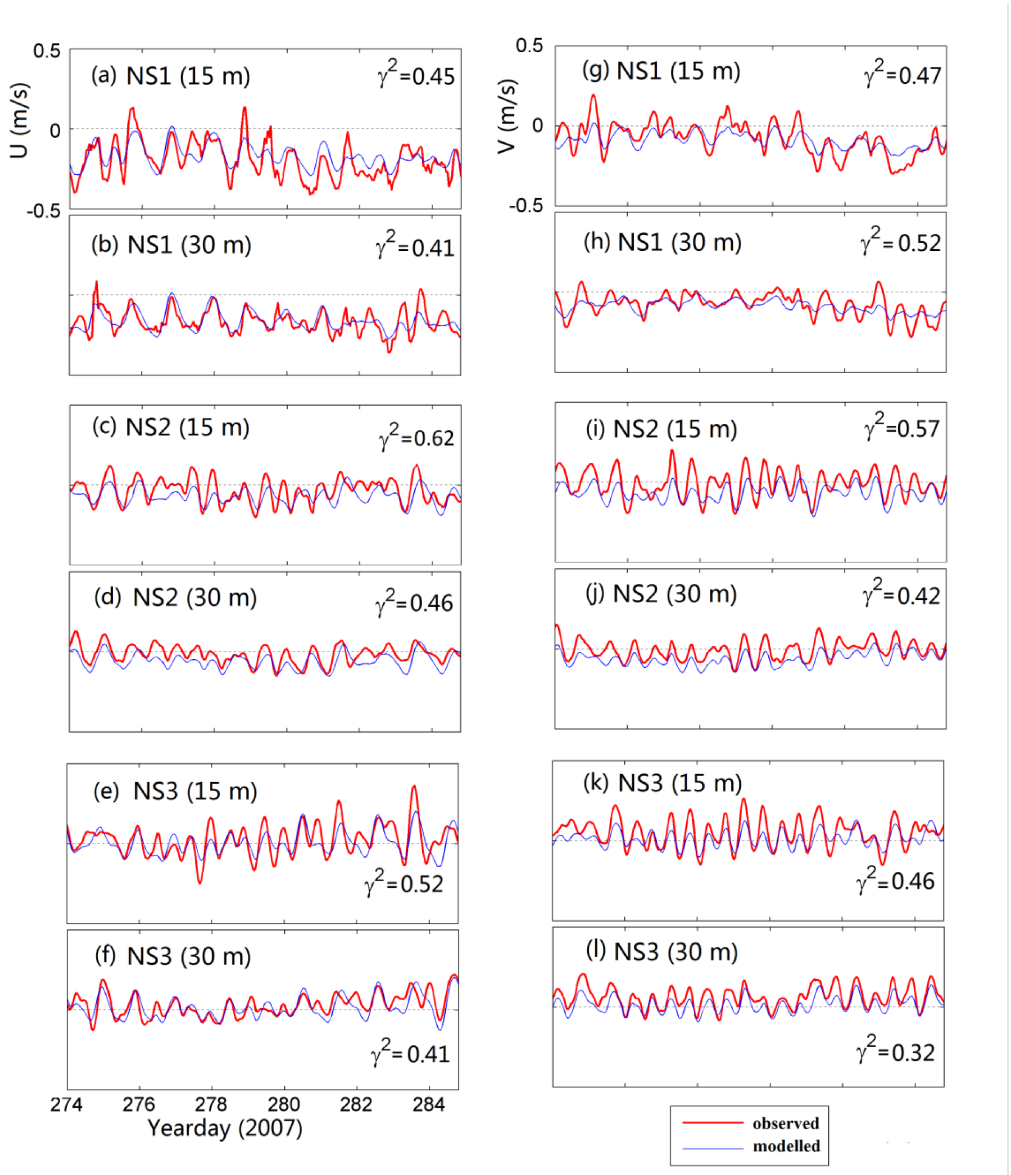

Figure 2.3: Time series of eastward (left) and northward (right) components of observed (red) and simulated (blue) sub-surface currents during a 11-day period in October 2007 at depths of 15 m and 30 m respectively at sites NS1, NS2, and NS3 along the Halifax Line over the central Scotian Shelf.

2.3.3 Particle Trajectories

To compare simulated trajectories calculated from model currents with observed trajectories of near-surface drifters, we conducted particle tracking experiments by releasing nearly 200 virtual particles (v-particles) uniformly over a circular area of 4.4 km^2 centered around the release location of each SLDMB drifter. The main reason for releasing the v-particles over a small area instead of at a specific point is that actual movements of drifters are affected by many physical processes, including some small-scale processes that are not resolved in the circulation model.

We assess the performance of the particle tracking model by comparing the observed trajectory of a near-surface SLDMB drifter with the simulated trajectory of the horizontal "center of mass (CoM)" for a group of v-particles. The simulated v-particles are released in an area surrounding the initial position of the real drifter. By calculating the CoM for a group of v-particles, stochastic property of v-particles which induced by the random walk component in particle tracking model is reduced significantly. In this study, v-particles are set to remain in the surface waters. The hourly simulated currents produced by the inner model are used to drive the particle tracking model.

Since a small part of each SLDMB drifter was above the sea surface (*van der Baaren and Tang,* 2009), the observed trajectory of the real drifter was affected by winds at the sea surface. To account for the effect of winds on the observed trajectory, the velocity vector $\vec{u}(\vec{x}, t)$ in Eq. (2.1) is replaced by

$$\vec{u}(\vec{x}, t) = (1 - \alpha) \times \vec{u}_o(\vec{x}, t) + \alpha \vec{u}_w(\vec{x}, t) \tag{2.4}$$

where $\vec{u}_o(\vec{x}, t)$ is the ocean velocity vector produced by the inner model, $\vec{u}_w(\vec{x}, t)$ is the wind velocity vector, and α is the wind transfer coefficient, which is dependent on the volume and shape of the SLDMB drifter exposed to the wind at the sea surface. The wind's effect on the drifter's movement is also known as the leeway factor and has been a subject of past studies. For example, *Smith* (1992) described a set of experiments using AST (Accurate Surface Tracker) in which a wind coefficient was parameterized in terms of the ratio of exposed to submerged frontal areas.

Figure 2.4 presents observed trajectories of type 1 SLDMB drifters (red solid lines) released at points very close to the ADCP sites NS1, NS2 and NS3 along the Halifax Line over the central Scotian Shelf (cScS). The four drifters were released between 11th October and 16th October 2007. For the two near-surface drifters released at points close to NS1, their trajectories over approximately five days after the release (Figs. 2.4a and 2.4b) demonstrate that these drifters moved southwestward along the coastline with average speeds of about 30 km/day. The near-surface drifter released at the point close to site NS2 (Fig. 2.4c) moved approximately westward at first and then southwestward, roughly parallel to the coastline, for five days, with a lower average speed of about 15 km/day. The near-surface drifter released at the point close to site NS3 drifted near its release point (Fig. 2.4d), moving northwestward, northeastward, then southeastward. The observed movements of the four near-surface drifters shown in Fig. 2.4 are roughly consistent with the general circulation over the cScS indicated by the sub-surface current measurements shown in Fig. 2.3.

The simulated (CoM) trajectories of v-particles with six different wind transfer coefficients (α) ranging between 0 and 0.03 (colored dashed lines) are also shown in Fig. 2.4. The v-particles released over a small area close to NS1 (with $\alpha \leq 0.03$) (Fig. 2.4a,b) have significant southwestward (alongshore) movements, which are very similar to the SLDMB drifters released at the same points. The v-particles released over a small area close to NS2 (Fig. 2.4c) have moderate alongshore movements in comparison with those shown in Fig. 2.4a,b. The v-particles released at a small area close to NS3 stay close to their release area (Fig. 2.4d), with much smaller net displacements in comparison with those in Fig. 2.4a-c. Some noticeable differences occur in simulated trajectories for different values of wind transfer coefficients (α), indicating the effects of surface winds on the movements of v-particles.

Figure 2.5 presents the observed trajectories for type 2 SLDMB drifters released at points close to sites CS1 and CS2 over western and eastern Cabot Strait respectively. The two drifters are released between 16th October to 20th October 2008. The two SLDMB drifters released at points close to CS1 had significant southeastward movements during the first three days then turned southwestward to move onto the eSCS on the last day (Fig.

2.5a,b). By comparison, the SLDMB drifters released at points close to CS2 moved northeastward during the first day (Fig. 2.5c,d). They reversed directions to travel southward, parallel to the local coastline, for the next two days and then moved westward/northwestward during the last two days. Fig. 2.5 also demonstrates that the v-particles released in small areas close CS1 and C2 (with $\alpha \leq 0.05$) have trajectories very similar to the observed trajectories of SLDMB drifters.

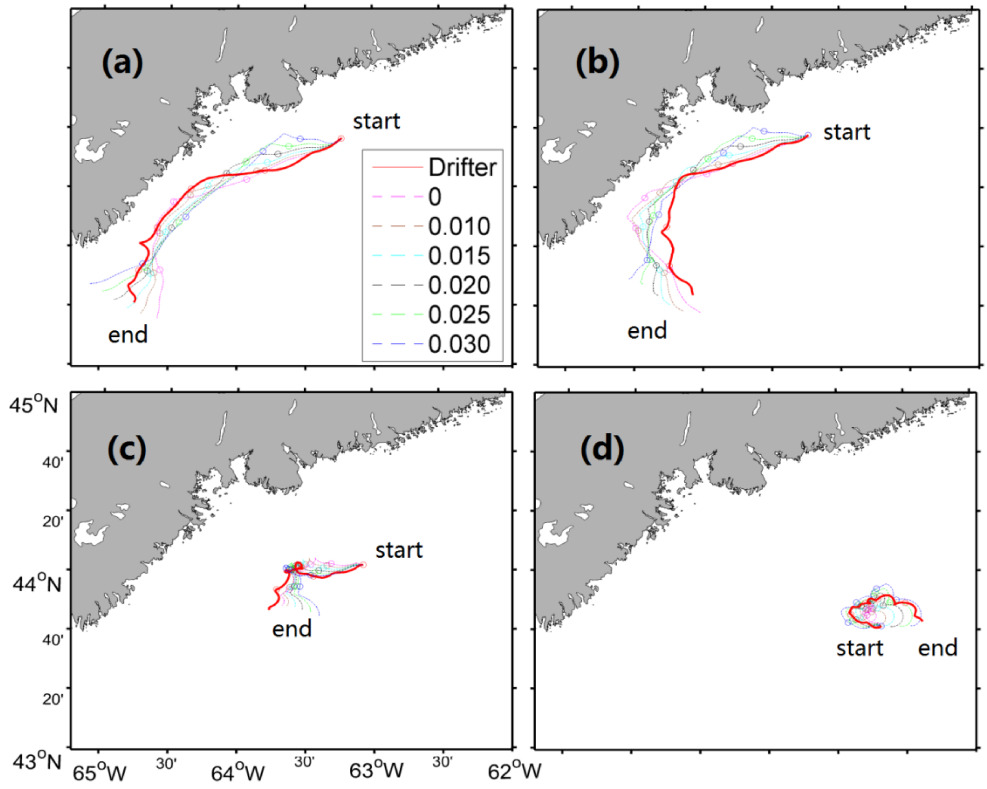

Figure 2.4: Comparisons of observed trajectories (red solid lines) with simulated CoM trajectories (coloured dashed lines) calculated by the particle tracking model with different wind transfer coefficients for v-particles released over a small area centered at (a) NS1, (b) NS1, (c) NS2 and (d) NS3 along the Halifax Line over the central Scotian Shelf. Circles mark positions at 24-hour intervals.

Based on time series of separation distances shown in Figs. 2.6a and 2.6c, we calculate the time mean separation distances averaged over 120 hours (mean error) and show them in Figs. 2.6b and 2.6d as a function of α. The optimal value for the wind transfer coefficient is $\alpha \approx 0.015$ for type 1 SLDMB drifters and $\alpha \approx 0.030$ for type 2 SLDMB

drifters.

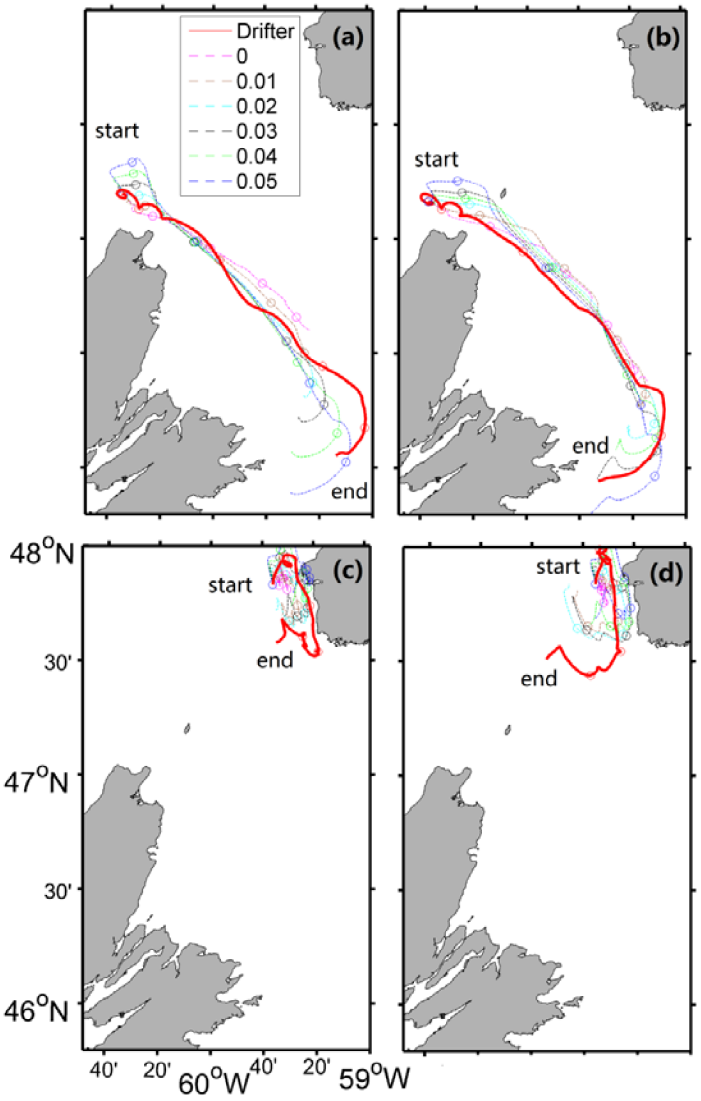

Figure 2.5: Comparisons of observed trajectories (red solid lines) with simulated CoM trajectories (coloured dashed lines) calculated by the particle tracking model with different wind transfer coefficients for v-particles released over a small area centered at (a) CS1, (b) CS1, (c) CS2 and (d) CS2 over Cabot Strait. The circles mark positions at 24-hour intervals.

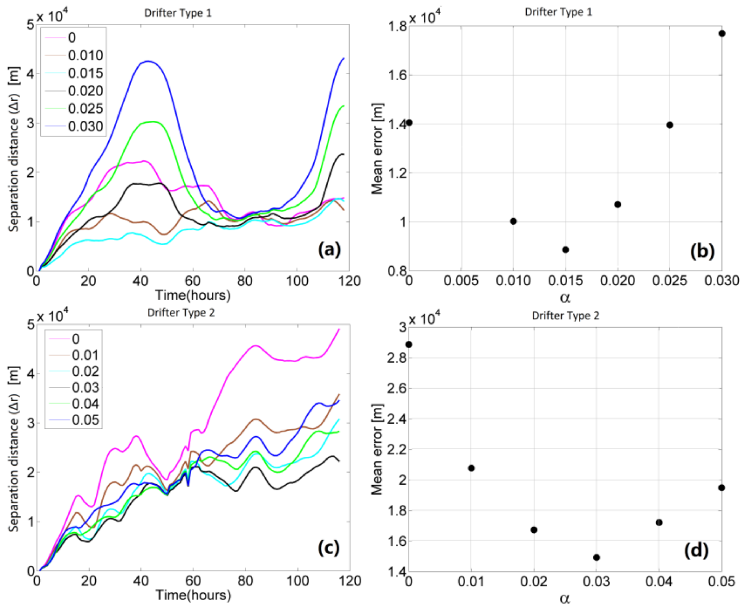

Figure 2.6: (a, c) Time series of separation distances (Δr) between real and simulated drifters in terms of different wind transfer coefficient values. (b, d) Separation distances averaged over the experiment period. Results are for (a) type 1 and (b) type 2 of SLDMB drifters.

2.4 Retention and Hydrodynamic Connectivity

Simulated trajectories of v-particles carried passively by ocean currents produced by the inner model of DalCoast (with $\alpha = 0$) are used to estimate the retention and hydrodynamic connectivity over the Scotian Shelf and adjacent waters (including the southwestern GSL, inner GoM and BoF).

2.4.1. Retention over the Eastern Canadian Shelf

To quantify retention of passive particles, we follow *Cong et al.* (1996) and introduce the retention index for a giving duration. The study area is first divided into subareas of equal size. The retention index is then defined as:

$$R(\vec{x}, t) = \frac{N(\vec{x},t)}{N(\vec{x},t_0)} \tag{2.5}$$

where $N(\vec{x}, t_0)$ is the number of v-particles released initially in a subarea of a given size centered at $\vec{x}$ at initial time t_0, and $N(\vec{x}, t)$ is the number of v-particles remaining within

the subarea at time t. Physically, the retention index represents the proportion of v-particles released in a giving subarea at time t_0 remaining over the duration of $(t - t_0)$. The value of retention index $R(\vec{x}, t)$ is between 0 and 1. A high value of $R(\vec{x}, t)$ corresponds to high retention of v-particles in the given subarea for the duration. In the case of $R(\vec{x}, t) = 0$, all the v-particles released at time t_0 are flushed out from the subarea during the given duration. The subarea used in this study is set to a square box with a horizontal dimension of 33×33 km^2. To eliminate the effect of small-scale circulation features from the experiment results, the distance between centers of two adjacent boxes is set to 3.5 km. To calculate the retention indices over the study region, the v-particles are released in a horizontally uniform pattern in the surface waters of top 5 m over the inner model domain. The initial horizontal distance between two adjacent v-particles is set to 2000 m (or ~270 v-particles per 1000 km^2). The retention indices are calculated based on movements of v-particles using the hourly surface currents produced by the inner model in February, May, August, and November 2007 (Fig. 2.7).

The horizontal distributions of retention indices on day 5 (R_5) have similar large-scale features (Fig. 2.7) in the four months, with relatively high retention indices (60-80 %) over the BoF, inner GoM, central and eastern Scotian Shelf, Northumberland Strait, and Magdalen Shallows. Relatively low retention indices (30-40 %) occur over narrow coastal zones over western and eastern Cabot Strait, and the inner shelf and the shelf break of the Scotian Shelf. The low retention indices over these regions are consistent with relatively strong surface currents (see more discussion in section 2.4.2). The R_5 distributions also have significant seasonal variabilities. Over the middle and outer shelf regions of the eSCS and cScS, the R_5 values are relatively high in February, August and November and relatively low in May. Over the Magdalen Shallows, the R_5 values are relatively high in February, May and August and relatively low in November. Over the inner GoM and BoF, the R_5 values are relatively high in November and relatively low in May and August.

The large-scale features of retention indices on day 10 (R_{10}) are similar to those on day 5, except that regions with high retention indices (60–80 %) on day 10 are significantly reduced (Fig. 2.7). In particular, the R_{10} values are low (less than 30%) in these four

months over western Cabot Strait, inner Scotian Shelf, outer shelf regions of the western Scotian Shelf. Relatively large R_{10} values (70%) occur over Northumberland Strait in the four months, over the middle of the eSCS in August and September, and over coastal waters off western Nova Scotia in February.

The retention indices on days 15 and 20 (R_{15} and R_{20}) are generally low over the study region, except for coastal waters around Northumberland Strait, some offshore areas of the ScS, and coastal waters in the BoF (Fig. 2.7).

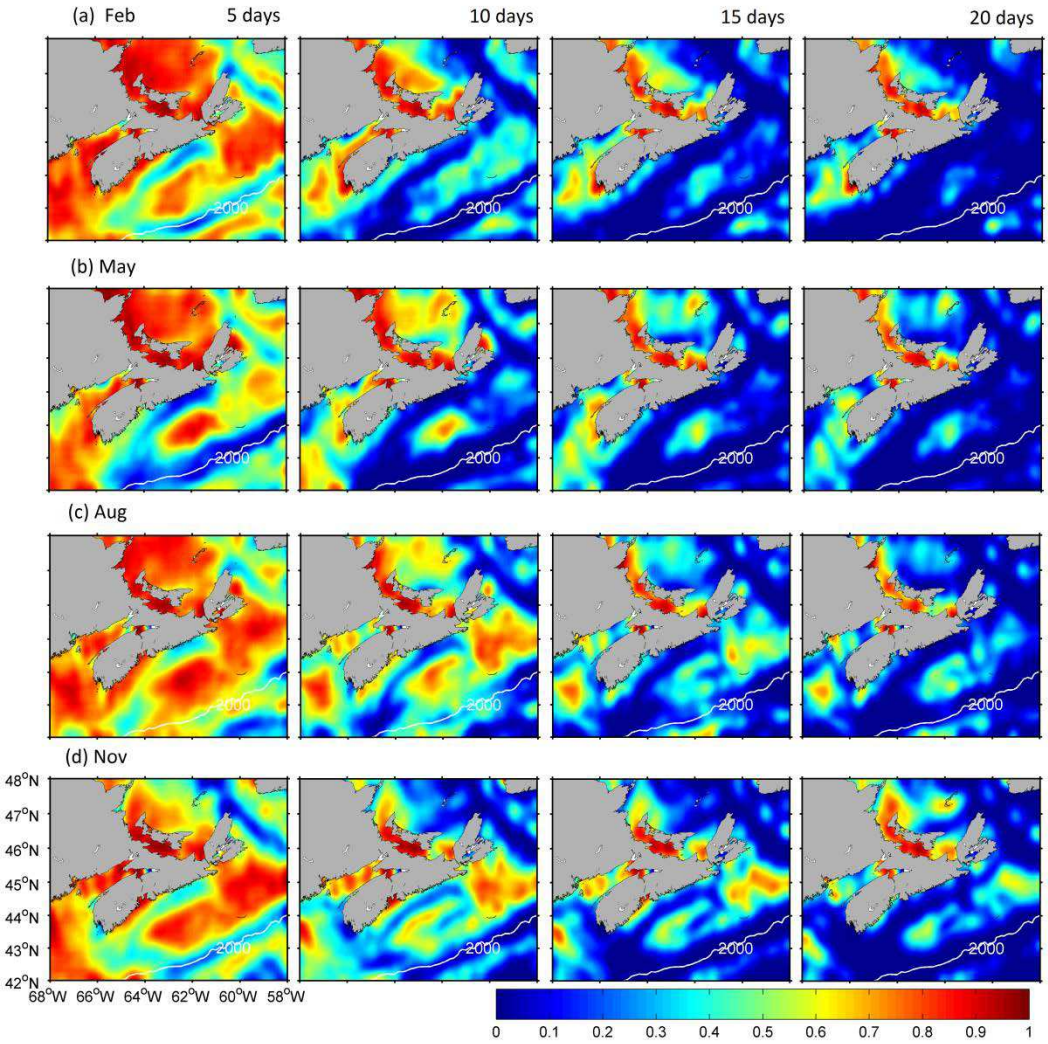

Figure 2.7: Distributions of retention indices over the Scotian Shelf and adjacent waters (including the southwestern GSL, inner GoM and BoF) calculated from horizontal movements of near-surface v-particles driven by hourly near-surface current produced by the inner model in (a) February, (b) May, (c) August, and (d) November 2007. The white contour line represents the water depth of 2000 m.

2.4.2 Physical Processes Affecting Retention

As shown in the previous section, the horizontal distributions of retention calculated from simulated trajectories of near-surface v-particles have significant temporal and spatial variability. To quantify the main physical processes affecting the retention over the Scotian Shelf and adjacent waters, three different numerical experiments were conducted. The model setups and the sub-grid scale mixing parameterizations are the same but the model's external forcings are changed among the experiments as follows:

1. Control Run (*CR*): The circulation modelling system (DalCoast) in this experiment is driven by all forcing terms as discussed in section 2.2, which include tidal forcing, wind forcing, atmospheric pressures, sea surface heat fluxes, river runoff and open boundary forcing.
2. No Tides Run (*NT*): Same as the *CR*, except that the tidal forcing is excluded from this experiment. Specifically, both the tidal currents and tidal elevations are set to zero along the open boundaries of the inner model.

3. No Wind Run (*NW*): Same as the *CR*, except that the local wind stress is set to zero in the inner model.

The model results from these three experiments are then used to quantify the role of the tides and local wind over the ScS and adjacent waters. Let φ_{CR}, φ_{NT}, φ_{NW} be the model results from the model run *CR*, *NT* and *NW*, respectively. The effects of the tidal forcing can be estimated by

$$\Delta\varphi_{tide} = \varphi_{CR} - \varphi_{NT} \tag{2.6}$$

Similarly, the effects of the local wind forcing can be quantified approximately by

$$\Delta\varphi_{wind} = \varphi_{CR} - \varphi_{NW} \tag{2.7}$$

Figure 2.8 presents the effect of tidal forcing ($\Delta\varphi_{tide}$) on retention indices over the Scotian Shelf and adjacent waters on day 20 in the four months of February, May, August, and November 2007. The common feature of the tidal effects in these four

months is that the tidal forcing reduces the retention indices in the BoF by about 40–50 %. The tidal forcing also reduces the retention indices over coastal waters off southwest Nova Scotia in May, August, and November, but enhances the retention indices over the same coastal waters in February.

Figure 2.9 presents the effect of local wind forcing ($\Delta\varphi_{wind}$) on retention indices over the Scotian shelf and adjacent waters on day 20 in the four months of February, May, August, and November. The wind forcing reduces the retention indices over the southwestern GSL and western Cabot Strait in the four months (with the most significant reduction in February when the local winds are strongest), and also reduces the retention indices over the eScS in February and May. But the wind forcing enhances the retention over coastal waters off the southwest Nova Scotia in February, May, and August and enhances the retention over the eScS in November.

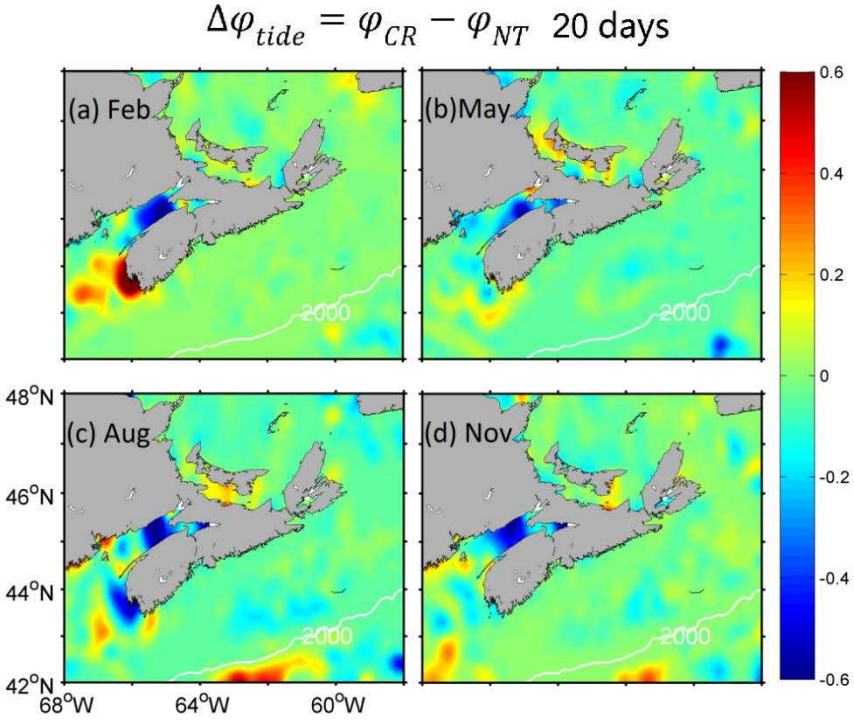

Figure 2.8: Distributions of retention indices due to the tidal forcing ($\Delta\varphi_{tide}$) on 20 days over the Scotian shelf and adjacent waters in (a) February, (b) May, (c) August, and (d) November 2007. The white contour line represents the water depth of 2000 m.

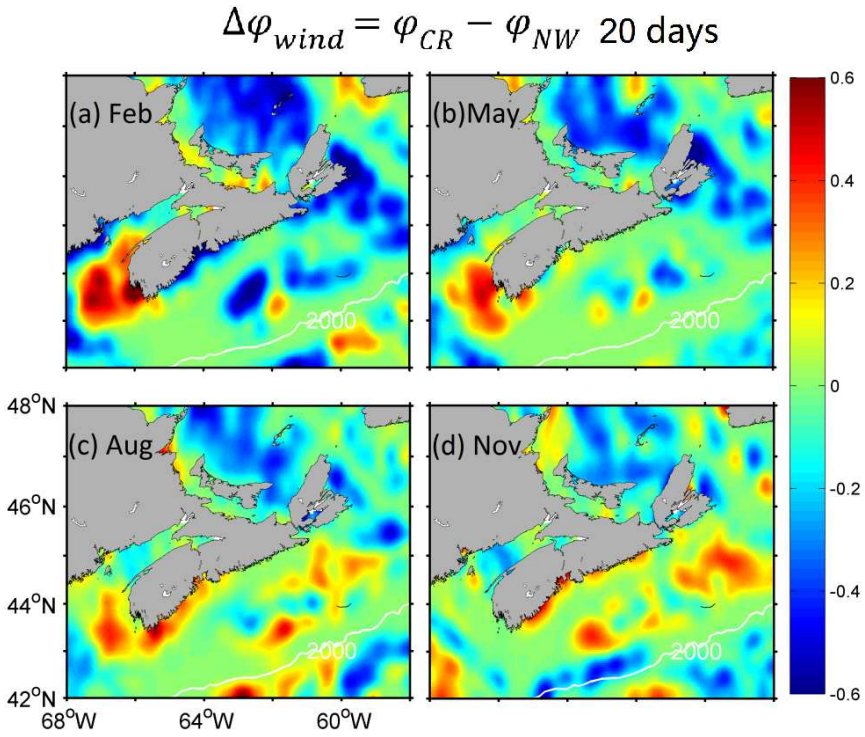

Figure 2.9: Distributions of retention indices due to wind forcing ($\Delta\varphi_{wind}$) on 20 days over the Scotian Shelf and adjacent waters in (a) February, (b) May, (c) August, and (d) November 2007. The white contour line represents the water depth of 2000 m.

It should be noted that the wind forcing over the study region exhibits strong seasonal variability (Fig. 2.10). In February and May of 2007, winds are roughly eastward. In August, winds blow from the southwest and are weaker than in other seasons. In November, winds are roughly southward in the GoM and northeastward over the ScS and the GSL. The large seasonal variability in the local wind forcing introduces large seasonal variability in the surface circulation over the study region, leading to large seasonal variabilities in the retention indices as shown in Fig. 2.9.

The local wind forcing enhances the surface currents over the Magdalen Shallows in all four months (Fig. 2.10). In consequence, the transportation of the near-surface particles from GSL to ScS is facilitated. In February, the eastward winds generate southeastward

offshore currents along the south coastline of Nova Scotia (Fig. 2.10a-1). This offshore current disperses the near-surface particles, which is consistent with the coastline retention reduction (Fig. 2.9a). In August and November, the northeastward winds decelerate the Nova Scotian current and even generate reverse flows along parts of the coastline (Fig. 2.10 c-1, d-1), which is consistent with the coastline retention addition (Fig. 2.9c, d). In February, May, and August, the eastward winds generate onshore surface current and enhance the retention indices along the western coastline of Nova Scotia. But in November, the southward winds do not have significant effects along the same location.

2.4.3 Hydrodynamic Connectivity

In this section we examine the hydrodynamic connectivity for three sensitive areas in the study region in terms of upstream and downstream areas using the simulated trajectories of near-surface v-particles. The upstream (or source) area of a given site (or area) is defined as the area from which particles (or material) are transported to the site. The downstream (or sink) area of a given site (or area) is defined as the area to which particles are transported from the site.

The three areas selected for this study are (a) St. Anns Bank, (b) Deep Panuke offshore oil and gas platforms, and (c) the outer Bay of Fundy (Fig. 2.11). St. Anns Bank has been selected by the Fisheries and Oceans Canada as a new area of interest for potential designation as a Marine Protected Area (*Ford and Serdynska,* 2013). The Bay of Fundy is known for its high tides with a maximum tidal range of about 16.9 m. A demonstration project for harnessing tidal energy using "In-stream turbine technology" has been conducted in the eastern part of the BoF (*Lambert,* 2016).

We follow *Tang et al.* (2006) and define the downstream area as the sum of all subareas to which more than 2% of particles originally released over the surface of a given source area travel within 20 days. Similarly, the upstream area of a designated sink area is defined as the sum of all subareas from which at least 2% of particles in the sink area originated during the previous 20 days. Physically, the downstream area defined here is a potential area to which the surface particles could be exported from the designated source

area within a given time as 20 days. The upstream area is a potential area from which the passive particles could be transported to a designated sink area within the same period. The size of the subareas used in this section is the same as that used in the calculation of retention indices discussed in section 2.4.1.

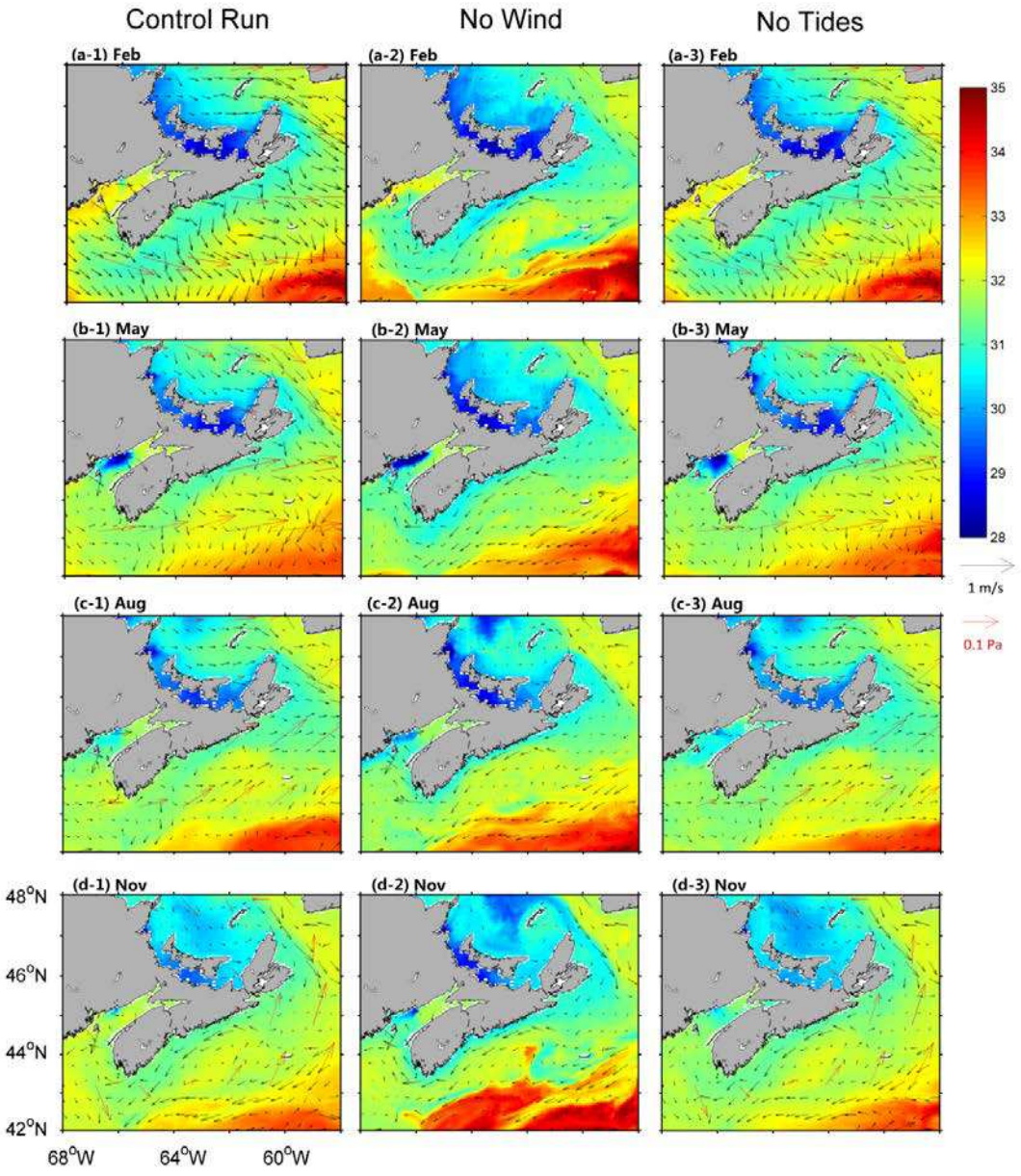

Figure 2.10: Mean surface currents and salinity fields (Control Run, No Wind and No tides) produced by inner model for 20 days in (a) February, (b) May, (c) August, and (d) November in 2007. Red arrows are wind stress vectors. For clarity, velocity vectors are plotted at every seventh model grid point.

It should be noted that the total number of v-particles over each subarea of the upstream and downstream areas are time and space dependent. In general, the total number of v-particles are higher over subareas closer to the initial v-particle release area.

The 20-day downstream (sink) area for the St. Anns Bank (DA_{SAB}) consists of the main part over the inner shelf of the eScS and a small part along the eastern flank of the eScS (Fig. 2.11). The former is associated with the main pathway of the southwestward Nova Scotia Current over the coastal waters of the eScS. The latter is associated with a small branch of the outflow emanating from the GSL that continues to flow southeastward along the eastern flank of the eScS. The pattern of DA_{SAB} has large seasonal variabilities. The main part of DA_{SAB} over the inner shelf of the eScS extends most significantly southwestward (alongshore) to reach coastal waters off Taylor Head in February (Fig. 2.11a) and spreads offshore most significantly to the middle of the eScS in November (Fig. 2.11d). A small part of DA_{SAB} reaches the shelf waters to the south of Misaine Bank and Eastern Shoal in February and May (Fig. 2.11a,b) and reaches the shelf break waters to the southern Banquereau Bank over the eScS in November.

The 20-day downstream area for the Deep Panuke offshore oil and gas platforms (DA_{DP}) cover a narrow corridor to the west/southwest of the platform as a result of the southwestward jet over the shelf break of the cScS. The narrow corridor is centered over the shelf break of the cScS in May, August, and November. In February, by comparison, the narrow corridor extends further southwestward to reach the northwest Atlantic Ocean waters off the shelf break of the western Scotian Shelf. The horizontal dimension of DA_{DP} is about 400 km by 100 km in February and 200 km by 200 km in other months. In August, the DA_{DP} also has a narrow stripe extending northward from the platforms to the inner shelf of the eScS.

The 20-day downstream area for the outer Bay of Fundy (DA_{BoF}) covers over the coastal waters outside the BoF and off the western Nova Scotia in the four months (Fig. 2.11). In May, August and November, DA_{BoF} also includes the surface waters over the inner BoF. It should be noted that D_{BoF} is significantly smaller than DA_{SAB} and DA_{DP}. The reason is the general mean currents in BoF is relatively weaker than the counterparts over the

eastern flank of the eScS and the shelf break of the cScS, even though the tides are strong in BoF.

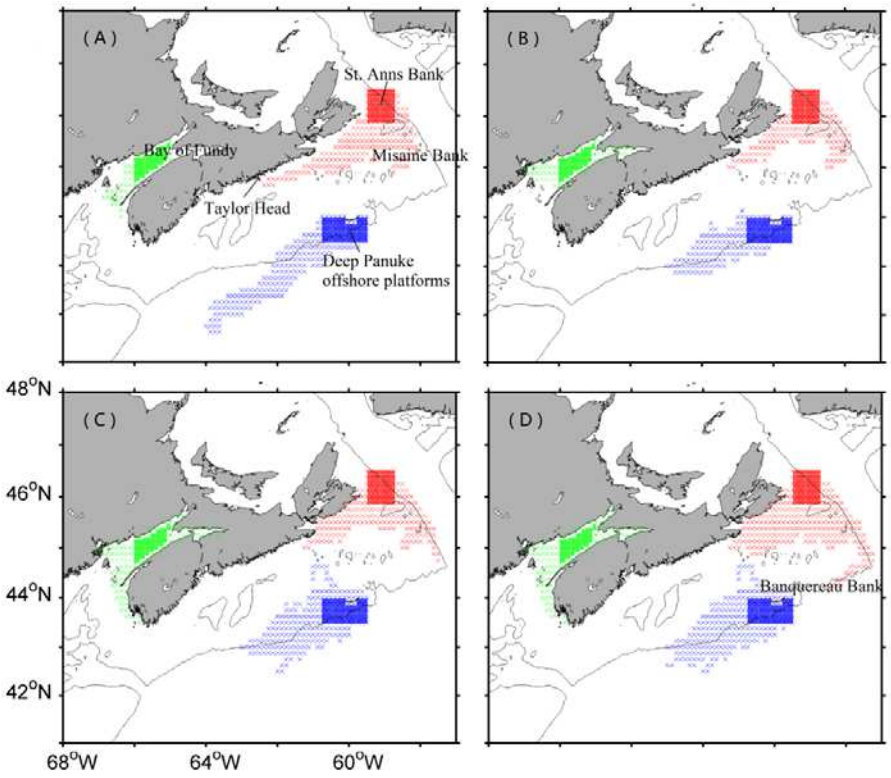

Figure 2.11: Downstream (sink) areas for St. Anns Bank (red), the Deep Panuke Offshore Platforms (blue), and the outer Bay of Fundy (green) within 20 days calculated from the hourly current field produced by the inner model in (a) February, (b) May, (c) August, and (d) November 2007. The 200-m water depth contours are shown as black lines.

Figure 2.12 presents the 20-day upstream (source) areas for the above three selected shelf areas in February, May, August and November. The 20-day upstream area for St. Anns Bank (UA_{SAB}) covers surface waters over western Cabot Strait and adjacent southern GSL and centered over waters of about 200 m depth in the four months, associated with the southeastward flow from the GSL to the eScS. The upstream area UA_{SAB} extends significantly northward to the central GSL in February and November in comparison with those in May and August (Fig. 2.12b,c). The upstream area UA_{SAB} is largest in November (Fig. 2.12d) and smallest in August among the four months. Furthermore, the source area for St. Anns Bank also includes surface waters over the western Grand Banks in February and November (Fig. 2.12a,d), associated with a cross-channel flow from the western

Grand Banks to the eScS in these two months.

The 20-day upstream area for the Deep Panuke offshore oil and gas platforms (UA_{DP}) is a narrow zone centered around the 200-m water depth over the shelf break to the east of the platforms in the four months and some surface waters over the western side of the mouth of the Laurentian Channel (Fig. 2.12). The pattern of UA_{DP} is consistent with the southwestward jet over the shelf break of the eScS.

The 20-day upstream area for the outer Bay of Fundy (UA_{BoF}) includes surface waters over the inner BoF and the Saint John River, with some surface waters outside the BoF (Fig. 12). In comparison with St. Anns Bank and Deep Panuke platforms, the outer Bay of Fundy has a much smaller source region, is limited mainly to the inner BoF.

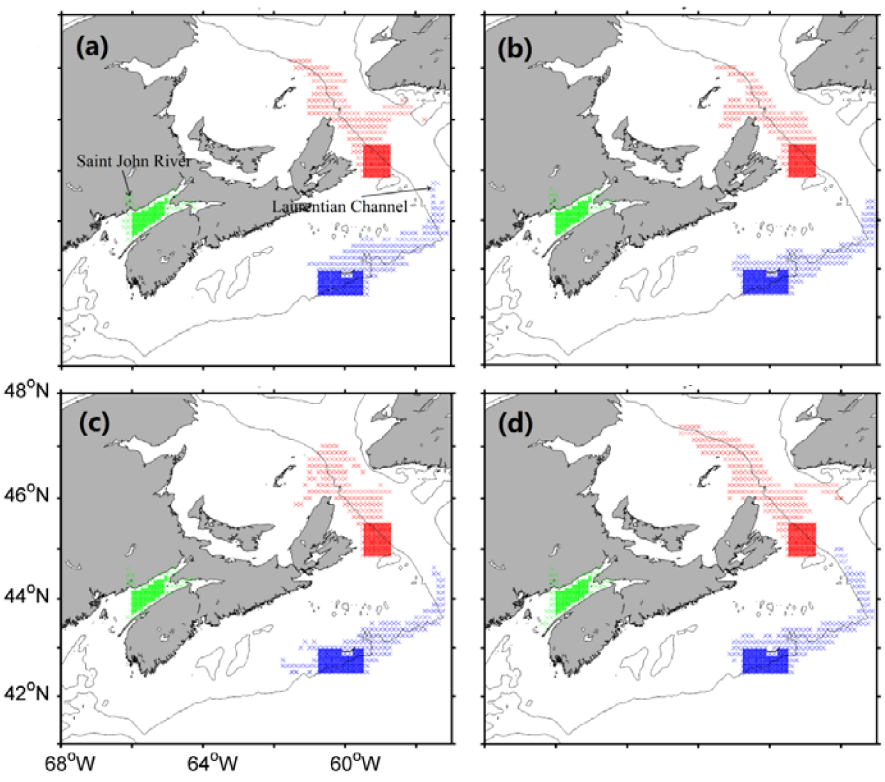

Figure 2.12: Upstream (source) areas for (a) St. Anns Bank (red), (b) the Deep Panuke Offshore Platforms (blue), and (c) the outer Bay of Fundy (green) within 20 days calculated from the hourly current field produced by the inner model in (a) February, (b) May, (c) August, and (d) November 2007. The 200-m water depth contours are shown as black lines.

2.5 Summary and Conclusions

A nested-grid circulation modelling system and a Lagrangian particle tracking model were used to study the three-dimensional circulation, particle movements, retention and connectivity over the Scotian Shelf, southern Gulf of St. Lawrence (GSL), inner Gulf of Maine (GoM), Bay of Fundy (BoF) and their adjacent deep ocean waters. The circulation modelling system has a fine-resolution baroclinic inner model nested inside the coarse-resolution barotropic outer model. A conventional one-way nesting technique was used to transfer information from the outer model to the inner model. The model validation presented in this study and in previous studies made by *Thompson et al.* (2007), and *Ohashi et al.* (2009a,b) and *Ohashi and Sheng* (2013) demonstrated that the inner model has reasonable skills in simulating sea surface elevations, ocean currents, temperature and salinity over the study region. Hourly inner model currents were used to track movements of near-surface virtual particles (v-particles) over the study region. Retention indices (R) for surface waters over the study region were calculated based on the simulated movements of v-particles carried passively by surface ocean currents. It was found that the retention within 10 days is relatively high for surface waters in Northumberland Strait, over the outer shelves of the eastern and central Scotian Shelf (eScS and cScS), in the outer and central BoF, and over the inner GoM. By comparison, the retention is relatively low for surface waters over western Cabot Strait and the part of southern GSL adjacent to it, over the inner shelf of the eScS and cScS, and outer shelf of the western Scotian Shelf (wScS), and along the shelf break and its adjacent waters of the Scotian Shelf. The regions with low retention are associated with relatively strong and persistent surface currents.

Regarding the relationship between retention discussed in this Chapter and spread of particles (or tracers), two different methodologies have been used to measure the spread of water particles (or tracers): the absolute dispersion and relative dispersion (*Enrile et al.,* 2019; *Haza et al.,* 2008). The absolute dispersion is defined as spreading of water particles due to the combined effect of advection and diffusion. Advection is referred to as movements of water particles carried passively by ocean currents. Diffusion is referred

to as the random motion of water particles due to turbulence (or molecular) in the water (*Hassan et al.,* 2002). The relative dispersion can be estimated by removing the effects of advection on the absolute dispersion (*Enrile et al.,* 2019; *Haza et al.,* 2008). In this study, we quantified the retention (*R*) of surface waters, which is negatively correlated with the absolute dispersion.

There are several different ways to investigate the hydrodynamic connectivity of oceans and other water fields. A numerical method of tracking particles is one of the best ways to examine the particulate material transport (*Salamon et al.,* 2006). The numerical particle tracking method can be implemented in numerical circulation models (online) or used separately based on given ocean currents (offline). The accuracy of particle tracking requires high temporal and spatial resolutions of simulated currents, which indicates high computational expenses. Considering drawbacks of the conventional particle tracking method, a concept of dynamical system analyses called the Lagrangian Coherent Structures (LCS) was used to visualize hydrodynamic connectively of ocean (*Zhang et al., 2006*). Previous studies revealed that the LCS can be considered as a kind of material surface or line which does not allow materials to pass through. Based on such characteristics, the LCS can roughly construct the particle trajectories and the transport mechanism of particles might be studied only by analyzing LCS even without releasing particles (*Choi and Hwang*, 2002). However, the reliability of using LCS as tool to evaluate the material transport in the ocean required further studies.

The knowledge of the retention and hydrodynamic connectivity of surface waters over the GSL-ScS-GoM is important to economic activities and management of ecosystem dynamics over the region. For example, the retention rates of the surface water can be used to interpret the spatial distributions of abundance and size of larval fish (e.g., Atlantic herring, Atlantic cod, silver hake, while capelin) over the ScS (*Reiss et al*., 2000). Previous studies suggested that strong advection (low retention rate) of the surface waters may result in extensive mortality among the larvae fish. High concentrations of larvae fish were found to occur within the region of high retention waters (*Reiss et al*., 2000).

The upstream (source) and downstream (sink) areas for surface waters over (a) St. Anns Bank, (b) Deep Panuke offshore oil and gas platforms and (c) the outer BoF were also calculated from simulated movements of near-surface v-particles. The main upstream area for surface waters over St. Anns Bank is a narrow corridor to the northeastward of the Bank, which covers offshore surface waters centered around the 200-m water depth over western Cabot Strait and adjacent southern GSL. The downstream area for surface waters over St. Anns Bank covers mainly surface waters over the inner shelf of the eScS. For the Deep Panuke offshore oil and gas platforms, the upstream area is a narrow strip over the shelf break of the eScS, and the downstream area is the relatively broad strip of surface waters over the shelf break and adjacent deep ocean waters off the cScS. By comparison, the upstream area for the outer BoF is very small and limited mostly to surface waters over the inner Bay of Fundy and the Saint John River. The downstream area for the outer BoF includes coastal waters outside the BoF and off western Nova Scotia and also some surface waters over the inner BoF. In this study, the density of v-particles in upstream and downstream areas for surface waters is not calculated. More studies should be conducted to show how many particles there are in each grid cell. It should be noted that the simulated movements of v-particles, retention indices, and upstream and downstream areas have significant seasonal variability. More studies are needed to examine the interannual and decadal variabilities of circulation, retention and hydrodynamic connectivity of surface and sub-surface waters over the Scotian Shelf and adjacent waters.

CHAPTER 3

NUMERICAL STUDY OF LANDWARD INTRUSION OF OFFSHORE SUB-SURFACE WATERS INTO BEDFORD BASIN

3.1 Introduction

As discussed in the Chapter 2, the three-dimensional (3D) circulation and hydrography over the Scotian Shelf (ScS) are strongly affected by winds, tides, local topography and other physical processes. In this Chapter, the 3D currents, temperature and salinity in Halifax Harbour (HH), and main processes affecting the landward intrusion of offshore sub-surface waters into Bedford Basin (BB) are studied using a nested-grid ocean modelling system.

HH consists of the Outer Harbour (OH), Inner Harbour (IH), Northwest Arm, Narrows and BB, and is situated on the south coast of Nova Scotian (Fig. 3.1). The Harbour is one of the world's largest natural harbours and has significant environmental and economic values (*William,* 2010*; Shan et al.*, 2011). HH is encircled by the largest urban population centre in eastern Canada. As the inner portion of HH, BB is accessible and very important to the community (Fig. 3.1). BB is a bowl-shaped estuary with a surface area of ~17 km^2, a volume of ~500 km^3, and a maximum depth of ~71 m. The Basin is connected with the adjoining coastal waters of the ScS through a narrow and shallow channel known as the Narrows (Fig. 3.1). The Narrows is ~500 m wide, 3 km long, and with the mean depth of about ~20 m (*Fader and Miller*, 2008).

The largest single freshwater source for HH is the Sackville River at the northwestern end of BB. The freshwater discharges from the Sackville River account for about 1/3 of the total freshwater discharges for HH, with the annual mean discharge of about 5.41 m^3s^{-1} (*Buckley and Winters*, 1992). Time series of daily mean discharges of the Sackville River in 2014 is shown in Fig. 3.2. The freshwater discharges of the Sackville River are affected by large precipitations including both rain and snow. In 2014, there are two large

peaks in the rate of discharge occurring respectively in January and December (Fig. 3.2). As the ice and snow melt in spring, the discharge of the Sackville River increases rapidly, resulting in several large peaks in April 2014. The remaining freshwater discharge in HH comes from a number of small streams and sewage and waste waters with 16 % of the total delivered by the Halifax wastewater treatment system (*Fader & Buckley*, 1995). Due mainly to the freshwater discharge, the time mean current pattern in HH is a two-layer estuarine-type circulation, with lower-density upper waters flowing towards the open sea and saline waters flowing into BB in the lower layer through the Narrows (*Heath, 1973*; *Petrie and Yeats*, 1990; *Shan and Sheng*, 2012).

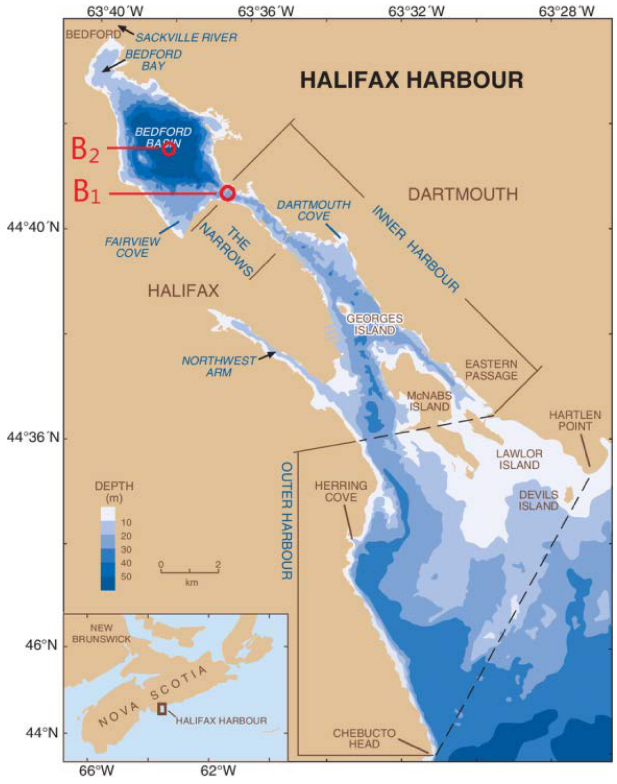

Figure 3.1: Map of Halifax Harbour, Nova Scotia, Canada (*Fader and Miller*, 2008). B_1 shows the location of Bedford Basin tidal gauge station. B_2 shows the location of the observation made by Bedford Basin Monitoring Program (BBMP).

The 3D circulation, temperature and salinity in HH are also affected by winds and tides. Winds in HH exhibit significantly large temporal variability including large synoptic and seasonal variability. The prevailing winds over this area are predominantly

southerly/southwesterly in the summer and westerly/northwesterly in the winter (*Environmental Assessment Report*, 2013). Previous studies suggested that the predominant westerly or northwesterly winds in the winter can enhance the two-layer estuarine circulation in HH, leading to strong intrusion into BB (*Shan*, 2010). During periods of predominant southwesterly winds in summer, the water temperature in HH can be cooled by a few degrees due to advection of cool upwelling waters generated along the south shore of Nova Scotia (*Petrie et al*., 1987).

Tides in HH were found to be mainly semi-diurnal, which are relatively weak in BB and relatively strong in the Narrows (*Petrie and Yeats*, 1990). The mean and maximum tidal ranges in HH are ~1.3 m and ~2.1 m, respectively. The M_2 tidal component has an amplitude of about 63 cm and accounts for about 60% of the total tidal sea level in HH (*Lawrence*, 1989). The tidal currents can reach up to 15-35 cm/s in the Narrows and 5-15 cm/s in the IH and OH (*MacLaren Plansearch Limited*, 1991).

Significant efforts have been made in monitoring oceanographic conditions in HH due to its importance to the local community. The earliest recorded collection of in-situ temperature and salinity observations in BB was made by *Huntsman* (1924). The first field program was conducted from July 1969 to September 1971, with temperature and salinity measurements made monthly at eight cross-sections (*Jordan*, 1972). Observational studies on the ecological dynamics in BB were also made in 1970s (*Lewis and Platt*, 1982). An on-going field program in BB (44° 41' N, 63° 38' W) started in 2004 with weekly or bi-weekly observations (including temperature, salinity, fluorescence, nitrate concentration, and dissolved oxygen concentration), which has been made by the Bedford Basin Monitoring Program (BBMP, www.bio.gc.ca/science/monitoring-monitorage/bbmp-pobb/bbmp-pobb-en.php). The in-situ observations made by the BBMP are used in this study.

Several numerical models with different levels of complexity have been used in the past for simulating circulation and temperature/salinity in HH. A simple box model based on the conservation of mass and salt was used in studying the metal, suspended solids and nutrients distributions in BB (*Petrie and Yeats*, 1990). Using this box model and salinity

observations as input, *Petrie and Yeats* (1990) demonstrated that the time-mean density driven circulation in the Basin is a classical two-layer estuarine type as the low-salinity upper layer waters flowing toward the open sea and the sub-surface saltier waters moving toward the Basin. *Tee and Petrie* (1991) used a two-dimensional (2D) baroclinic circulation model and demonstrated that the time mean estuarine circulation in HH is driven primarily by freshwater discharges from the Sackville River. A 2D hydrodynamic model driven by the principal lunar semi-diurnal constituent M_2 and idealized wind forcing was developed by *MacLaren Plansearch Limited and Martec Limited* (1991) to simulate tides and wind-driven circulation in HH. A finite element model was used in simulating the effects of tsunami on the 2D circulations in HH during the 1917 explosion (*Greenberg et al*., 1993). A 3D hydrodynamic model based on the S-Coordinate Rutgers University Model (SCRUM, *Song and Haidvogel*, 1994) was used by *Zhang* (1998) in simulating the circulation patterns and temperature/salinity distributions in HH. A 3D linear harmonic finite element model was also used by *Greenberg* (1999) in simulating the M_2 tide in the Harbour. Recently, a nested-grid ocean circulation modelling system was used by *Shan et al.* (2011) in simulating circulation, temperature/salinity and associated variability in HH.

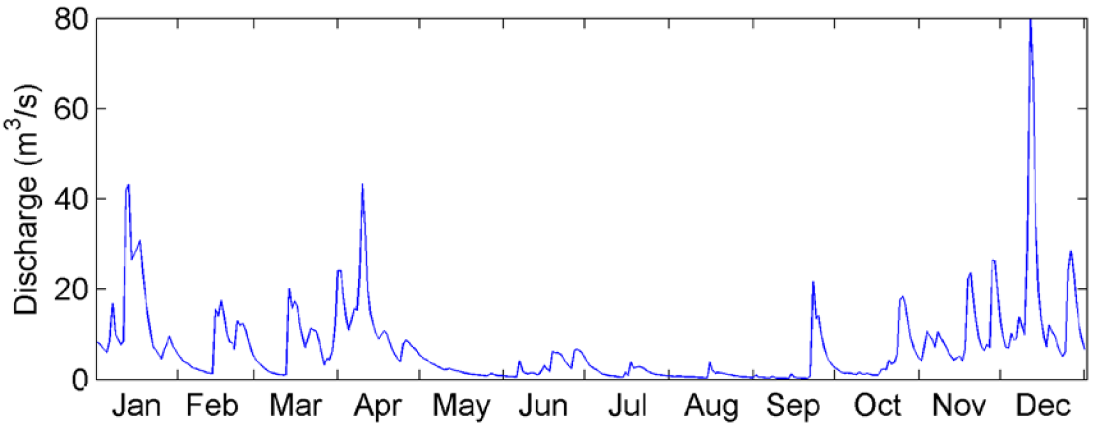

Figure 3.2: Time series of the daily mean freshwater discharges from the Sackville River in 2014. The discharges of the Sackville River were extracted from the Canada's National Water Data Archive (HYDAT) database.

Previous observational and numerical studies demonstrated that HH is seasonally stratified almost year-round, evident from the vertical distribution of temperature and salinity (*Lewis and Platt*, 1982; *Li and Harrison*, 2008). The salinity is relatively low in the surface waters and high in the deep waters of BB. In some years, however, the deep waters in BB can be replenished by high salinity waters occasionally (*Platt et al*., 1972; *Punshon & Moore*, 2004; *Burt et al.,* 2013). One plausible explanation is the lateral intrusion, which brings offshore sub-surface waters into the deep layer of BB through the Narrows. It was suggested that the lateral intrusion may result from strong and persistent winds, storm events, or a build-up of coastal sea levels (*Platt et al*., 1972; *Heath, 1973*; *Burt et al.,* 2013). During the intrusion events, the observed salinity in BB, particularly in the lower layer changed abruptly (*AMEC Earth and Environmental LTD,* 2011; *Burt et al.,* 2013). Although several intrusion events in BB have been identified in the past, the main processes affecting these intrusion events occurred were not well studied. In this Chapter, we further investigate the relationship between the intense intrusion events and local winds based on model results. The main objectives of this Chapter are:

i) To present a four-level nested-grid 3D ocean circulation model for HH and adjacent shelf waters of the ScS.
ii) To examine main processes affecting the landward intrusion of offshore sub-surface waters into BB using the nested-grid circulation model.
iii) To conduct a process study using the nested-grid circulation model to investigate the cumulative effects of winds and tides in affecting the time-mean circulation, temperature and salinity in HH.

The structure of this Chapter is as follows. Section 3.2 describes the setup and forcing of the nested-grid ocean circulation model. Section 3.3 presents the assessment of the model performance. Section 3.4 presents the general mean temperature/salinity and circulation in HH. Section 3.5 presents the analysis of model results during several intrusion events. Section 3.6 presents the process study of the cumulative effects of winds and tides on the 3D time-mean hydrodynamics in HH. The last section presents the summary and conclusions.

3.2 Nested-Grid Modelling System

A nested-grid ocean circulation model over the southeastern Canadian shelf (NGMS-seCS) was developed and validated (*Pei et al.,* 2022). NGMS-seCS is a four-level multi-nested coastal circulation-ice modelling system with four nested domains of progressively smaller areas and finer horizontal resolutions. This coupled circulation-ice modelling system is based on the Regional Ocean Modelling System (ROMS, *Shchepetkin and McWilliams,* 2005; *Fennel et al., 2006; Haidvogel et al*., 2008; *Brennan et al., 2016*) and the Los Alamos Sea Ice Model (CICE, zenodo.org/record/1205674). An external coupler (github.com/kshedstrom/roms) enables two-way coupling between ROMS and CICE. In this Chapter, NGMS-seCS is used to examine the variance in the distributions of circulation, temperature, salinity, and to define the time-varying 3D circulation in BB.

3.2.1 Model Setup

NGMS-seCS uses ROMS for simulating the 3D circulation and temperature/salinity, and CICE for simulating the sea ice condition (including the sea ice concentration and thickness). NGMS-seCS has four submodels (L1~L4). The domains and setup of submodels L1-L3 are the same as in *Pei et al*., (2022). Submodel L4 is newly-developed. The domain of submodel L1 covers the southeastern Canadian Shelf (seCS) and adjacent deep ocean waters between 80° W and 40° W, and between 34° N and 55° N (Fig. 3.3a), with a horizontal resolution of 1/12°. The domain of submodel L2 covers the Gulf of St. Lawrence-Scotian Shelf-Gulf of Maine (GSL-ScS-GoM) and adjacent deep ocean waters between 71.5° W and 56° W, and between 38.5° N and 52° N (Fig. 3.3b), with a horizontal resolution of 1/36°. The domain of submodel L3 covers the coastal and shelf waters of the southwestern ScS and adjacent waters between 66° W and 63° W, and between 43° N and 44.75° N (Fig. 3.3c), with a horizontal resolution of 1/108° (~1 km). The domain of submodel L4 covers HH and adjacent offshore waters of the ScS with a horizontal resolution of about 185 m (Fig. 3.3d).

A one-way nesting technique is used in the coupled modelling system, in which

information from the upper-level submodel is transferred to the lower-level submodel. Specifically, hourly model results of sea surface elevations, currents, temperature, salinity and sea ice conditions produced by submodel L1 are used to specify open boundary conditions for submodel L2. Similarly, hourly model results of submodel L2 (L3) are used to specify open boundary conditions for submodel L3 (L4). The main advantage of the nested-grid modelling system is that the lower-level submodel can resolve spatial features over a focal area relatively better than the upper-level submodel by using the dynamically consistent open boundary conditions provided by the upper-level submodel.

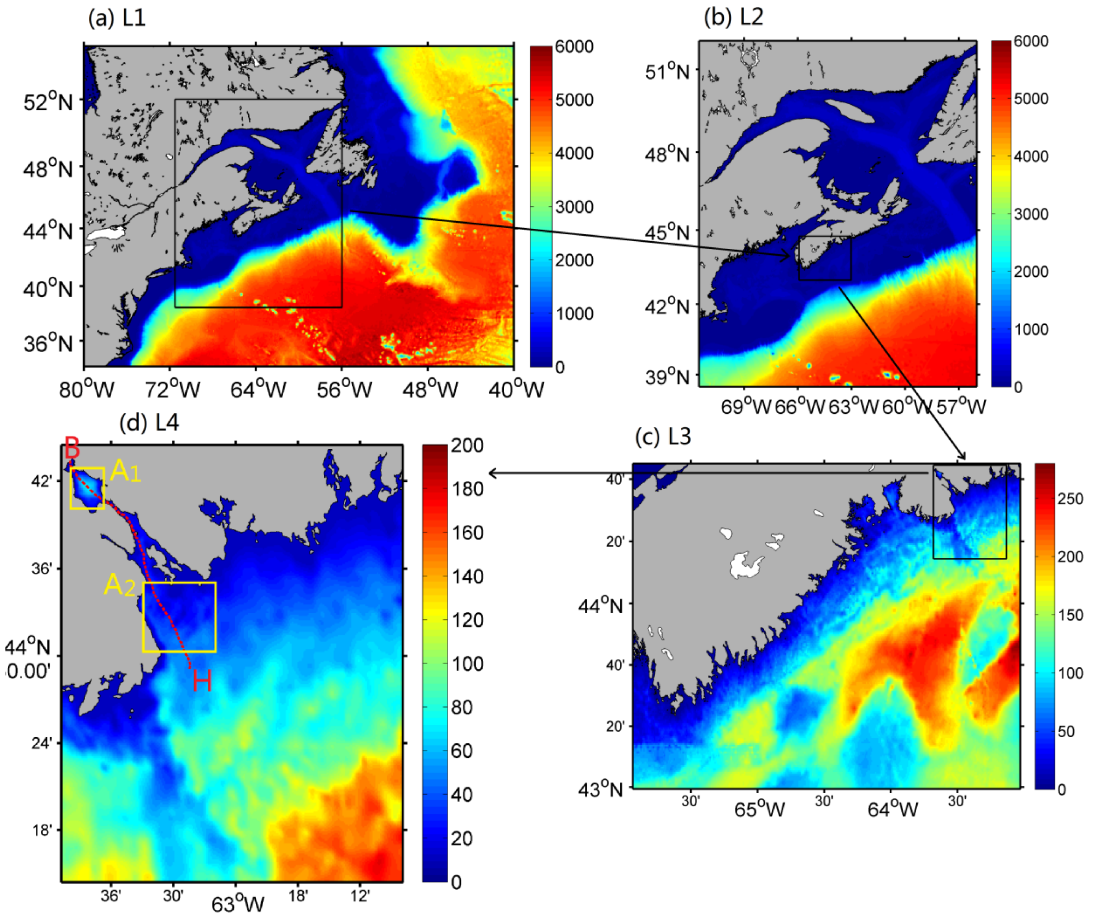

Figure 3.3: Major topographic features and domains of four submodels for a nested-grid coupled circulation-ice modelling system (NGMS-seCS) for the southeastern Canadian Shelf and adjacent deep ocean waters of the northwestern Atlantic Ocean. The horizontal resolutions of submodels (a) L1, (b) L2, (c) L3, and L4 are respectively 1/12°, 1/36°, 1/108° (~1 km) and ~180 m. The color image in each subplot represents water depths. The two yellow boxes shows the areas of A_1 and A_2. The red line in (d) is the longitudinal transect (BH) in Halifax Harbour.

ROMS is a free-surface, terrain-following, primitive-equation ocean circulation model. The circulation model for each submodel (L1~L4) has 40 S-coordinate levels in the vertical with relatively finer vertical resolutions near the sea surface and sea bottom. The S-coordinate transformations used in ROMS is defined as

$$z(x,y,\sigma,t) = \eta(x,y,t) + [\eta(x,y,t) + H(x,y)]\, S(x,y,\sigma), \tag{3.1}$$

$$S(x,y,\sigma) = \frac{H_c\sigma + H(x,y)C(\sigma)}{H_c + H(x,y)} \tag{3.2}$$

where $S(x,y,\sigma)$ is a nonlinear vertical transformation functional, $\eta(x, y, t)$ is the time-varying free-surface, and $z = -H(x,y)$ is the ocean bottom. Here σ is a fractional vertical stretching coordinate ranging from $-1 \le \sigma \le 0$, $C(\sigma)$ is a nondimensional, monotonic, vertical stretching function ranging from $-1 \le C(\sigma) \le 0$, and H_c is a positive thickness controlling the stretching (*Haidvogel et al*., 2008). The MATLAB programs provided by the ROMS website (www.myroms.org) are used to transfer the model results from each S-coordinate to Z-coordinate. ROMS has been used extensively over many different parts of the CSWs (e.g., *Fennel et al., 2006*; *Hu et al.,* 2012; *Brennan et al., 2016; Song et al.,* 2016a,b; *Takakura et al.*, 2019; *Pei et al*., 2022). Previous studies also demonstrated that ROMS has good performance in simulating 3D currents and temperature/salinity over the CSWs.

The model bathymetry for NGMS-seCS is based on the General Bathymetric Chart of the Oceans (GEBCO) 2014 dataset with a horizontal resolution of 30 arc-seconds (*Weatherall et al*., 2015). For submodel L4, the model bathymetry is constructed based on two datasets, including (1) the high-resolution model topography (which covering BB and the IH) used by *Shan and Sheng* (2012) with a horizontal resolution of about 200 m and (2) GEBCO (which covering the OH and adjacent waters). The sub-grid scale horizontal mixing used in NGMS-seCS is parameterized using the shear and grid size dependent scheme of *Smagorinsky* (1963). Vertical mixing in NGMS-seCS is parameterized using the *Mellor and Yamada* (1982) level-2.5 turbulent closure scheme.

CICE is a sea ice model for simulating the thickness, concentration and velocity of sea ice. It solves numerically two main sets of governing equations for the sea ice:

(a) Newton's second law for sea ice and (b) the sea ice thickness distribution for different thicknesses spread of the area (*Hunke et al.,* 2010). The sea ice thickness distribution is due to the thermodynamics of ice growth and melt, including the ice temperature resulting from radiative, turbulent, and conductive heat fluxes (*Lipscomb*, 2010). More details and governing equations of CICE are given in Appendices C. Development of CICE began in 1994 at Los Alamos National Laboratory (*Hunke*, 2010). Since its initial release in 1998, CICE has been substantially developed by an international community of model users and developers (*Hunke*, 2014).

In this thesis, an external coupler (github.com/kshedstrom/roms) is used for two-way coupling between CICE and submodel L1~L2 of ROMS. The two-way coupling between ROMS and CICE increases the computation time of the nested-grid modelling system by 30%~40%, which depends on conditions of the high-performance computing platform provided by the Digital Research Alliance Compute Canada (DRAC).

3.2.2 Model Forcing

NGMS-seCS is driven by tides, freshwater discharges, and atmospheric forcing including the atmospheric pressure at the mean sea level and wind stress. The atmospheric pressure was extracted from the three-hourly North American Regional Reanalysis dataset (NARR; *Mesinger* et al., 2006). The wind stress was calculated from the wind velocity extracted from the NARR dataset (at the 10 m above sea level) using the bulk formula of *Large and Pond* (1981). The ocean circulation model (ROMS) is also forced at the sea surface by the net heat flux, calculated from the sea surface temperature (computed by the ocean circulation model) in combination with three-hourly NARR fields of wind speed, air pressure, air temperature, cloud cover, downward shortwave radiation flux, and precipitation (*Mellor,* 2004). The tidal forcing including tidal sea levels and depth-mean currents is specified at the open boundaries of submodel L1. The harmonic constants of these 11 major tidal constituents (M_2, S_2, N_2, K_2, K_1, O_1, P_1, Q_1, M_4, MS_4, and MN_4) were extracted from the results produced by the Oregon State University Tidal Inversion System (OTIS, *Egbert and Erofeeva,* 2002), with a horizontal resolution of 1/6°.

In submodels L1 and L2, the freshwater discharges from 49 major rivers over the seCS are specified using the monthly mean climatological data (*Lin*, 2021; *Lin et al.,* 2021), except for the freshwater discharges from St. Lawrence River. The St. Lawrence River discharges are specified based on the monthly mean values published by the St. Lawrence Global Observatory (SLGO). These monthly mean values published by the SLGO were estimated using a regression model (*Bourgault and Koutitonsky,* 1999) based on the observed water levels. In submodel L3, the monthly mean freshwater discharges from the Sackville River are specified. In submodel L4, the daily mean freshwater discharges from 17 major freshwater runoff are specified. The freshwater discharges from the Sackville River and 16 sewage ports were taken from *Buckley and Winters* (1992). These freshwater inputs are specified in submodel L4 (as well in other submodels) using the idealized channels cut into the coastline (*Ohashi and Sheng*, 2015).

In submodels L1 and L2, the spectral nudging technique (*Thompson et al.,* 2007) and the semi-prognostic method (*Sheng et al.,* 2001) are applied to reduce the model systematic bias and drift from the seasonal cycle of temperature/salinity in the model. In this study, the 30-year climatological temperature/salinity calculated by the Global Ocean Physics Reanalysis (GLORYS) 12V1 dataset is used for the spectral nudging. For the spectral nudging technique, the model-computed temperature and salinity are nudged toward the climatological values in the prescribed frequency-wavenumber bands (*Thompson et al.,* 2007). It should be noted that the spectral nudging method is only applied at depths greater than 30 m in submodel L1 and L2. The non-dimensional spectral nudging coefficients increase from 0 to 0.0011 linearly with depths from 30 to 40 m and equal to 0.0011 at depths greater than 40 m.

The main idea of the semi-prognostic method is to add a correction term (i.e., an interactive forcing) to the horizontal momentum equations based on differences between the model density and climatological density through the model hydrostatic equation (*Sheng,* 2001). The correction term affects directly the model-computed circulations and indirectly the model temperature/salinity. In this study, the value of β for the semi-prognostic method is set to 0.15. More details on the semi-prognostic method and spectral nudging method are given in Appendices A and B.

Several numerical experiments were conducted in this study (Table 1). The first numerical experiment is the Control Run (CR), in which the model is driven by all external forcing discussed in section 3.2.3. The model results of case CR are used to assess the model performance and study the 3D circulation and temperature/salinity in HH. The second numerical experiment is case NoWind (NW), which is the same as case CR except for the exclusion of winds in submodels L4. The third numerical experiment is case NoTide, which is the same as Control Run except for the exclusion of tidal forcing in submodel L4. Four additional numerical experiments (CW-NW, CW-NE, CW-SE, CW-SW) were conducted to investigate the main processes affecting the intrusion of offshore deep waters into BB (see Table 1). The model setup and forcing in these four additional experiments are respectively the same as in case CR, except that the steady and uniform winds (10 m/s) in four different directions (i,e., northwesterly, northeasterly, southeasterly, southwesterly) are used to drive submodel L4 separately.

Table 3.1. List of seven numerical experiments using NGMS-seCS.

Index	Numerical Experiment	Wind forcing in submodel L4	Tidal Wind forcing in submodel L4	Other forcing
1	CR	Yes	Yes	Yes
2	NW	No	Yes	Yes
3	NT	Yes	No	Yes
4	CW-NW	Northwesterly	Yes	Yes
5	CW-NE	Northeasterly	Yes	Yes
6	CW-SE	Southeasterly	Yes	Yes
7	CW-SW	Southwesterly	Yes	Yes

The nested-grid circulation modelling system is initialized based on the daily mean GLORYS 12V1 dataset. The open boundary conditions of submodel L1 are also taken from the GLORYS 12V1 dataset. The modelling system (ROMS and CICE) is integrated for 24 months from the beginning of January 2013 to the end of December 2014. The

model results in 2014 are used for the model validation and analysis.

3.3 Model Performance

The performances of submodel L1 and L2 in simulating the sea levels, currents, temperature, salinity, and ice concentrations were assessed recently by *Pei et al.* (2022) using in-situ oceanographic observations and satellite remote sensing data in 2018. Additional assessments of submodel L1 in simulating the monthly-mean temperature, salinity, and general circulation in 2014 using the Global Ocean Physics Reanalysis (GLORYS) dataset are given in Appendix C. The main reason for using the GLORYS in validating the model performance of NGMS-seCS is that the GLORYS dataset was found to represent reasonably well the observed distributions and variability of 3D large-scale currents and temperature/salinity in the global ocean (*Jean-Michel et al.,* 2021).

In this Section, the performance of submodels L3 and L4 for NGMS-seCS is further assessed by comparing model results with the GLORYS dataset and other in-situ oceanographic observations. It should be noted that the horizontal resolution of GLORYS dataset is about 6 km × 9 km over the southwestern Scotian Shelf (swScS), which is very coarse and does not resolve well the fine-scale features of circulation and temperature/salinity over the swScS. Furthermore, the tidal forcing is excluded in GLORYS. As discussed in *Pei et al.* (2022), tidal mixing plays an important role in affecting the circulation and temperature/salinity over the swScS.

The February-mean SST produced by submodel L3 in 2014 ranges from -2 °C to 1 °C over the inner shelf and ranges from 2 °C to 4 °C in the offshore waters of the swScS (Fig. 3.4a). In several bays over the inner shelf of the swSCS, the February-mean SST is low due mainly to the smaller heat storage over coastal shallow waters than in the offshore deep waters. The Nova Scotia Current (about 0.3 m/s) flows northeastward over the middle shelf of the swSCS (Fig. 3.4a). The Current bifurcates into two branches over the middle shelf of the swScS. The inshore northeastward jet over the inner shelf of the swScS is driving mainly by the strong local winds, which result in relatively cool SST over inshore waters of the submodel L3 domain, due mainly to the wind-induced coastal

upwelling and vertical mixing (*Pei et al.,* 2020).

The February-mean GLORYS dataset does not have the cool SST over the inner shelf and the bifurcation of the Nova Scotia Current (Fig 3.4b). The main reason is the horizontal resolution of GLORYS is too coarse to resolve fine-scale topographic and hydrodynamic features over the swSCS, particularly over the inner shelf.

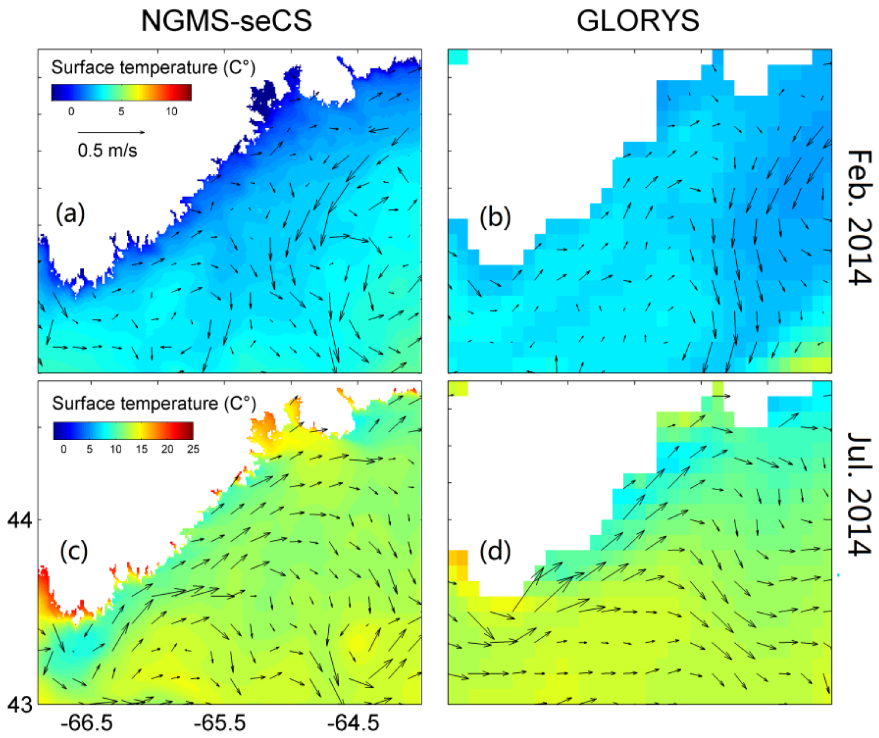

Figure 3.4: Monthly mean temperature and currents at the sea surface in (a,b) February and (c,d) July 2014 calculated from results generated by (a,c) submodel L3 and (b,d) GLORYS dataset. For clarity, velocity vectors are plotted at every 16th model grid point.

The July-mean SST produced by submodel L3 in 2014 is relatively warmer than the February-mean SST in 2014 (Fig. 3.4a,c). The July-mean SST ranges between 10 °C and 20 °C over the inner shelf and ranges between 12 °C and 15 °C in the offshore waters of the swScS (Fig. 3.4c). In several coastal embayments over the inner shelf of the swSCS, the July-mean SST is relatively warm. Again, this is due to the small heat storage over shallow waters. The July-mean SST is relatively cool (about 8 °C) over the coastal area of Cape Sable (43.6 °N, 66.5 °W). The low SST is caused by strong tidal mixing that

blends cold deep waters with the warmer surface waters. An intense (about 0.2 m s^{-1}) northeastward coastal jet in this month occurs over the inner shelf of the swSCS (Fig. 3.4c). This inshore jet in July is driven mainly by the strong southwesterly winds. The persistent southwesterly winds lead to relatively cool SST over the inner shelf, due mainly to coastal upwelling and vertical mixing (*Pei et al.,* 2022).

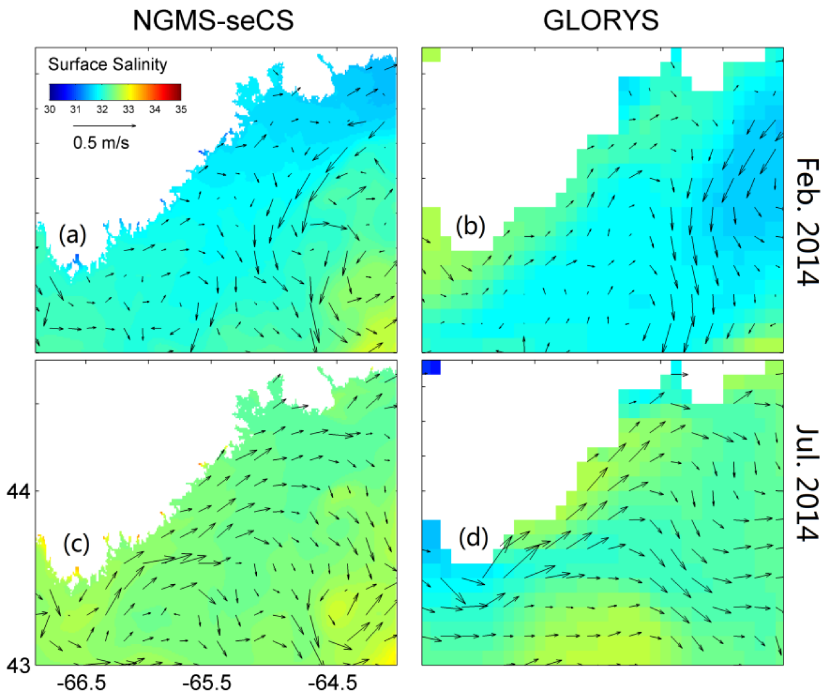

Figure 3.5: Monthly mean salinity and currents at the sea surface in (a,b) February and (c,d) July 2014 calculated from results generated by (a,c) submodel L3 and (b,d) the GLORYS dataset. For clarity, velocity vectors are plotted at every 16th model grid point.

The July-mean GLORYS also has cool SST and an inshore northeastward jet along the coast over the inshore waters (Fig 3.4d). Large differences of the SST occur, especially over the coastal area of Cape Sable Island. The plausible reasons include: (1) the horizontal resolution of the GLORYS dataset is not fine enough to resolve fine-scale topographic and circulation features over the swSCS and (2) the tidal currents and mixing were not included in the GLORYS. For the comparison between SST produced by submodel L3 and GLORYS over the submodel L3 domain, the relative bias is ~21.64% (~3.47%) and root mean square error (RMSE) is ~1.02 °C (~1.26°C) in February (July)

2014 (Table. 3.2).

The February-mean SSS produced by submodel L3 in 2014 ranges between 31 and 32 over the inner shelf and between 32 and 33 in the offshore waters of the swScS (Fig. 3.5a). The relatively low SSS over the inner shelf is caused by the low salinity waters carried by the Nova Scotia Current. The relatively high SSS occurs in the offshore waters of the swScS, caused by the high salinity waters from the meanders of the Gulf Stream. A comparison between the February-mean SSS in 2014 produced by submodel L3 and the GLORYS dataset demonstrates that the low salinity waters carried by the Nova Scotia Current flows into the middle shelf of the swSCS.

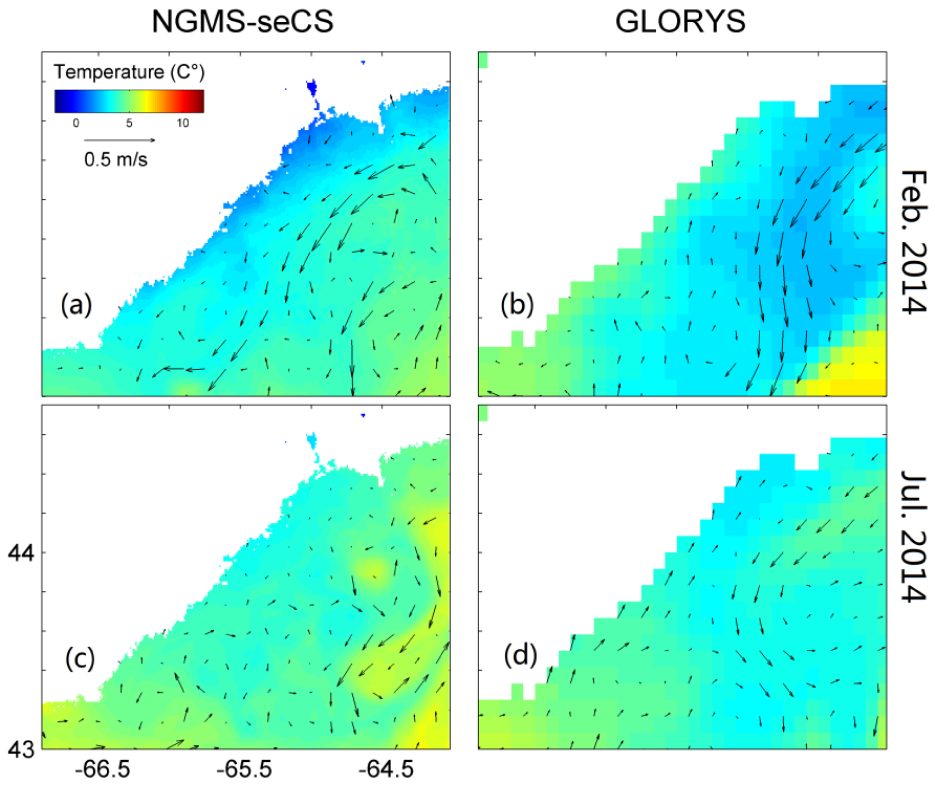

Figure 3.6: Monthly mean temperature and currents at 50 m in (a,b) February and (c,d) July 2014 calculated from results generated by (a,c) submodel L3 and (b,d) GLORYS dataset. For clarity, velocity vectors are plotted at every 16th model grid point.

The July-mean SSS produced by submodel L3 in 2014 ranges between 32.5 and 33 over

the swScS. A comparison between the July-mean SSS produced by submodel L3 (Fig. 3.5c) and the GLORYS dataset (Fig. 3.5d) demonstrates that large differences in the SSS between the two fields occur over the coastal area of Cape Sable. The main reason is again due to the strong tidal mixing, which is relatively strong over the coastal area of Cape Sable, in the submodel L3 results. By comparison, the tidal forcing is not included in the GLORYS dataset. For the comparison between SSS produced by submodel L3 and GLORYS, the relative bias is ~0.34% (~0.52%) and RMSE is ~0.50 (~0.55) in February (July) 2014 (Table. 3.2).

The performance of submodel L3 in simulating the sub-surface (50 m) temperature and currents is assessed using the February-mean GLORYS dataset (Fig. 3.6a,b). The February-mean sub-surface (50 m) temperature produced by submodel L3 in 2014 ranges between 5°C and 6 °C over the inner shelf and between 6 °C and 8°C over the offshore waters of the swScS (Fig. 3.6a). The July-mean sub-surface (50 m) currents produced by submodel L3 flow northeastward over the inner shelf and southwestward over the offshore waters of the swSCS.

The July-mean GLORYS temperature at 50 m shows the relatively lower temperature of about 5 °C in the offshore waters of the swScS and relatively higher temperature of about 7 °C over the Cape Sable (Fig. 3.6a). The July-mean GLORYS currents at 50 m run northeastward over the inner shelf and southwestward over the offshore waters of the swSCS. For the comparison between submodel L3 and GLORYS sub-surface temperature, the relative bias is ~17.69% (~14.72%) and RMSE is ~1.18°C (~1.15°C) in February (July) 2014 (Table. 3.2).

The simulated July-mean salinity at 50 m in 2014 produced by submodel L3 is about 32.5 over the inner shelf and about 34 over the offshore waters close to the eastern and southern open boundaries of the model domain (Fig. 3.7c). In comparison, the July-mean GLORYS salinity is about 32 over the inner shelf and about 32.5~33 over the offshore deep waters (Fig. 3.7d). The results indicate that submodel L3 reproduces the similar general salinity features as the GLORYS over the submodel L3 domain in 2014. For the comparison between submodel L3 and GLORYS sub-surface salinity, the relative bias is

~2.32% (~-0.54%) and RMSE is ~0.90 (~0.26) in February (July) 2014 (Table. 3.2).

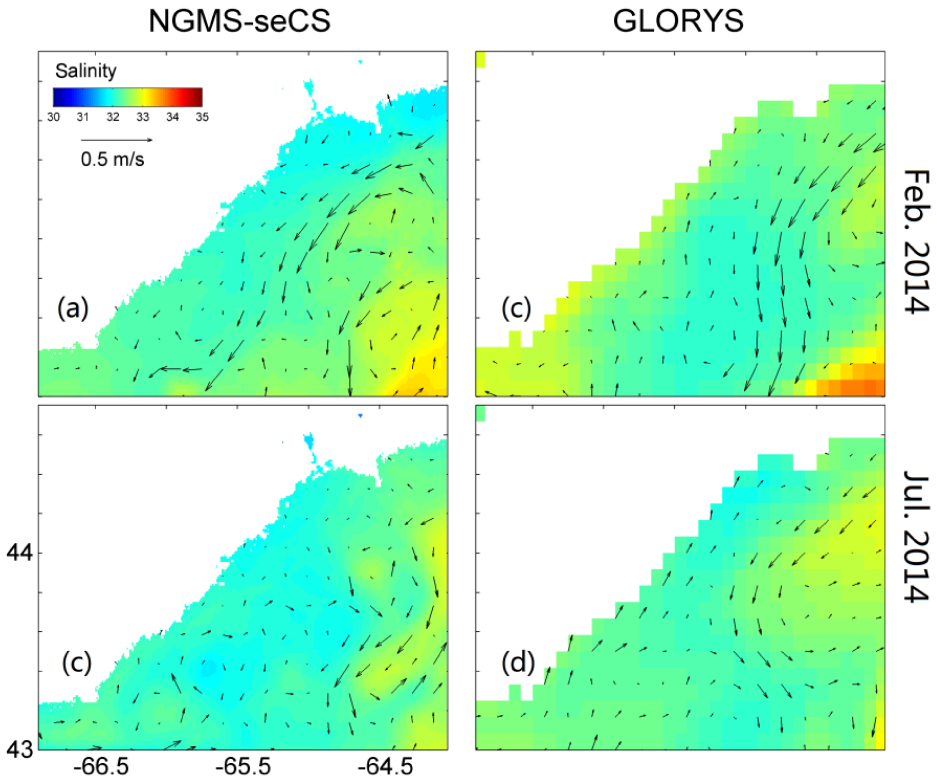

Figure 3.7: Monthly mean salinity and currents at 50 m in (a,b) February and (c,d) July 2014 calculated from results generated by (a,c) submodel L3 and (b,d) GLORYS dataset. For clarity, velocity vectors are plotted at every 16th model grid point.

Table 3.2: Values of two error metrics for quantifying performance of submodel L3 in simulating temperature and salinity using GLORYS dataset in February and July 2014. The two error metrics include relative bias (RB) and root mean square error (RMSE).

Depth	Index	Temperature		Salinity	
		February	July	February	July
Sea surface	RB (%)	21.64	3.47	0.34	0.52
	RMSE (°C for Temperature)	1.02	1.26	0.50	0.55
50 m	RB (%)	17.69	14.72	2.32	-0.54
	RMSE (°C for Temperature)	1.18	1.15	0.90	0.26

To further assess the model performance in reproducing the temporal variability of temperature, the daily-mean simulated SST (produced by submodel L3) averaged over the submodel L3 domain (Fig. 3.8a, red line) is compared with the counterpart (Fig. 3.8a, black line) calculated from daily GHRSST L4 ESA CCI OSTIA 0.05deg Sea Surface Temperature Reanalysis (CDR v2.1). Over the submodel L3 domain, the daily observed SST gradually decreased from about 3.5 °C to about 0.9 °C between 1 January and 3 March 2014, mainly due to the negative surface heat fluxes in winter (Fig. 3.8a). From 4 March to 25 August in 2014, the daily observed SST over the submodel L3 domain gradually increased from about 0.9 °C to about 19 °C mainly due to the positive net heat flux at the sea surface from spring to summer. From 26 August to 31 December 2014, the daily observed SST decreased from about 19 °C to about 5.5 °C mainly due to the negative surface heat fluxes.

A comparison between model results and remote sensing observations indicates that submodel L3 performs reasonably well in reproducing the general seasonal cycle of SST over the L3 domain, with the correlation coefficient of ~0.973, γ^2 of ~0.057, and the root mean square error (RMSE) of ~1.42 °C (Fig. 3.8a). However, submodel L3 overpredicts the SST in winter months and underpredicts the SST in summer model. This deficiency of submodel L3 is mostly likely due to the inaccuracy of the net heat flux at the sea surface. A comparison between GLORYS SST (Fig. 3.8a, blue line) and remote sensing observations indicates that GLORYS with data assimilation performs better than submodel L3 in reproducing the seasonal cycle of SST over the L3 model domain, with the correlation coefficient of ~0.983, γ^2 of ~0.013, and RMSE of ~0.77 °C. It should be noticed that the spectral nudging technique and the semi-prognostic method are not applied in submodel L3. It means that submodel L3 is purely prognostic.

The daily-mean simulated temperature at 50 m averaged over the submodel L3 domain (red line in Fig. 3.8b) is compared with the counterpart (blue line) calculated from GLORYS. The simulated temperature at 50 m is relatively higher than the counterpart calculated from GLORYS, with the correlation coefficient of ~0.968, γ^2 of ~0.064, and RMSE of ~1.20 °C. As mentioned above, submodel L3 is prognostic without any data assimilation. In comparison, GLORYS was generated using data assimilation.

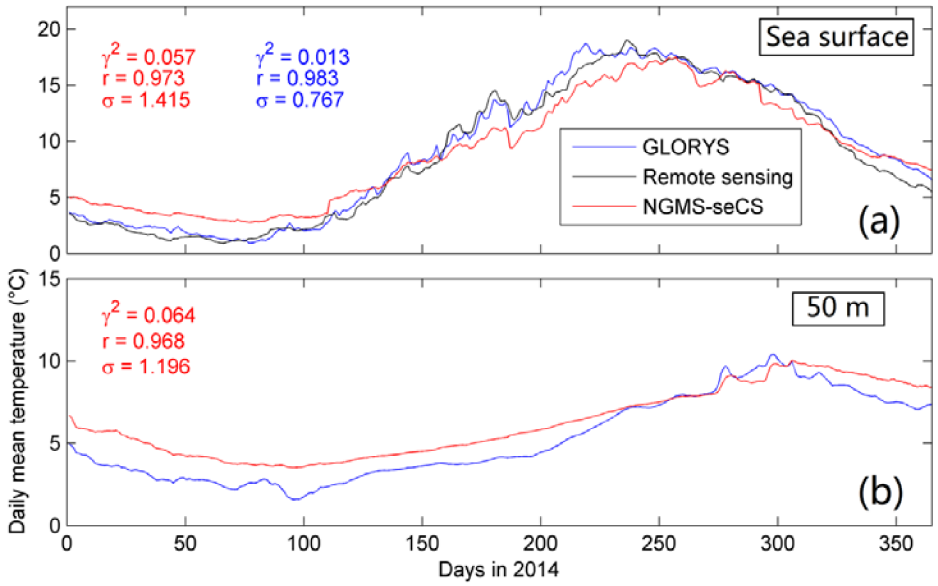

Figure 3.8: Time series of daily mean temperature produced by submodel L3 (red lines) and GLORYS dataset (blue lines) at (a) the sea surface and (b) 50 m in 2014 averaged over the submodel L3 domain. The black line in (a) represents the remote sensing SST extracted from the daily GHRSST reanalysis (CDR v2.1).

We next assess the performance of submodel L4 in simulating tidal and non-tidal sea levels using the in-situ tide gauge data at location B_1 in BB. The location of B_1 is shown in Fig. 3.1. The in-situ observations of sea surface elevations were obtained from the Marine Environmental Data Service of Fisheries and Oceans Canada.

Time series of observed (red line) and simulated (blue) total sea levels produced by submodel L4 at location B_1 for the period of 1-31 March, 2014 are shown in Fig. 3.9a. The observed total sea levels are dominated by the semi-diurnal tides with roughly two high and two low tidal elevations each day. The spring and neap tides are also presented in the total observed sea levels, which due mainly to the combined effect of the M_2 and S_2 tidal constituents. During the spring tide period, the maximum range of observed tidal elevations is about 1.0 m. During the neap tide period, the minimum range of tidal elevations is about 0.4 m. The simulated total sea levels agree very well with the observations with the small value of γ^2(about 0.07), which indicates the satisfactory performance of submodel L4 in simulating the total sea levels in BB (Fig. 3.9a). The observed and simulated total sea levels are decomposed into the tidal and non-tidal components using t_tide (*Pawlowicz et al.,* 2002). A low-pass filter is used to eliminate

any remaining high-frequency variabilities with periods of less than 3 hours in the non-tidal sea levels. As shown in Figure 3.9b, Submodel L4 performs very well in simulating the tidal sea levels, with small γ^2 values of about 0.02. The γ^2 value is about 0.39 for submodel L4 in simulating the non-tidal sea levels, which is larger than the γ^2 value for simulating the tidal elevations. One plausible reason is that the horizontal resolution of submodel L4 is not fine enough to resolve fine-scale topographic features, particularly over the Narrows of HH. The other reason is that atmospheric conditions including winds and atmospheric pressures over the submodel L4 domain are not well represented by the North American Regional Reanalysis. Although larger than the values for tidal elevations, the γ^2 value for the non-tidal elevations is highly comparable to the counterparts published in the literature (*Shan,* 2010; *Shan and Sheng,* 2012; *Pei et al.,* 2022).

The performance of submodel L4 in simulating temperature/salinity and their seasonal variability is assessed using the in-situ hydrographic observations at Location B_2 in BB in 2014. The observations were made by the Bedford Basin Monitoring Program (BBMP).

The time-depth distribution of the observed salinity at location B_2 in BB (Fig. 3.1) in 2014 is shown in Fig. 3.10b. The salinity in the surface layer at location B_2 in BB is relatively low and about 28, due to the freshwater discharges from the Sackville River and sewage ports in BB (Fig. 3.10b). The surface salinity in BB is relatively lower in February, April, and November than in other months. The main reason is that the freshwater discharges from the Sackville River in these three months are relatively larger than the counterparts in other months (see Fig. 3.2). Submodel L4 is able to generate the similar vertical distribution and the seasonal cycle as the observed salinity in BB (Fig. 3.10a,b). Both the simulated and observed results demonstrate that the salinity in BB quickly increased on around 10 July 2014 when the Hurricane “Arthur” swept by Nova Scotia and produced strong winds.

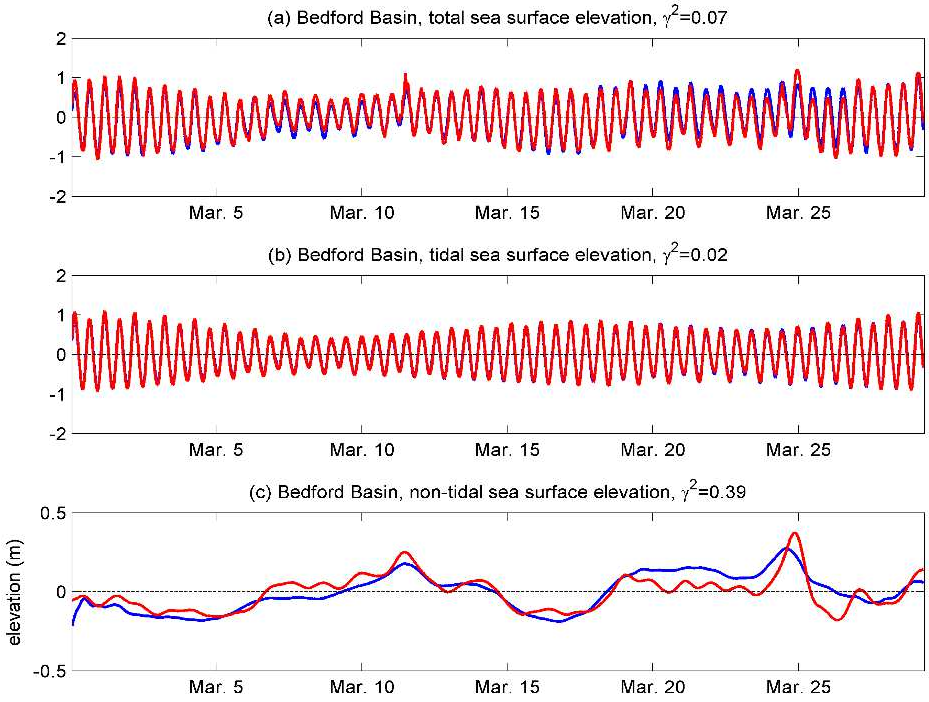

Figure 3.9: Time series of observed (red) and simulated (blue) (a) total, (b) tidal and (c) non-tidal sea levels at the tide gauge station in Bedford Basin for the period of 1-31 March, 2014. The simulated results are produced by submodel L4.

Time series of the observed temperature shows that the cold waters are generated initially at the sea surface of BB in winter due to the large negative net heat flux at the sea surface (Fig. 3.10d). The cold surface waters sink into the deep layer known as the "winter convection". During winter, the surface water becomes cold and dense due to the larger negative net heat fluxes and strong winds, causing the surface water to sink to deeper layer and mix with the underlying water (*Bryan*, 1969b; *Mupparapu and Brown,* 2022). As the comparison, the simulated temperature produced by submodel L4 roughly agrees with the observations (Fig. 3.10c,d). In particular, Submodel L4 generates the similar vertical distribution and the seasonal cycle as the observed temperature in BB. However, submodel L4 underpredicts the temperature in the surface layer and overpredicts the temperature in the bottom layer. This model bias is likely due to the inaccuracy of the net heat flux at the sea surface and the coarse horizontal resolution of model topography and atmospheric forcing.

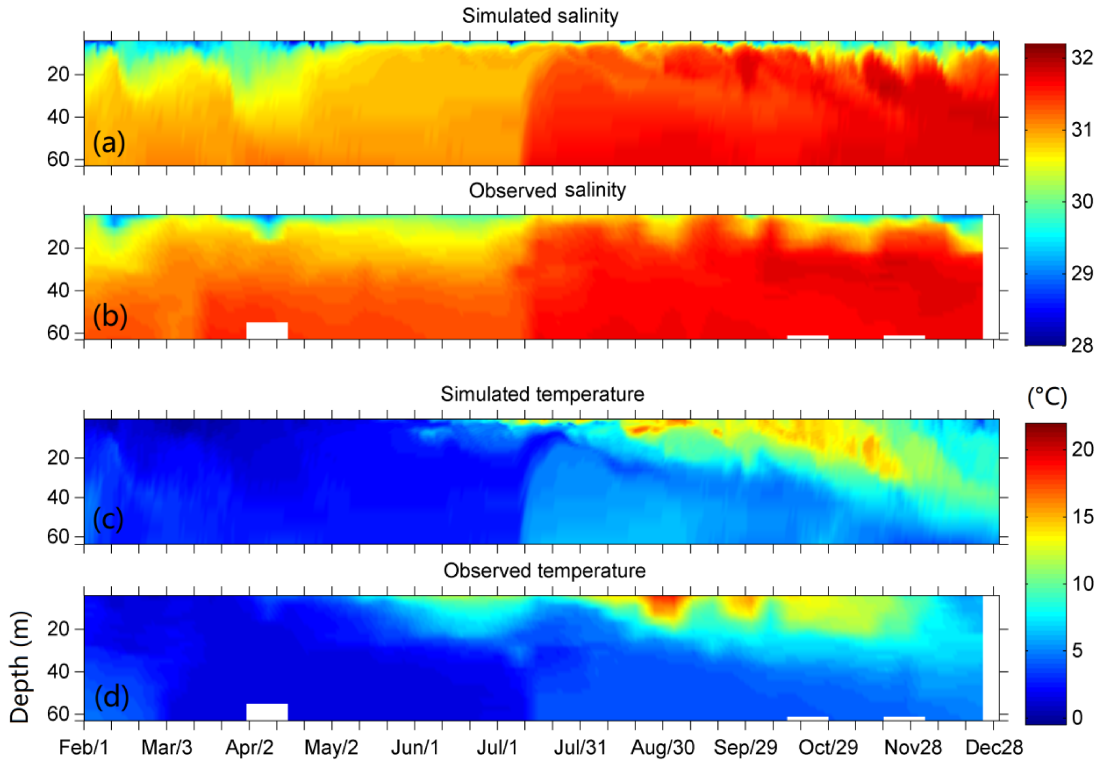

Figure 3.10: Time-depth distributions of (a,c) simulated and (b,c) observed (a,b) salinity and (c,d) temperature at location B_2 in Bedford Basin in 2014. The simulated results are produced by submodel L4. The weekly observations at this location were made by the Bedford Basin Monitoring Program (BBMP).

3.4 General Mean Temperature/salinity and Circulation in Halifax Harbour

The main focus of this Section is on examinations of the 3D circulation, hydrography (i.e., temperature and salinity in this thesis), and associate variability in HH. The 3D currents and hydrography in HH in 2014 produced by submodel L4 are analysed here.

3.4.1 Annual Mean Temperature, Salinity and Circulation in Halifax Harbour

The annual mean currents and temperature/salinity in 2014 in HH and adjacent waters are calculated from model results produced by submodel L4. The annual mean near-surface salinity at 2 m gradually increases from about 28 near the mouth of the Sackville River to about 32.5 in the OH, due mainly to freshwater discharges from the Sackville River and sewage outfalls in HH (Fig. 3.11a). The near-surface salinity is also relatively low and

about 29 in the Northwest Arm. The annual mean sub-surface salinity at 12 m is relatively uniform and gradually increases from about 32 in BB to about 33 in the OH (Fig. 3.11b). The simulated annual mean near-surface and sub-surface salinity produced by submodel L4 have large-scale distributions similar to the simulated annual mean results in 2006 by *Shan and Sheng* (2012).

The annual mean near-surface (2 m) temperature in HH and adjacent waters gradually increases from about 6 °C near the mouth of the Sackville River to about 8 °C in the OH , and is relatively low and about 6 °C in the Northwest Arm (Fig. 3.12a). The annual mean sub-surface (12 m) temperature also gradually increases from about 4 °C in BB to about 7 °C in the OH (Fig. 3.12b), which is lower than the counterpart near the surface.

The annual mean currents in HH and adjacent waters produced by submodel L4 are characterized by a typical two-layer estuarine circulation (*Heath*, 1973; *Petrie and Yeats*, 1990; *Shan et al.,* 2011), with seaward currents in the upper layer and landward return currents in the lower layer (Fig. 3.11a,b). The annual mean currents are relatively weak in BB, and relatively strong in the Narrows (about 4 cm/s), the IH and the OH. In the OH, the annual mean near-surface circulation is characterized as a southward jet near the western coastline and the southeastward currents from the IH which join the northeastward currents from the offshore waters and run eastward together (Fig. 3.11a). The annual mean sub-surface (12 m) currents in HH are landward and relatively weaker than the near-surface currents (Fig. 3.11b). The simulated annual mean near-surface and sub-surface currents shown in Figs. 3.11 and 3.12 have similar circulation features as the model results in 2006 produced by Shan and Sheng (2012). Major differences in the near-surface currents between our results and the results by Shan and Sheng (2012) occur over the OH where the currents are southwestward in Shan and Sheng (2012). These differences are due mainly to the interanual variability of local winds.

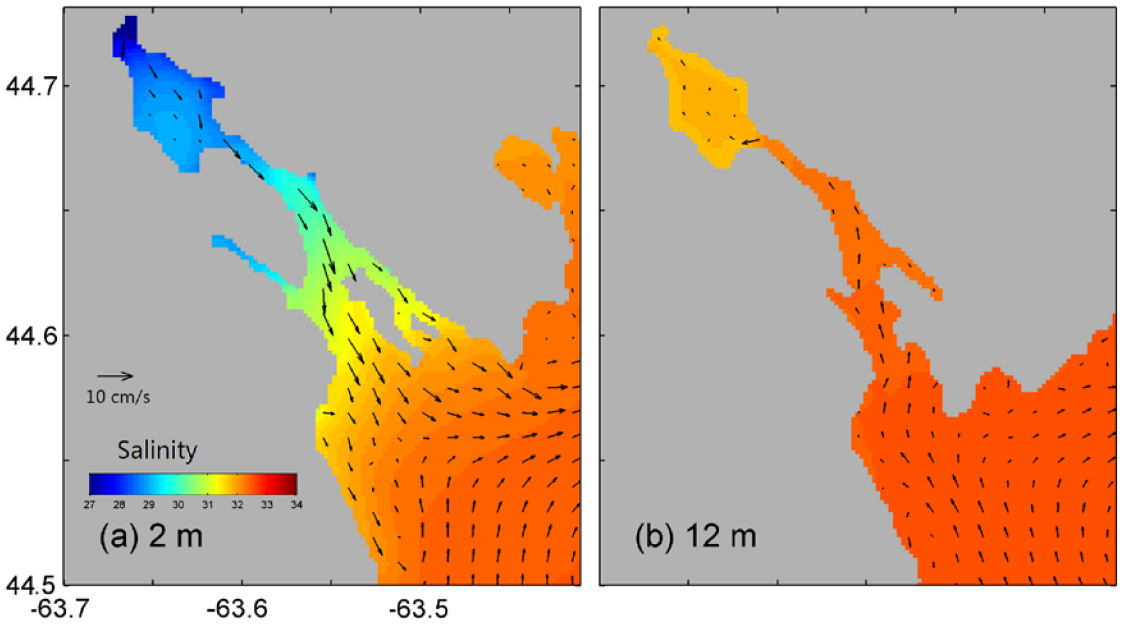

Figure 3.11: Annual mean salinity and currents in 2014 at (a) 2 m and (b) 12 m in Halifax Harbour and adjacent waters calculated from results produced by submodel L4. For clarity, velocity vectors are plotted at every 6th model grid point.

To examine the vertical distribution of the annual mean currents in HH, the vertical profiles of the along-transect and vertical components of annual mean currents in 2014 are calculated from the submodel L4 results (Fig. 3.13). A longitudinal transect BH is chosen from the mouth of the Sackville River to the OH (marked in Fig. 3.3d). The seaward annual mean currents in 2014 produced by submodel L4 occur in the top 5 m, and the landward currents occur below 5 m (Fig. 3.13). In BB, the annual mean currents are relatively large (up to about 10 cm/s) in the surface layer and relatively weak below 25 m. Due mainly to the rough topography, the simulated currents have large horizontal and vertical variability in the IH and OH. Over the Narrows, the landward currents in the bottom boundary layer follow closely with topography to flow into the lower layer of BB.

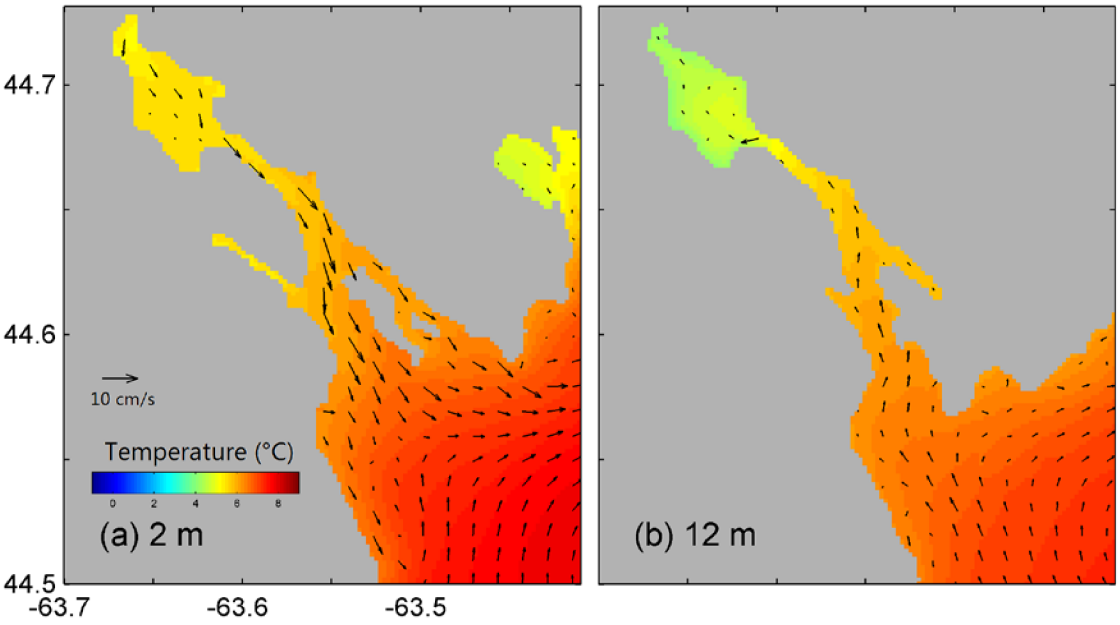

Figure 3.12: Annual mean temperature and currents in 2014 at (a) 2 m and (b) 12 m in Halifax Harbour and adjacent waters calculated from results produced by submodel L4. For clarity, velocity vectors are plotted at every 6th model grid point.

The vertical distribution of the annual mean currents shown in Fig. 3.13 is very similar to the counterpart in 2006 produced by *Shan and Sheng* (2012) at the large-scale. Major differences occur over the Narrows, where the near-surface seaward currents are relatively weak in *Shan and Sheng* (2012). In addition, the downwelling feature of the sub-surface currents over the Narrows was not presented by *Shan and Sheng* (2012). Note that the simulated mean currents in *Shan and Sheng* (2012) are produced by the CANDIE (*Sheng et al.,* 1998), which is a 3D z-coordinate ocean circulation model. The conventional z-coordinate models have large model errors in representing topographic features (e.g. the step-like representation of the topography) in the model.

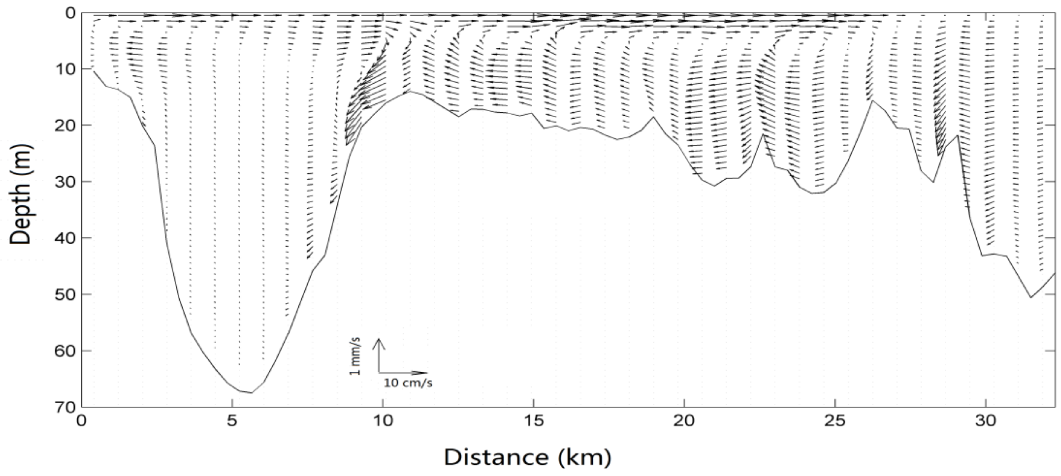

Figure 3.13: Vertical distributions of annual mean currents in 2014 along the longitudinal transect (BH) from the Sackville River to the Outer Harbour calculated from daily mean results produced by submodel L4.

3.4.2 Seasonal Variability of Temperature/salinity and Circulation in Halifax Harbour

To examine the seasonal variability of the 3D circulation and hydrography in HH, the monthly mean temperature/salinity, and currents in four months in 2014 are calculated from daily mean results produced by submodel L4.

In February, the monthly mean near-surface salinity at 2 m gradually increases from about 25 near the mouth of the Sackville River to about 32 in the OH (Fig. 3.14a), due mainly to freshwater discharges from the Sackville River and sewage outflows in HH. The near-surface salinity is also low and about 30 in Northwest Arm. The monthly mean near-surface temperature in February is relatively low, and ranges between about -1 °C in BB and about 3 °C in the OH (Fig. 3.15a). The near-surface low temperature is due mainly to the strong net heat loss to the atmosphere. The horizontal distribution of the near-surface temperature is due to small heat storage over shallow waters. The monthly mean near-surface currents in February are mainly seaward (southeastward) in BB, the Narrows, and IH (Fig. 3.14a). In the OH, the monthly mean near-surface circulation is characterized by the southeastward currents from the IH that join the northeastward

currents from the offshore waters from the ScS and run eastward, due to the effect of local winds and general circulation over the inner shelf of the ScS.

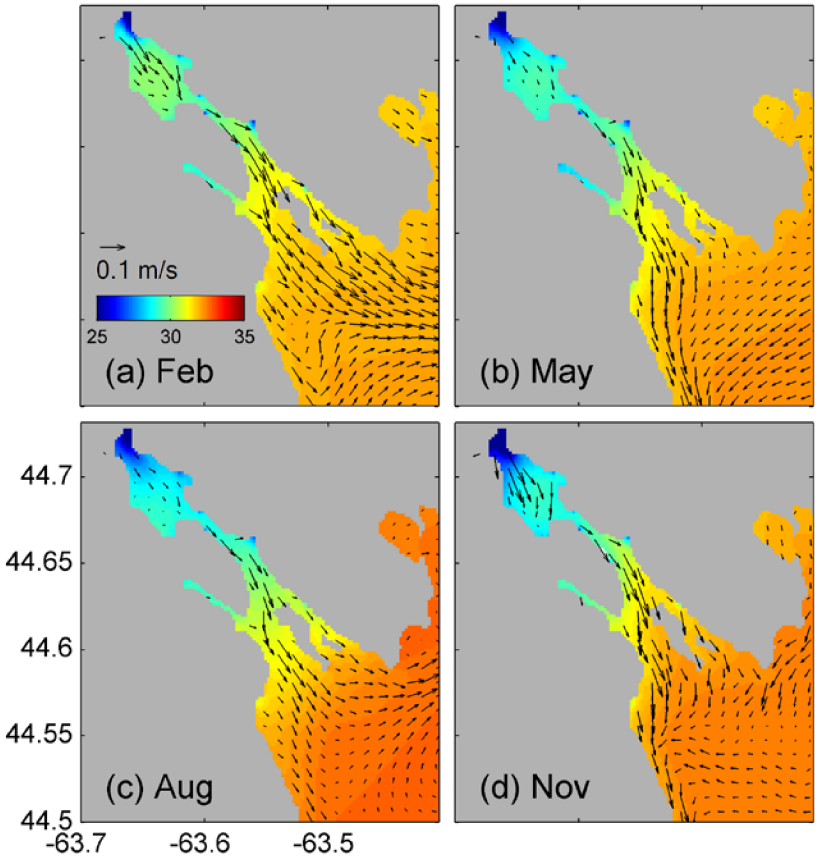

Figure 3.14: Monthly mean near-surface salinity and currents at 2 m in (a) February, (b) May, (c) August and (d) November 2014 in HH and adjacent waters calculated from model results produced by submodel L4.

In May, the monthly mean near-surface (2 m) salinity in BB is about 29, which is relatively lower than the counterpart in February (Fig. 3.14b). This is due mainly to large freshwater discharges associated with ice and snow melt and relatively weak vertical mixing in spring. The monthly mean near-surface temperature in May is warmer than the counterpart in February and ranges between about 1 °C in BB and about 4 °C in the OH (Fig. 3.15b). In BB, the monthly mean near-surface currents in May are seaward and relatively weaker than the counterparts in February. In the OH, the near-surface currents in May are approximately southward along the western coastline of the OH and

southwestward over the inner shelf (Fig. 3.14b). The differences in the near-surface currents between February and May are due mainly to the different wind conditions between these two months.

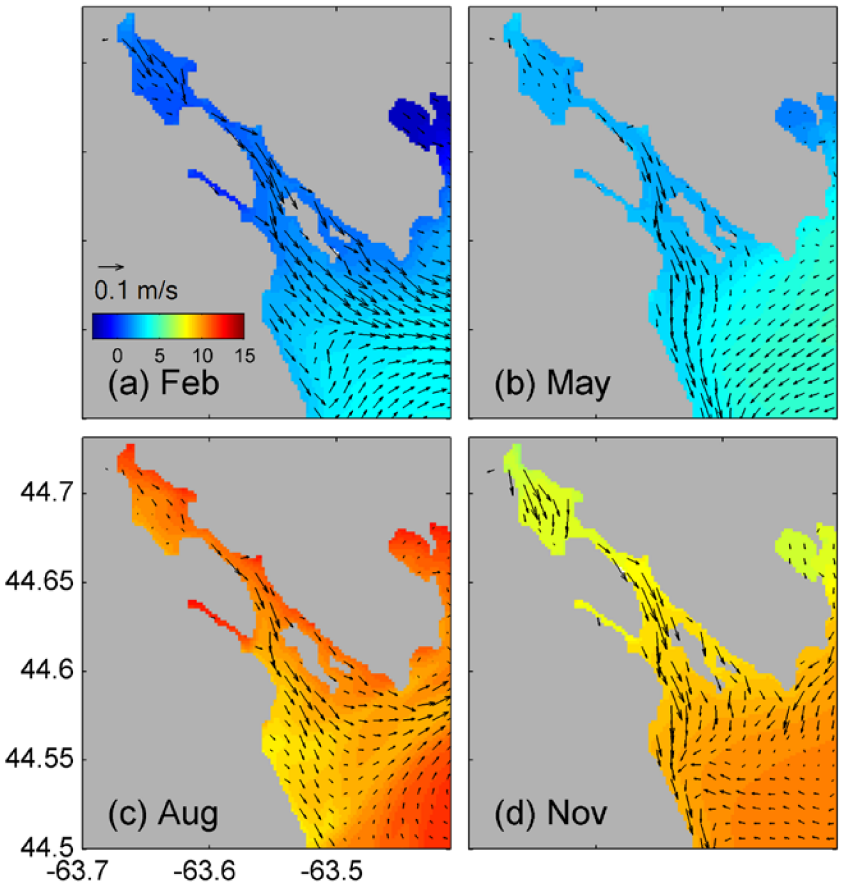

Figure 3.15: Monthly mean near-surface temperature and currents at 2 m in 2014 in HH and adjacent waters calculated from model results produced by submodel L4. Otherwise as in Fig.3.14.

In August, the monthly mean near-surface (2 m) salinity in BB is also relatively low and about 28, due to the large freshwater discharges associated with large precipitation in the summer (Fig. 3.14c). In the OH, the monthly mean near-surface salinity in this month is about 32.5, which is slightly higher that the counterparts in February and in May. One of the plausible reasons is the northward near-surface wind-driven currents, which transport the relatively salty coastal waters from the inner ScS into the OH. The monthly mean near-surface temperature in August is relatively warm and about 13 °C in BB (Fig. 3.15c).

This is due mainly to the positive surface heat fluxes gained by the sea surface waters in this month. In, August, the monthly mean surface water temperature in the OH is lower than the counterpart in BB. The main reason is that the surface waters over the OH are affected significantly by the local upwelling due to the strong southerly winds in August. The monthly mean near-surface currents in August are also seaward and relative weaker than the counterparts in February and May (Fig. 3.14c). The reason is that the southerly winds reduce the seaward near-surface currents in HH.

In November, the monthly mean near-surface (2 m) salinity in BB is about 27 and the lowest among these four months (Fig. 3.14d), due mainly to the significantly large freshwater discharges from the Sackville River and sewage outflows. The monthly mean near-surface temperature in BB drops to 7 °C in November (Fig. 3.15d). The monthly mean near-surface seaward currents are relatively large in this month, due mainly to the large freshwater discharges from the Sackville River (Fig. 3.14d).

The monthly mean sub-surface (12 m) temperature/salinity and currents produced by submodel L4 are used to investigate their seasonal variability. In February, the monthly mean sub-surface salinity is relatively higher than the counterpart near the surface, which gradually increases from about 31 near the mouth of the Sackville River to about 32 in the OH (Fig. 3.16a). The monthly mean sub-surface temperature in this month is relatively higher than the counterpart near the sea surface, which ranges between about 2.5 °C in BB and about 4 °C in the OH (Fig. 3.17a). The monthly mean sub-surface currents are landward in BB, the Narrows and the IH in February (Fig. 3.16a). In the OH, the sub-surface circulation has the similar feature to the counterpart near the surface in February, and is characterized as the southeastward currents from the IH which join the northeastward currents from the offshore waters from the ScS and run eastward.

In May, the monthly mean sub-surface (12 m) salinity in BB is about 31.5, which is higher than the counterpart in February (Fig. 3.16b). It is mainly due to the relatively weak wind-induced vertical mixing in May. The monthly mean sub-surface temperature in May is slightly higher than the counterpart in Feb, which ranges between about 3 °C in BB and about 4.5 °C in the OH (Fig. 3.17b). In BB, the seaward near-surface currents in

May are relatively weaker than the counterpart in February. In the OH, the sub-surface currents are southeastward (Fig. 3.16b). The main differences between the sub-surface currents in February and the sub-surface currents in May are due mainly to the different direction of the general mean circulation near the coastline of ScS.

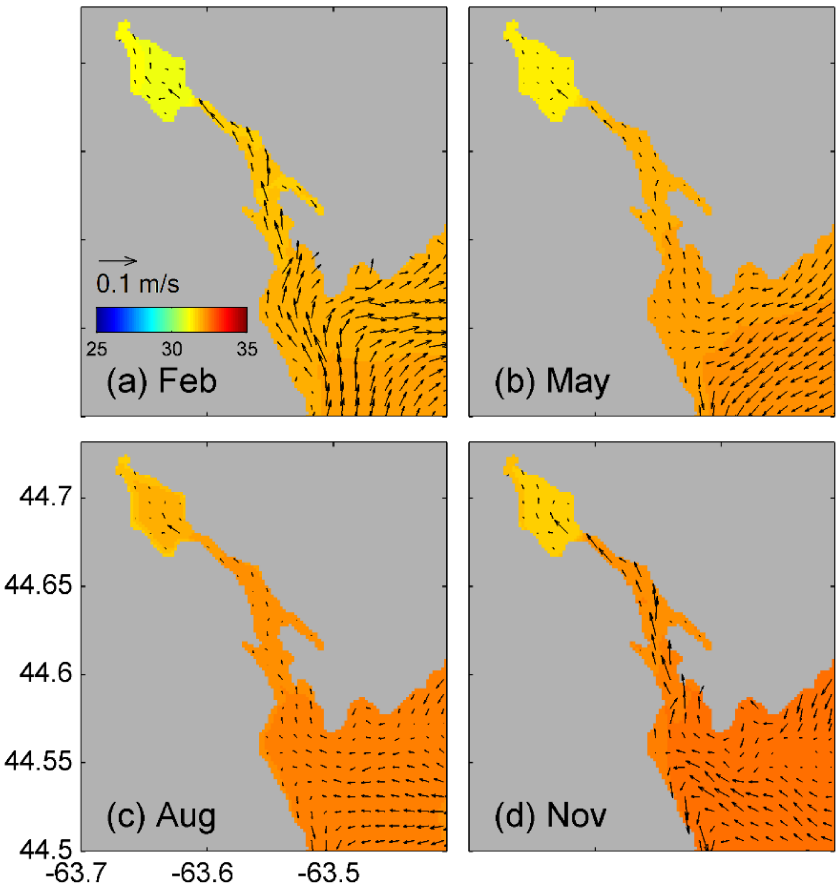

Figure 3.16: Monthly mean sub-surface salinity and currents at 12 m in 2014 in HH and adjacent waters calculated from model results produced by submodel L4. Otherwise as in Fig.3.14.

In August, the monthly mean sub-surface (12 m) salinity in BB increases to about 31.5 (Fig. 3.16c), since the vertical mixing in BB is relatively weak in August. The monthly mean sub-surface temperature in August is relatively lower than the counterpart near the sea surface, which ranges between about 6 °C in BB and about 9 °C in the OH (Fig. 3.17c). The sub-surface currents are also landward, which are weaker than the counterpart near the surface currents in August (Fig. 3.16c).

In November, the monthly mean sub-surface (12 m) salinity in BB gradually increases from about 32 near the mouth of the Sackville River to about 33 in the OH (Fig. 3.16d). In BB, the monthly mean sub-surface salinity in November is slightly higher than the counterpart in August, due mainly to the significantly large freshwater discharges from the Sackville River and sewages and relatively strong winds in November. The monthly mean sub-surface temperature in November is lower than the counterpart in August, which ranges between about 5.5 °C in BB and about 13 °C in the OH (Fig. 3.17d). The monthly mean sub-surface currents in November are relatively larger than that in February and August (Fig. 3.16d). The main reason is that the monthly mean sub-surface currents are enhanced by the relatively strong near-surface currents in November.

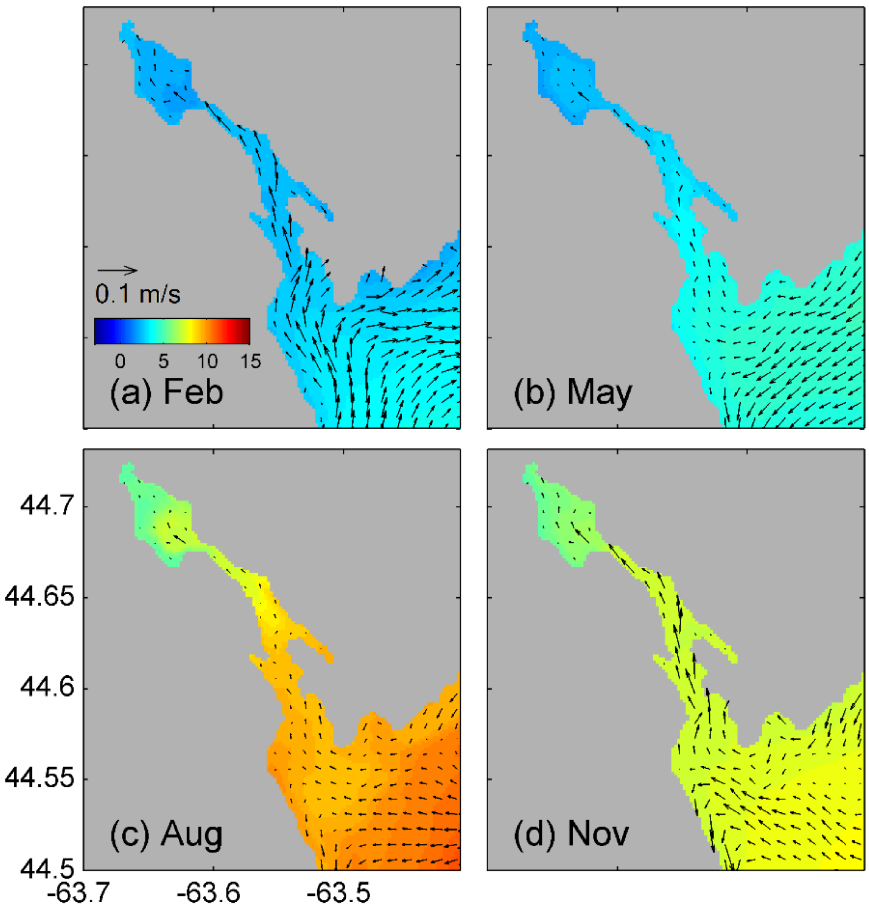

Figure 3.17: Monthly mean sub-surface temperature and currents at 12 m in 2014 in HH and adjacent waters calculated from model results produced by submodel L4. Otherwise as in Fig.3.14.

3.5 Landward Intrusion of Offshore Sub-Surface Waters into Bedford Basin

3.5.1 Cases of Intense Landward Intrusion

As discussed in the previous Section, the annual and monthly mean currents in HH are characterized as a two-layer estuarine circulation, with seaward currents in the upper layer and landward currents in the lower layer. Dynamically, the landward currents transport offshore sub-surface high-salinity waters into the intermediate and lower layers of BB. The analysis of in-situ observations at location B_2 in BB demonstrates that the intense landward intrusion of offshore sub-surface salty waters into the lower layer of BB during short periods of a few days or longer (*Punshon & Moore*, 2004; *Burt et al.,* 2013).

Based on model results in 2014 produced by submodel L4, we first consider two interesting events in 2014 in this Section. The simulated instantaneous salinity produced by submodel L4 along the longitudinal transect (transect BH shown in Fig. 3.3c) in HH during two intense intrusion events are examined. For simplicity, the depth of the isohaline for 31.5 (32) is used as the position of the upper boundary of high salinity near-bottom waters in HH for the first (second) event based on model results. Similarly, the depth of the isohaline of 30 is used for the lower boundary of low-salinity near-surface waters in HH.

The first event occurs around 3 February 2014. Before the start of this intense intrusion event (Fig. 3.18), the salinity in the surface layer in HH gradually increases from about 28 in BB to about 31.5 in the OH, due to the seaward spreading of low-salinity waters in the surface layer driven by the freshwater discharges from the Sackville River and sewages. The salinity is relatively high and about 31.5 in the bottom layer of BB. The isohaline of 31.5 tilts from the surface of the OH to bottom of the IH at 00:00 on 3 February (Fig. 3.18a). When the intrusion event starts around 23:00 on 3 February, the high-salinity near-bottom waters, with the upper boundary marked by the isohaline of 31.5, begin to intrude from the OH and reach the bottom of the Narrows (Fig. 3.18b). The isohaline of 31.3 in BB is elevated up and shallower than the counterpart before the intrusion event, which indicates the increasing the salinity in the lower layer of BB. Over the southeastern flank of BB, the isohaline of 31.3 tilts downward, which indicates the

downslope movement of the high-salinity waters in the bottom boundary layer from the Narrows to BB.

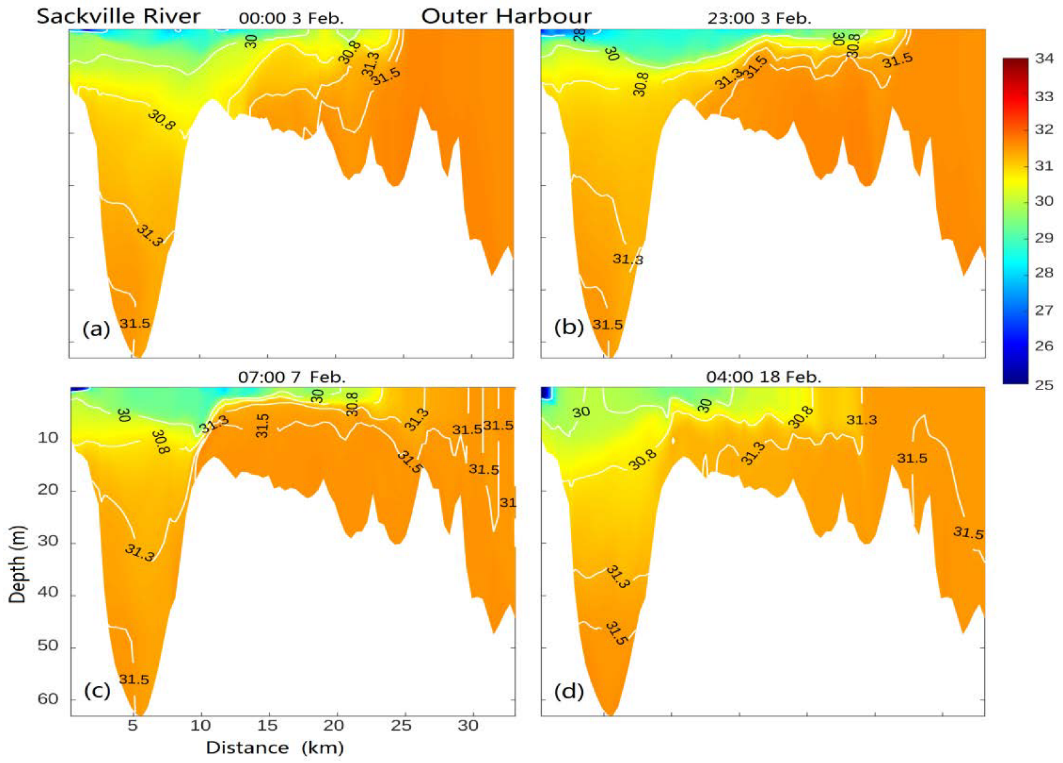

Figure 3.18: Vertical distribution of instantaneous salinity along the longitudinal transect BH at (a) 00:00 on 3, (b) 23:00 on 3, (c) 7:00 on 7, and (d) 4:00 on 18 in February 2014 based on results produced by the NGMS-swCS submodel L4.

During the intense intrusion (Fig. 3.18c), the isohaline of 30 is shallower than the counterparts before the intrusion event. It means local upwelling occurs near the mouth of the Sackville River in the surface layer of BB due to the strong northerly winds. The isohaline of 31.5 enters BB in the bottom boundary layer from the Narrows. After entering the lower water columns of BB, the high-salinity waters mix with the relatively low-salinity waters in the deep layer of BB, making the salinity in the deeper waters of BB to be higher than the counterparts before the intrusion event. At this time, the isohaline of 31.3 in BB is elevated up and much shallower than the counterpart before the intrusion event (Fig. 3.18c). After the intrusion (Fig. 3.18d), the high salinity waters from the OH (shown by the isohaline of 31.5) gradually retreats from BB to the OH.

The second intense intrusion event occurs around 3 July 2014 (Fig. 3.19). Before the start of this event (Fig. 3.19a), the salinity in the surface layer at 19:00 on 1 July gradually increases from about 28 in BB to about 32 in the OH. At this time, the isohaline of 32 (31.5) tilts downward from the surface of the OH to the bottom of the IH (Narrows). When the intrusion starts (Fig. 3.19b), the isohaline of 32 reaches the bottom of the Narrows and the isohaline of 31.5 reaches the lower layer of BB at 7:00 on 3 July.

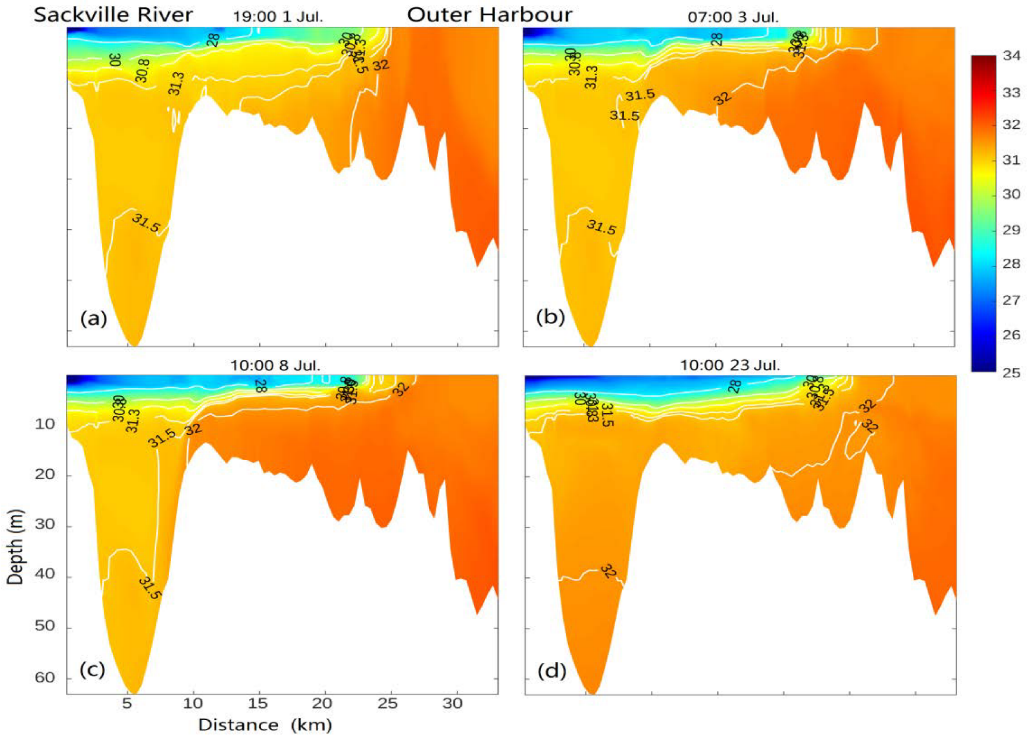

Figure 3.19: Vertical distribution of instantaneous salinity along the longitudinal transect BH at (a) 19:00 on 1, (b) 07:00 on 3, (c) 10:00 on 8, and (d) 10:00 on 23 July 2014 based on results produced by the NGMS-swCS submodel L4.

During the second intense intrusion event (around 10:00 on 8 July), the high salinity waters (with the upper boundary marked by the isohaline of 32 in Fig. 3.19c) intrude from the OH and enter BB. At this time, the isohaline of 31.5 tilts downward from the surface of the OH to the bottom of BB (Fig. 3.19c). It indicates the high-salinity waters intrude from the OH into BB during this event. After the intrusion (Fig. 3.19d), the high-

salinity waters from the OH gradually retreat from BB to the IH at 10:00 on 23 July. The salinity in the intermediate and bottom boundary layers of BB at this time increases, respectively. This intrusion event is caused by strong local winds associated with Hurricane Arthur. This hurricane swept through the Gulf of Maine, southwestern Nova Scotia, Bay of Fundy and eastern New Brunswick as a post-tropical storm on 5 July 2014. The observations at location B_2 in BB made by BBMP also showed the effects of this intrusion event in the observed temperature and salinity in BB (Fig. 3.10).

3.5.2 Dependence of Landward Intrusion on Wind Directions

To further examine the main physical processes affecting the landward intrusion of offshore sub-surface high-salinity waters into BB, three-hourly domain-averaged wind vectors and associate wind speeds in February (a) and July (b) 2014 are calculated from the NARR reanalysis over the submodel L4 domain (Fig. 3.20). The winds veer from westerly to northwesterly during the initial period of the first intrusion event and veer from northeasterly to southwesterly during the intermediate period of the first intrusion event. The strong southwesterly winds prevail during the second intrusion event from around 3 to 21 July 2014. It should be noted that strong northwesterly (southwesterly) winds are dominated over the submodel L4 domain before about 2 days of the first (second) intrusion event.

To examine the relationship between the winds and the intrusion events in HH, we follow *Shan et al* (2022) and use the wind impulse at a given time *I(t)* defined as the integration of the wind stress during the recent past period:

$$I(t) = \int_{t-T}^{t} \tau_a(t')dt' \tag{3.9}$$

where τ_a is the wind stress in the longitudinal axis of HH and T is the duration set to be 3 days in this study. For calculating $I(t)$, the three-hourly winds are rotated by 45° in the clockwise direction to get the along-longitudinal and cross-longitudinal components of winds, with the positive direction of along-transect (cross- transect) wind stress vectors are northwesterly (southwesterly). This along-longitudinal direction is in the similar direction of transect BH (Fig. 3.3d). The along-transect wind impulses are positive before

and during the two intrusion events (shown by the grey colour, Fig. 3.21a). It indicates that two intrusion events in HH are correlated strongly with the persistent winds, mainly northwesterly/southwesterly winds.

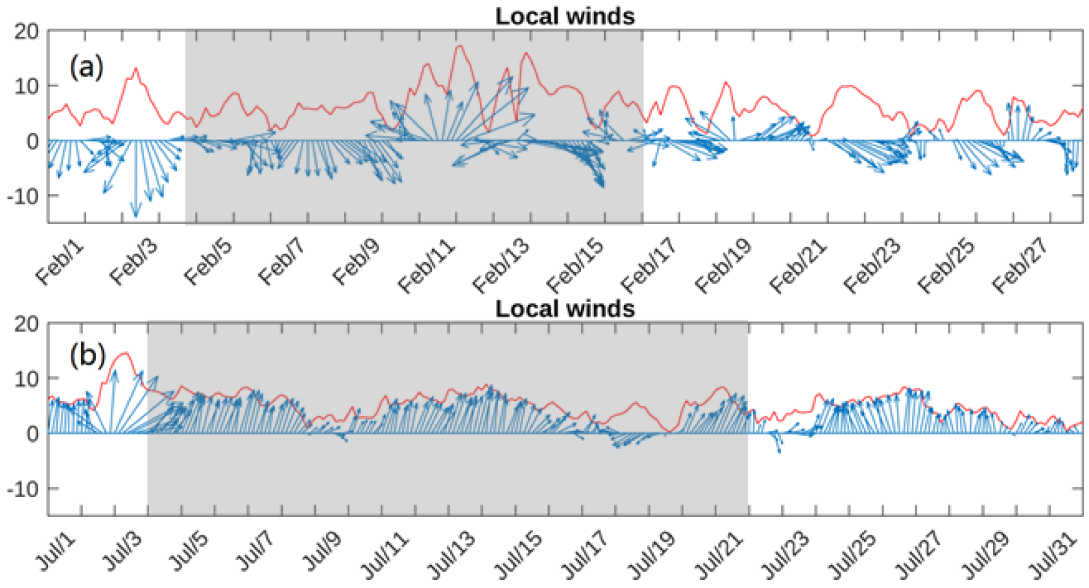

Figure 3.20: Time series of three-hourly wind velocity vectors averaged over the submodel L4 domain (blue arrows) and associate wind speed (red line) in (a) February and (b) April 2014 based on the NARR reanalysis. The grey boxes mark the periods of two selected intrusion events.

The time-mean circulation below the surface layer of the Narrows is landward as the relatively salty waters flowing from the OH toward BB. To further examine the landward transport of high-salinity near-bottom waters in the intrusion events, the near-bottom salinity (S_N) in the Narrows (at bout 0.25 m above the bottom) is averaged over its central area (around 44°40′ N, 63°35′ W). The S_N increases from about 31.1 to about 31.6 between 3 and 7 February 2014, and increases from about 31.4 to about 32 between 1 and 10 on July 2014 (Fig. 3.21b). During the period of the first intense intrusion event (from 23:00 on 3 to 00:00 on 16 February 2014), the correlation coefficient between the total wind stress impulse and the S_N is about 0.62 with a time shift of -1 day (Fig. 3.22). In the period of the second intrusion event (from 7:00 on 3 to 00:00 on 22 July 2014), the correlation coefficient between the total wind stress impulse and the S_N is about 0.91 with

a time shift of -3 day (Fig. 3.22). The negative time shift means the wind stress impulse leads S_N.

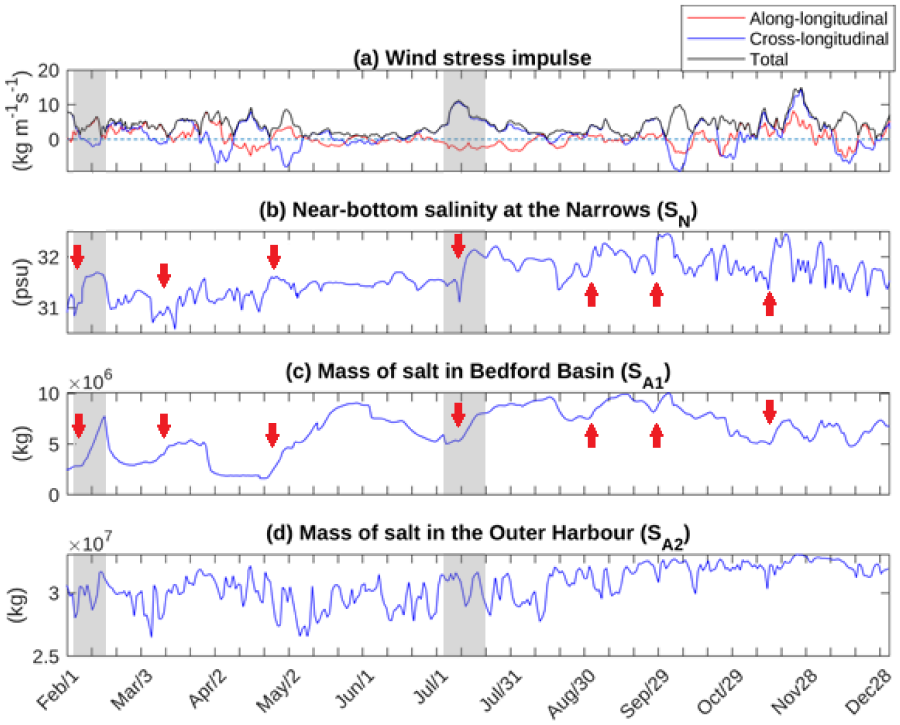

Figure 3.21: (a) along-longitudinal (red line), cross-longitudinal (blue line) components of the wind impulse, (black line) total wind impulse, (b) near-bottom salinity at the middle of the Narrows, (c) mass of salt of the high salinity waters (>31.5) in BB (area A_1 shown in Fig. 3.3c), and (d) mass of salt of the high salinity waters (>31.5) in the Outer Harbour (area A_2 shown in Fig. 3.3d) in 2014. The grey colour shows the two intrusion events presented in Fig. 3.18 and Fig. 3.19. Red arrows in (b) and (c) represent approximately starting times of seven intense intrusion events.

To investigate the relationship between the sub-surface salinity in BB and the intrusion, the total mass of the salt (S_{A1}) of the salty waters (>31.5) in BB (the area A_1 shown in Fig. 3.3d) is calculated from model results in case CR. The time series of S_{A1} has several peaks (Fig. 3.21c). That rapid increase of S_{A1} indicates the start of an intense intrusion event which influences significantly the salinity in the intermediate and bottom layers of BB. The S_{A1} increases from about 2.8×10^6 to about 7.7×10^6 between 3 and 13 February 2014, and increases from about 31.4 to about 32 between 1 and 10 July 2014.

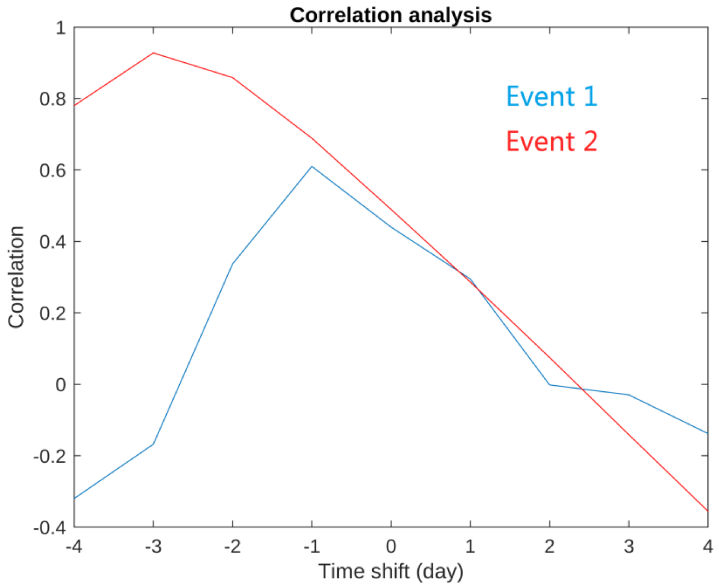

Figure 3.22: Correlation analysis between the total wind stress impulse and near-bottom salinity at the Narrows for two events discussed in Fig. 3.27 and Fig. 3.28.

Time series of total mass of salt (S_{A2}) for the sub-surface high-salinity waters (>31.5) in the OH (the area A_2 shown in Fig. 3.3d) is also calculated from model results in case CR (Fig. 3.21d). The time series of S_{A2} in the OH has high-frequency variability, which is much higher than S_{A1}. It is due mainly to the filtering effect of the shallow topography in the Narrows.

To further investigate the relationship between the intrusion events in BB and the winds, four additional numerical experiments were conducted (Table. 3.1). The model setup and forcing in these four additional experiments are the same as in case CR, except for steady and uniform winds (10 m/s). The four different wind directions in four different directions (either southwesterly, northwesterly, northeasterly, or southeasterly) are used to drive submodel L4. All other model setup and forcing in these additional experiments are the same as those in case CR. These additional numerical experiments were initialized on 1 March 2014 and integrated for 3 days.

The daily mean near-surface (sub-surface) salinity and currents at 2 m (12 m) in HH and adjacent are shown in Figure 3.24 (3.25). In the case with steady and uniform northwesterly winds (CW-NW), the near-surface salinity increases from about 29 in BB to about 31.5 in the OH (Figs. 3.23a and 3.24a). The near-bottom salinity in BB is about 31.5 (Fig. 3.23a). In this case, the high salinity waters from the OH (shown by the isohaline of 31.5) intrude toward BB and reach the bottom of the Narrows (Fig. 3.23a). This indicates that this intense intrusion event induced by the steady northwesterly winds. Physically, the steady northwesterly winds enhance the near-surface seaward currents in HH, since the wind direction is in the similar direction with the seaward currents in the surface layer (Fig. 3.24a). The enhanced near-surface seaward currents result in the strong landward currents in the lower layer in HH (Fig. 3.25a). In this case, the surface salinity in BB is about 29, with the local upwelling induced by strong offshore currents over the northwestern area of BB near the mouth of the Sackville River.

In the experiment with steady and uniform southwesterly winds (CW-SW), the near-surface salinity in central area of BB is about 28 (Fig. 3.23b, Fig. 3.24b), which is lower that the counterpart in case CW-NW. The near-surface salinity is relatively low (high) and about 26 (31) over the northeastern (southwestern) area of BB (Fig. 3.24b). It is due to the southwesterly winds that push the low-salinity near-surface water to northeastward and generates upwelling in the southwestern area of BB. The high-salinity waters from the OH (shown by the isohaline of 31.5) in case CW-SW do not reach the Narrows, and reaches only the central area of the IH due to landward intrusion (Fig. 3.23b). The landward sub-surface currents in IH in case CW-SW are weaker than the counterparts in the experiment CW-NW.

In the experiment with steady and uniform northeasterly winds (CW-NE), the high salinity near-bottom waters from the OH (shown by the isohaline of 31.5) reach the boundary between the IH and the OH (Fig. 3.23c). It means that the landward intrusion in case CW-NE is relatively weak and the near-bottom salinity in BB is not affected significantly by the high-salinity waters from the OH. The near-surface salinity is relatively low (high) and about 26 (30.5) over the southwestern (northeastern) area of BB (Fig. 3.24c).

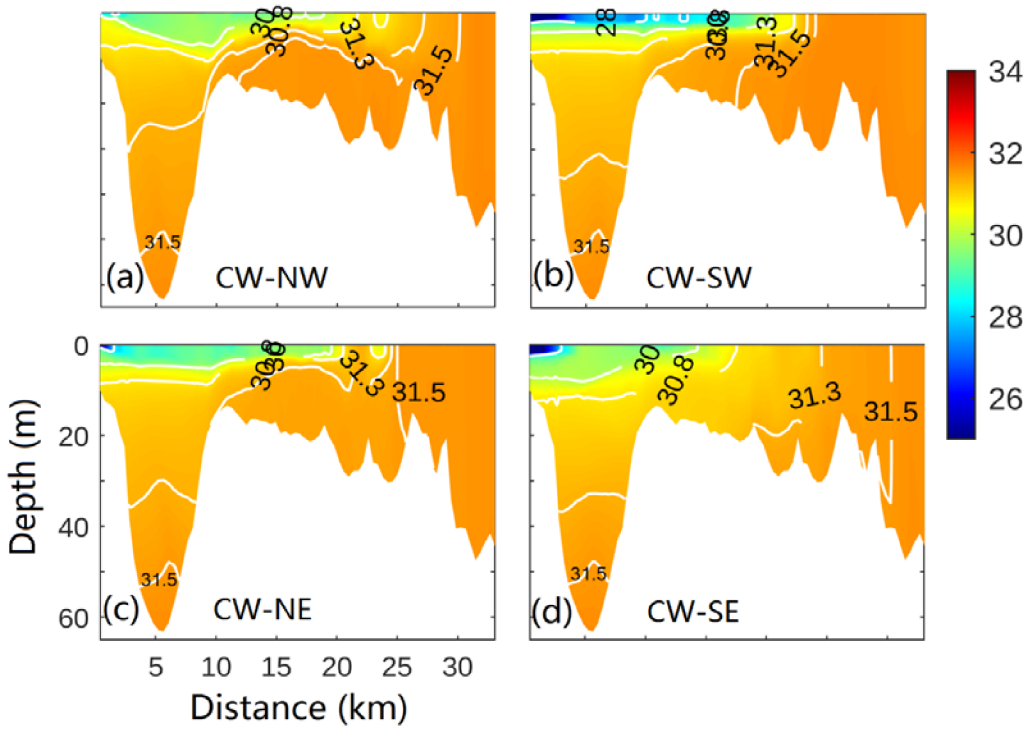

Figure 3.23: Daily mean salinity distributions at transect BH in Halifax Harbour based on model results in four additional experiments with steady and uniform winds blowing (a) northwesterly (CW-NW), (b) southwesterly (CW-SW), (c) northeasterly (CW-NE), (d) and southeasterly (CW-SE) over 3 days.

In the experiment with steady and uniform southeasterly winds (CW-SE), the near-surface low-salinity waters occur in the surface layer from the mouth of the Sackville River to the Narrows, with the lowest salinity to be about 28 (Fig. 3.23d, 3.24d). The seaward spreading of the low-salinity waters is weakest in the case CW-SE among the four cases. This is because the southeasterly winds reduce significantly the near-surface seaward currents in HH, due to the fact that the wind direction is in the opposite direction with the seaward currents in the surface layer. In this case, the high-salinity waters (shown by the isohaline of 31.5) remain in the OH. The landward sub-surface currents in case CW-SE are weakest among the four cases.

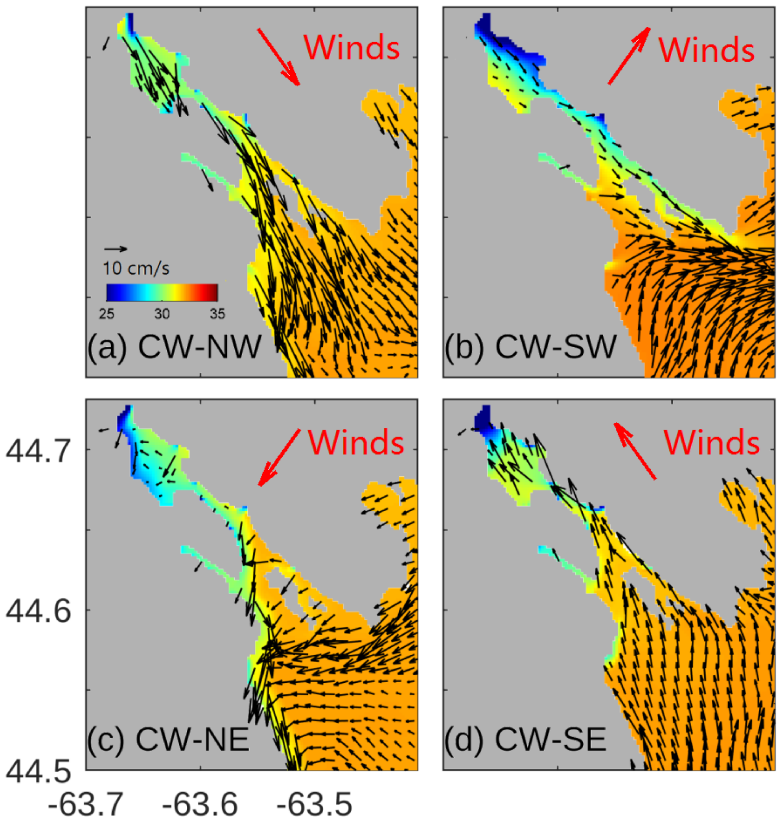

Figure 3.24: Daily mean near-surface salinity and currents at 2 m in HH and adjacent waters based on model results produced by submodel L4 in four additional experiments with steady and uniform winds blowing (a) northwesterly (CW-NW), (b) southwesterly (CW-SW), (c) northeasterly (CW-NE), (d) and southeasterly (CW-SE) over 3 days.

The along-transect and vertical components of daily mean currents at transect BH on 3 March are shown in Figure 3.25 for numerical experiments with steady-winds. In these four cases, the general currents at transect BH are the two-layer estuarine circulation, with surface waters flowing toward the Outer Harbour and sub-surface waters flowing toward BB (Fig. 3.25). The near-surface seaward currents and landward sub-surface current in case CW-NW are strongest among the four cases (Fig. 3.25a, 3.26a). This is because the wind direction in case CW-NW is roughly in the same direction of the transect and the winds enhance significantly the seaward currents in the surface layer.

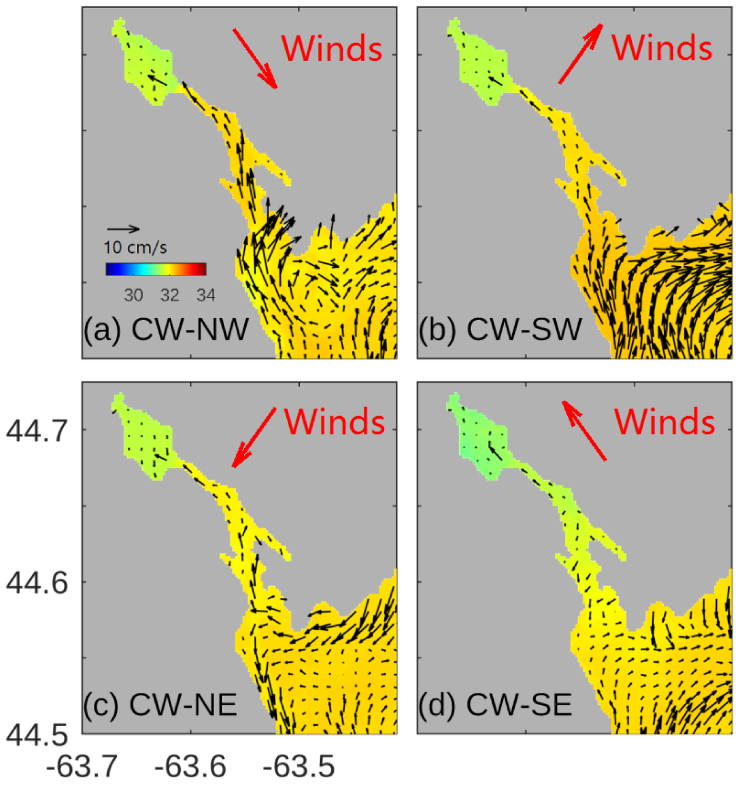

Figure 3.25: Daily mean sub-surface salinity and currents at 12 m in HH and adjacent waters based on model results produced by submodel L4 in four additional experiments with steady and uniform winds blowing (a) northwesterly (CW-NW), (b) southwesterly (CW-SW), (c) northeasterly (CW-NE), (d) and southeasterly (CW-SE) over 3 days.

The strong seaward sub-surface currents are accompanied with the intense sub-surface landward intrusion under the steady and northwesterly winds in case CW-NW. In case CW-NW, upwelling occurs near the mouth of the Sackville River to compensate the relatively strong surface seaward currents in BB. In case CW-SW, the near-surface seaward currents and sub-surface landward currents are relatively weaker than the counterparts in case CW-NW (Fig. 3.26b). In case CW-NE, the two-layer circulation in HH is modulated by the steady northeasterly winds and is relatively weak (Fig. 3.26c). In case CW-SE, the two-layer circulation is the weakest in the four additional experiments (Fig. 3.26d). It indicates the southeasterly winds reduce significantly the two-layer estuarine type circulation in HH.

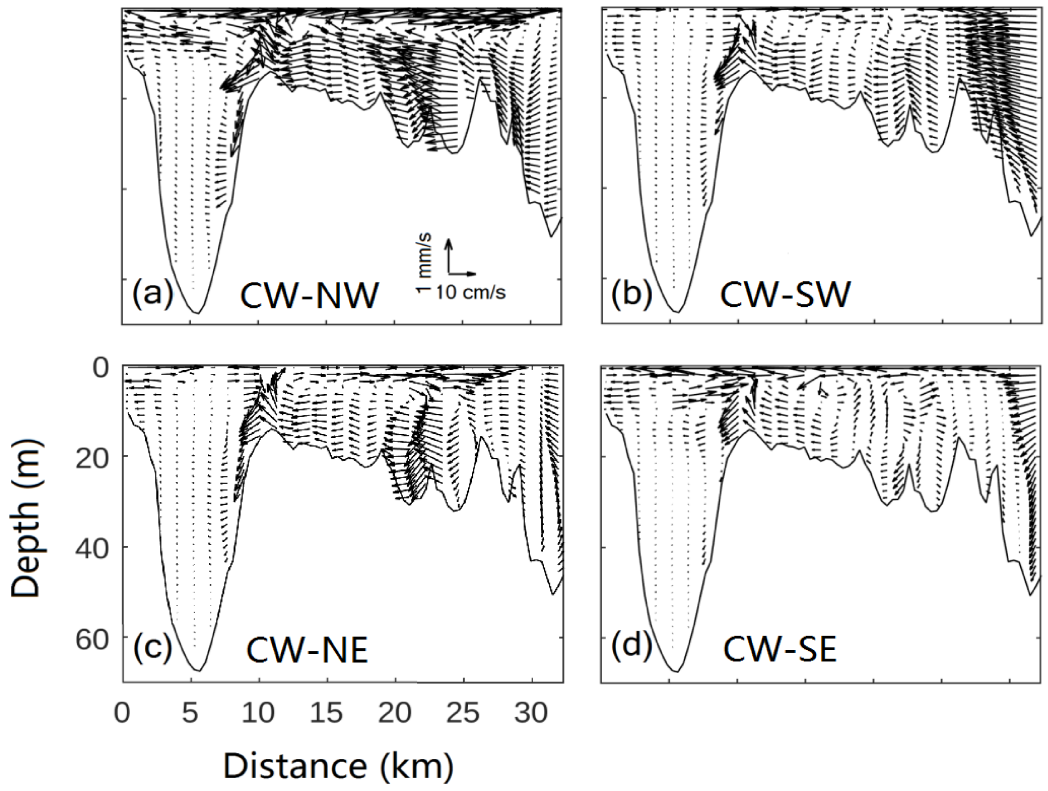

Figure 3.26: The along-transect and vertical component of daily mean currents at transect BH in Halifax Harbour based on model results in four additional experiments with steady and uniform winds blowing (a) northwesterly (CW-NW), (b) southwesterly (CW-SW), (c) northeasterly (CW-NE), (d) and southeasterly (CW-SE) over 3 days.

The model results in these four additional numerical experiments indicate that the intense landward intrusion of offshore deep waters into BB is generated by strong winds, particularly the persistent and strong northwesterly and southwesterly winds. The persistent northwesterly and southwesterly winds enhance the near-surface time-mean seaward currents in HH. The enhanced near-surface seaward currents result in strong landward currents in the bottom layer and generate intense landward intrusion into BB. In comparison, the persistent northwesterly has larger effects than persistent southwesterly winds on triggering the landward intrusion into BB.

3.6 Process Study of Hydrodynamics in Halifax Harbour

To examine the cumulative effects of winds and tides on the time-mean circulation and hydrography in HH, two additional numerical experiments (Table 3.1) were conducted. In Case NW (NT), the wind (tidal) forcing is excluded over the submodel L4 domain.

3.6.1 Roles of Winds

To examine the cumulative roles of winds in HH, the daily mean model results produced by submodel L4 in cases CR and NW on 21 March 2014 are examined first. This particular day was selected since strong southwesterly winds occur over the submodel L4 domain on this day. The differences in the daily mean model results between the two cases are used to quantify the role of winds on the 3D circulation and temperature/salinity.

The daily mean near-surface salinity at 2 m on 21 March 2014 in case CR (Fig. 3.27a) gradually increases from about 25 near the mouth of the Sackville River to about 33 in the OH, due mainly to the freshwater discharges from the Sackville River and sewage discharges in HH as mentioned before. On this day, the daily mean near-surface salinity over the southwestern area of BB is relatively higher than the counterpart over the northwestern area, due mainly to the local upwelling over the southwestern area of BB generated by the southwesterly winds. The daily mean near-surface temperature on 21 March 2014 in Case CR gradually increases from about -1.5 °C in BB to about 3 °C in the OH (Fig. 3.28a). The near-surface temperature is also low and about -1.5 °C in the Northwest Arm. The relatively low temperature waters in BB and the Northwest Arm are generated mainly by negative surface net heat flux in March. The daily mean near-surface currents on this day in Case CR are seaward (southeastward) in BB and the Narrows. In the OH, the daily mean near-surface currents on this day are eastward in the western area and northeastward over the eastern area. The eastward and northeastward currents in the OH are driven by strong southwesterly winds (Fig. 3.27a).

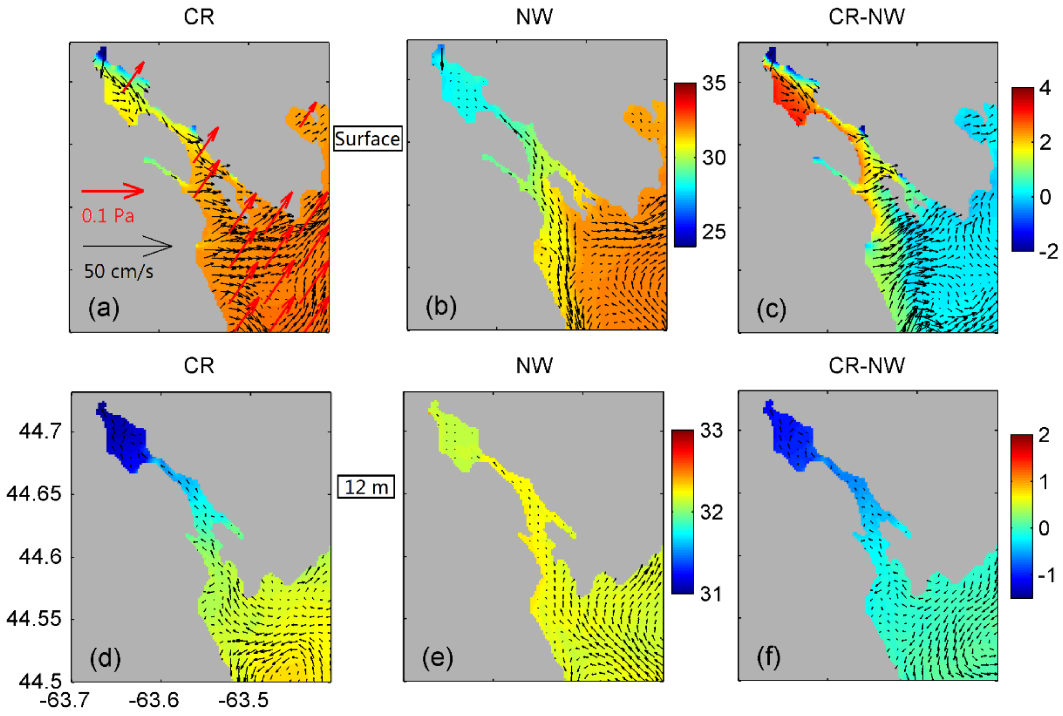

Figure 3.27. Daily mean salinity and currents on 21 March 2014 produced by submodel L4 at (a,b) 2 m and at (d,e) 12 m in cases (a,d) CR and (b,e) NW. Differences in the salinity and currents between cases CR and NW at (c) 2 m and at (f) 12 m. Red arrows are wind stress vectors. For clarity, velocity vectors are plotted at every 4th model grid point.

In case NW, the daily mean near-surface (2m) salinity is relatively lower than the counterpart in case CR, especially over the southwestern area in BB, in the Narrows, and over the western area of the OH (Fig. 3.27b). In this case, the relatively low salinity of near-surface waters over the western area of the OH is caused by the seaward spreading of the estuarine plume of low salinity waters from BB. The daily mean near-surface temperature is relatively lower than the counterpart in case CR (Fig. 3.28b). In case NW, the daily mean near-surface temperature is relative low in BB of about -2 °C and also low over the western area of the OH and about -1.5 °C (Fig. 3.28b). The relatively cool near-surface temperature over the western area of the OH is again caused by the seaward spreading of the estuarine plume of low temperature waters from BB. In case NW, the daily mean near-surface currents on 21 March 2014 are much weaker than the counterparts in case CR (Fig. 3.27b). In case NW, the daily mean near-surface currents

are southward over the western area near the coast in the OH. The differences of the near-surface currents between the two cases are due mainly to the wind-driven currents in case CR.

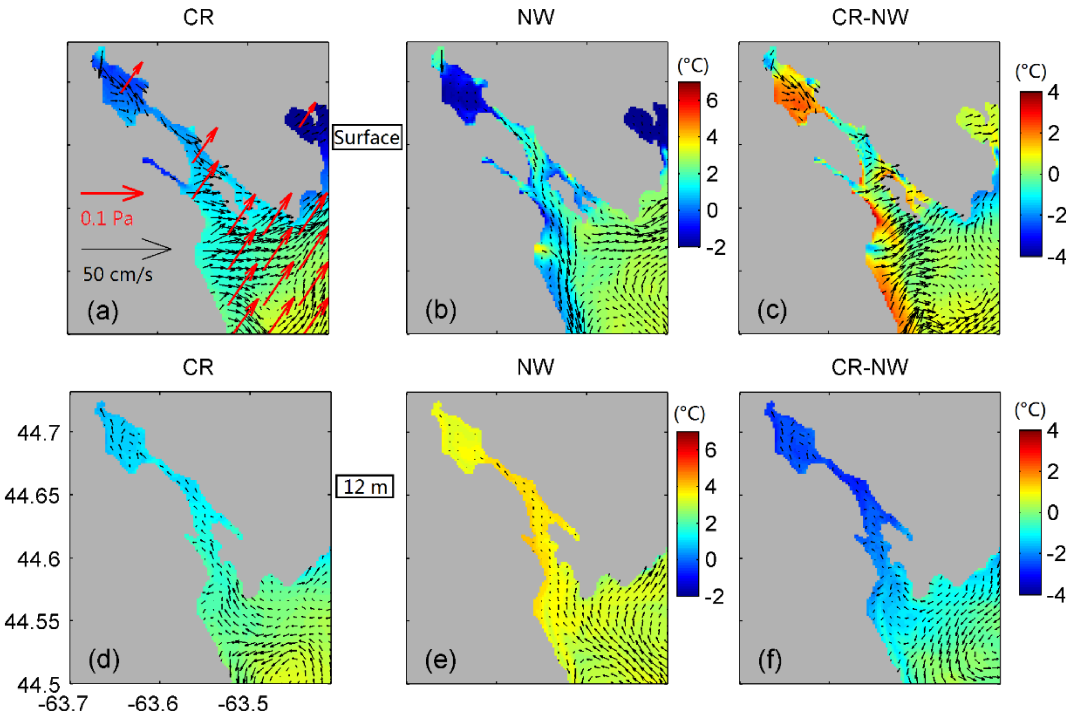

Figure 3.28. Same as Figure 3.27, except for the daily mean temperature and currents (upper panels) at 2 m and (lower panels) at 12 m.

Differences in the daily mean near-surface salinity ($\Delta\bar{S}_2^{CR-NW}$) at 2 m between cases CR and NW are presented in Figure 3.27c. The values of $\Delta\bar{S}_2^{CR-NW}$ are positive over the southwestern area of BB, in the Narrows, and in the western area of the OH, with the maximum value of about 3. The differences in the daily mean near-surface temperature ($\Delta\bar{T}_2^{CR-NW}$) and currents ($\Delta\bar{U}_2^{CR-NW}$) between cases CR and NW are presented in Figure 3.28c. The values of $\Delta\bar{T}_2^{CR-NW}$ are positive in BB and over the western area of the OH, with the maximum value of about 2 °C. The currents of $\Delta\vec{\bar{U}}_2^{CR-NW}$ are eastward over the southwestern area of BB and in the OH. The offshore eastward currents over the western area of BB are wind-driven currents, which associated with the coastal wind-driven

upwelling. The differences can be explained by (1) lack of wind-driven currents in the upper layer, (2) lack of wind-induced vertical mixing, and (3) lack of wind-driven costal upwelling in cast NW. This indicates that winds play a very important role in affecting the near-surface currents and temperature/salinity in HH by modulating the 3D circulation and enhance the vertical mixing in HH.

The daily mean sub-surface salinity at 12 m on 21 March 2014 in case CR (Fig. 3.27d) is relatively higher than the counterpart near the surface (Fig. 3.27a), which increases from about 31 near the mouth of the Sackville River to about 33 in the OH. The daily mean sub-surface temperature on this day in case CR (Fig. 3.28d) is relatively warmer that the counterpart near the surface and ranges from about -1 °C in BB to about 3 °C in the OH (Fig. 3.28a). The daily mean sub-surface currents in this case are landward (northeastward) in BB and the Narrows (Fig. 3.27d), and significant weaker than the counterpart near the surface (Fig.3.27a). A branch of southwestward sub-surface currents compensate the strong wind-driven near-surface northeastward currents in the OH (Fig. 3.27d).

In case NW, the daily mean sub-surface salinity (Fig. 3.27e) is relatively higher than the counterpart in case CR (Fig. 3.27d), which gradually increases from about 32 near the mouth of the Sackville River to about 32.3 in the OH. In this case, the daily mean sub-surface temperature on 21 March 2014 is relatively uniform about 3 °C in HH (Fig. 3.28e), which is higher than the counterpart in case CR (Fig. 3.28d). The daily mean sub-surface currents in case NW are also landward (northeastward) in BB and in the Narrows (Fig. 3.27e).

Differences in the daily mean sub-surface salinity ($\Delta\bar{S}_{12}^{CR-NW}$) at 12 m between cases CR and NW are presented in Figure 3.27f. The values of $\Delta\bar{S}_{12}^{CR-NW}$ are negative everywhere, and about -1 in BB and about -0.6 in the OH, due to the blending of low-salinity upper-layer waters with high-salinity lower-layer waters associated with wind-induced vertical mixing in case CR. The differences in the daily mean sub-surface temperature ($\bar{T}_{12}^{CR-NW}$) and currents ($\Delta\vec{\bar{U}}_{12}^{CR-NW}$) at 12 m between cases CR and NW are shown in Figure. 3.28f. The values of $\Delta\bar{T}_{12}^{CR-NW}$ increase from about -2 °C in BB to about 0 °C in the OH. The

negative values of $\Delta\bar{T}_{12}^{CR-NW}$ in BB and the Narrows are again due mainly to the effect of wind-induced vertical mixing and wind-driven upwelling. The currents of $\Delta\vec{\bar{U}}_{12}^{CR-NW}$ are southwestward which compensate the strong wind-driven near-surface northeastward currents in the OH (Fig. 3.28f). The results show winds also play a very important role in affecting the sub-surface currents and temperature/salinity in HH.

3.6.2 Roles of Tides

The daily mean model results produced by submodel L4 in cases CR and NT on 21 March 2014 are analysed to examine the roles of tides in HH. The differences in the daily mean model results between the two cases are used to quantify the role of tidal forcing on the 3D circulation and temperature/salinity. At that day, the ranges of observed and simulated tidal elevations at location B_1 (Fig. 3.1) are about 0.7 m (Fig. 3.9) during the period between the spring tides and neap tides.

In case NT, the daily mean near-surface salinity and currents at 2 m are similar as the counterparts in case CR (Fig. 3.29a,b), except for the Narrows. In this case, the near-surface salinity in the Narrows is relatively lower than the counterpart in Case CR, due mainly to lack of tidal mixing in the Narrows in Case NT. The Narrows is a dynamically active area in HH, with strong tidal currents. The strong tidal currents result in strong mixing (horizontal and vertical) in the Narrows. The daily mean near-surface temperature and currents at 2 m in case NT are similar as the counterparts in Case CR (Fig. 3.29a,b). In the OH, the near-surface currents in case NT are slightly larger than the near-surface currents in case CR (Fig. 3.29b), due mainly to the effect of tidal forcing on the path way of the surface currents in the OH.

Differences in the daily mean near-surface salinity ($\Delta\bar{S}_2^{CR-NT}$) at 2 m between cases CR and NT are shown in Fig. 3.29c. The values of $\Delta\bar{S}_2^{CR-NW}$ are small in HH, except in the Narrows about 1. This indicates that the effects of tides are small in affecting the near-surface salinity and currents in HH, except for the Narrows. The differences in the daily mean near-surface temperature ($\Delta\bar{T}_2^{CR-NT}$) and currents ($\Delta\vec{\bar{U}}_2^{CR-NW}$) between cases CR and NT are shown in Figure. 3.30c. The values of ΔT_2^{CR-NW} are relatively small in HH,

with the largest magnitude about -0.3 °C in the middle area of the OH. It is due to the tidal forcing influences the pathway of the surface currents in the OH, which transport the relatively cool offshore waters to the OH.

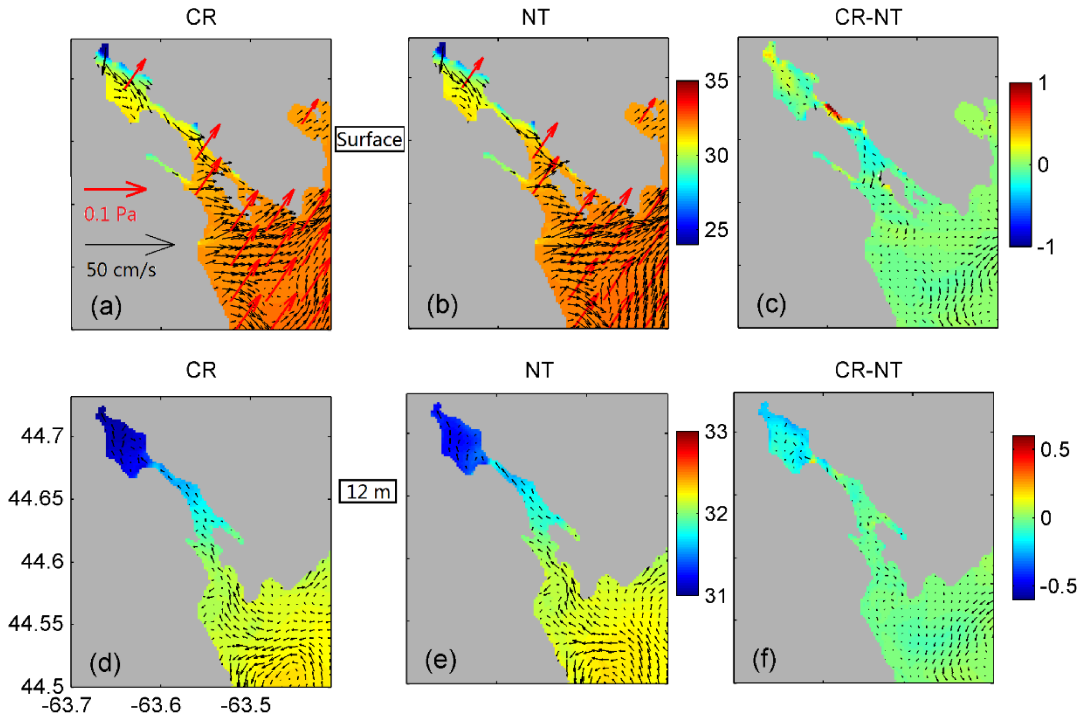

Figure 3.29. Daily mean salinity and currents on 21 March 2014 produced by submodel L4 at (a,b) 2 m and at (d,e) 12 m in cases (a,d) CR and (b,e) NT. Differences in the salinity and currents between cases CR and NT at (c) 2 m and at (f) 12 m. Red arrows represent wind stress vectors. For clarity, velocity vectors are plotted at every 4th model grid point.

In Case NT, the daily mean sub-surface salinity at 12 m is similar as the counterpart in case CR (Fig. 3.29d,e). The daily mean sub-surface temperature and currents in Case NT are also similar as the counterparts in case CR (Fig. 3.30d,e).

Differences in the daily mean sub-surface salinity ($\Delta\bar{S}_{12}^{CR-NT}$) at 12 m in cases CR and NT are shown in Fig. 3.29f. The values of $\Delta\bar{S}_{12}^{CR-NW}$ are relatively small in HH, with the largest value of about -0.2 in BB. The differences in the daily mean sub-surface temperature ($\Delta\bar{T}_{12}^{CR-NT}$) and surface currents ($\Delta\vec{\bar{U}}_{12}^{CR-NT}$) between cases CR and NT are

shown in Fig. 3.30f. The values of $\Delta\bar{T}_{12}^{CR-NT}$ are also relatively small in HH, with the largest value of about -0.3 °C in BB. This indicates that, in comparison with local winds, the effects of tides are relatively small in affecting the time-mean currents and temperature/salinity in HH, except for the Narrows.

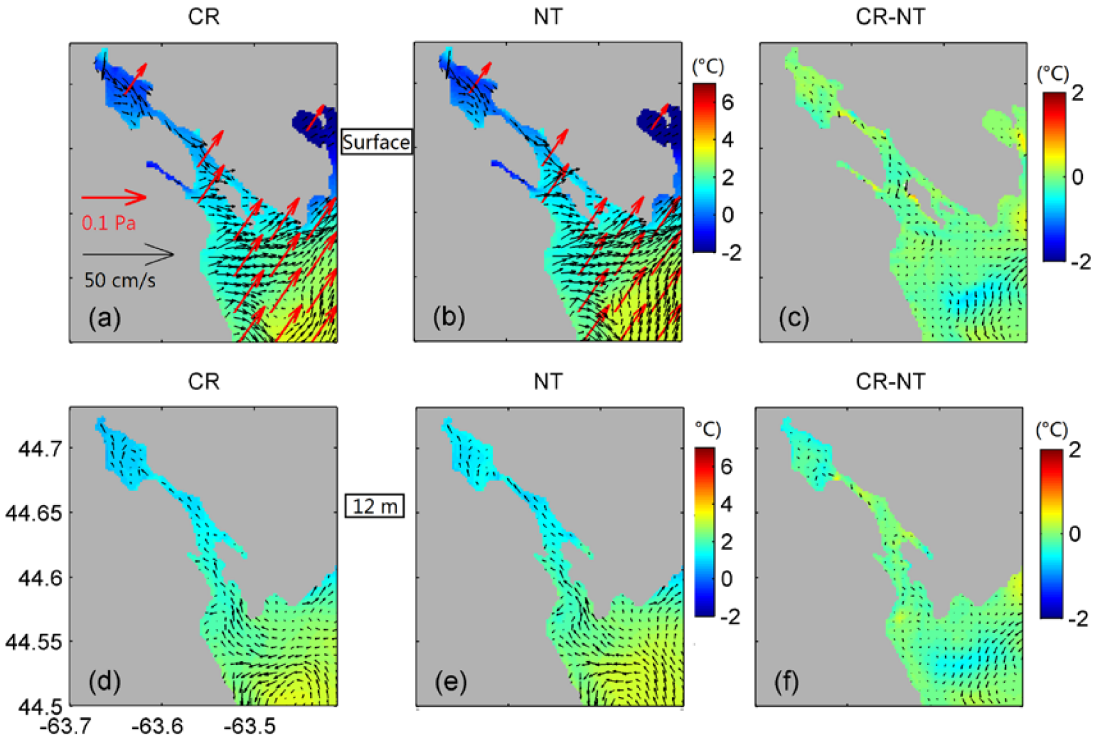

Figure 3.30. Same as Figure 3.29, except for the daily mean temperature (upper panels) at 2 m and (lower panels) at 12 m.

3.7 Discussion

In this Chapter, a state-of-the-art, nested-grid modelling system (NGMS-seCS) based on ROMS (*Shchepetkin and McWilliams* 2005; *Haidvogel et al*., 2008) and CICE (*Hunke et al.,* 2010) was applied to Halifax Harbour (HH) and adjacent waters of the Scotian Shelf (ScS) with the four-level nested-grid setup. It was the first time that seasonal variability of three-dimensional (3D) circulation and landward intrusion of offshore sub-surface waters in HH were studied using a high-resolution and S-coordinate ocean circulation model. The model external forcing includes tides, atmospheric forcing and freshwater

discharges. The inner-most submodel (L4) for HH and adjacent waters has the resolution about 180 m in the horizontal direction and 40 S-coordinate levels in the vertical direction. The performance of nested-grid modelling system was validated using observations and reanalysis data available to this study.

For quantifying the general mean state of hydrodynamics and stratification in HH, the annual mean temperature, salinity and currents in HH in 2014 were constructed based on results of submodel L4. The annual mean near-surface salinity gradually increases from about ~28 at the mouth of the Sackville River to 32.5 over the Outer Harbour (OH). The annual mean near-surface temperature also gradually increases from about 6 °C at the mouth of the Sackville River to 8 °C over the OH. At depths greater than 10 m, the annual mean sub-surface salinity and temperature in HH also have noticeable spatial variability from the mouth of the Sackville River to the OH.

The annual mean circulation in HH is characterized by the two-layer estuarine circulation, with seaward (southeastward) currents of the near-surface waters (at depths less than 5 m) and landward (northwestward) currents of sub-surface waters (at depths greater than 5 m). The main physical processes for the annual-mean circulation and stratification in HH are threefold: the freshwater discharges from the Sackville River and sewage outfalls in HH, horizontal pressure gradients, and strong entrainment between low-salinity waters in the upper layer and high-salinity waters in the lower layer of HH. The annual mean two-layer estuarine circulation inn HH produced by the nested-grid S-coordinate modelling system is consistent with the previous studies (*Petrie and Yeats, 1990*; *Tee and Petrie 1991*; *Shan et al.,* 2011). It should be noted that the annual mean circulation and stratification presented in this Chapter are better than previous studies due to the fact that our modelling system is better and the model forcing is more realistic in comparison with previous modelling studies.

Analyses of monthly mean model results in 2014 demonstrated that the two-layer estuarine circulation and stratification in HH have significant seasonal variability, due mainly to large seasonal variability in freshwater discharges from the Sackville River, net heat fluxes at the sea surface, winds and wind-induced vertical mixing. The near-surface

salinity in Bedford Basin (BB) is relatively lowest in November and highest in August in 2014. Over the OH, the near-surface salinity is highest in August and lowest in February and May in 2014. Due mainly to the large seasonal variability in the net heat fluxes and wind-induced vertical mixing, the near-surface temperature in BB is cool in February (~ -1 °C) and May (~ 1 °C), relatively warm in November (~ 7 °C), and warmest in August (~ 13 °C). Over the OH, the near-surface temperature is also relatively cool in February (~ 3 °C) and May (~4 °C), warm in November (~ 9 °C) and warmest in August (~ 12 °C), due to the joint effect of the net heat flux at the sea surface and landward transport of offshore water masses over the inner ScS.

The 3D circulation in HH has large seasonal variability, due mostly to the large seasonal variability in winds and buoyancy forcing associated with freshwater discharges and net heat fluxes at the sea surface. In 2014, the seaward (landward) currents in the surface (lower) layer of HH are stronger in February and November and weaker in May and August. Analyses of model results also demonstrated that, on the monthly mean time scale, stronger seaward currents in the surface layer are accompanied by stronger landward currents in the lower layer in HH. The seasonal variability of temperature/salinity and 3D circulation in HH were studied previously by *Shan and Sheng* (2012). However, the z-coordinate model used in *Shan and Sheng* (2012) did not resolve well the local topography in the Narrows and therefore had large model errors in simulating the 3D circulation and hydrography in the Narrows. In this study, the monthly mean model results and associated seasonal variability produced by the advanced S-coordinate modelling system (ROMS) are more robust than the previous studies.

The landward intense intrusion events in HH were identified in several previous studies based on in-situ observations in BB (*Platt et al*., 1972; *Punshon & Moore*, 2004; *Burt et al.,* 2013). However, the main physical processes triggering these intrusion events are not well understood. Based on model results in 2014 produced by submodel L4, two intense intrusion events of offshore sub-surface waters into BB were chosen for analysis. These intense intrusion events differ from the annual-mean or monthly mean landward currents associated with the freshwater charges in HH discussed above. These intense intrusion events were identified based on the rapidly increase of salinity in the bottom layer of BB

during short periods from a few hours to a few days. The intense intrusion events of offshore sub-surface waters into BB have significant effects on affecting the hydrography, biological components, and 3D circulation in HH over time scales much shorter than the annual mean and monthly mean time scales. A better understanding of the dynamics of intense intrusion events of offshore sub-surface waters into BB is important to economic activities and the management of ecosystem (i.e., sewage discharges and spring bloom).

There are several important physical processes affecting the landward intense intrusions, including the local processes (such as the local winds and freshwater discharges) and non-local (or remote) processes (such as shelf waves and large-scale circulation over the inner ScS). As the first attempt to define a useful index for predicting the intense landward intrusion in HH, we introduced the wind impulse, which is defined as the integration of the wind stress during the recent past period, and found that the intense landward intrusion is correlated partially with the wind impulse. Four numerical experiments with steady and uniform winds in four different directions were conducted for investigating the relationship between the intrusion events and wind directions. It was the first time that we demonstrated that the northwesterly persistent winds play the most important role in triggering the intense landward intrusion in HH among the four cases. This is because seaward (landward) currents in the surface (lower) layer in HH are the strongest if the persistent winds are northwesterly, which are approximately in the same direction of the seaward currents. The southwesterly persistent winds can also generate the intense landward intrusion, but less effective than the northwesterly winds. The southeasterly persistent winds, by comparison, put off the intense intrusion in HH.

The performance of submodel L4 in simulating temperature/salinity and their seasonal variability was assessed using the in-situ hydrographic observations in BB in 2014. Submodel L4 generates the vertical distribution and the seasonal cycle of temperature and salinity similar to the observed temperature/salinity in BB. It should be noted that submodel L4 has significant deficiency. For example, submodel L4 underpredicts the temperature in the surface layer and overpredicts the temperature in the bottom layer in BB. This model bias is likely due to the inaccuracy of the net heat flux at the sea surface and the coarse horizontal resolution of submodel L4 and atmospheric forcing. Specially,

the horizontal resolution of submodel L4 (~180 m) is not sufficient to resolve the local topography of the Narrows which is ~500 m wide. A numerical model with fine horizontal resolutions (60 m or finer) should be used in order to simulate accurately the 3D currents and stratification in the Narrows and IH. In addition, the boundary conditions for submodel L4 were taken from results produced by submodel L3. Therefore, the performance of submodel L4 is also affected by the performance of submodels L3. Data assimilation should be used in submodel L3 to reduce the model errors.

3.8 Conclusion

The nested-grid circulation-ice modelling system (NGMS-seCS) was used in this Chapter to investigate the 3D circulation, temperature/salinity and associated variability in HH and adjacent waters. This coupled circulation-ice modelling system is based on the Regional Ocean Modelling System (ROMS, *Shchepetkin and McWilliams* 2005; *Haidvogel et al*., 2008) and the Los Alamos Sea Ice Model (CICE, https://zenodo.org/record/1205674). This modelling system was driven by tides, freshwater discharges, and three-hourly atmospheric forcing including sea-level atmospheric pressures and winds. The performance of the NGMS-seCS was assessed recently by *Pei et al.* (2022). In this Chapter, the model performance was further assessed using available observations and reanalysis data in 2014. It was found that the NGMS-seCS reproduces reasonably well the sea levels, temperature, salinity, and currents in HH. The annual mean circulation in HH produced by submodel L4 is characterized by the typical two-layer estuarine circulation, with the near-surface waters flowing seaward and sub-surface waters flowing landward. It was found that submodel L4 can reproduce the observed temperature, salinity and associated seasonal and synoptic variability in HH. The model results indicate that the circulation, temperature, and salinity in HH have large seasonal variability. For example, the surface currents in this area are larger in winter than the counterparts in the summer due to the strong winds in winter.

Model results produced by submodel L4 of the NGMS-seCS were used in examining the main processes affecting landward intrusions of offshore deep waters into BB. One of important findings based on model results is that the persistent northwesterly winds can

generate the intense landward intrusion of offshore sub-surface waters into the intermediate and bottom layers of BB. The persistent southwesterly winds can also generate the intense landward intrusion, but less effective than the northwesterly winds. In comparison, the persistent southeasterly winds reduce significant the seaward currents in the surface layer of HH and the landward intrusion of offshore sub-surface salty waters ino BB.

We also followed *Shan and Sheng* (2022) and used the wind impulse to identify the accumulate effects of winds. The along-longitudinal (seaward) wind impulse enhanced the near-surface time-mean seaward currents in the HH. The enhanced near-surface seaward currents resulted in strong landward currents beneath the surface layer, and generate the landward intrusion into BB.

A process study was conducted using the NGMS-seCS to investigate the cumulative effects of winds and tides on the 3D time-mean temperature, salinity and currents in HH and adjacent waters. The model results demonstrated that local winds played a very important role in affecting the 3D currents and temperature/salinity in HH, through the wind-induced vertical mixing, wind-driven currents, and wind-driven coastal upwelling. Tides played the secondly role in affecting the 3D currents and temperature/salinity in BB. By comparison, the tidal effects are very important in the Narrows.

CHAPTER 4

STUDY OF STORM-INDUCED CHANGES IN CIRCULATION AND TEMPERATURE OVER THE NORTHERN SOUTH CHINA SEA DURING TYPHOON LINFA

4.1 Introduction

The main focus of this Chapter is on the process study of hydrodynamic response of the South China Sea (SCS) during the extreme weather conditions. The SCS is an arm of the western Pacific Ocean in Southeast Asia, and is one of the largest semi-enclosed marginal seas in the world. The SCS is bordered by southern China to the north, Vietnam and the Gulf of Thailand to the west, Malay Peninsula to the south, and Philippines and a chain of islands and straits to the east (Fig. 4.1). The SCS has a surface area of about 3.5×10^6 km^2 and the maximum water depth is greater than 5000 m (*Yang et al.,* 2002, *Wang and Li*, 2009).

The ocean circulation and temperature/salinity in the SCS have significant temporal and spatial variability, due mainly to large seasonal variabilities in atmospheric forcing associated with monsoon winds in the region (*Hu et al.,* 2000; *Yang et al.,* 2002). In winter, the northeasterly winds prevail over the SCS, with the mean speed of 9 m s^{-1} in winter (*Hellerman and Rosenstein*, 1983; *Hu et al.,* 2000). In summer, by comparison, the southwesterly winds with the mean speed of about 6 m s^{-1} occur over most parts of the SCS. The wind directions in summer change to more southerly over the northern South China Sea (nSCS). The seasonal circulation and temperature/salinity over the nSCS are also affected significantly by water exchanges between the SCS and the East China Sea through Taiwan Strait and between the SCS and the Kuroshio Current through Luzon Strait (*Hu et al.,* 2000).

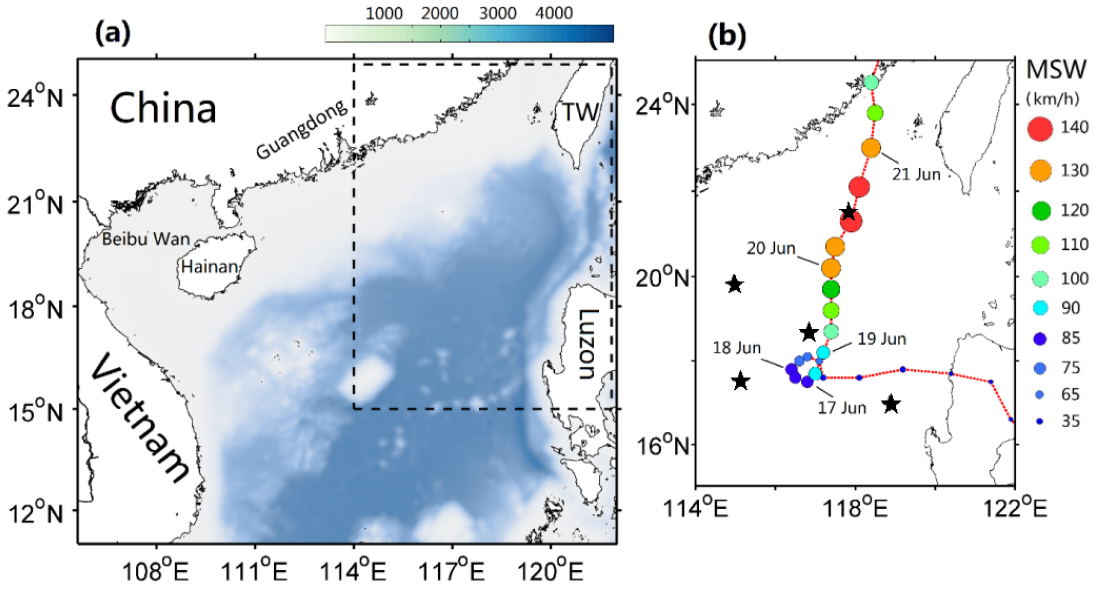

Figure 4.1: (a) Major bathymetric features over the northern South China Sea, and (b) the 6-hourly storm track of Typhoon Linfa in June 2009 with maximum sustained winds (MSW) based on the data extracted from the Physical Oceanography Distributed Active Archive Center (http://podaac.jpl.nasa.gov.) Abbreviation is used for Taiwan (TW). The stars in (b) represent locations of Argos.

The SCS is one of regions on the Earth affected significantly by tropical cyclones and typhoons (*Wang et al*., 2007). A tropical cyclone (TC, or typhoon) can generate significant changes in the ocean temperature, salinity, primary production, and other biogeochemical conditions, particularly in the upper ocean. Previous studies demonstrated that the storm-induced vertical mixing and upwelling can result in significant cooling in the sea surface temperature (SST) (*Subrahmanyam et al.,* 2002; *Lin et al.,* 2003; *Davis and Yan*, 2004; *Walker et al.,* 2005; *Zheng and Tang*, 2007). Vertical mixing is an entrainment process produced by the wind-induced velocity shear (*Shay et al,.* 2000; *James and Shay,* 2009). Upwelling in the upper water column can be induced by the Ekman pumping effect induced by TC's cyclonic winds and the TC-induced near-inertial currents (*Price et al,.* 1994; *Huang et al*., 2011). The study of the storm-induced circulation during Tropical Cyclone Ernie (1996) in the SCS demonstrated an intense upwelling in the sub-surface layer and surface cooling to the right of the storm track (*Chu et al.,* 2000). Rapid upwelling responses were also inferred from the satellite-derived data

along the east of Hurricane Ivan's path in the Gulf of Mexico (*Walker et al.,* 2005). The previous study of the upper ocean response to Typhoon Krovanh in 2003 demonstrated that the typhoon-induced SST cooling was caused mainly by vertical mixing (*Jiang et al.,* 2009). Similarly, the numerical study made by *Sheng et at*. (2006) on the storm-induced circulation during Hurricane Juan (2003) over the Eastern Canadian Shelf demonstrated that the vertical mixing plays the dominant role in the SST cooling to the right of the storm track. Therefore, scientific debates about the dominant role of storm-induced vertical mixing and upwelling for the SST cooling during extreme weather conditions will continue.

Typhoon Linfa (2009) is considered in this Chapter. Linfa originated from a tropical depression over the western Pacific Ocean on 13 June 2009. This storm moved to the nSCS on 16 June and reached a category-12 typhoon status during 17-19 June, with maximum sustained wind speeds up to 140 km h^{-1} (Fig. 4.1b). Linfa made a landfall in Jinjiang of Fujian on 22 June and caused significant property damage worth about $45 million (*State Oceanic Administration*, 2009), including structural damages of 256 fishing boats and loss of aquaculture areas of about 125 km^2.

In-situ oceanographic observations in the vicinity of the storm track during the passage of Linfa were too sparse in time and space to be useful in generating a synopsis of storm-induced changes in time-varying and three-dimensional (3D) currents and temperature/salinity. Analyses of satellite remote sensing data demonstrated the occurrence of significant changes in marine conditions over the nSCS during the passage of Linfa. Based on satellite remote sensing data, *Chen and Tang* (2010) found an eddy-feature manifesting as a phytoplankton bloom and a coincident cold eddy that occurred over areas around the storm track over the nSCS during Typhoon Linfa. *Liu et al.* (2019) confirmed Chen and Tang's finding based on different satellite remote sensing data. We calculated the differences in the daily mean SST between 22 and 17 June 2009 based on the satellite remote sensing data from the Level 4 Group for High-Resolution SST and obtained the similar pattern of the SST cooling during the period of Typhoon Linfa (Fig. 4.2). The differences in SST were relatively small over areas far from the storm track of Linfa. There was systematic SST cooling centred about 55 km to the right side of the storm track (when facing in the direction taken by the typhoon), which was arguably

generated by Linfa. The maximum storm-generated SST cooling was about -3 °C (Fig. 4.2).

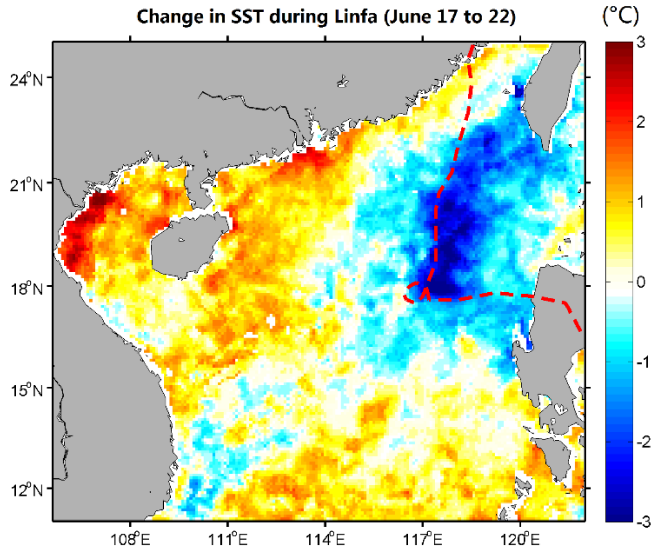

Figure 4.2: Differences in the daily mean sea surface temperature over the northern South China Sea during the period of Typhoon Linfa calculated from satellite remote sensing SST data on 22 and 17 June 2009 (Level 4 Group for High-Resolution SST). The red dashed line represents the storm track of Linfa.

Numerical ocean circulation models have increasingly been used in simulating typhoon-induced changes in physical and biogeochemical conditions. Sun et al. (2011) numerically examined the near-inertial oscillations (NIOs) trapped and amplified by background flow over the nSCS during Typhoon Faith in 1998, although they did not examine the thermal response to the storm. *Tang et al*. (2012) numerically studied the storm-induced circulation and hydrographic distributions and retention of near-surface particles over the Pearl River Estuary (PRE) and its adjacent shelf waters of the nSCS during Super Typhoon Koryn in 1993. *Lee and Chen* (2012) used a coupled atmosphere–wave–ocean model in investigating the air–sea coupling processes and their impacts on the structure of the hurricane boundary layer. *Zhan et al.* (2014) suggested the oceanic processes rather than the air-sea heat flux dominated the thermal response based on numerical model results of upper ocean response to typhoon Kalmaegi. Many important scientific questions on the storm-induced processes in the upper ocean, however, remain

to be addressed. The main objective of this Chapter is to quantify the main processes affecting storm-induced changes in 3D circulation and temperature/salinity and near-inertial oscillations (NIOs) over the nSCS Linfa using an ocean circulation model.

The structure of this chapter is as follows. Section 4.2 presents observations and reanalysis data used in this Chapter. Section 4.3 describes the shelf circulation model setup and forcing. Section 4.4 presents the assessment of model performance. Section 4.5 presents analyses of main processes of storm-induced changes in 3D currents and temperatures over the nSCS during the passage of Typhoon Linfa. The last section presents the summary and conclusions.

4.2 Observational and Reanalysis Data

4.2.1 Typhoon Linfa

Typhoon Linfa originated from a tropical depression generated over the northwest Pacific Ocean on 13 June 2009. The storm moved northwestward to the Philippines on 15 June, with the maximum sustained wind (MSW) of ~28 km h^{-1} (Fig. 4.1b). Linfa moved westward and passed over the Luzon Island on 16 June to enter the nSCS. Linfa intensified as a tropical cyclone with the MSW of about 72 km h^{-1} and made an anticlockwise loop around the area centered at about (116.5°E, 18.0°N) on 17-19 June. On these three days, the translational speeds of Linfa were relatively slow and about 7.2 km h^{-1}. On 20 June, Linfa passed over Dongsha Atoll (116.8°E, 20.7°N) and intensified to a category-12 typhoon status (or a category-1 hurricane in the Saffir-Simpson tropical cyclone scale), with the MSW of about 140 km h^{-1} and the translational speed of about 21 km h^{-1} (Fig. 4.1b). At 12:30 UTC on 21 June, Typhoon Linfa made a landfall in Jinjiang of Fujian province, China.

The 6-hourly best storm track data constructed by the Japan Meteorological Agency for Typhoon Linfa (including the cyclone center position, intensity, and central atmospheric pressure) are used to develop high-resolution winds and atmospheric pressures during the passage of Linfa (see section 4.3.2 for more details). These best storm track data were obtained from the National Institute of Informatics website (http://www.nii.ac.jp/).

4.2.2 Observed Temperature and Chlorophyll-a Concentrations at Sea Surface

The daily satellite SST data used in this Chapter (Fig. 4.3a,b) were extracted from the Group for High-Resolution SST (GHRSST) level 4 dataset (5 km × 5 km) constructed by the Physical Oceanography Distributed Active Archive Center (available at poet.jpl.nasa.gov). The daily mean sea surface chl-a concentration data used here (Fig. 3c and d) were extracted from the standard Level 2 Moderate Resolution Imaging Spectroradiometer (MODIS) dataset (1 km × 1 km) provided by the NASA's Ocean Color Working Group (available at http://oceancolor.gsfc.nasa.gov/).

4.2.3 Argo Data

The vertical temperature profiles observed by five Argo floats near the storm track of Linfa during the study period are used to validate the model performance in section 4.4.2. The locations of these Argo floats are shown in Fig. 4.1b. The observation times for these Argo data to be used here are shown in Table 4.3. The hydrographic profiles of Argo floats were extracted from the dataset produced by the International Argo Program (www.argodatamgt.org/).

4.2.4 HYCOM Reanalysis

The three hourly HYCOM Global 1/12° Reanalysis data (http://www.hycom.org) are used in the model initialization and specification of open boundary conditions in section 4.3 and validation of the model performance in section 4.4.2. The global version of the HYCOM has has the advantage of an eddy-resolving resolution (1/12°), which is about 9 km within the nSCS. HYCOM uses 32 hybrid layers in the vertical direction. The hybrid layer structure in the HYCOM was chosen to have sufficient vertical resolutions in the mixed layer with increasingly thicker isopycnal layers with depth. The HYCOM Reanalysis was generated using the HYCOM with the Navy Coupled Ocean Data Assimilation (NCODA) system (*Cummings,* 2005; *Cummings and Smedstad*, 2013) for data assimilation. The performance of the HYCOM reanalysis was extensively validated in the past. *Kara et al.* (2008) used multiple statistical metrics to evaluate the performance of the HYCOM and demonstrated that the reanalysis has the ability to

reproduce the past SST events in climatological and interannual simulations. Based on a global HYCOM simulation, *Metzger et* al. (2010) reported high correlations between the simulated and observed Indonesian Throughflow. *Chen et al.* (2018) demonstrated that the global HYCOM model results agree well with 23-year observations.

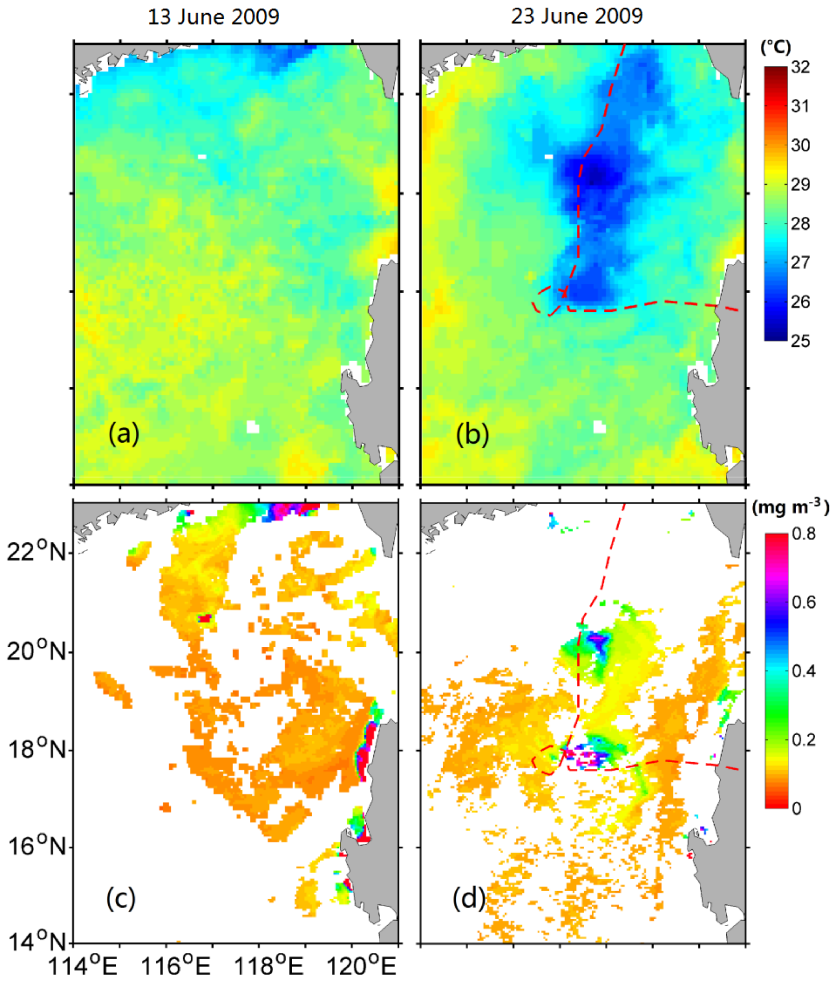

Figure 4.3: Distributions of (a, b) satellite-derived daily mean SSTs and (c, d) daily mean sea surface chl-a concentrations over the northeast South China Sea before (13 June, left panels) and after (23 June, right panels) Typhoon Linfa. The daily mean SSTs were calculated from daily satellite SST data extracted from Level 4 Group for High-Resolution SST (GHRSST). The daily mean Chl-a data were extracted from standard Level 2 products of the Moderate Resolution Imaging Spectroradiometer (MODIS).

4.2.5 Atmospheric Reanalysis Data

The atmospheric data were extracted from the Climate Forecast System Reanalysis

(CFSR, *Saha et al.,* 2010). The horizontal resolutions of the CFSR fields are about 0.3° and 0.5° respectively for the winds and SLPs. The atmospheric data used to drive the circulation model in this study include 6-hourly fields of air temperature, specific humidity, wind velocity at 10 m above the mean sea level (MSL), atmospheric pressure at the MSL (SLP), cloud cover, total precipitation, and solar radiation.

4.3 Circulation Model Setup and Forcing

4.3.1 Model Setup

The Regional Ocean Modeling System (ROMS) (*Shchepetkin and McWilliams* 2005; *Haidvogel et al*., 2008) is applied to the nSCS for simulating storm-induced changes in the 3D circulation and temperature/salinity during Typhoon Linfa. ROMS is a free-surface, terrain-following, primitive equation ocean model. ROMS model has been used extensively (e.g., *Hu et al.,* 2012; *Song et al.,* 2016a,b; *Takakura et al.,* 2019). Previous studies demonstrated that ROMS has good performance in simulating 3D currents and temperature/salinity over many different coastal and shelf waters.

The domain of the shelf circulation model for the nSCS (hereafter ROMS-nSCS) covers the region between 105.6 °E and 122 °E and between 11 °N and 25 °N (Fig. 4.1a), with a horizontal resolution of 1/18° (about 6 km) in both longitude and latitude. ROMS-nSCS has 40 σ (terrain-following) levels, with relatively finer vertical resolutions near the sea surface and bottom. The model bathymetry is based on the General Bathymetric Chart of the Oceans (GEBCO) data with a resolution of 30 arc-seconds (*Weatherall et al.,* 2015). The sub-grid scale horizontal mixing is parameterized using the shear and grid size dependent scheme of *Smagorinsky* (1963). The vertical mixing is parameterized using the *Mellor and Yamada* (1982) level-2.5 turbulent closure scheme. The lateral open boundary condition and the initial condition for the ROMS-nSCS are specified based on 3 hourly HYCOM Global 1/12° Reanalysis data set (*Cummings and Smedstad*, 2013).

4.3.2 Model Forcing

The ROMS-nSCS is driven by six-hourly fields of SLPs and surface winds extracted from the CFSR dataset (*Saha et al.,* 2010) as mentioned in section 2.5. The CFSR surface

wind velocity is converted to wind stress using the bulk formula of *Large and Pond* (1981). The surface net heat flux is computed based on the model-calculated surface temperature in the combination with six-hourly CFSR fields of wind speed, air pressure, air temperature, cloud cover, downward shortwave radiation flux, and precipitation (*Mellor,* 2004).It should be noted that the horizontal resolutions of the CFSR fields are about 0.3° and 0.5° for the winds and SLPs respectively, which are not fine enough to resolve well the fine structure of the wind and SLP fields associated with tropical storms or hurricanes (*Chawla et al.,* 2013). To improve the representation of wind and SLP fields associated with Typhoon Linfa, a parametric vortex suggested by *Hu et al.* (2013) is inserted into the CFSR winds and SLPs at each model time step. The parametric vortex suggested by *Hu et al.* (2013), which was modified from the Holland-type vortex model (*Holland,* 1980), can be expressed as

$$p(r) = p_c + (p_n - p_c)e^{-(R_m/r)^B} \tag{4.1}$$

$$v_g(r) = \sqrt{\frac{B}{\rho_a}(\frac{R_m}{r})^B(p_n - p_c)e^{-(R_m/r)^B} + (\frac{rf}{2})^2} - \frac{rf}{2} \tag{4.2}$$

where $p(r)$ and $v_g(r)$ are, respectively, the SLP and the gradient wind at radius r, p_n is the ambient atmospheric pressure, p_c is the central pressure, R_m is the radius of maximum wind, ρ_a is the air density, f is the Coriolis parameter, and B is the hurricane shape parameter defined by Eq. (4) in *Hu et al.* (2013).

The positions of the storm center, translational velocities, and all available wind parameters archived by the National Institute of Informatics are used in constructing the SLP and wind fields associated with Typhoon Linfa based on Eqs. (4.1) and (4.2). The modified CFSR winds for driving the ROMS-nSCS are constructed by combining the original CFSR winds and SLPs and a parametric vortex using a spatial interpolation at each model time step. Similar vortex insertion methods were used in many previous studies (*Wang and Sheng,* 2016; *Lin and Sheng,* 2017).

4.3.3 Model Experiments

Model results in three basic numerical experiments (CFSR, Control Run, and Smooth, see Table 1) are analyzed to examine the impact of Typhoon Linfa on the upper ocean dynamics over the nSCS. These three experiments use the ROMS-nSCS with different combinations of wind fields and SLPs. All other external model forcing, such as the net heat flux at the sea surface and boundary forcing at the model open boundary are the same in the three experiments.

(1) In experiment CFSR, the original 6-hourly CFSR winds and SLPs are used in driving the ROMS-nSCS. As mentioned above, the temporal and spatial resolutions of the original CFSR reanalysis data are relatively coarse for Typhoon Linfa. Hence, the model results in this experiment are used to demonstrate the importance of accurate representations of atmospheric forcing associated with the storm in simulating the hydrodynamics during storm events such as Typhoon Linfa.

(2) In experiment CR (Control Run), the combination of the parametric vortex and the original CFSR reanalysis data are used. Since the parametric vortex is a good approximation of storm-induced forcing in time and space, the model results in this experiment can be used in examining the total hydrodynamics over the nSCS during Typhoon Linfa.

(3) In experiment Smooth, the ROMS-nSCS is forced by the Smooth fields of CFSR winds and SLPs averaged over a circle centered at each model grid point. The radius of the circle is set to 300 km, which is the typical diameter of typhoon Linfa. As a result, the main hurricane feature associated with Linfa is eliminated in the Smooth CFSR winds and SLPs. The differences in simulated currents and temperature/salinity between experiments Vortex and Smooth can be used to represent the storm-induced ocean responses during Linfa.

Table 4.1: Model forcing and advection terms for temperature in six numerical experiments.

Experiment	Atmospheric Forcing	Advection terms in the model temperature equation
CFSR	6-hourly CFSR	on
Control Run (CR)	6-hourly CFSR+Vortex	on
Smooth	Smooth 6-hourly CFSR	on
CFSR_NoAdv	6-hourly CFSR	off
NoAdv	6-hourly CFSR+Vortex	off
Smooth_NoAdv	Smooth 6-hourly CFSR	off

Distributions of wind stress at 0000 UTC (Coordinated Universal Time) on 20 June 2009 are shown in Fig. 4.4 based on (a) the original CFSR, (b) modified CFSR (i.e., the parametric vortex inserted into the original CFSR), and (c) Smooth CFSR respectively to demonstrate the major differences of winds over the area covered by the storm in these three cases. At this time, the wind stress in the original CFSR case (Fig. 4.4a) is large and cyclonic over the northeastern region and relatively weak over other regions of the nSCS. The intense cyclonic wind stress over the northeastern region of the nSCS is associated with Typhoon Linfa. As mentioned in section 4.3.2, the original CFSR data do not have a fine horizontal resolution to resolve well the winds within Linfa. In comparison, the wind stress in the modified CFSR case (Fig. 4.4b) is much stronger than the counterpart in the original CFSR case within the area affected directly by Linfa (AADL), and is the same as the original CFSR case outside of the area. In the Smooth CFSR case (Fig. 4.4), by comparison, the strong wind stress associated with Linfa was successfully eliminated as expected.

Model results in three additional numerical experiments (Table 4.1) are also examined to investigate the effects of upwelling and vertical mixing in storm-induced circulation and cooling in the upper ocean during Typhoon Linfa. The model setup and forcing in these three additional experiments (CFSR_NoAdv, NoAdv, and Smooth_NoAdv) are respectively the same as in experiments CFSR, Control Run (CR), and Smooth, except that the advection (horizontal and vertical) terms in the model temperature equations are switched off.

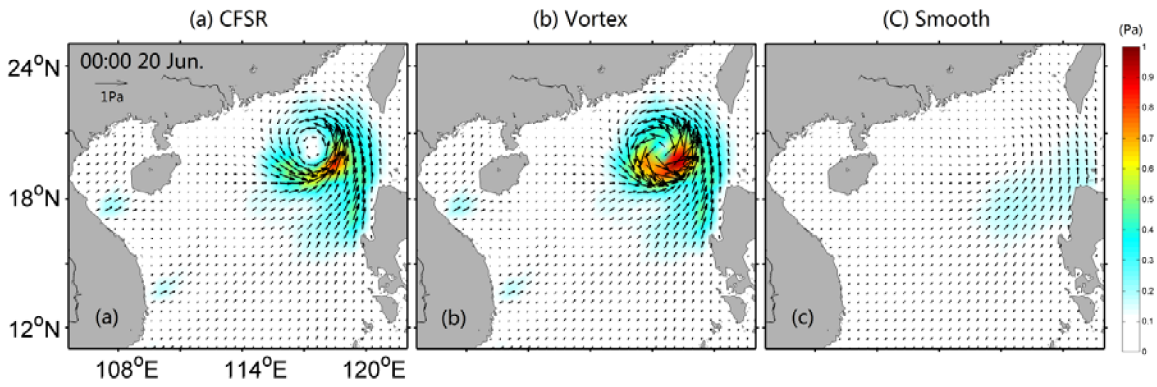

Figure 4.4: Distributions of vectors (arrows) and amplitudes (image) of wind stress at 00:00 on 20 June 2009, calculated from (a) the original CFSR wind fields, (b) modified CFSR winds with an insertion of a parametric vortex, and (c) Smooth CFSR winds. For clarity, wind stress vectors are plotted at every 8th model grid point.

4.4 Model Performance

We assess the performance of the ROMS-nSCS by comparing model results in experiment CR with various types of observations, including in-situ observations, satellite remote sensing data, and with the global ocean reanalysis produced by the HYCOM.

The general features of 3D circulation over the nSCS produced by the ROMS-nSCS are in a good agreement with previous observational and numerical studies (*Hu et al.,* 2000; *Huang et al.,* 2011; *Zhao et al.,* 2020). Figure 4.5a1 presents the daily mean currents and SST produced by the ROMS-nSCS on 16 June 2009 (before the passage of Linfa). The daily mean surface circulation on this day features a strong northeastward coastal jet known as the Vietnam Offshore Current (VOC) off southeastern Vietnam (at about 11.5 ^{o}N, see Fig. 4.5a1). The VOC runs first northeastward and then bifurcates into two branches: the inshore and offshore branches. The inshore branch of the VOC flows northward approximately along the east coast of Vietnam and then turns northeastward before reaching coastal waters off eastern Hainan Island. The offshore branch of the VOC first runs eastward to the central SCS and then separates into two parts, with the main part turning northward to join the above-mentioned inshore branch of the VOC. Over the northwestern region of the nSCS, the main part of the offshore branch and the inshore

branch of the VOC turn southeastward and then turn northward to form a strong coastal jet off northwestern Philippines (Fig. 4.5a1). This strong coastal jet flows northward over Luzon Strait (known as the Northwest Luzon Coastal Current, wnLCC) and splits two branches before reaching coastal waters of southwestern Taiwan Island. One branch of the nwLCC joins Kuroshio to flow northeastward off eastern Taiwan Island, and the second branch of the nwLCC turns northwestward off western Taiwan Island. (Fig. 4.5a1).

On 16 June 2009 (before the passage of Linfa), the simulated daily mean SST produced by the ROM-nSCS is about 29 °C over the central nSCS, relatively warm of about 30 °C over coastal waters of the Northern Bay, and relatively cool and 27-28 °C over Taiwan Strait and offshore waters off southeastern Vietnam (Fig. 4.5a1). The general distribution of SST produced by the ROMS-nSCS shown in Fig. 4.5a1 is in a good agreement with the satellite SST data shown Fig. 4.5a3.

A comparison of surface currents in Figs. 4.5a1,a2 demonstrates that the general surface circulation features produced by the ROMS-nSCS are in a good agreement with the HYCOM analysis, particularly over the northeastern region of the nSCS. Large differences occur, however, over several subregions of the nSCS. Over coastal waters off south central Vietnam (at about 15 ^{o}N), for example, the HYCOM reanalysis has an intense northeastward (seaward) jet with relatively strong convergent currents near the coast, while the ROMS-nSCS does not generate this northeastward jet and nor the strong convergent currents near the coast. Although exact reasons are not known for these large differences, one plausible reason is differences in the atmospheric forcing used in driving the two models.

One question raised is how representative the model results on 16 June 2009 (before the passage of Linfa) produced by the ROMS-nSCS are for the normal hydrodynamic conditions in summer months over the nSCS. In comparison with the 5-year (2007-2011) averaged monthly mean circulation in June based on data-assimilative HYCOM results (Fig. E1 in Appendix E), the large-scale features of surface currents, including the VOC, nwLCC and their branches, on 16 June shown in Figure 4a1 are in a good agreement with the June-mean surface currents shown in Fig. E1a. Some noticeable differences occur in

the small-scale circulation features, particularly over the area to the southwest of Taiwan Island. The general features of the simulated SST by the ROMS-nSCS shown in Fig. 4.5a1 are also similar to the June mean SST shown in Fig. D1a over the northern part of the nSCS and along the main pathways of the VOC and its extensions. In comparison with the June mean SST shown in Figure A1a, however, the simulated SSTs produced by the ROMS-nSCS are significantly cooler over the southeastern part of the nSCS, and significantly warmer in Beibu Wan (to the west of Hainan Island) due mainly to the particular distributions of the net heat fluxes at the sea surface over the nSCS during the first two weeks of June 2009. This indicates that the temperature/salinity and circulation before the storm produced by the ROMS-nSCS are typical summer-time oceanographic conditions over the nSCS.

The simulated SST field produced by ROMS-nSCS on 19 June features the storm-induced cooling around the area centered at about (116.5 °E, 18.0 °N), where Linfa looped for more than 2 days (Fig. 4.5b1). The simulated SST cooling over this area is about -3 °C (from 29 to 26 °C). Strong wind-driven surface currents produced by ROMS-nSCS occur over this cooling area on 19 June. On June 22 when Linfa made a landfall over Fujian Province of China, the simulated surface cooling induced by Linfa mainly occurs over the AADL and the wake of Linfa and the cooling is biased to the right-hand side of the track (Fig. 4.5c3).

The simulated currents and temperatures produced by the ROMS-nSCS are compared with the HYCOM analysis (middle panels of Fig. 4.5). Before the arrival of Linfa, the 3D circulation and temperature/salinity produced by ROMS-nSCS are very similar with the counterparts produced by HYCOM over the nSCS (Fig. 4.5a1 and a2). On June 19, the ROMS-nSCS generates the intense SST cooling over the area under the direct influence of Linfa (Fig. 4.5b1), which differs significantly from the HYCOM results. HYCOM reanalysis instead has the SST cooling over the northeastern region of the nSCS including southwestern Taiwan Strait on 19 June (Fig. 4.5b2). On June 22, the SST cooling generated by HYCOM occurs mainly around coastal areas rather than along the storm track of Linfa (Fig. 4.5c2), which differs from the ROMS-nSCS results (Fig. 4.5c1).

The right three panels of Fig. 4.5 present the observed SST fields inferred from the satellite remote sensing data. A comparison of simulated and observed SSTs shown in Fig. 4.5 demonstrates that the ROM-nSCS reproduces reasonably well the satellite derived SSTs over the northeastern region of the nSCS during the passage of Typhoon Linfa. In comparison, the HYCOM reanalysis represents less well the observed SST cooling over the AADL and the wake of Linfa.

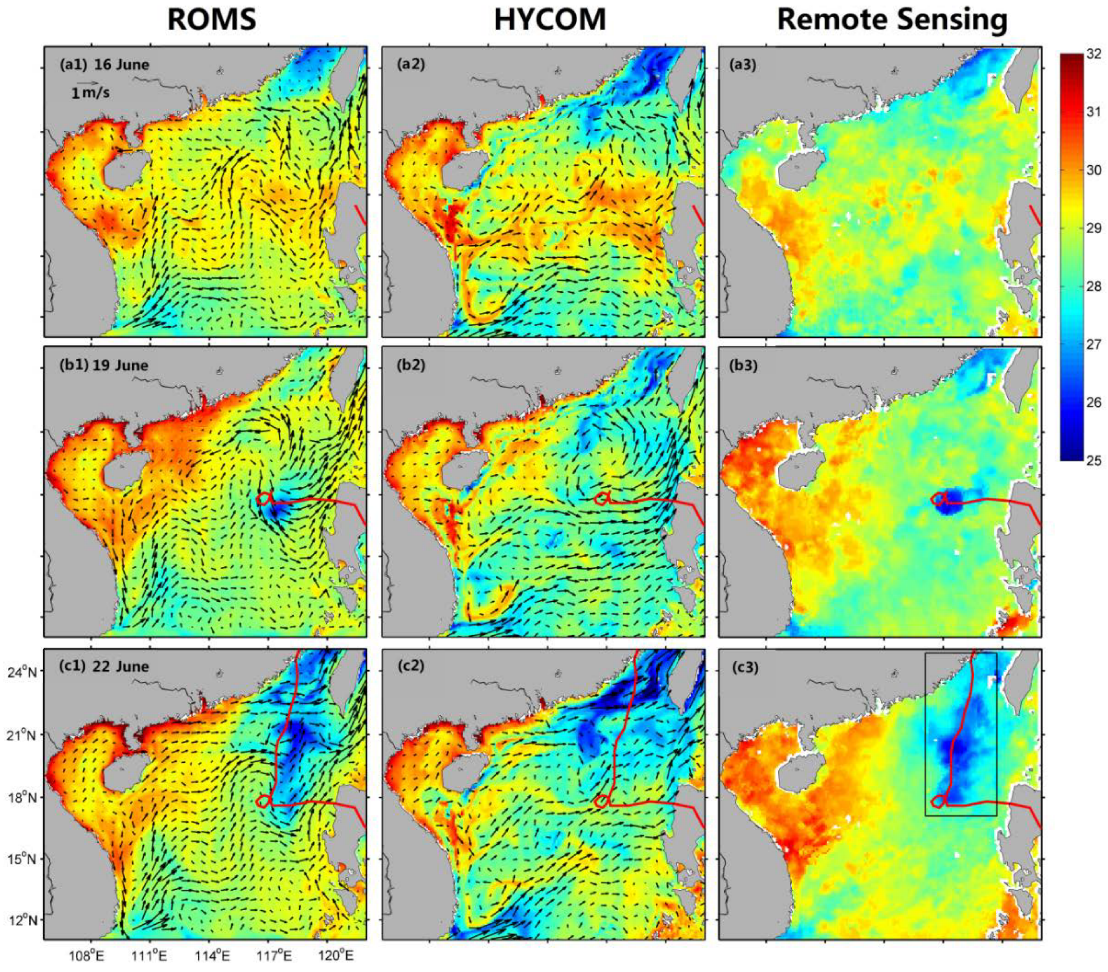

Figure 4.5: Distributions of daily mean sea surface temperatures (SSTs, °C) and surface currents produced by (left panels) the ROM-nSCS and (middle panels) HYCOM reanalysis and (right panels) SSTs calculated from the daily satellite remote sensing data on (top) 16, (central) 19, and (bottom) 22 June 2009. For clarity, surface current vector in right (middle) panels are plotted at every 9th (6th) model grid point of the ROMS-nSCS (HYCOM). The black box in c3 shows the region of AADL.

Table 4.2: Values of four error metrics for quantifying performances of ROMS-nSCS and HYCOM in simulating the SST over the AADL using satellite-derived SST fields on each day between 16 and 25 June (10 days of typhoon period). The four error metrics include the scatter index (SI), relative bias (RB), Root Mean Square Error (RMSE), and correlation coefficients (CORR).

	Date in June / Index	16	17	18	19	20	21	22	23	24	25
ROMS	SI (%)	2.43	2.79	3.38	2.68	2.72	2.56	3.02	2.59	2.61	2.44
	RB (%)	2.00	-2.25	2.77	1.90	0.01	-0.31	1.31	1.22	1.29	1.03
	RMSE (°C)	0.69	0.80	0.96	0.75	0.75	0.70	0.82	0.72	0.73	0.69
	CORR (%)	73.58	51.65	28.45	68.10	63.55	59.69	52.50	53.15	40.79	48.43
HYCOM	SI (%)	2.38	2.43	2.18	3.23	4.23	4.14	4.06	3.38	3.48	3.06
	RB (%)	-0.23	0.22	0.05	-0.25	1.43	0.56	0.66	-0.79	-1.26	-0.56
	RMSE (°C)	0.68	0.69	0.61	0.91	1.16	1.14	1.11	0.94	0.98	0.86
	CORR (%)	73.67	63.61	51.89	4.50	-20.56	-11.64	8.45	37.81	40.86	47.27

Prior to Typhoon Linfa's arrival in the nSCS on 16-17 June, both the ROMS-nSCS and HYCOM have similar values of four metrics (Table 4.2), except that the HYCOM has relatively smaller values of SI and RB and slightly higher values of CORR than the ROMS-nSCS on these two days. This indicates that the ROMS-nSCS performs slightly less than the HYCOM in simulating SSTs over the AADL before the arrival of Linfa.

During the passage of Linfa over the nSCS on 17-22 June 2009, the ROMS-nSCS has significantly smaller values of SI and RMSE, and significantly higher positive values of CORR than the HYCOM in simulating SSTs on 18-21 June, except that the ROMS-nSCS has relatively larger values of SI, SI and RMSE than the HYCOM (Table 4.2). On 19-21 June, in particular, the ROMS-nSCS has large and positive values of CORR, while the HYCOM has very small positive and even negative values of CORR. This indicates that the ROMS-nSCS performs significantly better than the HYCOM in generating the SST cooling over the AADL and in the wake of Linfa.

After the departure of Linfa from the nSCS, the ROMS-nSCS has smaller values of SI and RMSE than the HYCOM in the wake of Linfa on 22-25 June 2009 (Table 4.2). The ROMS-nSCS has significantly larger values of CORR on the first two days (22-23 June) and similar values of CORR on the last two days (24-25 June) after the storm, in

comparison with the values for the HYCOM. This indicates again the satisfactory performance of the ROMS-nSCS in simulating the storm-induced SST cooling in the wake of Linfa.

Figure 4.6 presents scatterplots of observed and simulated hourly SSTs over the area marked by the black box in Fig. 4.5c3 on three days: 16, 19, and 22 June 2009. Figure 4.6a1 demonstrates that, on 16 June (before the storm), the hourly SSTs produced by the ROMS-nSCS follow reasonably well, and slightly above, the line of perfect fit, which indicates that the ROMS-nSCS performs reasonably well in generating the spatial distribution of the observed SSTs with a positive bias of about 2% over the AADL and in the wake of Linfa. By comparison, the hourly HYCOM SST data on 16 June have relatively small bias, but do not follow closely the line of perfect fit (Fig. 6a2). An examination of Fig. 4.5a2 and a3 demonstrates that the HYCOM overpredicts the north-south gradients of observed SSTs on 16 June.

On 19 June 2019 when the center of Linfa reached the location of about (117.20 °E, 18.20 °N), the hourly SST values of ROMS-nSCS follow roughly, and noticeably above, the line of perfect fit (Fig. 4.6b1), with a certain degree of scatters. By comparison, the hourly HYCOM SST data do not follow well the line of perfect fit (Fig. 4.6b2). This indicates that ROMS-nSCS performs significantly better than the HYCOM in generating the spatial variability of observed SSTs and storm-induced SST cooling over the AADL on 19 June.

On 22 June 2009 (after the storm), the hourly SSTs of ROMS-nSCS also follow roughly the line of perfect fit, although with a large degree of scatters (Fig. 4.6c1). By comparison, the hourly HYCOM SST data do not follow the line of perfect line and have a very large degree of scatters (Fig. 4.6c2) on 22 June. This demonstrates that the ROMS-nSCS reproduces significantly better than the HYCOM in generating the general structure of the observed SST, particularly the storm-induced SST cooling, over the AADL after the passage of Linfa.

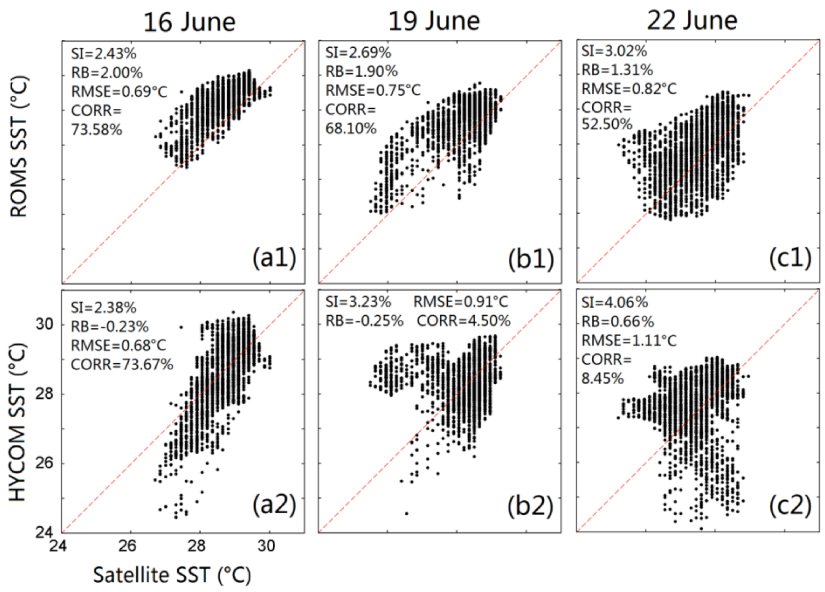

Figure 4.6: Scatter plots of observed and simulated hourly SSTs over the areas affected directly by Linfa over the nSCS on (left) 16 June, (middle) 19 June, and (right) 22 June 2009. The simulated hourly values were calculated from model results produced by (top panels) the ROMS-nSCS and (bottom panels) HYCOM. The red dashed line is the line of perfect fit. Four values in each panel are the Scatter Index (SI), Relative Bias (RB), Root Mean Square Error (RMSE) and Correlation Coefficient (CORR).

We next assess the performance of the ROMS-nSCS in simulating vertical structures of temperature/salinity. Figure 4.7 presents vertical profiles of simulated and observed temperatures in the top 150 m at locations of five Argo floats before and after the passage of Linfa during the period between 03:15:00 (UTC) 14 June and 00:07:19 23 June 2009. At depths below 150 m the temporal changes in the observed temperatures were relatively small during this period and are not considered here. These five Argo floats were located approximately at P_1 (118.92 °E, 16.96 °N), P_2 (115.62 °E, 17.51°N), P_3 (116.68 °E, 18.56 °N), P_4 (114.71 °E, 19.79 °N), and P5 (117.80 °E, 21.53 °N) respectively (marked in Fig. 4.1b) during this period. Table 4.3 provides information on positions of these five Argo floats and times of observations of these floats used in this study.

The observed temperatures at 00:53:54 on 15 June (before the storm) at location P_1 were nearly uniform in the vertical in the top 35 m and decreased with depth from about 28.5

°C at 40 m to 18.0 °C at 150 m (Fig. 4.7a). The temperature profile observed at 00:56:54 on 19 June (after the storm) is highly similar to the pre-storm profile at P_1, except for about 0.5 °C cooler in the surface mixed layer after the storm than before the storm. This indicates that the storm-induced changes in the vertical stratification by Linfa were very small at location P_1 during this period. This is expected since P_1 is located at about 80 km to the left of the storm track when Linfa was in the early development stage with the MSW of about 28 km h^{-1}. Figure 4.7a demonstrates that the ROMS-nSCS reproduces very well the pre-storm and post-storm profiles of observed temperatures at P_1, with the RMSEs of about 0.41 °C and 0.31 °C before and after Linfa respectively.

Table 4.3: Identifications (ID) and positions of five Argo floats and observation times before and after Typhoon Linfa.

Index	Argo ID	Position	Observation time	
			before Linfa	after Linfa
P_1	2900825	118.92°E, 16.96°N	00:53:54,15-June-2009	00:56:54, 19-June-2009
P_2	2900834	115.62°E, 17.51°N	03:54:00, 14-June-2009	02:30:19, 22-June-2009
P_3	2900834	116.68°E, 18.56°N	01:53:37, 16-June-2009	01:55:12, 20-June-2009
P_4	2901139	114.71°E, 19.79°N	00:04:24, 15-June-2009	00:07:19, 23-June-2009
P_5	2901170	117.80°E, 21.53°N	20:05:32, 18-June-2009	20:32:02, 21-June-2009

At 03:54:00 on 14 June (before the storm) the vertical temperature profile observed at P_2 (Fig. 4.7b) is very similar to the pre-storm profile at location P_1 (Figs. 4.7a). At 02:30:19 on 22 June (after the storm), however, the bottom of the surface mixed layer was shallower about 10 m than with the counterpart before the storm at P_2. Figure 4.7b also demonstrates that the ROMS-nSCS reproduces reasonably well the pre- and post-storm observed temperature profiles at P_2, with the RMSEs of about 0.43 °C and 0.31 °C before and after the storm respectively. The ROMS-nSCS particularly reproduces the storm-induced changes of the bottom of the surface mixed layer at P_2.

Both P_3 and P_5 are very close to the storm track of Typhoon Linfa, with the MSWs of about 100 km h^{-1} and 140 km h^{-1} respectively. Significant storm-induced changes in the vertical stratification were observed at these two locations. At 01:53:37 on 16 June (before the storm), the pre-storm temperature profile observed at P_3 (Fig. 4.7c) is very

similar to the pre-storm profiles at P_1 and P_2. The post-storm temperature profile observed at P_3 (01:55:12 on 20 June) had an upward shift from the pre-storm profile in the top 150 m (Fig. 4.7c), due mainly to storm-induced upwelling. The post-storm temperature observed at P_3 was about 1.4 °C cooler than the pre-storm values in the top 20 m due mainly to storm-induced vertical mixing. Meanwhile, the post-storm mixing layer depth at P_3 was about 18 m and about 8 m deeper than the pre-storm values, which due to storm-induced vertical mixing. The post-storm temperature observed at P_3 was about 3 °C cooler than the pre-storm values at the 40 m depth due mainly to storm-induced upwelling. The post-storm temperature observed at P_5 was also about 1.4 °C cooler than the pre-storm temperature in the top 20 m (Fig. 4.7e), due also mainly to the storm-induced vertical mixing. Between 40 m and 150 m, however, the post-storm temperature observed at P_5 had a downward shift due to storm-induced downwelling. The ROMS-nSCS reproduces reasonably well the vertical temperature profiles observed at locations P_3 and P_5 before and after the storm (Figs. 4.7c,e), with the RMSEs of about 0.42-0.47 °C at P_3 and about 0.36-0.42 °C at P_5.

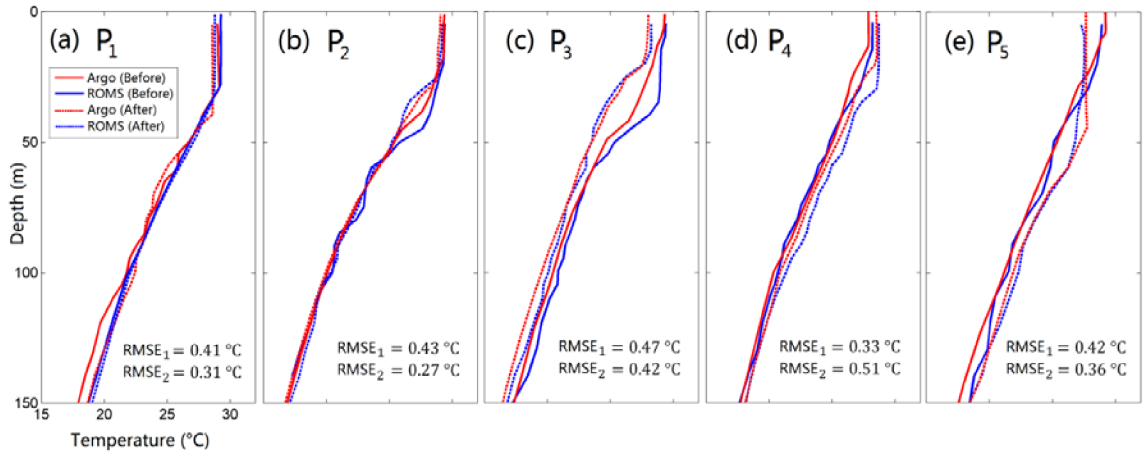

Figure 4.7: Vertical profiles of observed (red) and simulated (blue) temperature profiles at five Argos before and after the passage of Typhoon Linfa. Positions of Argo floats (P_1, P_2, P_3, P_4, and P_5) are marked in Fig. 1b. The observation time for each profile is listed in Table 4.2)

The pre-storm temperature profile observed at location P_4 (00:04:24 on 15 June) is very similar to the counterpart at location P_5 (Fig. 4.7d, e). The post-storm temperature profile observed at P_4 (00:07:19 on 23 June) had a downward shift between 40 m and 150 m.

which is also similar to the post-storm profile at P_5. Overall, the ROMS-nSCS reproduces reasonably well the observed temperature profiles at P_4 (Fig. 4.7d), with the RMSEs of about 0.33 °C and 0.51 °C before and after Linfa respectively.

4.5 Results

Model results produced by the ROMS-nSCS in different numerical experiments are analyzed in this section to examine the main processes affecting the circulation and variability during Typhoon Linfa over the northeastern region of the nSCS.

4.5.1 Storm-induced Circulation and Cooling during Typhoon Linfa

To examine the storm-induced changes in the 3D temperature field over the nSCS during Linfa, the differences in the daily mean temperature ($\Delta\bar{T}$) between 21 June (after the storm) and 18 June (before the storm) in 2009 are computed (Fig. 4.8) based on model results produced by the ROMS-nSCS in the control run (CR). The model generates significant SST cooling in the wake of Linfa to the southwest of Taiwan Strait, with the maximum cooling about -2.5 °C (Fig. 4.8a). The simulated SST cooling is bias to the right of the storm track. The values of $\Delta\bar{T}$ at the sea surface are relatively small and positive over areas far from the storm track, particularly over coastal waters off Guangdong Province of China and southeastern Vietnam. The general features of simulated SST changes over the nSCS, including significant cooling in the wake of Linfa and slightly warming over areas far from the storm track of Linfa (Fig. 4.8a), are in very good agreement with the satellite SST data shown in Fig. 4.2.

The cooling also occurs at other depths in the top 150 m in the wake of Linfa to the south of Taiwan Strait (Figs. 4.8b-c). At 30 m, significant cooling occurs over two specific areas (Fig. 4.8b). The first cooling area is centred at about (117.17 °E, 15.93 °N) to the southeast of the looping area of Linfa (hereafter LAL), and the second cooling area is located at about (119.17 °E, 19.42 °N) to the south of Taiwan Strait (Fig. 4.8b). The two cooling areas also appear in Figs. 4.8c,d, indicating existence of negative values of $\Delta\bar{T}$ in the top 150 m over these two specific areas. The values of $\Delta\bar{T}$, by comparison, are

slightly positive over the coastal waters to southwest of Taiwan Strait at 20 m (Fig. 4.8b), and also slightly positive over areas to the east of the cooling areas at 60 m (Fig. 4.8c). It should be noted that, in addition to the role of Typhoon Linfa, other processes such as large-scale circulation also affect the temporal changes of daily mean temperatures shown in Fig. 4.8.

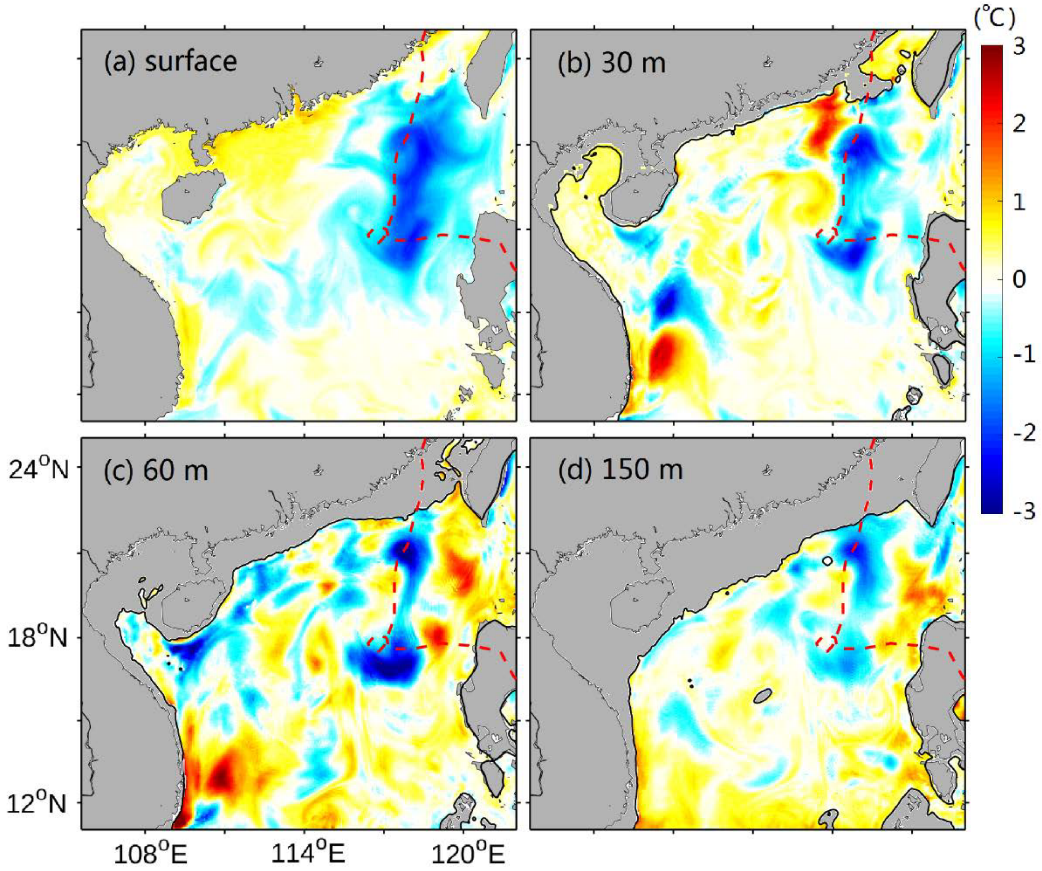

Figure 4.8: Differences in the daily mean temperature ($\Delta\bar{T}$) at (a) the sea surface, (b) 30 m, (c) 60 m, and (d) 150 m calculated from daily mean model results on 21 and 18 June 2009 produced by the ROMS-nSCS in case CR. The red dashed line represents the storm track of Typhoon Linfa.

To quantify the role of Typhoon Linda on the circulation and temperature/salinity over the northeastern region of the nSCS, we calculate the differences in the instantaneous currents and temperature based on model results produced by the ROMS-nSCS in cases CR and Smooth. We use these differences to represent the storm-induced changes in temperature and storm-induced currents by Linfa. Figure 9a presents the storm-induced

changes in surface currents and temperatures over the northeastern region of the nSCS at 00:00 on 19 June 2009. By this time, Linfa had completed the anticlockwise loop and moved northward. The storm center of Linfa at this time reached the location of (117.2 °E, 18.2 °N), with the MSW of about 83 km h^{-1} (as the category of a tropical storm). The storm-induced surface ocean response produced by the ROMS-nSCS at this time is characterized by strong outward surface currents forced by the local wind stress and significant SST cooling over the AADL and in the wake of the storm. The maximum storm-induced SST cooling of about -2.0°C occurs at about 40 km to the south of the LAL (Fig. 4.9a). The area with the maximum cooling at this time (centered at about 117.4 °E and 17.6 °N, Fig, 4.9c) is labelled as area as A_1 for simplicity of discussion in this section.

Linfa reached the location of (117.4 °E, 20.2 °N) at 00:00 on 20 June 2009, with the MSW of about 120 km h^{-1} (category-12 typhoon, or category one hurricane). At this time, the significant storm-induced SST cooling occurs over area A_1 (Fig. 4.9b). The storm-induced SST cooling is biased to the right hand of the storm track after Linfa left from the LAL. The storm-induced surface currents produced by the ROMS-nSCS at this time are characterized by intense wind-driven surface currents over the storm-covered area and intense inertial currents behind the storm (Fig. 4.9b).

At 00:00 on June 21, Linfa maintained the status of category-12 typhoon and its center of Linfa reached the location of (118.40 °E, 23.00 °N). The SST cooling extends from area A_1 to coastal waters. Intense storm-induced SST cooling (Fig. 4.9c) occurs over area A_1 and area A_2 centered at about (117.40 °E, 21.40 °N), with the maximum cooling of about -3 °C. To the north of these two cooling areas, there is an additional storm-induced SST cooling area over coastal waters of Guangdong province (Fig. 4.9c). The storm-induced surface currents at 00:00 on June 21 produced by the ROMS-nSCS are characterized by strong wind-driven currents over the AADL, intense near-inertial currents in the wake of Linfa, and strong along-shore currents over coastal waters of Guangdong (Fig. 4.9c). By comparison, the storm-induced currents are relatively weak over area A_1. Both the storm-induced SST cooling and surface currents are biased significantly to the right of the storm track. Furthermore, the storm-induced SST cooling and surface currents are also affected

by the large-scale circulation over the nSCS.

The storm-induced SST cooling 00:00 on 22 June 2009, which is about 12 hours after Linda made a landfall, occurs in the areas from area A_1 to area A_2 (Fig. 4.9d), with the intense SST cooling of about -2 °C over area A_2. The storm-induced currents are characterized by inertial currents in the wake of Linfa and adjacent waters. Same as at previous times, both spreading of storm-induced SST cooling and currents in the directions normal to the storm track at 00:00 on 22 June are affected significantly by the large-scale circulation over the nSCS (Fig. 4.9d).

At 00:00 on 19 June 2009 (Fig. 4.10a), the maximum storm-induced cooling of about -2.0 °C occurs over area A_1 at 60 m. By comparison, storm-induced warming of about 0.5 °C occurs over areas to the west of A_1 and a small area to the east of A_1 at 60 m due to storm-induced downwelling over these areas. The storm-induced currents at 60 m at 00:00 on 19 June are cyclonic over the cooling area (i.e., of A_1) and anticyclonic over the warming areas.

At 00:00 on 21 June (Fig. 4.10b), the storm-induced changes in temperatures at 60 m are characterized by cooling of about -1.5 °C over areas A_1 and A_2, and warming over wide areas to the west and east of the cooling areas. The maximum warming of about 1.0 °C occurs over the area about 200 km to the east of the LAL at 60 m. The storm-induced currents at 60 m at this time feature cyclonic circulation gyres over two cooling areas (i.e., areas A_1 and A_2) and anticyclonic gyres over the warming areas.

The storm-induced cooling at 60 m at 00:00 on June 21 occurs mainly in a narrow zone along the storm track from area A_1 to the shelf beak of Guangdong province (Fig. 4.10c). Storm-induced warming at 60 m at this time occurs over wide areas to the west and east of the narrow cooling zone, with significant spatial variability. The maximum warming of about 1°C at 60 m at this time appears over the area to the northeast of area A_2 (Fig. 4.10c). The storm-induced currents at 60 m at this time feature cyclonic circulation over area A_1, large-scale anticyclonic circulations over the large warming area to the west of the storm track, and intense offshore currents over the warming area to the northeast of area A_2 (Fig. 4.10c).

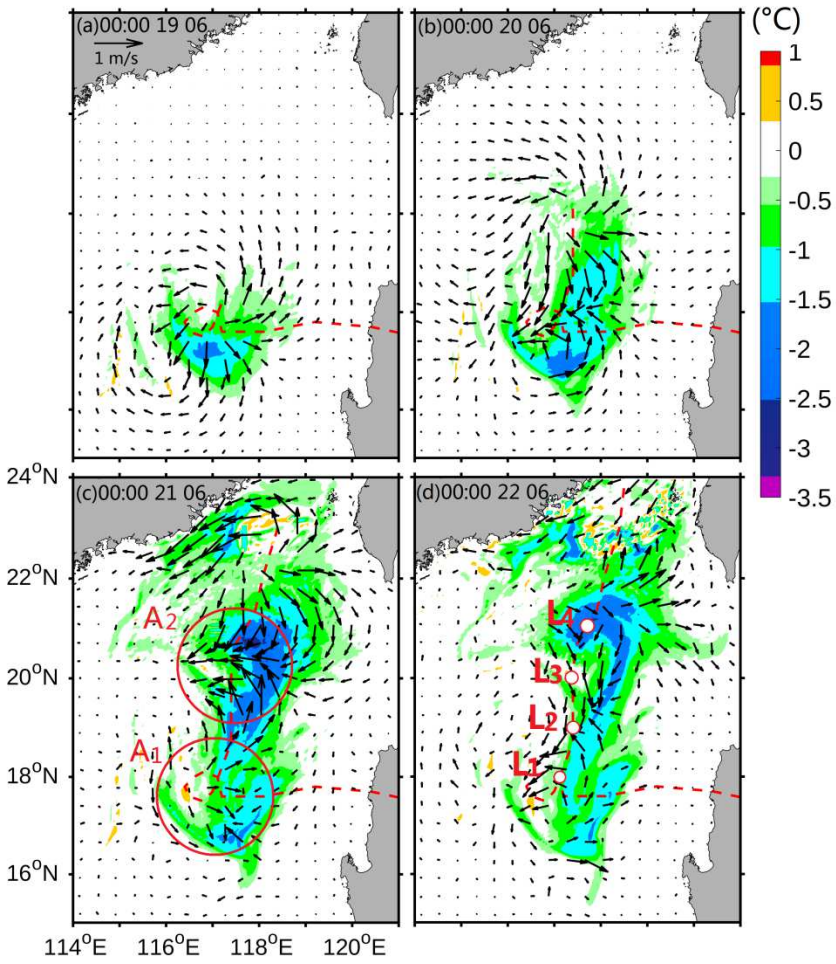

Figure 4.9: Differences in the instantaneous currents ($\Delta\vec{u}$ vectors) and temperatures (ΔT, image) at the sea surface between results produced by the ROMS-nSCS in cases CR and Smooth at 00:00 on (a) 19, (b) 20, (c) 21, and (d) 22 June, 2009. The red dashed line in each panel represents the storm track of Linfa. Two red circles in (c) mark two intense SST cooling areas (A_1 and A_2) along the storm track of Linfa. For clarity, surface current vectors are plotted at every 8th model grid point.

Different from the results at three previous times shown in Figs. 10a-c, there are several cooling and warming areas with complicated circulation patterns at 60 m at 00:00 on 22 June (Fig. 10d). The maximum cooling of about -2.5 °C at 60 m occurs over a small area to the north of area A_2, and the maximum warming of about 1 °C occurs outside the area with the maximum cooling (Fig. 4.10d).

At 120 m, the storm-induced cooling of about -1.0 °C occurs over area A_1, with relatively weak cyclonic currents at 00:00 on 19 June (Fig. 4.11a). Outside area A_1 at 60 m at this time, the storm-induced changes in currents and temperatures are small. At 00:00 on

other three days: 20, 21 and 22 June (Figs. 4.11b-d), the general features of storm-induced changes in currents and temperature at 120 m are similar to the counterparts at 60 m at the same times, except for smaller amplitudes for storm-induced currents and temperatures.

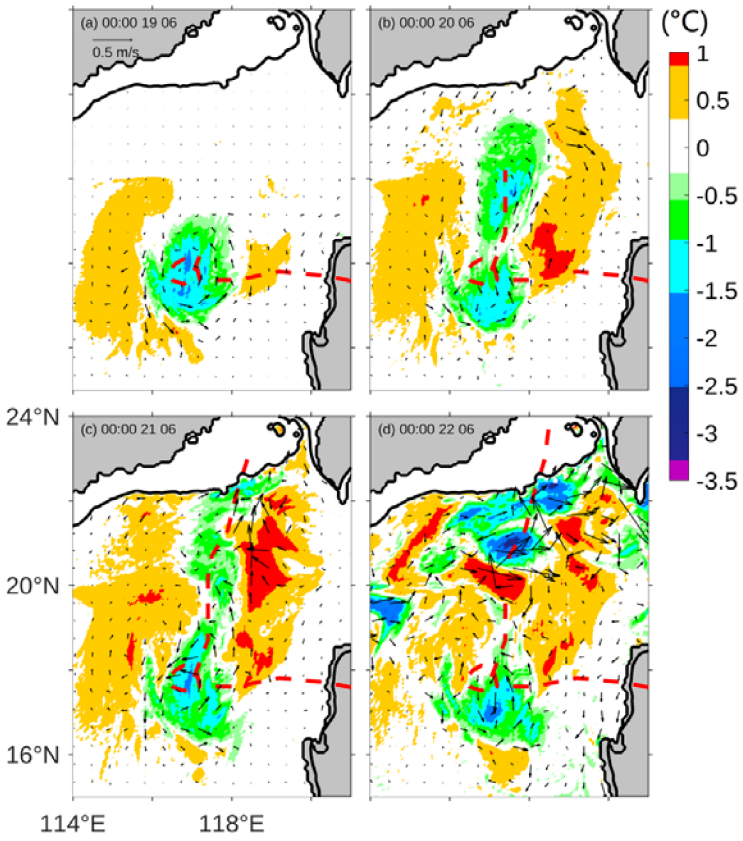

Figure 4.10: As in Fig. 4.9 but for differences in the instantaneous currents ($\Delta\vec{u}$, vectors) and temperatures (ΔT, image) at 60 m.

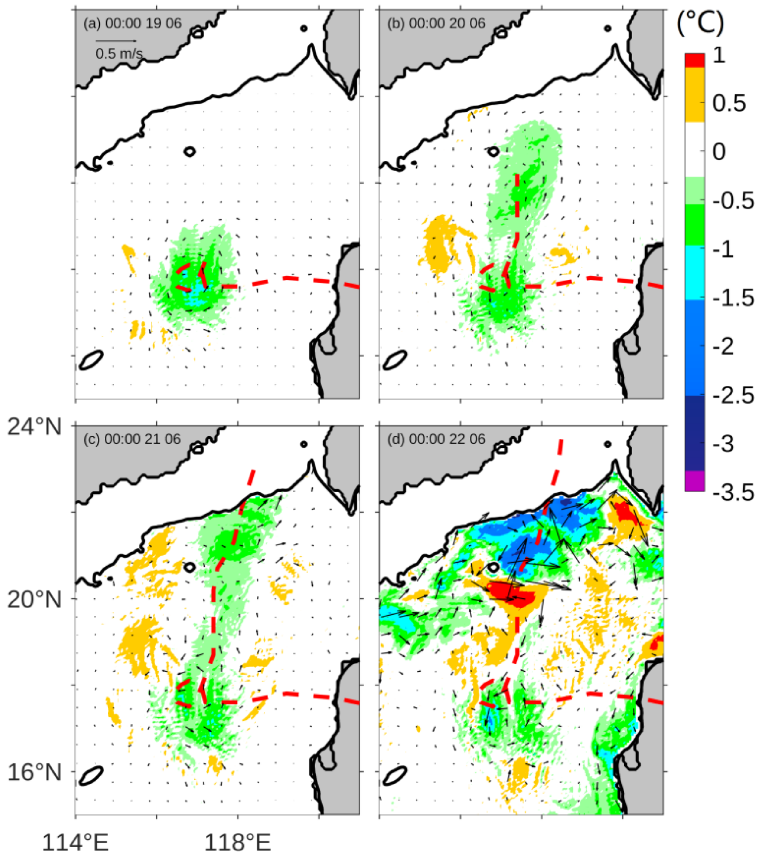

4.11: As in Fig. 4.9 but for differences in the instantaneous currents ($\Delta\vec{u}$, vectors) and temperatures (ΔT, image) at 120 m.

4.5.2 Main Processes for Storm-induced Surface Cooling

The temporal changes in the 3D temperature field during Typhoon Linfa, such as the large SST cooling in the wake of Linfa shown Figs. 8 and 9, are affected by several processes including the storm-induced mixing, storm-induced advection, and the net heat flux at the sea surface. The 3D temperature is simulated by the ROMS-nSCS based on

$$\underbrace{\frac{\partial T}{\partial t}}_{dT} = \underbrace{-\left(u\frac{\partial T}{\partial x} + v\frac{\partial T}{\partial y}\right)}_{Hadv} \underbrace{- w\frac{\partial T}{\partial z}}_{Vadv} + \underbrace{\frac{\partial}{\partial x}\left(A_h\frac{\partial T}{\partial x}\right) + \frac{\partial}{\partial y}\left(A_h\frac{\partial T}{\partial y}\right)}_{Hmix} + \underbrace{\frac{\partial}{\partial z}\left(K_h\frac{\partial T}{\partial z}\right)}_{Vmix} \tag{4.3}$$

subject to the boundary conditions for temperature at the sea surface and bottom. The term on the left-hand side of Eq. (4.3) is the rate of temperature change in time (dT). The terms on the right-hand side are horizontal advection (Hadv), vertical advection (Vadv),

horizontal mixing (Hmix), and vertical mixing (Vmix), respectively. For the convenience of discussion, the three advection terms in Eq. (4.3) are termed as ADV (Hadv+Vadv) and three mixing terms are termed as MIX (Hmix+Vmix).

Two different methods are used in this section to quantify the roles of storm-induced mixing and advection during the study period. In the first method, we examine the instantaneous magnitude of each term in Eq. (4.3) based on the diagnostics data produced by the ROMS-nSCS in case CR. The instantaneous fields of dT, ADV and MIX at 15 m are presented in Fig. 4.12 at 00:00 on 19, 20 and 21 June 2009, respectively. At 00:00 on 19 June 2009 as the early stage of Typhoon Linfa (Fig. 12a1-4), the rate of temperature change at 15 m is time (dT) is determined mainly by the storm-induced horizontal (Hmix) and vertical mixing (Vmix). At this time, the vertical advection (Vadv) makes a significant contribution to the sub-surface cooling over a small area over the southern LAL (A_1) (Fig. 4.12a4), while the horizontal advection (Hadv) plays a minor role over the LAL (Fig. 4.12a3). This indicates that, in the early stage of Typhoon Linfa, the storm-induced vertical mixing and upwelling are responsible for bringing the cool sub-surface waters to the surface layer and making the cooling at 15 m over the AADL. It should be noted that, at 00:00 on 19 June, both Hadv and Vadv in generating large values of dT at 15 m over the continental shelf region off Guangdong Province (Fig 4.12a3,a4). The large effects of Hadv and Vadv on dT over this shelf region is mostly associated with the large-scale circulation, rather than Typhoon Linfa since the storm is still far away from this shelf region at this time.

At 00:00 on 20 June, the storm-induced mixing (mainly Vmix) is the main cause for the storm-induced cooling in the wake of Linfa (Fig. 4.12b2). The horizontal advection (Hadv) at the same time, which is associated with the intense and spatially varying wind-driven currents, generates the warming over the LAL (A_1) and cooling over a small area to its southeast at 15 m (Fig. 4.12b3). By comparison, the storm-induced vertical advection contributes the temperature change at 15 m only over the LAL at this time (Fig. 4.12b4).

At 00:00 on 21 June as the center of Linfa reached the western end of Taiwan Strait, the storm-induced mixing (Fig. 4.12c2) remains to be dominant in generating the cooling in

the wake of the storm, particularly over area A_2. The horizontal advection associated with both the large-scale circulation and wind-induced currents at this time is responsible for SST warming over the AADL and SST cooling in areas outside of the AADL. The storm-induced vertical advection (Fig. 4.12c4) plays a moderate role over area A_2 at this time.

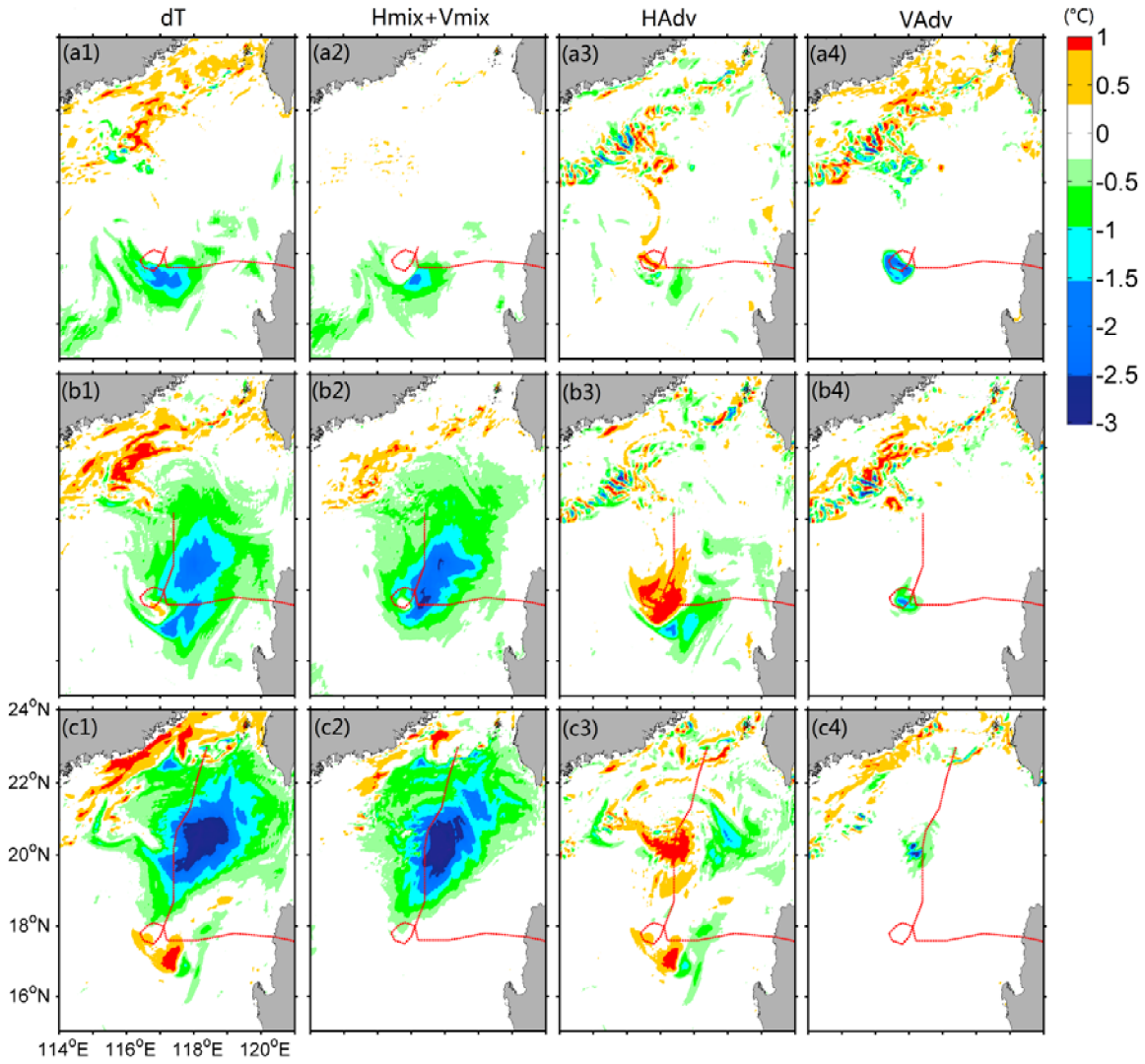

Figure 4.12: Distributions of (a1,b1,c1) rates of temperature change, temperature cooling by (a2,b2,c2) horizontal and vertical mixing, (a3,b3,c3) horizontal advection, and (a4,b4,c4) vertical advection at 30 m at 00:00 on (a1-4) 19, (b1-4) 20 and (c1-4) 21 June 2009, respectively. The red dashed line in each panel represents the storm track.

The diagnostic analysis presented above can only be used to examine the instantaneous effects of mixing and advections on temperature (and salinity). In the second method, the

accumulative effect of advection and mixing on the 3D temperature and circulation from the beginning of the storm to a particular time are estimated based on model results produced by the ROMS-nSCS with and without advection terms in the tracer equation (i.e., Eq. 4.3). Model results in six numerical experiments (Table 4.1) are considered. These six numerical experiments include three experiments discussed earlier (i.e, CFSR, CR, and Smooth), and three additional experiments. The three additional experiments (CFSR_NoAdv, NoAdv, and Smooth_Noadv) use the same external forcing as in cases CFSR, CR, and Smooth, except that the advection terms (ADV) for model temperature and salinity are turned off. The total storm-induced ocean response associated with the joint effect of ADV and MIX can be approximated by differences in model currents and temperatures between cases CR and Smooth (noted as $\Delta\vec{U}_{A+M}$ and ΔT_{A+M}). The storm-induced ocean response associated with MIX can be approximated by differences in model currents and temperatures between cases NoAdv and Smooth_NoAdv (noted as $\Delta\vec{U}_{M}$ and ΔT_{M}). The storm-induced changes in currents and temperatures associated with ADV (noted as $\Delta\vec{U}_{A}$ and ΔT_{A}) can then be calculated based on

$$\begin{cases} \Delta\vec{U}_A = \Delta\vec{U}_{A+M} - \Delta\vec{U}_M \\ \Delta T_A = \Delta T_{A+M} - \Delta T_M \end{cases} \tag{4.4}$$

Figure 4.13 presents the surface fields of ($\Delta\vec{U}_{A+M}$, ΔT_{A+M}), ($\Delta\vec{U}_{M}$, ΔT_{M}), and ($\Delta\vec{U}_{A}$, ΔT_{A}) at three different times. At 00:00 on 19 June 2009 as the early stage of Typhoon Linfa, the storm-induced changes in SST (ΔT_{A+M}) are affected mostly by the accumulative effect of the storm-induced advection (Fig. 4.13a3). The storm-induced changes in surface currents ($\Delta\vec{U}_{A+M}$), by comparison, are caused by the accumulative effect of storm-induced mixing and advection.

At 00:00 on 20 June, both ΔT_{A+M} and $\Delta\vec{U}_{A+M}$ (Fig. 4.13b1) are caused mainly by the accumulative effect of the storm-induced advection in the wake of Linfa and by the accumulative effect of storm-induced mixing over the AADL. At 00:00 on 21 June, the accumulative effect of both storm-induced advection and mixing plays a very important role for generating ΔT_{A+M} and $\vec{U}_{A+M}$ in the wake of Linfa except for area A_1 (Figs. 4.13c1-3). Over area A_1, the accumulative effect of storm-induced advection remains to play a dominant role for ΔT_{A+M} and $\Delta\vec{U}_{A+M}$. It should be noted that the vertical transport

associated with storm-induced upwelling and downwelling is the most important among all the advection terms over the AADL. Similarly, the accumulative effect of storm-induced vertical mixing is the most important among MIX over the AADL. Therefore, results in Fig. 4.13 demonstrate that the storm-induced upwelling plays a very important role for generating ΔT_{A+M} and $\Delta \vec{U}_{A+M}$ in the early stage of Linfa, and both storm-induced upwelling and storm-induced vertical mixing play important roles in the mature stage of Linfa over the AADL and in the wake of Linfa.

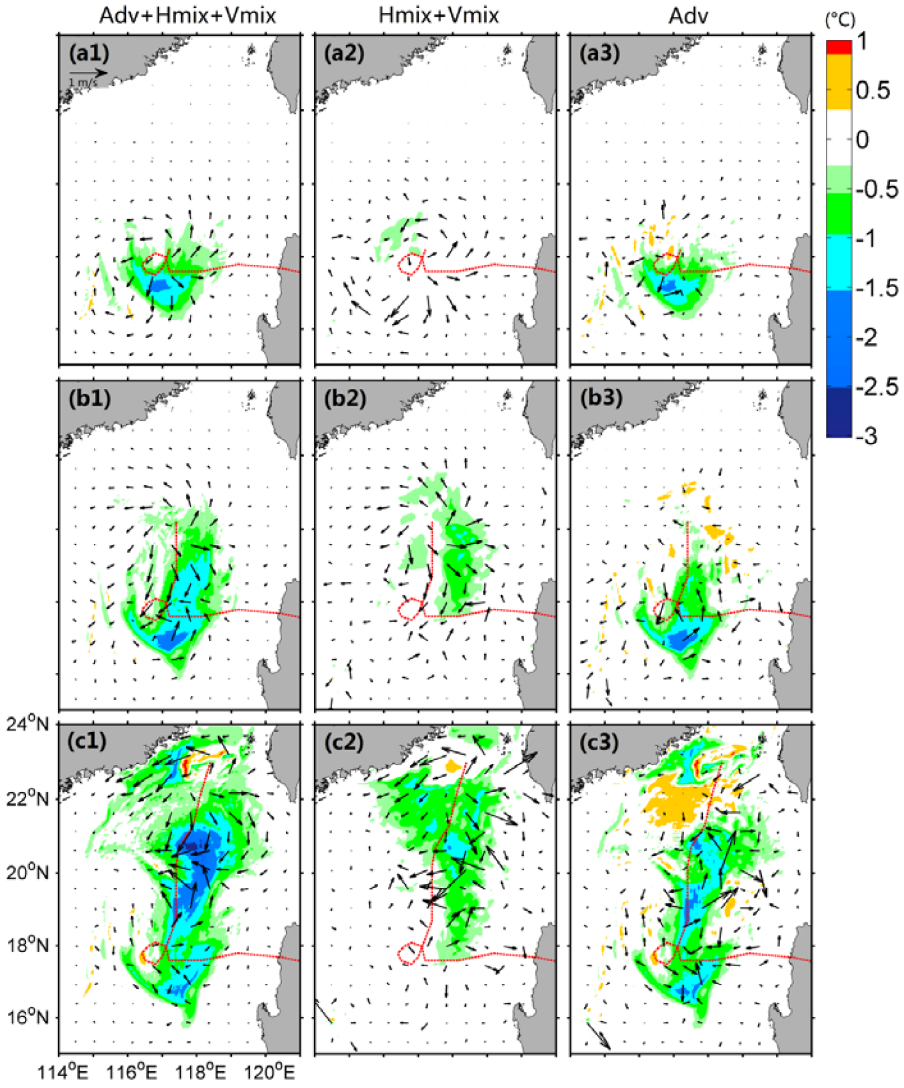

Figure 4.13: Distributions of (a1,b1,c1) $\Delta \vec{U}_{A+M}$ and ΔT_{A+M}, (a2,b2,c2) $\Delta \vec{U}_{M}$ and ΔT_{M}, and (a3,b3,c3) $\Delta \vec{U}_{A}$ and ΔT_{A} at the sea surface at 00:00 on (a1-3) 19, (b1-3) 20 and (c1-3) 21 June 2009, respectively. The red dashed line in each panel represents the storm track. For clarity, surface current vectors are plotted at every 9th model grid point.

We next examine the accumulative effect of advections and mixing in the vertical distribution of storm-induced changes in temperature. Figure 4.14 presents vertical distributions of ΔT_{A+M}, ΔT_A and ΔT_M along an east-west transect cross the storm center of Linfa at three different times. At 00:00 on19 June as the early stage of Typhoon Linfa, the maximum cooling of about -2.5 ^{o}C along the transect at 18.2 ^{o}N occurs in the thermocline at about 50 m within about 40 km from the storm track (Fig. 4.14a1). Significant cooling in the thermocline in the wake of Linfa is due mostly to the accumulative effect of storm-induced upwelling (Fig. 4.14a2). The accumulative effect of storm-induced (vertical) mixing leads to slightly warmer (cooler) waters in the lower (upper) part of the thermocline at this time (Fig. 4.14a3). In the surface mixed layer above the thermocline, large cooling of about -1.0 ^{o}C occurs mainly to the right of the storm track (Fig. 4.14a1), due to the accumulative effect of both the vertical upwelling and vertical mixing generated by Linfa (Fig. 4.14a2,a3). Beneath the thermocline, the storm-induced cooling in the wake of Linfa at this time (Fig. 4.14a1) is generated mostly by the accumulative effect of upwelling (Fig. 4.14a2).

At 00:00 on 20 June along the transect at 20.2 ^{o}N (Fig. 4.14b1), the intense upwelling induced by Typhoon Linda (Fig. 4.14b2) is also responsible for the maximum cooling in the thermocline and cooling beneath the thermocline in the wake of Linfa (Figs. 4.14b1,b2). The accumulative effect of storm-induced vertical mixing is responsible for significant cooling in the surface mixed layer at this time (Figs. 4.14b1,b3). The accumulative effect of storm-induced vertical mixing also results in slightly warmer (cooler) waters in the lower (upper) part of the thermocline in the wake of Linfa (Fig. 4.14b3). It should be noted that storm-induced cooling spreads significantly eastward in the surface mixed layer and westward in the thermocline and sub-surface layers beneath the thermocline along this transect at this time, due mainly to the transport by the horizontal advections (Fig. 4.14b2).

At 00:00 on 21 June, the large and wide-spread cooling in the surface mixed layer along the transect at 23.0 ^{o}N is generated by the combination of the storm-induced vertical mixing and transport by the horizontal advections (Figs. 4.14c1,c3). The maximum cooling in the thermocline and large cooling in the sub-surface layers in the wake of Linfa at this time are generated mainly by the storm-induced upwelling (Figs. 4.14c1,c2).

Within the thermocline in the wake of Linfa, the storm-induced vertical mixing results in slightly warmer (cooler) waters in the lower (upper) part of the thermocline (Fig. 4.14c3), which are similar to the effect of vertical mixing at previous times (Figs. 4.14a3,b3).

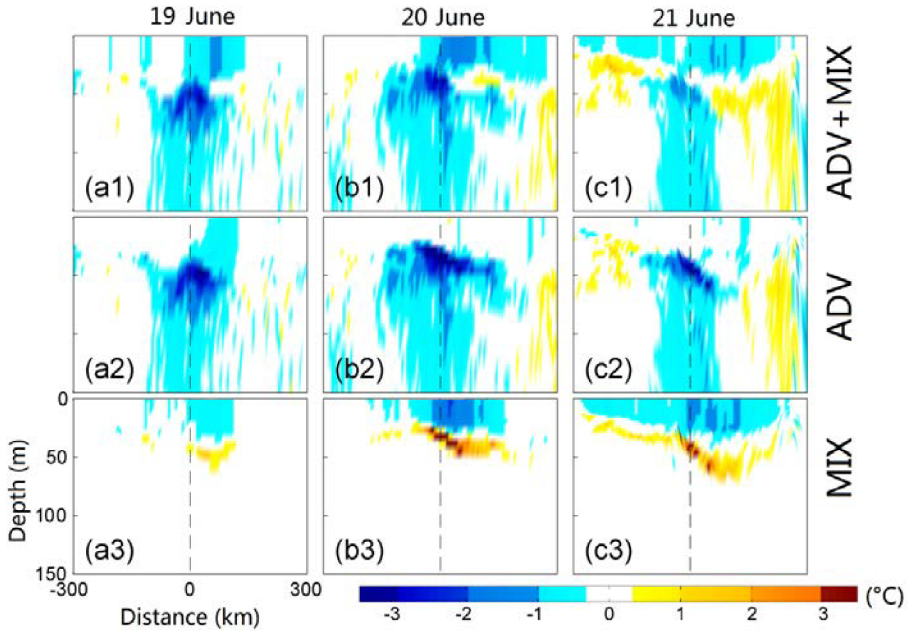

Figure 4.14: Vertical distributions of storm-induced changes in temperatures for ΔT_{AHV} (upper panels), T_A middle panels) and ΔT_{HV} (lower panels) along an east-west transect through the center of Linfa at 18.2 °N (left panels), 20.2 °N (central panels), and 23 °N (right panels) respectively at 00:00 on 19, 20, and 21 June 2009. The vertical dashed line indicates the location of the storm center of Linfa.

In addition to the instantaneous and accumulative effects of storm-induced upwelling and vertical mixing discussed above, temperature in the upper water column is also affected by the net heat flux at the sea surface (NHF) during the storm period. To quantify the effect of the NHF on temperature in the upper water column during the passage of Linfa, we examine the NHF over two intense SST cooling areas (A_1 and A_2 shown in Fig. 4.9) based on daily mean output of the ROMS-nSCS. The NHF includes four components: the short wave radiation (Q_I), long wave radiation (Q_B), latent heat flux (Q_L), and sensible heat flux (Q_S):

$$NHF = Q_I + Q_B + Q_S + Q_L \tag{4.5}$$

The daily mean values of these four components on the right hand side of Eq. (5) over

areas A_1 and A_2 on 18-21 June 2009 are calculated (Table 4.4). The short wave radiation (Q_I) is always positive (i.e., the heat transferred from the air to ocean waters), but highly variable due mainly to highly varying cloud covers over the two areas on the four days. The daily mean values of Q_I vary between 80.3 and 119.2 W m^{-2} over A_1 and between 129.1 and 187.6 W m^{-2} over A_2 during this period. The daily mean values of Q_B are always negative (i.e., the heat transferred from the ocean waters to air), and vary between -17.1 and -44.7 W m^{-2} over A_1 and between -16.3 and -30.1 W m^{-2} over A_2 due to changes in the SSTs and cloud covers during this period. The daily mean values of Q_S, which depend on the surface winds and differences between the air temperature and SST, are negative on the four days and vary between -8.6 and -16.8 W m^{-2} over A_1 and between -16.6 and -40.8 W m^{-2} over A_2. The daily mean values of Q_L, which depend on the evaporation rates, are significantly negative on the four days and vary between -101.4 and -181.9 W m^{-2} over A_1 and between -120.2 and -195.1 W m^{-2} over A_2.

The daily mean values of the net heat fluxes (NHF) over areas A_1 and A_2 on 18-21 June 2009 can be calculated based on Eq. (4.5) using the values of the four components listed in Table 4. The daily mean values of NHF over these two areas are all negative on the four days, and vary between -35.4 and -135.0 W m^{-2} over A_1 and between -3.41 and -78.7 W m^{-2} over A_2 (Table 4.4). By assuming the heat loss from the ocean water to air due to the negative NHF occurs in the top 30 m, the associated daily mean temperature change in the top 30 m can be estimated using $NHF \times \Delta t/(\rho_o c_p \Delta z)$, where $\Delta t = 8.64 \times 10^4$s, $\Delta z = 30$ m, ρ_o is the water density, and c_p is the heat capacity of sea water. The estimated daily mean temperature changes in the top 30 m vary between -0.02 and -0.1 ^oC over area A_1 and between -0.002 to -0.05 ^oC over area A_2 on 18-21 June of 2009 (Table 4.4), which are very small and can be ignored in comparison with the temperature changes generated by Linfa. The daily mean temperature change due to the negative NHF will be even smaller if the actual mixed layer depth during Linfa is used. Considering that the actual temperature changes are cooler than -2.0 C° over the area A_1 and areas A_2 (Fig. 4.8), the other oceanic processes (such as ADV and MIX) rather than the air-sea heat flux play a dominant role for generating temperature cooling in the upper water columns. Similar conclusions were made by Zhang et al. (2014) in their studies of the upper ocean response to typhoon Kalmaegi.

Table 4.4: Daily mean four components for the net heat flux (in units of W m-2) at the sea surface and temperature change (C°) in the top 30 m over two intense SST cooling areas (A_1 and A_2) on 18-21 June 2009.

Area	A_1				A_2			
Date in June	18	19	20	21	18	19	20	21
Short wave radiation	104.61	80.32	111.81	119.22	161.83	129.05	156.00	187.62
Long wave radiation	-21.56	-17.05	-28.17	-44.68	-28.76	-24.54	-16.29	-30.08
Sensible heat flux	-16.83	-16.32	-12.83	-8.58	-16.62	-18.33	-21.80	-40.77
Latent heat flux	-135.96	-181.94	-118.08	-101.39	-195.13	-135.60	-133.30	-120.18
Net heat flux	**-69.74**	**-134.99**	**-47.27**	**-35.43**	**-78.68**	**-49.39**	**-15.39**	**-3.41**
Temperature change in the upper layer of 30 m	-0.048	-0.093	-0.033	-0.024	-0.054	-0.034	-0.011	-0.002

4.5.3 Simulated Near-inertial Oscillations

Near-inertial oscillations (NIOs) are dynamically important in the ocean, particularly during extreme weather conditions. Previous studies revealed that intense NIOs were generated by typhoons or hurricanes (e.g., *Shay and Elsberry,* 1987; *Sheng et al.,* 2006; *Zheng et al.,* 2007). To demonstrate large NIOs generated by Typhoon Linfa, time series of simulated surface currents at four locations along the storm track of Typhoon Linfa produced by the ROMS-nSCS in case CR are shown in Fig. 4.15. The four locations (L_1, L_2, L_3, and L_4) are marked in Fig. 4.9d. The simulated surface currents at these four locations have significant temporal oscillations after the arrival of Linfa. The oscillation amplitude of the surface currents increases from about 15 cm s^{-1} at the beginning of the storm to the maximum speed of about 80 (100, 70, and 50) cm s^{-1} about one day later at location L_1 (L_2, L_3, L_4). The large oscillations of surface currents at these four locations can be explained by the storm-induced NIOs.

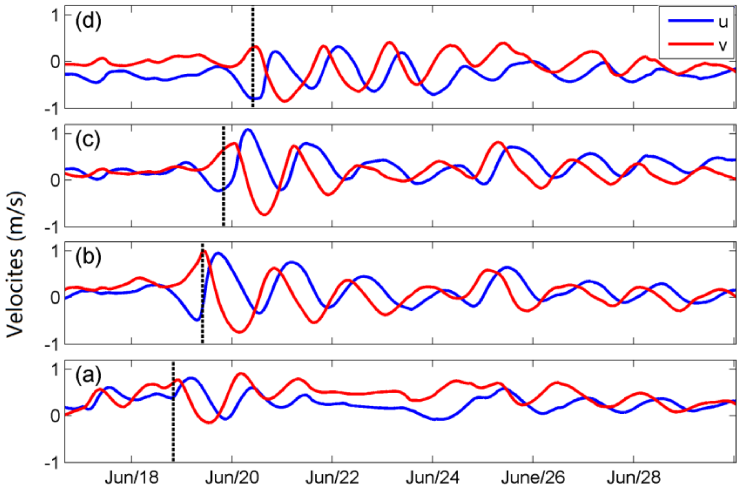

Figure 4.15: Time series of eastward (u) and northward (v) components of simulated surface currents in case CR at locations (a) L_1, (b) L_2 , (c) L_3, and (d) L_4 along the storm track of Typhoon Linfa. The vertical black dash line in each panel represents the arrival time of the storm center of Linfa.

To investigate the spatial structure of NIOs during the study period, the simulated surface currents at the four locations in case CR are band-pass filtered to get the near-inertial components. (The cutoff periods of the band-pass filter are 6 hours centered at the local inertial frequency). Based on the latitudes of $18.0, 19.0$, 20.0, 21.0 °N at the four locations, the local inertial frequencies at these locations are $f_{L1} = 0.62$, $f_{L2} = 0.65$, $f_{L3} = 0.68$, and $f_{L4} = 0.72$ cycles per day (cpd), respectively. The rotary spectra (*Gonella*, 1972) of surface currents at the four locations are calculated from model results during the period from 00:00 on 17 June to 24:00 on 30 June (Fig. 4.15). The peak frequencies of the NIOs at these four locations produced by the ROMS-nSCS in case CR are slightly higher than their local inertial frequencies, which are known as the blue shift (*Fu*, 1981). Previous studies suggested that the frequencies of NIOs can be modified by the background flow (*Mooers*, 1975; *Kunze*, 1985; *Wang* et al., 2019), and the effective inertial frequency f_e can be written as

$$f_e = f + \zeta/2 \tag{4.6}$$

where ζ is the relative vorticity of the background flow.

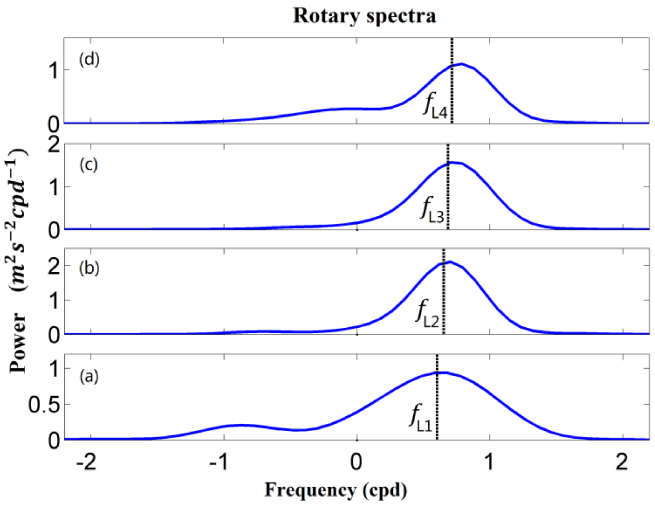

Figure 4.16: Rotary spectra of simulated surface currents at locations (a) L_1, (b) L_2, (c) L_3, and (d) L_4. The vertical dashed line in each panel represents the local inertial frequency at the location. The negative frequency represents the counterclockwise components.

The evolving rotary spectra (ERS) of the simulated surface currents in the near-inertial band are calculated using a sliding window of 10 days at locations L_1, L_2, L_3, and L_4 (Fig. 4.17). The duration of 10 days for the sliding window is selected as a compromise between the need for a long window to increase spectral resolution and a short window to capture the intermittency of NIOs. As shown in Fig. 4.17, intense NIOs are generated by Typhoon Linfa at these four locations. The peak frequencies f_{p} of the simulated NIOS (blue lines) are slightly higher than the local inertial frequencies f (yellow lines). The time-mean peak frequencies f_{p} (averaged from the arrival time of the center of Linfa to the end of June) of simulated NIOs are about $1.10f_{\mathrm{L1}}$, $1.09f_{\mathrm{L2}}$, $1.06f_{\mathrm{L3}}$, and $1.05f_{\mathrm{L4}}$ at locations L_1, L_2, L_3, and L_4 respectively. The effective inertial frequencies (f_e) at each location are also shown in Fig. 4.17, which were calculated based on Eq. 4.6 with the relative vorticity (ζ) computed from the simulated surface currents at each location. The similarity of the magnitudes of f_{e} and f_{p} demonstrates that the applicability of the effective inertial frequency in Eq. 6 for the approximation of the peak frequency of the NIOs during the passage of Typhoon Linfa. Noticeable differences, however, occur between f_{e} and f_{p} at the four locations (Fig. 4.17), indicating that more studies are needed.

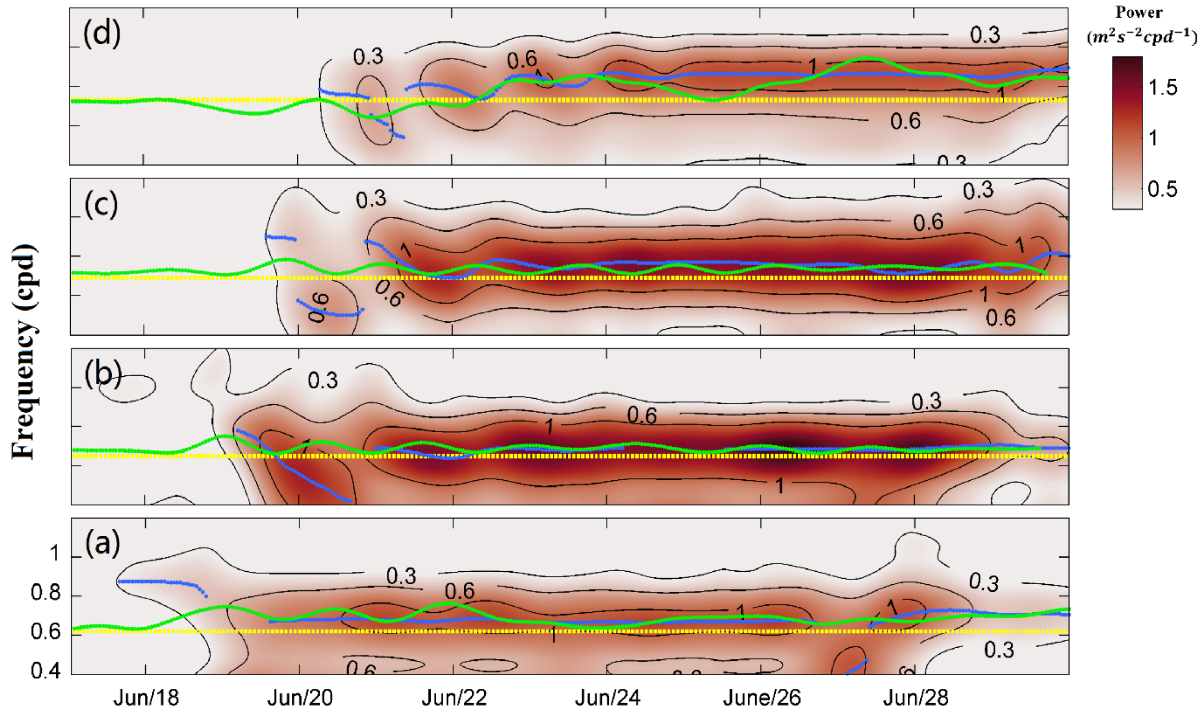

Figure 4.17: Evolving rotary spectra of simulated surface currents at locations (a) L_1, (b) L_2, (c) L_3, and (d) L_4. In each panel, the green line represents the effective frequency ($f_e = f + \zeta/2$), the yellow dashed line represents the local inertial frequency (f), and the blue line represents the peak frequency (f_p) at each location. ERS are calculated using a 10-day sliding window. The frequency axis is limited to the near-inertial band.

Distributions of NIOs at the sea surface at 00:00 on 22 June (Fig. 4.18) are calculated from the ban-pass filtered surface currents produced by the ROMS-nSCS in case CR. A band-pass filter centered at the local inertial frequency is used here. The maximum near-inertial currents (~30 cm s^{-1}) occur in the wake of Linfa between 19 and 22 °N, where Typhoon Linfa had the largest MSWs of about 120 km h^{-1}. The general features of the eastward and northward components of NIOs shown in Fig. 4.18 agree very well with previous modelling studies (*Price,* 1981; *Sheng et al.,* 2006; *Liu et al*., 2019).

Time-depth distributions of eastward and northward components of NIOs at location L_3 (marked in Fig. 4.9d) are calculated for the period from 17 to 30 June 2009 (Fig. 4.19). The amplitudes of NIOs are larger in the surface layer (0~20 m), relatively weaker below the mixed layer, and significantly weak below 100 m. The NIOs are vertically uniform in the surface mixed layer and have significant phase shifts beneath the thermocline due to

vertical shear. The strong NIOs lasts for about 8 days (19-27 June) after the typhoon passage (Fig. 4.19).

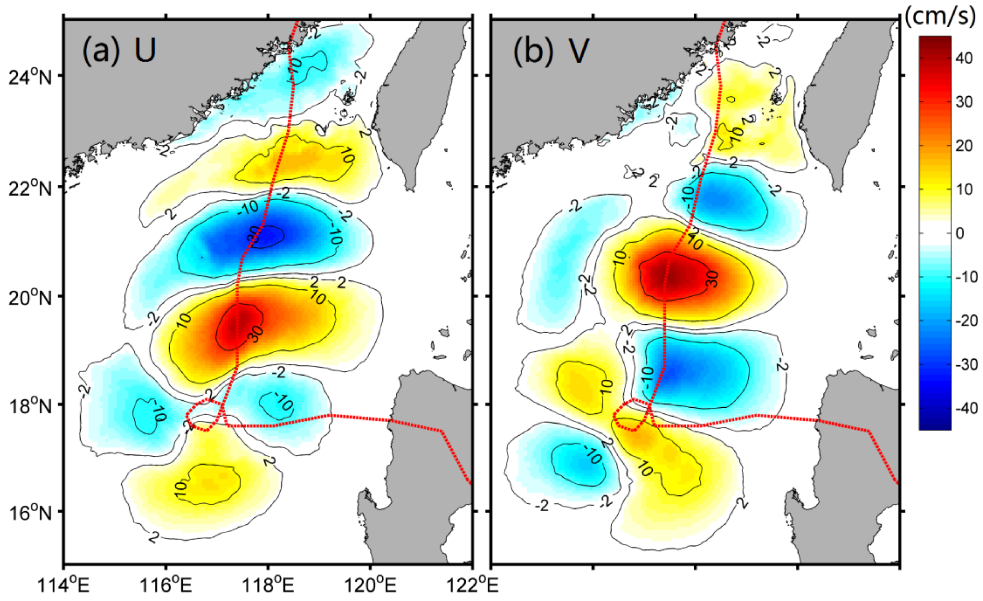

Figure 4.18: Distributions of (a) the eastward component, and (b) northward component of the near-inertial currents at the sea surface at 00:00 on 22 June 2009 based on model results produced by ROMS-nSCS. The red dashed line represents the storm track of Typhoon Linfa. The contours of -10, -2, 2 and 10 cm s^{-1} are shown.

To examine the distribution of storm-induced NIOs during Linfa, the kinetic energy at the sea surface defined as $(u^2 + v^2)/2$ is computed based on the band-pass filtered surface currents produced by the ROMS-nSCS in case CR. At 00:00 on 19 June, the near-inertial energy at the sea surface is relatively small and about 20 $cm^2\ s^{-2}$ over area A_1 (Fig. 4.20a). The near-inertial energy at the sea surface increases with time and spreads northward with the northward translation of Typhoon Linfa from the beginning of 19 June to the noon of 21 June (Figs. 4.20b-c). The near-inertial energy at the sea surface is also biased to the right of the storm track of Linfa due to the rightward bias in the storm-induced currents (*Price,* 1981). The maximum near-inertial kinetic energy at the sea surface is ~500 $cm^2\ s^{-2}$ on 22 June (Fig. 4.20d). After reaching the maximum, the near-inertial energy at the sea surface starts to decay, due to dissipation and also the vertical

propagation of the energy (Fig. 4.20e). The near inertial energy at the sea surface is small and about 20 $cm^2\ s^{-2}$ over area A_2 at 00:00 on 28 June (Fig. 4.20f). The near-inertial energy at the sea surface spreads significantly outside the wake of Linfa due to large-scale background currents over the study region (Figs. 4.20b-d).

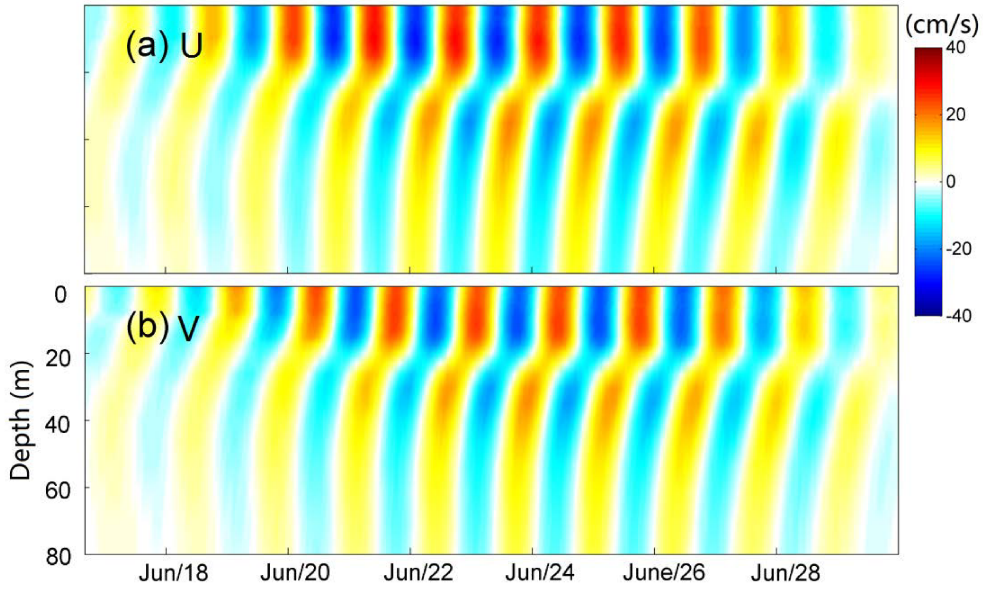

Figure 4.19: Time-depth distributions of (a) the eastward component and (b) northward component of near-inertial currents at position L_3 from 17 to 30 June 2009 based on model results produced by ROMS-nSCS.

4.6 Summary

A three-dimensional ocean circulation model (ROMS-nSCS) was used in the study of storm-induced circulation and temperature/salinity over the northern South China Sea (nSCS) during Typhoon Linfa in June 2009. The model performance was found to be satisfactory based on comparisons of model results with various types of observations, including in-situ observations, satellite remote sensing data, and the global ocean reanalysis produced by the HYCOM.

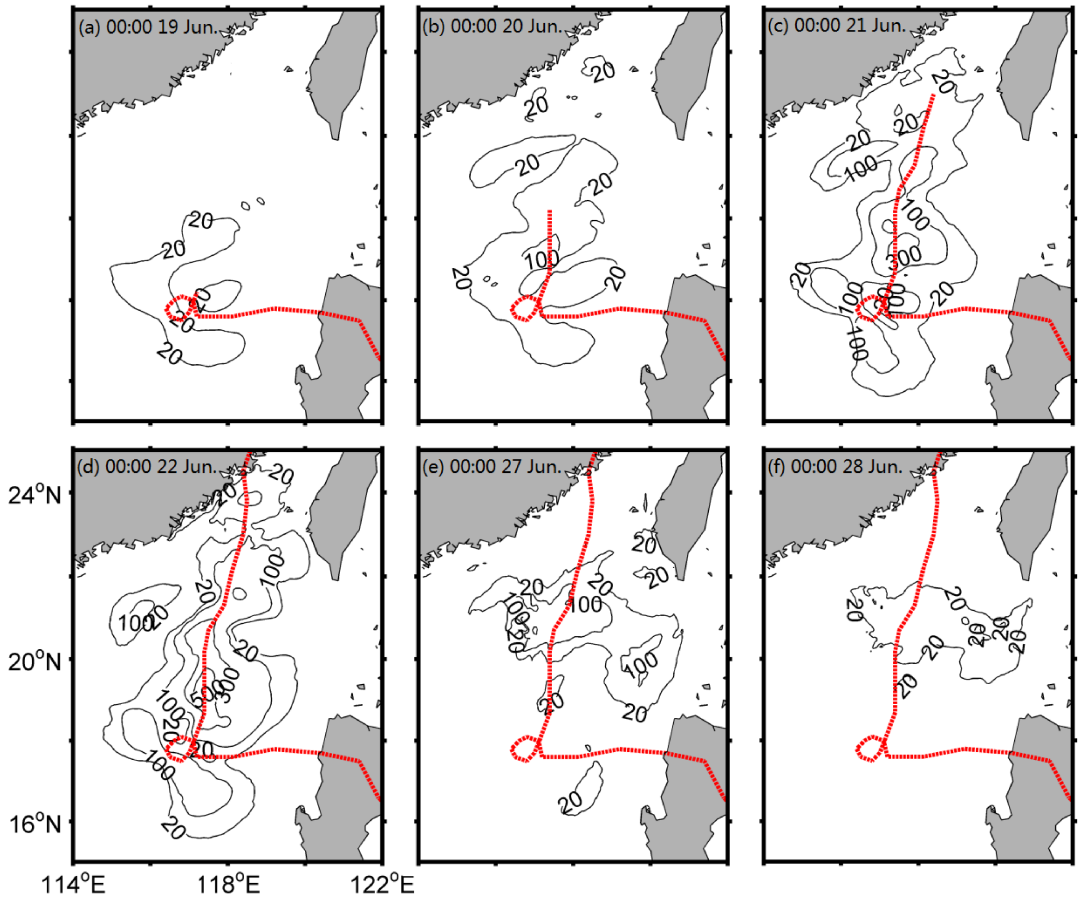

Figure 4.20: Distributions of the near-inertial energy (unit cm^2s^{-2}) at the sea surface over the northeastern nSCS calculated from simulated currents produced by the ROMS-nSCS in case CR at 00:00 on (a) 19, (b) 20, (c) 21 (d) 22, (e) 27 and (f) 28 June 2009. The red dashed line in each panel represents the storm track of Typhoon Linfa.

Model results in six different numerical experiments were analyzed to quantify the main processes affecting storm-induced changes in three-dimensional currents and temperatures during Linfa. It was found that the storm-induced cooling occurs over the area affected directly by Linfa (AADL) and in the wake of Linfa, due to the combined and accumulative effect of storm-induced upwelling and vertical mixing. The relative importance of storm-induced upwelling and vertical mixing varies in different stages of Linfa, which depends on the translational speeds, wind intensity and structure of the storm, and vertical stratification. In the early stage of Linfa when the storm made a small loop with relatively slow translational speeds and low sustained wind speeds, the storm-

induced upwelling effect is significant in generating cooling in the upper water column. In the mature stage of Typhoon Linfa when the storm had strong sustained wind speeds of about 80-120 km h^{-1}, the storm-induced mixing plays a dominant role in directly cooling the surface mixed layer. Nevertheless, the storm-induced upwelling is important as the precondition of cooling in both the thermocline and sub-surface layers beneath the thermocline in this stage. The storm-induced vertical mixing in the mature stage of the storm also results in cooling in the upper part of the thermocline and slightly warm in the lower part of the thermocline. The vertical mixing plays a minor role in cooling in the sub-surface layers below the thermocline. The oceanic response to a typhoon depends on characteristics of the storm including the storm intensity, size and translational speed. In general, strong intensity and slowly moving typhoons are expected to generate large ocean responses (*Zhao et al.,* 2017). For a slowly moving typhoon, the storm-induced cooling in the upper water columns is due to large storm-induced upwelling with the long residence time. The storm-induced upwelling can bring the cold sub-surface waters to the surface mixed layer, and make the entire upper water column to be cool in the wake of the storm. For Typhoon Linfa, the accumulative effect of upwelling and vertical mixing contributes the storm-induced temperature cooling in the upper water column in the wake of the storm. The storm-induced mixing plays a very important role in the surface mixed layer. The storm-induced upwelling, by comparison, is the main cause of cooling in the lower part of the thermocline (*Tsai et al.,* 2008). Several previous studies documented the dominance of the thermal response by storm-induced mixing (*Fedorov et al.,* 2010; *Korty et al.,* 2008; *Pasquero and Emanuel*, 2008). Our studies suggested that the whole surface mixing layer experiences cooling in the wake of typhoon Linfa in the early stage (Fig. 4.7c), due largely to the typhoon-driven upwelling. Our finding is also supported by the work of *Park et al.* (2011) who found no significant sub-surface warming under most of the TCs they analyzed.

The vertical structure of near-inertial oscillations in the wake of Linfa was also examined in this study. One of important findings is that the peak frequency of the NIOs is about 5~10% higher than the local inertial frequency, due to the effect of vorticity of background flow. It was found that the near-inertial currents occur over the looping area of Linfa in the early stage of the storm and spread northward with the northward

translation of Typhoon Linfa. The near-inertial currents and energy are biased to the right of the storm, with significant spreading in the directions normal to the storm track due to the background flow. The near-inertial currents lasted for about 8 days after Linfa swept the region.

Chapter 5

CONCLUSIONS

As an important link between the land and ocean interior, the coastal and shelf waters (CSWs) support a wide range of human activities including tourism, recreation, transportation, and fisheries. The CSWs also provide critical habitats for many marine species such as fish, marine mammals, coral reefs, sea turtles, and aquatic vegetation. Therefore, reliable knowledge of dynamics, temperature/salinity, and three-dimensional (3D) circulation over the CSWs is of great importance. The main goal of this thesis was to advance our quantitative and predictive understandings of major dynamic processes and their mechanisms over the CSWs.

Three numerical modelling systems with different complexity were used to study the dynamics, temperature/salinity, and 3D circulation over the CSWs. My doctoral research focused on following three specific aspects: (i) the circulation and retention of surface waters over the Scotian Shelf (ScS) and its adjacent coastal waters, (ii) the 3D circulation, temperature/salinity in Halifax Harbour (HH) and physical processes affecting the intense landward intrusion of offshore sub-surface water into Bedford Basin (BB), and (iii) the storm-induced changes in the 3D circulation and temperature/salinity during a typhoon event over the northern South China Sea (nSCS).

A Lagrangian particle tracking model was used in Chapter 2 to examine the particle movements, retention, and connectivity over the Scotian Shelf, southern Gulf of St. Lawrence (GSL), inner Gulf of Maine (GoM), Bay of Fundy (BoF) and the adjacent deep waters. The 3D currents used by the particle tracking model were produced by *Ohashi and Sheng* (2015) using a nested-grid circulation modelling system based on the Princeton Ocean Model (POM*; Mellor,* 2004). Chapter 2 was published in the Satellite Oceanography and Meteorology under the title of "Circulation, dispersion and hydrodynamic connectivity over the Scotian Shelf and adjacent waters" (*Sui et al,* 2017).

A nested-grid modelling system (NGMS-seCS) was used in Chapter 3 to study the 3D circulation, temperature/salinity and associated variability in HH and landward intrusion of offshore deep water into BB. This modelling system was based on the Regional Ocean Modeling System (ROMS, *Shchepetkin and Mcwilliams*, 2005; *Haidvogel et al*., 2008) and the Sea Ice Model (CICE, *Hunke et al.,* 2010).

A three-dimensional ocean circulation model (ROMS-nSCS) was used in Chapter 4 to study of storm-induced circulation and temperature/salinity over the northern South China Sea (nSCS) during Typhoon Linfa in June 2009. The circulation modelling was also based on ROMS. Chapter 4 was published in the Continental Shelf Research under the title of "Study of storm-induced changes in circulation and temperature over the northern South China Sea during Typhoon Linfa" (*Sui et al,* 2022).

The main reason for using three different modelling systems in my doctoral research is that different modelling systems are used to address specific research questions.

Research results were discussed extensively in individual chapters. A brief summary of major findings and their significance were summarized in section 5.1 to address the major scientific questions listed in Chapter 1. Future work is discussed in Section 5.2.

5.1 Main Results and Their Significance

In Chapter 2, the simulated particle movements and distributions were used to examine the retention and hydrodynamic connectivity of surface waters over the GSL-ScS-GoM. The major new findings include the relatively high retention rates of surface water in Northumberland Strait, over the outer shelves of the eastern and central Scotian Shelf (eScS and cScS), in the outer and central BoF, and over the inner GoM. The relatively low retention rates of surface waters were found over western Cabot Strait, the inner shelf of the eScS and cScS. The retention rates were also low over the outer shelf of the western Scotian Shelf and along the shelf break. It was found that the tidal currents significantly influence the retention of surface waters in the Bay of Fundy. The upstream and downstream areas for surface waters over St. Anns Bank, Deep Panuke offshore oil

and gas platforms and the outer BoF were also calculated from simulated movements of near-surface particles. Reliable knowledge of the retention and hydrodynamic connectivity of surface waters over the GSL-ScS-GoM is important to economic activities and management of ecosystem dynamics over the region.

In Chapter 3, the circulation, temperature/salinity, and their associated variability in HH were studied using the NGMS-seCS. The annual monthly mean circulation in HH is characterized by a typical two-layer estuarine circulation, with seaward currents in the upper layer and landward currents in the lower layer. The simulated annual mean near-surface and sub-surface currents have similar circulation features as the simulated results in 2006 by *Shan* and Sheng (2012), except for the direction of near-surface currents over the Outer Harbour (OH). The difference is due mainly to the interanual variability of winds. The temperature, salinity and 3D currents in HH have large seasonal and synoptic variability. The dynamics of landward intrusion of offshore sub-surface waters into BB were investigated. The model results showed the persistent northwesterly winds play an important role in strengthening the near-surface seaward currents and trigging the intense landward intrusion of offshore sub-surface waters through the bottom layer of HH. The persistent southwesterly winds can also trigger the intense landward intrusion, but are less effective than the northwesterly winds. The southeasterly winds, in comparison, reduce significantly the seaward currents in the surface layer of HH, and prevent the landward intrusion. The accumulative effects of winds and tides on temperature, salinity and currents in HH were also examined using the NGMS-seCS. The model results demonstrated that the winds play the major role in affecting the 3D currents and temperature/salinity in HH. By comparison, tides play a secondary role in affecting the 3D currents and temperature/salinity in HH, except for the Narrows. This study provides better understanding of the oceanographic conditions in HH and the research results will be very helpful in decision making for economic activities and ecosystem managements.

The simulated upper ocean response to Typhoon Linfa featured as strong wind-driven currents and storm-induced cooling in the upper ocean over the nSCS. The storm-induced cooling was found to results from the combined and accumulative effect of storm-induced upwelling and vertical mixing. The relative importance of storm-induced

upwelling and vertical mixing varies in different stages of Linfa, which depended on the translational speeds, wind intensity and structure of the storm, and vertical stratification. In the early stage of Linfa when the storm made a small loop with relatively slow translational speeds and low sustained wind speeds, the storm-induced upwelling effect was found to be significant in generating cooling in the upper water column. In the mature stage of Typhoon Linfa when the storm had strong sustained wind speeds, the storm-induced mixing played a dominant role in directly cooling the surface mixed layer. Several earlier studies suggested the dominance of the storm-induced thermal response by mixing (*Fedorov et al.,* 2010; *Korty et al.,* 2008; *Pasquero and Emanuel,* 2008). Our modeling results indicated that the whole surface mixing layer experienced an overall cooling in the wake of typhoon Linfa in the early stage, due largely to the typhoon-driven upwelling. Comparing with the storm-induced upwelling and mixing, the air-sea heat flux played a minor role for generating temperature cooling in the upper water columns during the passage of the storm. The vertical structures of storm-induced near-inertial oscillations (NIOs) were also examined based on model results. The rotary spectral analysis of model currents demonstrated that the peak frequency f_{p} of NIOs was about 9% greater than the local inertial frequency, which can be explained mostly by the background vorticity. Better scientific knowledge on wind-induced cooling and storm-induced currents during extreme weather conditions are provided by this study.

5.2 Future Work

Significant progress was made in my doctoral research for examining the temperature, salinity, and circulation over three specific CSWs. However, many important scientific questions remain to be addressed in the future.

Simulations of the retention and hydrodynamical connectivity over the ScS and its adjacent coastal waters were based on the model results in 2007 and 2008. Furthermore, our study focused on the retention only in the near-surface waters. Future studies should be conducted by using model results of multiple years to calculate the retention index and hydrodynamical connectivity. The numerical particles used in calculating the retention

indices did not include the vertical movement with the circulations. It is important to investigate the retention and hydrodynamical connectivity for the whole water column.

A nested-grid ocean circulation model NGMS-seCS was used to investigate the variability of temperature and salinity in HH. In order to simulate more accurately the 3D hydrodynamics in coastal waters such as HH, higher special resolutions of the meteorological forcing is needed. In addition, the nested-grid model systems used the conventional one-way nesting technique in which information from the upper-level (i.e., parent) submodel is transferred to the lower-level (i.e., child) submodel. The upper-level submodel results are not affected by the finer resolution lower-level submodel results. Two-way nesting techniques should be used in the future studies.

Our study of storm-induced hydrodynamics over the nSCS was limited to only Typhoon Linfa. Further studies on different storm events should make the conclusion more robust. The modelling system for the nSCS did not include tidal components. Interactions of storm-induced circulation with tides during extreme weather conditions deserve further investigations in terms of the changes of the circulation pattern, mixing, heat budget and water transport.

My doctoral research did not include the wave-current interactions (WCIs). WCIs were found to have significant influence on the circulation and temperature/salinity (*Lin et at.,* 2021). Future modelling studies should examine the effect of WCIs on the sea levels, temperature/salinity, and circulation over the three study regions of this thesis.

APPENDIX A

THE SEMI-PROGNOSTIC METHOD

In the semi-prognostic method, the model hydrostatic equation (*Sheng et al*., 2001)

$$\frac{\partial P}{\partial z} = -g\rho_m \tag{A.1}$$

is adjusted to

$$\frac{\partial P}{\partial z} = -g[\rho_m + \beta\overline{(\rho_C - \rho_m)}] \tag{A.2}$$

where ρ_m is the prognostic density calculated from model temperature and salinity, ρ_c is the density computed from the climatological (or observed) temperature and salinity values, and β is a coefficient between 0 and 1. The value of β is set to 0.15 in my thesis research. The operator $\overline{(\quad)}$ denotes the spatial average.

As a result, the semi-prognostic method introduces a correction term $-\frac{1}{\rho_0}\nabla\hat{P}$ to the horizontal momentum equations, where $\hat{P}$ satisfies

$$\frac{\partial \hat{P}}{\partial z} = -g\beta\overline{(\rho_C - \rho_m)}\,. \tag{A.3}$$

with $\hat{\mathrm{P}} = 0$ at z = 0.

Physically, the correction term $-\frac{1}{\rho_0}\nabla\hat{P}$ directly modifies the model-computed circulations and modifies indirectly the model temperature and salinity. More details of the semi-prognostic method can be found in *Sheng et al*. (2001) and *Greatbatch et al*. (2004).

APPENDIX B

THE SPECTRAL NUDGING METHOD

In the spectral nudging method, the model-computed temperature and salinity are nudged toward the climatological temperature and salinity values at certain frequency bands.

$$\frac{\partial T}{\partial t} + (u \cdot \nabla)T = A \cdot \nabla^2 T + \gamma < T_c - T > \quad \text{(B.1)}$$

The second term on the right hand side of Eq. (B1) is the nudging term given as

$$< T_c - T >= \int_{-\infty}^{0} \phi(\tau)[T_c(t+\tau) - T(t+\tau)]\, d\tau \quad \text{(B.2)}$$

which is a weighted average of differences between the climatological and prognostic temperature and salinity. In Eq. (B1), $\phi(\tau)$ is a weight function, T represents the prognostic temperature and salinity, T_c represents the climatological temperature or salinity, and u represents the 3D velocity vector. More details of the spectral nudging method can be found in *Thompson et al.* (2007).

APPENDIX C

Governing Equations of Los Alamos Community Ice Model

Los Alamos Community Ice Model (CICE) is a sea ice model for simulating the thickness, concentration and velocity of sea ice (*Hunke et al.,* 2010). It solves numerically two main sets of governing equations for the sea ice: (a) Newton's second law (momentum equations) for sea ice and (b) the sea ice thickness distribution for different thicknesses spread of the area (*Hunke et al.,* 2010).

The ice momentum equations in CICE on the Cartesian coordinate system are described by *Gao et al.* (2011) as:

$$m\frac{\partial u}{\partial u} + m\left(u\frac{\partial u}{\partial x} + v\frac{\partial u}{\partial y}\right) - mfv = \frac{\partial \sigma_{xy}}{\partial x} - mg\frac{\partial \eta}{\partial u} + \tau_{ax} + \tau_{wx} \quad \text{(C1)}$$

$$m\frac{\partial v}{\partial u} + m\left(u\frac{\partial v}{\partial x} + v\frac{\partial v}{\partial y}\right) - mfu = \frac{\partial \sigma_{xy}}{\partial y} - mg\frac{\partial \eta}{\partial y} + \tau_{ay} + \tau_{wy} \quad \text{(C2)}$$

where m is the combined mass of ice and snow per unit area, u and v are the x and y components of the ice velocity; f is the Coriolis parameter, g is gravity; η is the sea surface elevation; σ_{xy} is the internal stress tensor which is a function of the ice strain rate and strength by the constitutive law (*Hunke and Dukowicz,* 1997), (τ_{ax}, τ_{ay}) and (τ_{wx}, τ_{wy}) are the x and y components of sea surface wind and water stresses, respectively. The vector forms of these stresses follow *Connolley et al.* (2004), which are formulated as:

$$\overrightarrow{\tau_a} = cC_a\rho_a|\vec{u}_a|(\vec{u}_a cos\varphi + k \times \vec{u}_a sin\varphi) \quad \text{(C3)}$$

$$\overrightarrow{\tau_w} = cC_w\rho_w|\vec{u}_w - \vec{u}|[(\vec{u}_w - \vec{u})cos\theta + k \times (\vec{u}_w - \vec{u})sin\theta)] \quad \text{(C4)}$$

where c is the ice concentration ranging from 0 to 1, $\vec{u}$ is the surface velocity vector of ice, φ and θ are the air and water turning angles, C is the drag coefficient, and ρ is the density, respectively. The subscripts "a" and "w" represent the "air" and "water", respectively.

The thickness distribution function $\hat{g}(\vec{x}, h, t)$ contains the information of ice area, ice volume, snow volume, ice energy, snow energy and area-weighted surface temperature *Gao et al.* (2011). The evolution of $\hat{g}$ with time is described by *Rae et al.,* (2015) as:

$$\frac{\partial \hat{g}}{\partial t} = -\nabla \cdot (\hat{g}\vec{u}) - \frac{\partial (\Phi \hat{g})}{\partial h} \tag{C4}$$

where $\nabla \cdot (\hat{g}\vec{u})$ is the rate of change of g due to dynamical processes, h is the ice thickness, and Φ is the rate of change of ice thickness due to thermodynamic growth and melt. CICE sea ice model solves this equation to determine the evolution of g in time and space. Full details of the model are available in CICE user manual (*Hunke and Lipscomb*, 2010).

APPENDIX D

PERFORMANCE ASSESSMENT OF NGMS-SECS

The tide gauge data at Halifax (44° 39' N, 63° 34' W) were used by *Pei et al.* (2022) in assessing the model performance of submodel L1. The simulated and observed sea levels at Halifax tidal gauge station were decomposed to the tidal and non-tidal component for the period from February 5 to March 27, 2018 (Fig. D1). The in-situ observations of sea levels were obtained from the Marine Environmental Data Service of Fisheries and Oceans Canada (MEDS-DFO; isdm-gdsi.gc.ca). Good agreement was found between the simulated and observed sea levels at Halifax tide gauge (Fig. D1) with the small values γ^2, which indicate that submodel L1 has reasonable skill in simulating both total sea levels, tidal sea levels, and non-tidal levels over coastal waters of the ScS (*Pei et al.,* 2022).

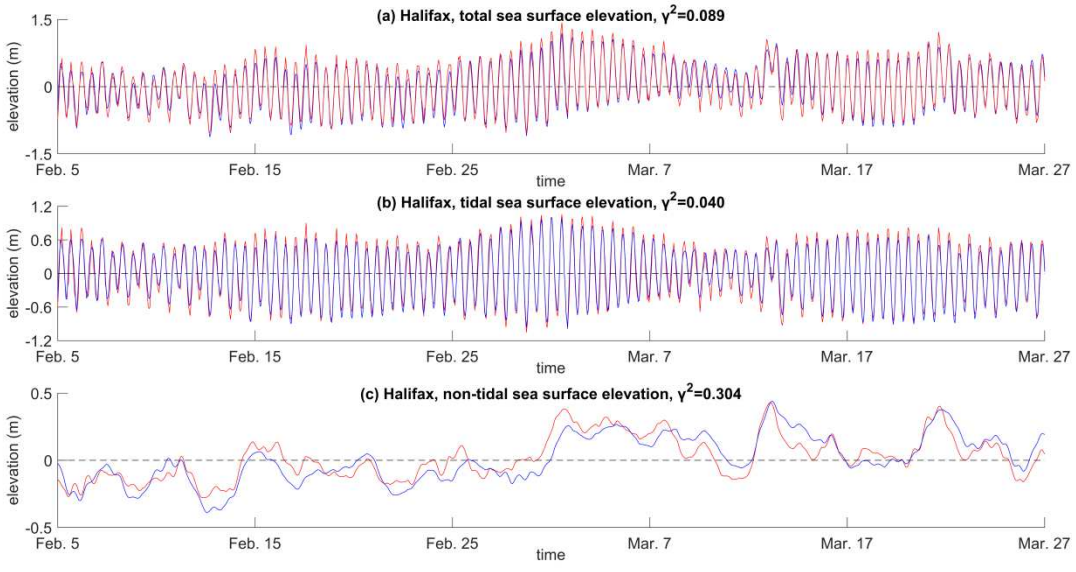

Figure D1. Time series of observed (red) and simulated (blue) (a) total, (b) tidal and (c) non-tidal sea levels at the Halifax tidal gauge station for the period from February 5 to March 27, 2018. The simulated results are produced by submodel L1. (adopted from Pei et al., 2022).

The performance of submodel L1 in simulating the tidal sea levels over the whole domain of submodel L1 were also assessed by *Pei et al.* (2022). Tidal harmonic analyses using t_tide were conducted to determine the amplitudes and phases of the M_2 and K_1 sea levels from hourly results produced by submodel L1 during the period of 1-30 June, 2018. The co-phases and co-amplitudes of the M_2 and K_1 tidal sea levels produced by the NGMS-seCS are compared with the counterparts taken from the OTIS (Fig. D2). It is found that submodel L1 reproduces reasonably well the distribution of co-amplitudes and co-phases of $M_2$and K_1 tidal sea levels over the seCS and adjacent deep ocean waters.

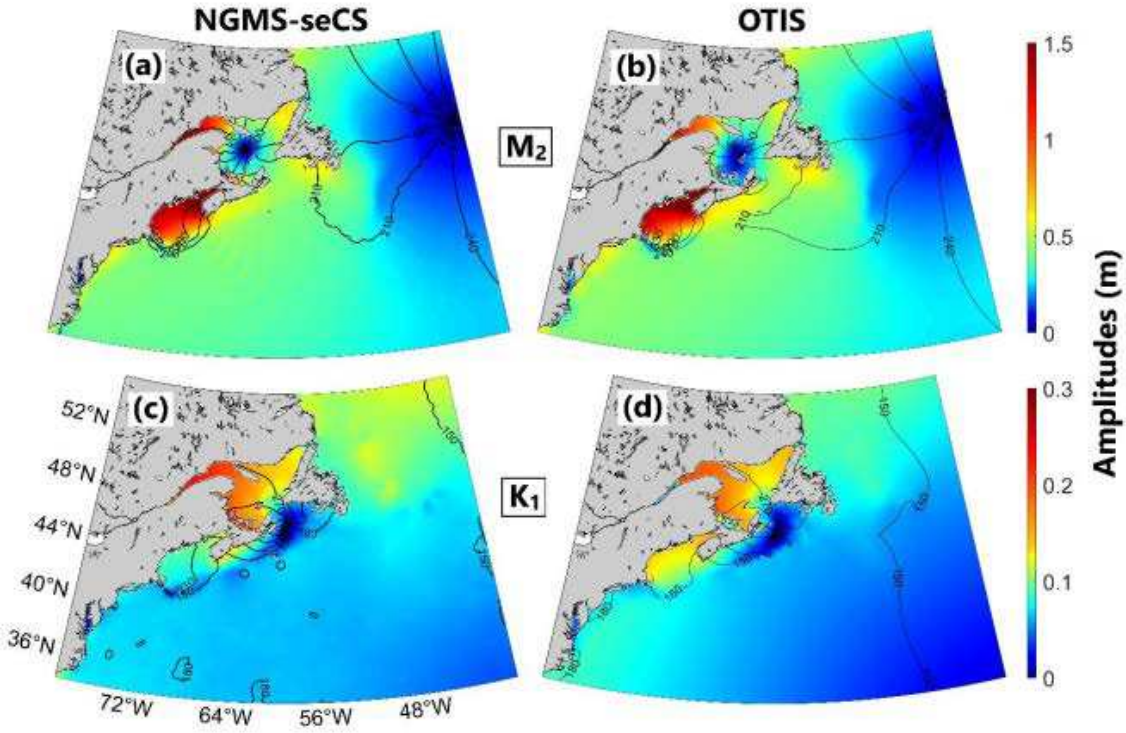

Figure D2: Co-phases (black contour lines) and co-amplitudes of the M_2 (upper panels) and K_1 (lower panels) tidal sea levels calculated from results produced by submodel L1 using t_tide (left panels) and taken from OTIS dataset (right panels) (adopted from *Pei et al.* 2022).

The performance of submodel L1 in simulating the monthly mean sea surface temperature (SST) and sea surface salinity (SSS) was assessed by *Pei et al.* (2022) using the satellite remote sensing data in March and September 2018. They demonstrated that

submodel L1 reproduces reasonably well the general large-scale features of the monthly mean SST and SSS in March and September 2018 over the submodel L1 domain (*Pei et al.,* 2022). We further access the performance of submodel L1 in simulating the monthly mean temperature, salinity, and circulations in 2014 using the daily mean reanalysis data of GLORYS over the submodel L1 domain. The GLORYS data with data assimilation was found to represent reasonably well the large-scale variability of ocean dynamics (*Jean-Michel et al.,* 2021).

The performance of submodel L1 in simulating the SST, SSS and surface circulation is assessed by comparing the monthly mean model results with the GLORYS dataset in 2014 over the submodel L1 domain. The monthly mean GLORYS results are calculated from the daily mean GLORYS dataset. The monthly mean GLORYS SST in March 2014 (Fig. D3b) is relatively cool and ranges from -2 °C to 5 °C over the ScS, Gulf of St. Lawrence (GSL), Bay of Fundy (BoF), Labrador Shelf (LS), Newfoundland Shelf (NFS), and Grand Banks (GB). The Labrador Current (about 0.3 m/s) in the monthly mean GLORYS dataset flows southeastward over the LS and adjacent deep waters. In the GoM, the slope water region of the seCS, and deep ocean waters off the LS, NFS, and GB, the March-mean GLORYS SST in 2014 ranges from 5 °C to 12 °C. Over the deep waters to the south of the seCS, the March-mean GLORYS SST is relatively warm and ranges from 15 °C to 23 °C. Some small-scale SST features associated with eddies and meanders of the Gulf Stream (up to about 1.5 m/s) in the deep ocean waters to the south of the ScS (Fig. D4b). Previous studies demonstrated that, after separating from Cape Hatteras (35.5 °N, 75.5 °W), the Gulf Stream turns eastward and changes from a fast and straight current to a slow and meandering one (*Zhang and McGillicuddy*, 2020).

In comparison, the monthly mean GLORYS SST in August 2014 is relatively warmer than the counterpart in March 2014 (Fig. D3b,d). The August-mean GLORYS SST ranges from 7 °C to 12 °C over the LS and adjacent deep waters. Over the southern GSL, ScS, and southwestern NFS, the August-mean GLORYS SST is between 16 °C and 21 °C. Over the deep waters, the August-mean GLORYS SST is warm and ranges between 25 °C and 28 °C.

A comparison between the monthly mean GLORYS dataset (Fig. D3b,d) and the monthly mean results produced by NGMS-seCS (Fig. D3a,c) demonstrates that submodel L1 reproduces reasonably well the general features of the monthly mean SST and general surface circulation over the submodel L1 domain, with the relative bias of ~5.42% (~2.55%), correlation coefficient of ~96.47% (97.36%), and root mean square error (RMSE) of ~1.47 °C (1.03 °C) in March (August) 2014 (Fig. D3, Table D.1). Submodel L1 reasonably reproduces the low SST over the GSL, GB, and coastal and shelf waters of the ScS, NFS and LS, and the warm SST in the deep ocean waters of the seCS. Submodel L1 also has reasonable skills in reproducing the large-scale circulation including the Labrador Current and the Gulf Stream (Fig. D3a,c). The circulation produced by submodel L1 features some small-scale features associated with thermal fronts over the deep waters to the south of the seCS. Nevertheless, Submodel L1 has model deficiencies in generating the same small-scale features as the GLORYS data, such as meso-scale eddies and meanders associated with the Gulf Stream and Labrador Currents.

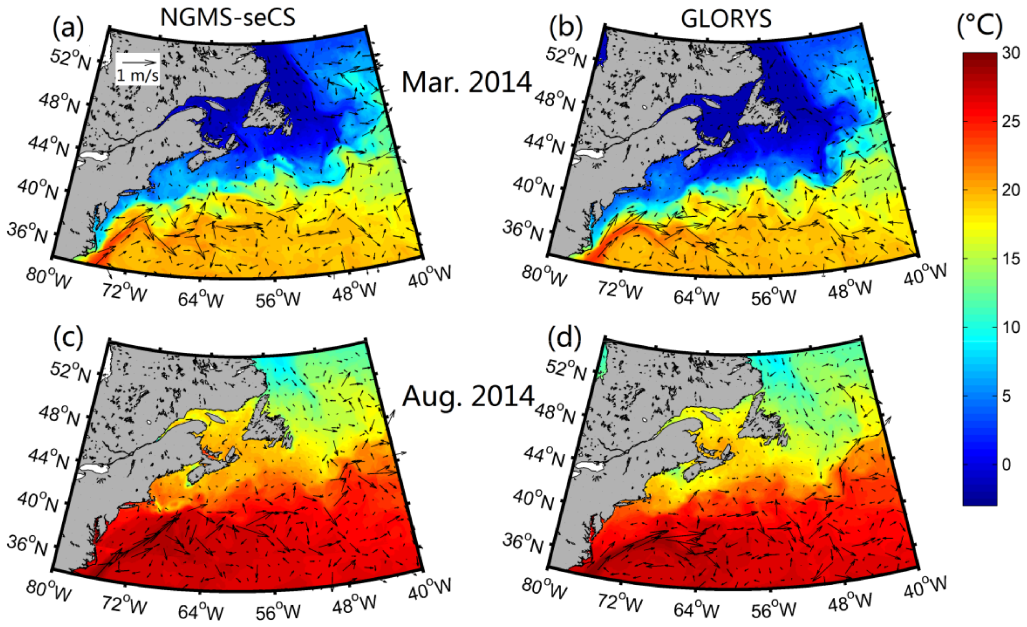

Figure D3: Monthly mean temperature and currents at the sea surface in (a,b) March and (c,d) August 2014 calculated from results generated by (a,c) submodel L1 and (b,d) GLORYS dataset. For clarity, velocity vectors are plotted at every 14th model grid point.

The monthly mean GLORYS SSS in March 2014 are relatively low and varies from 26 to 30 over the St. Lawrence Estuary (SLE) and coastal waters of PEI (Fig. D4), mainly due to the large amount of freshwater discharges from the St. Lawrence River. Over the BoF, GoM, ScS, eastern GSL, LS, NFS, and the GB, the March-mean GLORYS SSS is generally between 30 and 33. Over deep ocean waters off the seCS, the March-mean GLORYS SSS is relatively high and ranges from 35 to 36. The March-mean GLORYS SSS also has some relatively fine-scale frontal structures over slope waters of the seCS and adjacent deep waters (Fig. D4).

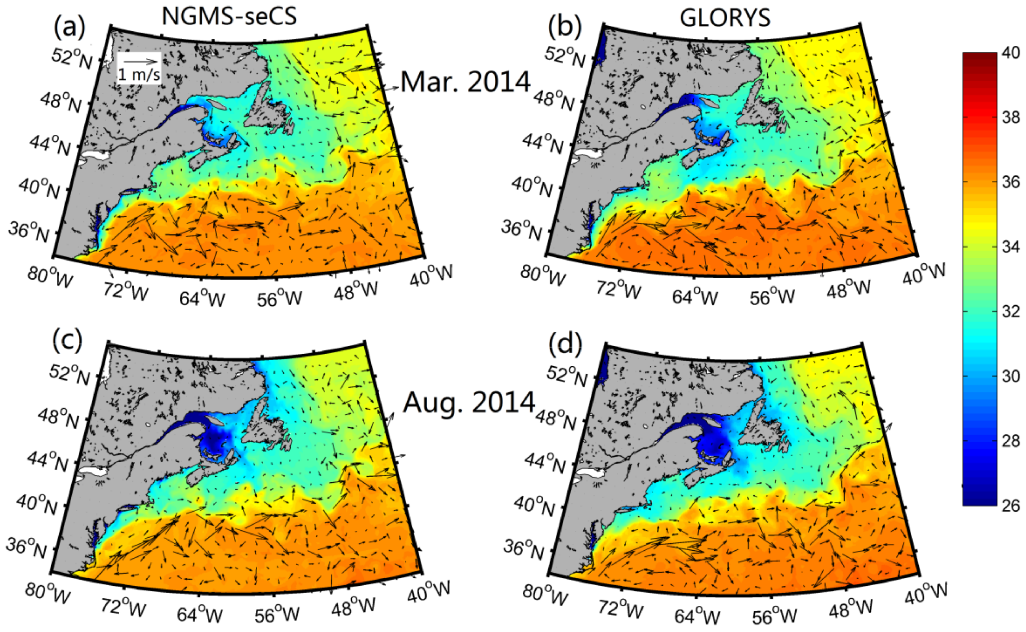

Figure D4: Monthly mean salinity and currents at the sea surface in (a,b) March and (c,d) August 2014 calculated from results generated by (a,c) submodel L1 and (b,d) GLORYS dataset. For clarity, velocity vectors are plotted at every 14th model.

The monthly mean GLORYS SSS in August 2014 is relatively low and ranges from 26 to 29 over most of the western GSL and coastal waters off Cape Breton Island (CBI). Over the western GSL and coastal waters off CBI, the monthly mean GLORYS SSS is lower in August than in March 2014 (Fig. D4). The SSS in the GLS, ScS, and GOM is significantly affected by the discharges from major rivers (including the SLR) over these regions. Base on the St. Lawrence Global Observatory (SLGO) dataset (*Bourgault and*

Koutitonsky, 1999), the monthly mean SLR discharges were largest during March-June in 2014. *Ohashi and Sheng* (2013) demonstrated that the freshwater signal from the SLE takes about 100 days to reach Cabot Strait. Therefore, the relatively low SSS over the western GSL and coastal waters of CBI in August 2014 is due mainly to the seaward transport of the large SLR discharges between March and June.

A comparison between the monthly mean GLORYS SSS (Fig. D4b,d) and the monthly mean SSS produced by NGMS-seCS (Fig. D4a,c) demonstrates that submodel L1 has reasonable skill in reproducing the main features of the monthly mean SSS over the domain of submodel L1, with the relative bias of ~0.81% (~0.71%), correlation coefficient of ~92.65% (94.91%), and RMSE of ~0.84 (0.83) in March (August) 2014. However, NGMS-seCS has deficiencies in generating the SSS over the southern GSL and thermal fronts associated with the Gulf Stream.

The monthly mean GLORYS sub-surface temperature at 760 m (Fig. D5a,c) is relatively lower than the counterpart at the sea surface (Fig. D3a,c). The monthly mean GLORYS sub-surface temperature at 760 m in March 2014 ranges from 2 to 7 °C over the southwestern NFS and the slope water region of the seCS. Over the deep waters to the south of the seCS, the March-mean GLORYS sub-surface temperature ranges from 10 to 17 °C. The relatively warm temperature occurs over the deep waters to the south of the seCS are associated with the meanders of the Gulf Steam. The monthly mean sub-surface circulation of GLORYS dataset is weaker than the counterpart at the sea surface. The Labrador Current at 760 m is about 0.2 m/s and the Gulf Stream at 760 m is about 0.5 m/s. The monthly mean GLORYS sub-surface temperature in August 2014 is slightly higher than the counterpart in March (Fig. D5b,d). A comparison between the monthly mean sub-surface GLORYS results (Fig. D5b,d) and the monthly mean results produced by NGMS-seCS (Fig. D5a,c) demonstrates that submodel L1 has good performance in reproducing the main features of the monthly mean sub-surface temperature, with the relative bias of ~1.73% (~1.71%), correlation coefficient of ~94.02% (94.99%), and RMSE of ~1.08 °C (1.01 °C) in March (August) 2014.

The monthly mean GLORYS sub-surface salinity at 760 m (Fig. D6a,c) is relatively

lower than the counterpart at the sea surface (Fig. D4a,c). The large-scale distributions of GLORYS sub-surface salinity at 760 m in March are similar with the conterpart in August (Fig. D6a,c). The monthly mean GLORYS sub-surface salinity at 760 m in 2014 is about 34.5 over the south western NFS and ranges from 35 to 36 over the deep waters to the south of the seCS. A comparison between the monthly mean sub-surface GLORYS salinity (Fig. D6b,d) and the monthly mean sub-surface salinity produced by NGMS-seCS (Fig. D6a,c) demonstrates that submodel L1 has reasonable skill in simulating main features of the monthly mean sub-surface salinity, with the relative bias of ~0.73% (~0.64%), correlation coefficient of ~91.42% (93.51%), and RMSE of ~0.11 (0.10) in March (August) 2014.

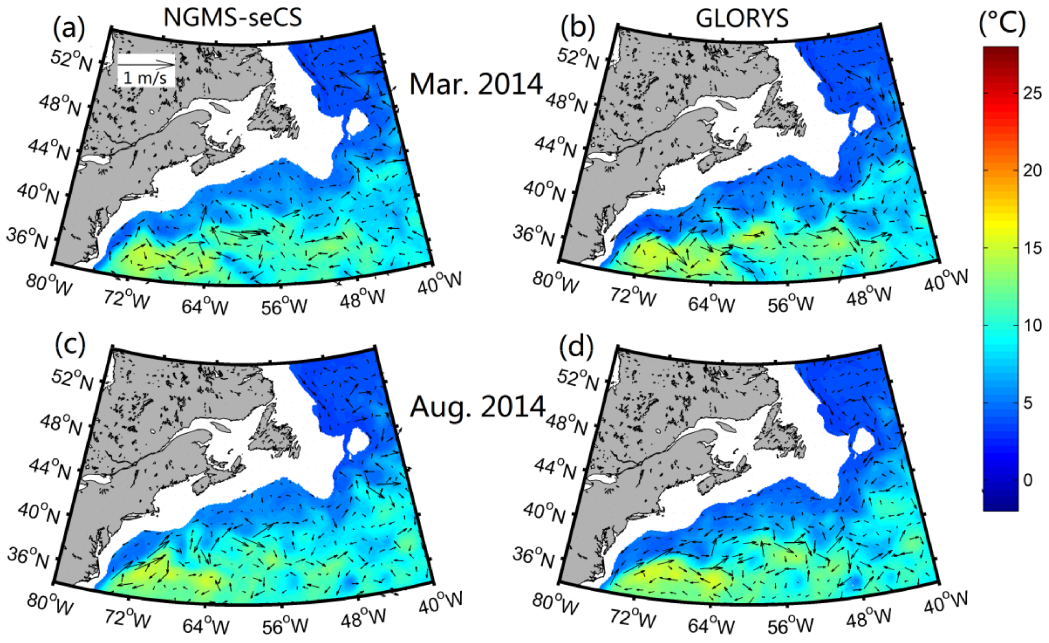

Figure D5: Monthly mean temperature and currents at 760 m in (a,b) March and (c,d) August 2014 calculated from results generated by (a,c) submodel L1 and (b,d) GLORYS dataset. For clarity, velocity vectors are plotted at every 14th model grid point.

The performance of submodel L1 in simulating monthly mean sea ice concentrations over the seCS was also evaluated by *Pei et al.* (2022) using the monthly mean ice concentrations inferred from the GHRSST Level 4 CMC Global Foundation Sea Surface

Temperature Analysis (GDS version 2) in February 2018. In this Chapter, we further assess the performance of submodel L1 in simulating the sea ice concentrations using the NOAA High-resolution Blended Analysis dataset in March 2014, which were inferred from the daily 0.25 degree NOAA High-resolution Blended Analysis dataset (Fig. D7b). The NOAA result features high sea ice concentrations over the northeastern NFS, the SLE, and Strait of Belle Isle. Over these sub-regions, the local ice production is large in winter months associated with the strong negative heat flux (i.e., the net heat loss from the ocean surface to the atmosphere) and relatively low SSS in comparison with other subregions of the seCS. The freezing temperature points for the sea ice are warmer for lower salinity waters, leading to more local ice production. *Urrego-Blanco and sheng* (2014b) demonstrated that both thermodynamics and sea ice dynamics play important roles in affecting sea ice concentrations in the GSL. Furthermore, over the LS and northern NFS, the sea ice conditions are also affected by the southward advection of some Arctic and Sub-Arctic sea ice equatorward carried by the Labrador Current in winter months (*Reeh,* 1985; *Mertz et al.,* 1993). Base on the comparison between the model results and the NOAA data (Fig. D7a,b), submodel L1 has good performance in reproducing the monthly mean NOAA sea ice concentrations over the LS, Strait of Belle Isle, northern GSL, and northeastern NFS.

It should be noted that submodel L1 has deficiencies in simulating sea ice concentrations over the southeastern NFS, western GSL, and coastal waters of ScS. One of plausible reasons is that the thermodynamics of sea ice over these local areas are not well reproduced due to the less reliable calculating of the net heat fluxes over this marginal sea ice zone.

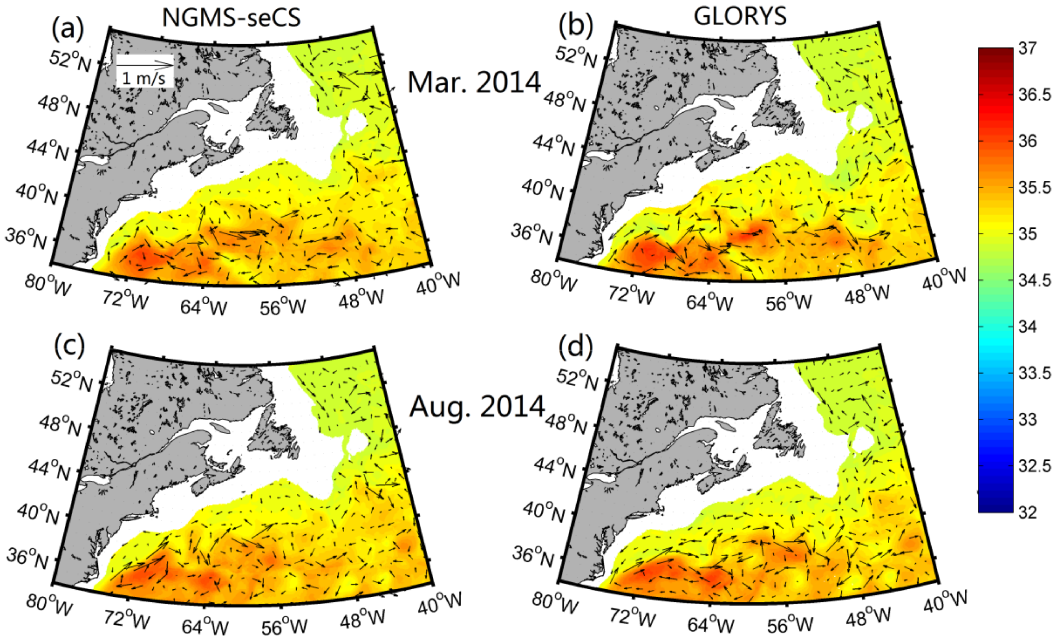

Figure D6: Monthly mean salinity and currents at 760 m in (a,b) March and (c,d) August calculated from results generated by (a,c) submodel L1 and (b,d) GLORYS dataset. For clarity, velocity vectors are plotted at every 14th model grid point.

Table D.1: Values of three error metrics for quantifying performance of submodel L1 in simulating temperature and salinity using GLORYS dataset in March and August 2014. The three error metrics include relative bias (RB), root mean square error (RMSE), and correlation coefficients (CORR).

Depth	Index	Temperature		Salinity	
		March	August	March	August
Sea surface	RB (%)	5.42	2.55	0.81	0.71
	RMSE (°C/PSU)	1.47	1.03	0.84	0.83
	CORR (%)	96.47	97.36	92.65	94.91
760 m	RB (%)	1.73	1.71	0.73	0.64
	RMSE (°C/PSU)	1.08	1.01	0.11	0.10
	CORR (%)	94.02	94.99	91.42	93.51

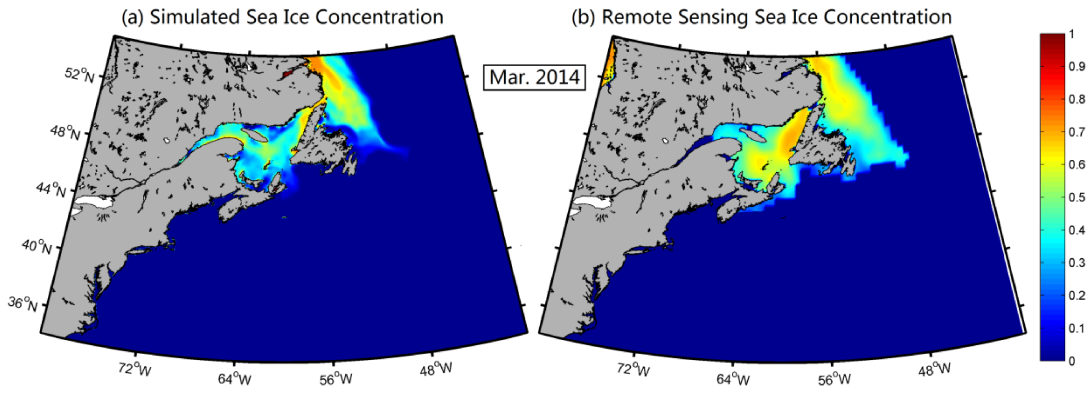

Figure D7: Monthly mean sea ice concentrations in March 2014 (a) produced by NGMS-seCS and (b) inferred from the daily 0.25 degree NOAA High-resolution Blended Analysis dataset over the submodel L1 domain.

APPENDIX E

MONTHLY MEAN TEMPERATURE AND CURRENTS OVER THE NORTHERN SOUTH CHINA SEA

The 5-year averaged monthly mean circulation and temperature in June (during the Southwest Monsoon) and December (during the Northeast Monsoon) over the northern South China Sea (nSCS) (Fig. E1) are calculated from the three hourly HYCOM reanalysis (with a horizontal resolution of $1/12^{o}$) over the period 2007-2011. The HYCOM Reanalysis was generated using the HYCOM with the NCODA system for data assimilation (*Cummings and Smedstad,* 2013).

The 5-year averaged monthly mean currents over the nSCS are characterized by the large-scale anticyclonic circulation in June and cyclonic circulation in December (Fig. E1), due mainly to large differences in the atmospheric forcing between the prevailing Southwest Monsoon in summer months and the Northeast Monsoon in winter months (*Huang et al,* 1994; *Zhang,* 2021). In June, the surface anticyclonic circulation is characterized by the northeastward coastal flow off Vietnam known as the Vietnam Offshore Current (VOC) (Fig. E1a). The VOC transports relatively cool and fresh waters from the coastal waters of Vietnam to the central region of the nSCS. The northeastward currents over the central region of the nSCS turn approximately eastward to reach the offshore waters of northwestern Luzon Island and then turn northward to form the Northwest Luzon Coastal Current (nwLCC). The nwLCC runs northward to join the semi-loop current associated with the Kuroshio Current over western Luzon Strait. In June and other summer months, a narrow coastal jet flows northeastward over the inner continental shelf off western Guangdong Province and northeastern Hainan Island (Fig. D1a). The large-scale circulation at 20 m (Fig. E1b) are very similar to the counterpart at the sea surface in June over the nSCS (Fig. E1a), except for relatively weaker currents at 20 m.

The 5-year averaged monthly mean SSTs in June are warm and about 29.5 ^{o}C over the southern and central regions and relatively cooler and about 27.5 ^{o}C over the northern

region of the nSCS (Fig. E1a). Over southwestern Taiwan Strait, the June-mean SST is coolest and about 25 ^{o}C. A narrow band of relatively cool surface waters occurs near the coast of Vietnam and western Guangdong Province due mainly to the wind-induced coastal upwelling in summer months (Fig. E1a). The June-mean temperatures at 20 m have similar spatial features as the SSTs, except for slightly low values of about 29.0 ^{o}C over the southern and central regions and lower values of about 27.0 ^{o}C over the northern region of the nSCS at 20 m.

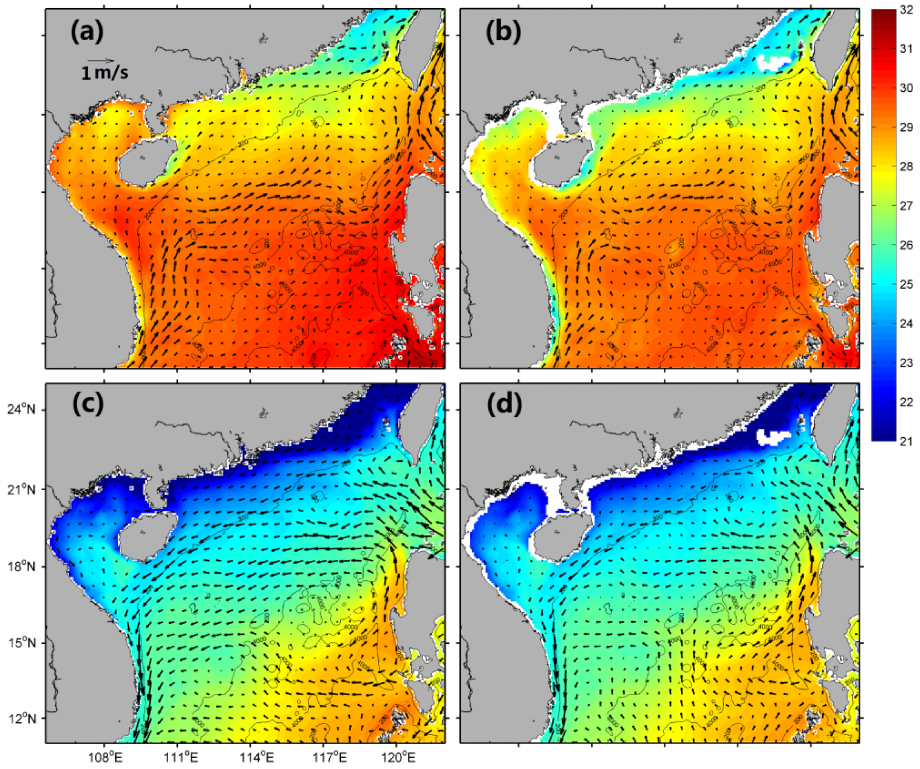

Fig. E1. Distributions of five-year averaged monthly mean currents and temperatures in (a, b) June and (c, d) December (a, c) the sea surface and (b, d) 20 m based on the HYCOM reanalysis in the period 2007-2011. The water depth of 200 m and 400 m are shown by contour lines.

In December, the 5-year averaged monthly mean surface circulation is characterized by a narrow coastal jet known the nwLCC flowing northward along the coast of nwLI, and broad and southwestward currents over the northern and central regions of the nSCS (Fig. E1c). These southwestward surface currents merge over the coastal waters off Vietnam to

form a narrow and southward coastal jet (Fig. E1c). Over the southern region of the nSCS, the December-mean surface currents run westward and northwestward to join the southward coastal jet off Vietnam. The December-mean surface currents at 20 m (Fig. E1d) have similar horizontal features as the surface currents over the nSCS, except for weaker currents at 20 m.

The 5-year averaged December-mean SSTs are about 28.5 ^{o}C over the southeastern region, relatively cool and about 26 ^{o}C over the central and western region, and much cooler and about 24.0 ^{o}C over the northern region of the nSCS (Fig. E1c). The December-mean SSTs are coolest and about 21.0 ^{o}C over the shelf region of western Guangdong Province. The December-mean sub-surface temperatures at 20 m (Fig. E1d) have the similar horizontal distribution to the counterpart at the sea surface.

BIBLIOGRAPHY

AMEC Earth and Environmental LTD. (2011). Halifax Harbour Water Quality Monitoring Program Final Summary Report. *Halifax Water*, pp.111.

Bleck, R. (2002). An oceanic general circulation model framed in hybrid isopycnic-Cartesian coordinates. *Ocean Model.,* 4, 55–88.

Blondeau-Patissier, D., Gower, J., Dekker, A., Phinn, S., and Brando, V. (2014). A review of ocean color remote sensing methods and statistical techniques for the detection, mapping and analysis of phytoplankton blooms in coastal and open oceans. *Prog. Oceanogr.,* 123–144. 10.1016/j.pocean.2013.12.008.

Blumberg, A. F., and Goodrich, D. M. (1990). Modeling of wind-induced destratification in Chesapeake Bay. *Estuaries,* 13, 236–249. doi: https://doi.org/10.2307/1351914.

Blumberg, A. F., and Mellor, G. L. (1987). A Description of a Three-Dimensional Coastal Ocean Circulation Model. *Heaps, N.S., Ed., Estuar. Coast. Shelf Sci.,* Book 4, American Geophysical Union, 1–6.

Bourgault, D., and Vladimir, G. K. (1999). Real-time monitoring of the freshwater discharges at the head of the St. Lawrence Estuary, *Atmos. Ocean*, 37(2), 203–220. doi: 10.1080/07055900.1999.9649626.

Brennan, C. E., Bianucci, L., and Fennel, K. (2016). Sensitivity of northwest North Atlantic shelf circulation to surface and boundary forcing: A regional model zssessment, *Atmos. Ocean,* 54(3), 230–247. doi: 10.1080/07055900.2016.1147416.

Bryan, K. (1969a). A numerical model for the study of the circulation of the world ocean, *J. Comput. Phys.*, 4, 347–376.

Bryan, K. (1969b). A numerical investigation of the dynamics of the sea in the presence of a thermocline. *J. Phys. Oceanogr.,* 1(3), 194-205.

Buckley, D. E., and Winters, G. V. (1992). Geochemical characteristics of contaminated surficial sediments in Halifax Harbour: impact of waste discharge. *Can. J. Earth Sci.*, 29, 2617–2639.

Burt, W. J., Thomas, H., and Auclair, J. P. (2013). Short-lived radium isotopes on the Scotian Shelf: Unique distribution and tracers of cross-shelf CO_2 and nutrient transport. *Mar. Chem.*, 156, 120–129.

Cai, Z. Y., Liu, Z., Chen, Z., Guo, Y., and Gao, H. W. (2014). Temporal and spatial distribution of the summertime sea currents in the Jiaozhou Bay Mouth, *J. Ocean Univ. China*, 4, 86–92.

Carpenter, M. H., Kennedy, C. A., and Bijl, H. (2005). Fourth-order Runge-Kutta schemes for fluid mechanics applications. *J. Sci. Comput.*, 25, 157–194 https://doi.org/10.1007/s10915-004-4637-3

Chassignet, E. P., Smith, L. T., Bleck, R. and Bryan, F. O. (1996). A model comparison: numerical simulations of the North and Equatorial Atlantic Ocean circulation in depth and isopycnic coordinates. *J. Phys. Oceanogr.,* 26, 1849-1867.

Chawla, D., Spindler, D. M, and Tolman, H. L. (2013). Validation of a thirty year reanalysis using climate forecast system reanalysis winds. *Ocean Model.*, 70, 189–206.

Chegini, F., Lu, Y., Katavouta, A., and Ritchie, H. (2018). Coastal upwelling off southwest Nova Scotia simulated with a high-resolution baroclinic ocean model. *J. Phys. Oceanog.*, 123, 2318–2331.

Chen, Y., and Tang, D. (2012). Eddy-feature phytoplankton bloom induced by a tropical cyclone in the South China Sea. *Int. J. Remote Sens.*, 33(23), 7444–7457.

Chen, Y. L., Yan, C. X., Zhu, J., and Li, Y. N. (2018). Evaluation of a global eddy-permitting hybrid coordinate ocean model. *Atmos. Ocean. Sci. Lett.,* 11,4, https://doi.org/10.1080/16742834.2018.1490625, 345–251

Choi, S., and Hwang, J. H. (2002). Lagrangian coherent structure analysis on the vegetated compound channel with numerical simulation. *Water*, 14, 406. https://doi.org/10.3390/w14030406.

Chu, P. C., Veneziano, J. M., Fan, C., and Carron, M. (2000). Response of the South China Sea to Tropical Cyclone Ernie 1996. *J. Geophys. Res. Atmos.*, 105 (C6), 20. https://doi.org/10.1029/2000JC900035.

Cong, L., Sheng J., and Thompson, K. T. (1996). A retrospective study of particle retention on the outer banks of the Scotian Shelf 1956-1993, Can. Tech. Rep. *Hydrogr. Ocean*, 170, pp.111.

Connolley, W. M., Gregory, J. M., Hunke, E., and McLaren, A.J. (2004). On the consistent scaling of terms in the sea-ice dynamics equation, *J. Phys. Oceanogr.,* 34 (7), pp. 1776-1780.

Corell, H. (2012). Applications of Ocean Transport Modelling. Ph.D. thesis, *University of Stockholm*, pp. 40.

Cummings, J. A. (2005). Operational multivariate ocean data assimilation. *Quart. J. Royal Met. Soc*., 131(613), 3583–3604. http://dx.doi.org/10.1256/qj.05.105.

Cummings, J. A., and Smedstad, O. M. (2013). Variational data analysis for the global ocean. *Data Assimilation for Atmospheric, Oceanic and Hydrologic Applications*, Vol. II, pp. 303–343. https://doi.org/10.1007/978-3-642-35088-7.

Davis, A., and Yan, X. H. (2004). Hurricane forcing on chlorophyll-a concentration off the northeast coast of the U.S. *Geophys. Res. Lett*., 31, L17304. https://doi.org/10.1029/2004GL020668.

Dever, M., Hebert D., Greenan B. J. W., Sheng J., and Smith P. C. (2016). Temperature/salinity and coastal circulation along the Halifax Line and the connections with the Gulf of St. Lawrence. *Atmos-Ocean,* 54, 199–217.

Dietrich, D. E., Marietta, M. G., and Roache, P. J. (1987). An ocean modelling system with turbulent boundary layers and topography: numerical description. *Int J Numer Methods Fluids,* 7, 833–855. https://doi.org/10.1002/fld.1650070805.

Dietrich, D. E., and Lin, C. A. (1994). Numerical studies of eddy shedding in the Gulf of Mexico. *J. Geophys. Res.,* 99, 7599–7615.

Egbert, G. D. and Erofeeva, S. Y. (2002). Efficient inverse modeling of barotropic ocean tides. *J. Atmos Ocean Technol*, 19(2), 183–204.

Ekman, V. W. (1905). On the influence of the earth's rotation on ocean-currents. *Arkiv. Mat. Astr. Fys.,* band 2, pp. 52.

El-Sabh, M. I. (1976). Surface circulation pattern in the Gulf of St. Lawrence. *J. Fish. Res. Board Can.*, 33, 124–138.

Enrile, F., Besio, G., Stocchino, A., and Magaldi. M.G. (2019). Influence of initial conditions on absolute and relative dispersion in semi-enclosed basins. *PLoS ONE*., 14(7), e0217073. https://doi.org/10.1371/journal.pone.0217073.

Ezer, T., and Mellor, G. (2004). A generalized coordinate ocean model and a comparison of the bottom boundary layer dynamics in terrain-following and in z-level grids. *Ocean Model.,* 6, 379–403.

Fader, G. B., and Buckley, D. E. (1995). Environmental Geology of Halifax Harbour, Nova Scotia. Geoscience Canada, 22(4).

Fedorov, A. V., Brierley, C. M., Emanuel, K. (2010). Tropical cyclones and permanent El Niño in the early Pliocene epoch. *Nature*, 463(7284), pp.1066-70. Doi: 10.1038/nature08831. PMID: 20182509.

Fennel, K., Wilkin, J., Levin, J., Moisan, J., O'Reilly, J., and Haidvogel, D. (2006). Nitrogen cycling in the Mid Atlantic Bight and implications for the North Atlantic nitrogen budget: Results from a three-dimensional model. *Global Biogeochem. Cycles*, 20, GB3007. doi:10.1029/2005GB002456.

Fennel, K., Hu, J., Laurent, A., Marta, M., and Hetland, R. (2013). Sensitivity of hypoxia predictions for the northern Gulf of Mexico to sediment oxygen consumption and model nesting. *J. Geophys. Res. Oceans,* 118(2), 990-1002.

Feng, S. Z., Ju. L., and Jiang, W. S. (2008). A Lagrangian mean theory on coastal sea circulation with inter-tidal transports I. Fundamentals. *Acta Oceanol. Sin.,* 27 (6), 1–16. doi: 10.3969/j.issn.0253-505X.2008.06.001.

Feng, T., Stanley, R. R. E., Wu, Y., Kenchington, E., Xu, J., and Horne, E. (2022). A High-resolution 3-D circulation model in a complex archipelago on the coastal Scotian Shelf. *J. Geophys. Res*: *Oceans*, 127, e2021JC017791. https://doi.org/10.1029/2021JC017791.

Fong, D. A., and Geyer, W. R. (2001). Response of a river plume during an upwelling favorable wind event. *J. Geophys. Res*: *Oceans*, 106, 1067–1084. https://doi.org/10.1029/2000jc900134.

Fox-Kemper, B., Adcroft, A., Boning, C., Chassignet, E., Curchitser, E., Danabasoglu, G., Eden, C., England, M. H., Gerdes, R., Greatbatch, R. J., Griffies S. M., Hallberg, R. W., Hanert, E., Heimbach, P., Hewitt, H. T., Hill, C. N., Komuro, Y., Legg, S., Le Sommer, J., Masina, S., Marsland, S.J., Penny, S. G., Qiao, F., Ringler, T. D., Treguier, A. M., Tsujino, H., Uotila, P., and Yeager, S. G. (2019). Challenges and prospects in ocean circulation models. *Front. Mar. Sci.,* 6, 65. doi: 10.3389/fmars.2019.00065.

Frischknecht, M., Munnich, M., and Gruber, N. (2015). Remote versus local influence of ENSO on the California Current System. *J. Geophys. Res. Oceans.,* 120 (2), 1353–1374. https://doi.org/10.1002/2014JC010531.

Gao, G., Chen, C., Qi, J., and Beardsley, R. C. (2011). An unstructured-grid, finite-volume sea ice model: Development, validation, and application. *J. Geophys. Res*., 116, C00D04. doi:10.1029/2010JC006688.

Geshelin, Y., Sheng, J., and Greatbatch, R. J. (1999). Monthly mean climatologies of temperature and salinity in the western North Atlantic, Canadian Data Report of Hydrography and Ocean Sciences, 153.

Greenberg, D. A. (1999). Atlas of Tidal Currents for Halifax Harbour, http://www.mar.dfo-mpo.gc.ca/science/ocean/coastal hydrodynamics/atlas/atlas.pdf.

Greenberg, D. A., Murty, T. and Ruffman, A. (1993), A numerical model for the Halifax Harbour tsunami due to the 1917 explosion. *Mar. Geod.,* 16, 1536, G

Griffiths, R. W., and Linden, P. F. (1981). The stability of vortices in a rotating, stratified fluid. *J. Fluid Mech.,* 105, 283–316.

Gruber, N., Frenzel, H., Doney, S., Marchesiello, P., McWilliams, J., Moisan, J., Oram, J., Plattner, G., Stolzenbach, K. (2006). Eddy-resolving simulation of plankton ecosystem dynamics in the California Current System. *Deep Sea Research,* 53, 1483–1516. https://doi.org/10.1016/j.dsr.2006.06.005.

Haidvogel, D. B., Arango, H., Budgell, W. P., Cornuells, B. D., Curchitser, E., Di Lorenzo, E., Fennel, K., Geyer, W. R., Hermann, A. J., Lanerolle, L., Levin, J., McWilliams, J. C., Miller, A. J., Moore, A. M., Powell, T. M., Shchepetkin, A. F., Sherwood, C. R., Signell, R. P., Warner J. C., and Wilkin, J. (2008). Ocean forecasting in terrain-following coordinates: Formulation and skill assessment of the Regional Ocean Modeling System. *J. Comput. Phys.,* 227, 3595–3624.

Halliwell, G. R., Bleck, R., and Chassignet, E. (1998). Atlantic Ocean simulations performed using a new hybrid-coordinate ocean model. EOS, Fall 1998 AGU Meeting.

Hassan, A. E., Andricevic, R., and Cvetkovic, V. (2002). Evaluation of analytical solute discharge moments using numerical modeling in absolute and relative dispersion frameworks. *Water Resour. Res.,* 38(2), 1–1. https://doi.org/10.1029/2001WR000267.

Havik, L., and Vage, K. (2018). Wind-driven coastal upwelling and downwelling in the shelfbreak East Greenland Current. *J. Phys. Oceanog.*, 123, 6106–6115.

Haza, A. C., Poje, A. C., Özgökmen, T. M., and Martin, P. (2008). Relative dispersion from a high-Resolution Coastal model of the Adriatic Sea. *Ocean Model.* 22 (1–2), 48–65.

Heath, R. A. (1973). Flushing of coastal embayments by changes in atmospheric conditions. *Limnology and Oceanography*, 18, 849-862.

Hellerman, S., and Rosenstein, M. (1983). Normal monthly wind stress over the world ocean with error estimates. *J. Phys. Oceanog.*, 13, 1093–1104.

Holland, G. J., (1980). An analytic model of the wind and pressure profiles in hurricanes. *Mon.*, 108, 1212–1218.Huang, P., Chou, C., & Hang, R. H. (2011). Seasonal modulation of tropical intraseasonal oscillation on tropical cyclone genesis in the western North Pacific. *J. Climate*, 24, 6339–6352. https://doi.org/10.1175/2011JCLI4200.1

Hu, J., Kawamura, H., Hong, H., and Qi, Y. (2000). A review on the currents in the South China Sea: Seasonal circulation, South China Sea warm current and Kuroshio intrusion. *J. Oceanogr.*, 56(6), 607–624. https://doi.org/10.1023/A:1011117531252.

Hu, J., Fennel, K., Mattern J. P., and Wilkin, J. (2012). Data assimilation with a local ensemble Kalman Filter applied to a three-dimensional biological model of the Middle Atlantic Bight. *J. Mar. Syst.*, 94, 145–156. http://dx.doi.org/10.1016/j.jmarsys.2011.11.016.

Hu, K., Chen, Q., and Kimball, S. K. (2013). Consistency in hurricane surface wind forecasting:an improved parametric model. *Nat. Hazards.* 61, 3, 1029–1050.

Huang, P., Chou, C., and Hang, R.H. (2011). Seasonal modulation of tropical intraseasonaloscillation on tropical cyclone genesis in the western North Pacific. *J. Clim*. 24, 6339–6352. https://doi.org/10.1175/2011JCLI4200.1

Huang, Q. Z., Wang, W. Z., Li, Y. S., and Li, C. W. (1994). Current characteristics of the South China Sea, *Oceanology of China Seas*. Springer, Dordrecht. pp. 39–47. https://doi.org/10.1007/978-94-011-0862-1_5.

Hunke, E. C. (2010). Thickness sensitivities in the CICE sea ice model, *Ocean Model.,* 34, 137–149. 10.1016/j.ocemod.2010.05.004 .

Hunke, E. C. (2014). Weighing the importance of surface forcing on sea ice—a September 2007 modeling study. *Q.J. Roy. Met. Soc.,* 142, 539–545. http://dx.doi.org/10.1002/qj.2353.

Hunke, E. C., and Dukowicz, J. K. (1997). An Elastic-Viscous-Plastic Model for Sea Ice Dynamics. *J. Phys. Oceanog.*, 27, 1849-1867. http://dx.doi.org/10.1175/1520-0485(1997)027<1849:AEVPMF>2.0.CO;2.

Huntsman, A. G. (1924). Circulation and pollution of water near and around Halifax Harbour, *Contributions to Canadian Biology,* 2, 71–81.

James, B., and Shay, L. K. (2009). Mixed layer cooling in mesoscale oceanic eddies during Hurricanes Katrina and Rita. *Mon. Weather Rev.,* 137(12), 4188–4207 https://doi.org/10.1175/2009MWR2849.1.

Jean-Michel, L., Eric, G., Romain, B., Garric, G., Angélique, M., Drevillon, M., Bricaud, C., Mathieu, H., Olivier, L., Charly, R., Candela, T., Charles-Emmanuel, T., Gasparin, F., Giovanni, R., Mounir, B., Yann, D., and Traon, P. (2021). The Copernicus Global 1/12° Oceanic and Sea Ice GLORYS12 Reanalysis. Front. *Earth Sci.,* 9. DOI:698876. 10.3389/feart.2021.698876.

Jiang, X., Zhong, Z., and Jiang, J. (2009). Upper ocean response of the South China Sea to Typhoon Krovanh. (2003). *Dyn. of Atmos. and Oceans*, 47, 165–175.

Jordan, F. (1972). Oceanographic data of Halifax Inlet, *BIO Data Series*, BI-D-72-8, pp. 248.

Kantha, L. H. and Clayson, C. A. (2000), Numerical Models of Oceans and Oceanic Processes, *Ukraine: Elsevier Science*. pp. 750. ISBN: 9780124340688

Kara, B., Metzger, E. J., Hurlburt, H. E., Wallcraft, A. J., and Chassignet, E. P. (2008). Multistatistics metric evaluation of ocean general circulation model sea surface temperature: application to 0.08° Pacific hybrid coordinate ocean model simulations. *J. Phys. Oceanogr*., 113, C12. https://doi.org/10.1029/2008JC004878.

Korty, R. L., Emanuel, K. A., and Scott, J. R. (2008). Tropical cyclone–induced upper-ocean mixing and climate: Application to equable climates. *Journal of Climate*, 21(4), 638–654. https://doi.org/10.1175/2007jcli1659.1

Lacava, T., and Ciancia, E. (2020). Remote sensing applications in coastal areas. *Sensors, 20*, 2673–2675. https://doi.org/10.3390/s20092673.

Lachkar, Z., and Gruber, N. (2011). A comparative study of biological production in eastern boundary upwelling systems using an artificial neural network. *Biogeosciences*, 9, 293–308.

Large, W., and Pond, S. (1981), Open ocean momentum flux measurements in moderate to strong winds. *J. Phys. Oceanogr.,* 11, 324-336, https://doi.org/10.1175/1520-0485(1981)011<0324:OOMFMI>2.0.CO;2.

Lawrence, D. (1989). Physical Oceanography and Modelling in Halifax Harbour: A Review, in investigations of marine environmental quality in Halifax Harbour, edited by Nicholls, H. *Fisheries and Oceans Canada*, 97. https://publications.gc.ca/site/eng/459625/publication.html.

Lechner, A., Keckeis, H., and Humphries, P. (2016). Patterns and processes in the drift of early developmental stages of fish in rivers: a review. *Rev. Fish. Biol. Fisheries,* 26, 471–489. https://doi.org/10.1007/s11160-016-9437-y

Lee, C. Y., and Chen, S. S. (2012). Symmetric and asymmetric structures of hurricane boundary layer in coupled atmosphere-wave-ocean models and observations. *J. Atmos. Sci.,* 69(12), 3576–3594. https://doi.org/10.1175/JAS-D-12-046.1.

Lewis, M. R., and Platt, T. (1982). Scales of variability in esturine ecosystems, Proceedings of the Sixth Biennial International Estuarine Research Conference, 3–20. https://doi.org/10.1016/B978-0-12-404070-0.50007-7.

Li, W. K. W., and Harrison, W. G. (2008). Propagation of an atmospheric climate signal to phytoplankton in a small marine basin, *Limnology and Oceanography*, 53, 1734–1745.

Lin, I., Liu, W. T., Wu, C.-C., Wong, G. T. F., Hu, C., Chen. Z., Liang, W.-D., Yang, Y., and Liu, K. K. (2003). New evidence for enhanced ocean primary production triggered by tropical cyclone. *Geophys. Res. Lett.*, 30(13), 1718–1723. https://doi.org/10.1029/2003GL017141.

Lin, L., Liu, Z., Xie, L., Gao, H., Cai, Z., Chen, Z., and Zhao, J. (2015). Dynamics governing the response of tidalcurrent along the mouth of Jiaozhou Bay to land reclamation. *J. Geophys. Res. Oceans.,* 120, 2958–2972. doi:10.1002/2014JC010434.

Lin, S. (2021). Study of Wave-Current-Ice Interactions over the Northwest Atlantic, PhD Thesis, *Dalhousie University*. pp. 203.

Lin, S., and Sheng, J. (2017). Assessing the performance of wave breaking parameterizations in shallow waters in spectral wave models. *Ocean Model.,* 120, 41–59. https://doi.org/10.1016/j.ocemod.2017.10.009.

Lin, S., Sheng, J., Ohashi, K., and Song, Q. (2021). Wave-current interactions during Hurricanes Earl and Igor in the northwest Atlantic. *J. Geophys. Res.: Oceans,* 126, e2021JC017609.

Liu, X., and Wei, J. (2015). Understanding surface and sub-surface temperature changes induced by tropical cyclones in the Kuroshio. *Ocean Dyn.*, 65, 1017–1027. https://doi.org/10.1007/s10236-015-0851-9.

Liu, X., Wei, J., Zhang, D. L., and Miller, W. (2019). Parameterizing sea surface temperature cooling induced by tropical cyclones: 1. Theory and An application to Typhoon Matsa. *J. Geophys. Res*., 124, 1215–1231. https://doi.org/10.1029/2018JC014117.

Loder, J. W., Petrie, B. and Gawarkiewicz, G. (1998). The coastal ocean off northeastern North America: a large scale view. In: Robinson AR, Brink KH (eds) The sea, 11. *The global coastal studies. Regional studies and syntheses. Wiley, New York,* pp 105–133.

MacLaren Plansearch Limited. (1991). Final Report to Halifax Harbour Cleanup Inc. on Physical Oceanography, *Technical Report*, Halifax, N.S.

MacLaren Plansearch Limited and Martec Limited. (1991). Final Report to Halifax Harbour Cleanup Inc. on Sediment Transport Modelling at Ives Point, *Technical Report*, Halifax, N.S.

Mellor, G. L. and Yamada, T. (1982). Development of a turbulence closure model for geophysical fluid problems, *Rev. Geophys.,* 20, 851-875. doi:10.1029/rg020i004p00851.

Mellor, G. L. (2004). Users Guide for a Three Dimensional, Primitive Equation, Numerical Ocean Model, *Program in Atmos. and Oceanic Sci.,* Princeton Univ. Princeton, N. J. pp. 42.

Mesinger, F., DiMego, G., Kalnay, E., Mitchell, K., Schaffran, P. C., Ebisuzaki, W., Jovic. D., Woollen, J., Rogers, E., Berbery, E. H., Fan, Y., Grumbine, R., Higgins W, Li, Lin, Y., Manikin, G., Parrish, D., and Shi, W. (2006). North American Regional Reanalysis. *Bull. Am. Meteorol.,* 87, 343–360. 10.1175/BAMS-87-3-343.

Metzger, E. J., Hurlburt, H. E., Xu, X., Shriver, J. F., Gordon, A. L., Sprintall, J., Susanto, R. D., and VanAken., H. M. (2010). Simulated and observed circulation in the Indonesian seas: 1/12° global HYCOM and the INSTANT observations. *Dyn. Atmos. Oceans*, 50, 275–300. https://doi.org/10.1016/j.dynatmoce.2010.04.002.

Mork, M. (1981). Circulation phenomena and frontal dynamics of the Norwegian coastal current. *Phil. Trans. R. Soc.,* A302, 635-647.

Munchow, A., and Garvine, R. W. (1993). Dynamical properties of a buoyancy-driven coastal current. *J. Geophys. Res*: *Oceans*, 98, 20063–20077.

Mupparapu, P., and Brown, W. S. (2002). Role of convection in winter mixed layer formation in the Gulf of Maine, February 1987. *J. Geophys. Res*: *Oceans*, 107, 22-1–22-18.

Needham, H. F., Keim, B. D., and Sathiaraj, D. (2015). A review of tropical cyclone-generated storm surges: Global data sources, observations, and impacts. *Rev. Geophys.,* 53, 545–591.

Ohashi, K., Sheng, J., Thompson, K., Hannah, C., and Ritchie, H. (2009a). Effect of stratification on tidal circulation over the Scotian Shelf and Gulf of St. Lawrence: a numerical study using a three-dimensional shelf circulation model, *Ocean Dyn.*, 59, 809–825. doi:10.1007/s10236-009-0212-7.

Ohashi, K., Sheng, J., Thompson, K., Hannah, C., and Ritchie, H. (2009b). Numerical study of three-dimensional shelf circulation on the Scotian Shelf using a shelf circulation model, *Cont. Shelf Res*., 29, 2138–2156. doi:10.1016/j.csr.2009.08.005.

Ohashi, K., and Sheng, J. (2013). Influence of St. Lawrence River discharges on the circulation and temperature/salinity in Canadian Atlantic waters, *Cont. Shelf Res*., 58, 32–49. Doi:10.1016 /j.csr.2013.03.005.

Ohashi, K., and Sheng, J. (2015). Investigating the effect of oceanographic conditions and swimming behaviours on the movement of particles in the Gulf of St. Lawrence using an individual-based numerical model, *Atmos-Ocean*, 54, 278–298. doi: 10.1080/07055900.2015.1090390.

Paiva, A. M., Chassignet, E. P., and Mariano, A. J. (2000). Numerical simulations of the North Atlantic subtropical gyre: sensitivity to boundary conditions, *Dyn. Atmospheres Oceans,* 32, 209–237.

Paradis, R., and Wood, S. L. (2013). Inexpensive expendable conductivity temperature and depth (CTD) sensor. *OCEANS - San Diego*, 1–12.

Park, J. J., Kwon, Y. O. and Price, J. F. (2011). Argo array observation of ocean heat content changes induced by tropical cyclones in the north Pacific, *J. Geophys. Res.,* 116, C12025. doi:10.1029/2011JC007165.

Pasquero, C., and Emanuel, K. (2008). Tropical cyclones and transient upper-ocean warming, *J. Clim.,* 21(1), 149-162.

Pawlowicz, R., Beardsley, B., Lentz, S. (2002). Classical tidal harmonic analysis including error estimates in MATLAB using T_TIDE. *Comput. Geosci.* 28, 929–937.

Pei, Q., Sheng, J., and Ohashi, K. (2022). Numerical study of effects of winds and tides on monthly mean circulation and temperature/salinity over the southwestern Scotian Shelf. *J.Mar. Sci. Eng.,* 10, 1706. https://doi.org/10.3390/jmse10111706.

Peng, M., Xie, L., and Pietrafesa, L. J. (2006). A numerical study on hurricane-induced storm surge and inundation in Charleston Harbor, South Carolina. *J. Geophys. Res*., 111, C08017. https://doi.org/10.1029/ 2004JC002755.

Petrie, B. (1987). Undulations of the Nova Scotia Current, *Atmos-Ocean*, 25, 1, 1–9. doi: 10.1080/07055900.1987.9649260.

Petrie, B., and Yeats, P. (1990). Simple models of the circulation, dissolved metals, suspended solids and nutrients in Halifax Harbour, Water Pollut. *Res. J. Can.,* 25, 325–349

Petrie, B., Topliss, B., and Wright, D. (1987). Coastal upwelling and eddy development off Nova Scotia, *J. Geophys. Res*., 92, 12979–12991.

Platt, T., Prakash, A., and Irwin, B. (1972). Phytoplankton nutrients and flushing of inlets on the coast of Nova Scotia, *Le Naturaliste Canadien*, 99, 2539atu.

Price, J. F. (1981). Upper ocean response to a hurricane. *J. Phys. Oceanogr.,* 11, 153–175. https://doi.org/10.1175/15200485(1981)011<0153:UORTAH>2.0.CO;2.

Price, J. F., Sanford, T. B., and Forristall, G. Z. (1994). Forced stage response to a moving hurricane. *J. Phys.Oceanogr.,* 24(2), 233–260. https://doi.org/10.1175/1520-0485(1994)024<0233:FSRTAM>2.0.CO;2.

Pritchard, D. W. (1952). Estuarine Hydrography Advances in Geophysics, *Elsevier*, pp. 243-280. http://10.1016/S0065-2687(08)60208-3.

Provan, M., Ferguson, S., and Murphy, E. (2022). Storm surge contributions to flood hazards on Canada's Atlantic Coast. *J. Flood Risk Manag*. 15, e12800.

Pugh, D. (2004). Changing Sea Levels, Effects of Tides, Weather and Climate. *Cambridge University Press*, Cambridge, pp. 280.

Punshon, S., and Moore, R. (2004). Nitrous oxide production and consumption in a eutrophic coastal embayment. *Mar. Chem.,* 91. 37-51. 10.1016/j.marchem.2004.04.003.

Rae, J. G. L., Hewitt, H. T., Keen, A. B., Ridley, J. K., West, A. E., Harris, C. M., Hunke, E. C., and Walters, D. N. (2015). Development of the Global Sea Ice 6.0 CICE configuration for the Met Office Global Coupled model. *Geosci. Model Dev*., 8, 2221–2230. https://doi.org/10.5194/gmd-8-2221-2015.

Rego, J. L., and Li, C. (2010). Nonlinear terms in storm surge predictions: effect of tide and shelf geometry with case study from Hurricane Rita. *J. Geophys. Res.,* 115, C06020. https://doi.org/10.1029/2009JC005285.

Reiss, C., Panteleev, G., Taggart, C., Sheng, J., and deYoung, B. (2000). Observations on larval fish transport and retention on the Scotian Shelf in relation to geostrophic circulation. *Fisheries Oceanography,* 9(3), 195-213.

Richardson, P. L. (1983). Eddy kinetic energy in the North Atlantic from surface drifter. *J. Geophys. Res.,* 88, 4355–4367.

Robinson, I. S. (1985). Satellite oceanpgraphy: an introduction for oceanographers and remote-sensing scientists. *Chichester: Ellis Horwood Ltd.* pp. 455

Rutherford, R. J., Herbert, G. J., and Coffen-Smout, S. S. (2005). Integrated ocean management and the collaborative planning process: The Eastern Scotian Shelf Integrated Management (ESSIM) Initiative. *Marine Policy,* 29, 75–83. doi:10.1016/j.marpol.2004.02.004.

Rutherford, K. and Fennel, K. (2018). Diagnosing transit times on the northwestern North Atlantic continental shelf, *Ocean Sci.*, 14, 1207-1221.

Saha, S., and Coauthors. (2010). The NCEP climate forecast system reanalysis. *Bull. Amer. Meteor. Soc.*, 91, 1015–1057.

Shan, S. (2010). Numerical Study of Three-Dimensional Circulation and Temperature/salinity in Halifax Harbour Using a Nested-Grid Ocean Circulation Model. Master's Thesis, *Dalhousie University*. pp. 114.

Shan, S., Sheng, J., Thompson, K., and Greenberg, David. (2011). Simulating the three-dimensional circulation and temperature/salinity of Halifax Harbour using a multi-nested coastal ocean circulation model. *Ocean Dyn.,* 61. 951–976. doi:10.1007/s10236-011-0398-3.

Shan, S., and Sheng, J. (2012). Examination of circulation, flushing time and dispersion in Halifax Harbour of Nova Scotia. *Water Quality Res. J. of Canada,* 47, 3–4. doi: 10.2166/wqrjc.2012.041.

Shan, S., and Sheng, J. (2022). Numerical study of topographic effects on wind-driven coastal upwelling on the Scotian Shelf. *J. Mar. Sci. Eng.*, 10, 497. doi.org/10.3390/jmse10040497.

Shan, S., Sheng, J., and Greenan, B. (2014). Modelling study of three-dimensional circulation and particle movement over the Sable Gully of Nova Scotia, *Ocean Dynamics*. 64, 117–142. doi: 10.1007/s10236-013-0672-7.

Shay, L. K., and Elsberry, R. L. (1987). Near-inertial ocean current response to Hurricane Frederic. *J. Phys. Oceanogr.*, 17, 1249–1269.

Shay, L. K., Goni, G. J., and Black, P. G. (2000). Effects of a warm oceanic feature on Hurricane Opal, *Mon. Weather Rev.,* 128, 1366–1383.

Shchepetkin, A. F, and McWilliams, J. C. (2005). The regional oceanic modeling system (ROMS): a split-explicit, free-surface, topography following-coordinate oceanic model. *Ocean Model.*, 9(4), 347–404.

Sheng, J., Greatbatch, R., and Wright, D. (2001). Improving the utility of ocean circulation models through adjustment of the momentum balance, *J. Geophys. Res.,* 106, 16711-16728, doi:10.1029/2000jc000680.

Sheng, J., and Rao, Y. R. (2006). Circulation and thermal structure in Lake Huron and Georgian Bay: Application of a nested-grid hydrodynamic model. *Cont. Shelf Res*., 26, 1496–1518.

Sheng, J., Wright, D. G., Greatbatch, R. J., and Dietrich, D. E. (1998). CANDIE: a new version of the DieCAST ocean circulation model. *J. Atmos. Ocean. Technol*., 15, 1414–1432, doi.org/10.1175/1520-0426(1998)015<1414:CANVOT>2.0.CO;2

Sheng, J., Zhao, J., and Zhai, L. (2009). Examination of circulation, dispersion, and retention in Lunenburg Bay of Nova Scotia using a nested-grid circulation model. *J. Mar. Sys,* 77, 350–365, doi:10.1016/j.jmarsys.2008.0.1.013.

Sheng, J. (2001). Dynamics of a buoyancy-driven coastal jet: the Gaspé current. *J. Phys. Oceanogr.*, 29, 1279–1301.

Sheng, J., Zhai, X., and Greatbatch, R. J. (2006). Numerical study of the storm-induced circulation on the Scotian Shelf during Hurricane Juan using a nested-grid ocean model. *Prog. Oceanogr*., 70, 233–254. https://doi.org/10.1016/j.pocean.2005.07.007.

Smagorinsky, J. (1963). General circulation experiments with the primitive equations. *Mon. Weather Rev.,* 91, 99–164.

Smith, P. C. (1992). Validation procedures for oil spill trajectory models, *Can.Tech.Rep. Hydrogr. Oceanol. Sci*., 140, 168–183.

Song, H., Edwards, C. A., Moore, A. M., and Fiechter, J. (2016a). Data assimilation in a coupled physical–biogeochemical model of the California Current System using an incremental lognormal 4-dimensional variational approach: part 2-joint physical and biological data ssimilation twin experiments. *Ocean Model.*, 106, 146–158. http://dx. doi.org/10.1016/j.ocemod.2016.04.001.

Song, H., Edwards, C. A., Moore, A. M., and Fiechter, J. (2016b). Data assimilation in a coupled physical–biogeochemical model of the California Current System using an incremental lognormal 4-dimensional variational approach: part 3-assimilation in a realistic context using satellite and in situ observations. *Ocean Model.*, 106, 159–172. http://dx.doi.org/10.1016/j.ocemod.2016.04.001.

Song, Y., and Haidvogel, D. (1994). A semi-implicit ocean circulation model using a generalized topography-following coordinate system, *J. Comput. Phys.,* 115, 228–244.

Soomere, T., Viikmäe, B., Delpeche, N., and Myrberg, K. (2010). Towards identification of areas of reduced risk in the Gulf of Finland, the Baltic Sea, *Proc. Est. Acad. Sci.,* 59, 156–165.

Subrahmanyam, B., Rao, K. H., Rao, N. S., Murty, V. S. N., and Sharp, R. J. (2002). Influence of a tropical cyclone on chlorophyll-a concentration in the Arabian Sea. *Geophys. Res. Lett.,* 29(22), 22-1–22-4. http:://doi.org/10.1029/2002GL015892.

Sui, Y., Sheng, J., Ohashi, K., and Wu, Y. (2017). Circulation, dispersion and hydrodynamic connectivity over the Scotian Shelf and adjacent waters. *Satell. Oceanogr. Meteorol.*, 2(2), 321–340. doi:0.18063/som.v2i2.321.

Sui, Y., Sheng, J., Tang, D., and Xing, J. (2022). Study of storm-induced changes in circulation and temperature over the northern South China Sea during Typhoon Linfa. *Cont. Shelf Res*., 249, 15, 104866.

Sun, L., Zheng, Q. A., and Tang, T. (2012). Upper ocean near-inertial response to 1998 Typhoon Faith in the South China Sea. *Acta Oceanol. Sin.,* 31(2), 25–32.

Takakura, T., Kawamura, R., Kawano, T., Ichiyanagi, K., Tanoue, M., and Yoshimura, K. (2019). An estimation of water origins in the vicinity of a tropical cyclone's center and associated dynamic processes. *Clim. Dynam*., 50, 555–569. https://doi.org/10.1007/s00382-017-3626-9.

Tang, C. L. (1980). Mixing and circulation in the northwestern Gulf of St. Lawrence: A study of a buoyancy-driven current system. *J. Geophys. Res.*, 85, 2787–2796.

Tang, L., Sheng, J., Hatcher, B. G., and Sale, P. F. (2006). Numerical study of circulation, dispersion, and hydrodynamic connectivity of surface waters on the Belize shelf. *J. Geophys Res*, 111, C01003, doi:10.1029/2005JC002930.

Tang, L., Sheng, J., and Chai, Y. H., (2012). Storm-induced circulation in the Pearl River Estuary of China during super Typhoon Koryn. *Water Qual. Res. J. Can.*, 47, 314–332

Taylor, G. (1922). Diffusion by continuous movements, *Proc. London Math. Soc.,* 2, 196–212.

Tee, K. T., and Petrie, B. (1991). A two-dimensional baroclinic model for the Halifax Harbour, in Proceedings Second Halifax Inlet Research Workshop.

Thompson, K. R., and Sheng, J. (1997). Subtidal circulation on the Scotian Shelf: assessing the hindcast skill of a linear, barotropic model. *J. Geophys. Res*., 102, C11, 24, 987–25, 003.

Thompson, K. R., Dowd, M., Shen, Y., and Greenberg, D. A. (2002). Probabilistic characterization of tidal mixing in a coastal embayment: a Markov chain approach. *Cont. Shelf Res*., 22, 11, 1603–1614.

Thompson, K. R., Loucks, R. H., and Trites, R. W. (1988). Sea surface temperature variability in the shelf-slope region of the Northwest Atlantic. *Atmos-Ocean,* 26, 282–299.

Thompson, K. R., Ohashi, K., Sheng, J., Bobanovic, J., and Ou, J. (2007). Suppressing bias and drift of coastal circulation models through the assimilation of seasonal climatologies of temperature and salinity, *Cont. Shelf Res*., 27, 1303–1316, doi:10.1016/j.csr.2006.10.011.

Treguier, A. M., Ferron, B., and Dussin, R. (2012). Buoyancy driven currents in eddying ocean models. In E. Chassignet, & J. Verron (Eds.), Buoyancy driven flows (chap. 7), *Cambridge University Press*, pp. 281–311.

Tsai, Y., Chern, C. S., and Wang, J. (2008). The upper ocean response to a moving typhoon. *J. Oceanogr*., 64, 115–130. https://doi.org/10.1007/s10872-008-0009-1.

Tseng, R. S. (2002). On the dispersion and diffusion near estuaries and around islands. *Estuar. Coast. Shelf Sci.,* 54(1), 89–100.

Turi, G., Lachkar, Z., and Gruber, N. (2014). Spatiotemporal variability and drivers of pCO2 and air–sea CO2 fluxes in the California Current System: an eddy-resolving modeling study, *Biogeosci.*, 11, 671–690. https://doi.org/10.5194/bg-11-671-2014.

Urho, L. (1999). Relationship between dispersal of larvae and nursery areas in the Baltic Sea. *J. Mar. Sci.* 56, 114–121.

Urrego-Blanco, J. and Sheng, J. (2012). Numerical investigation of interannual variability of circulation and temperature/salinity over the eastern Canadian shelf. *Atmos-Ocean*, 50, 277–300. doi: 10.1080/07055900.2012.680430.

Urrego-Blanco, J., and Sheng, J. (2014a). Study on subtidal circulation and variability in the Gulf of St. Lawrence, Scotian Shelf and Gulf of Maine using a nested-grid coupled ocean-ice model. *Ocean Dyn.,* 64, 385–412. doi: 10.1007/s10236-013-0688-z.

Urrego-Blanco, J., and Sheng, J. (2014b). Formation and distribution of sea ice in the Gulf of St. Lawrence: A process-oriented study using a coupled ocean-ice model. *J. Geophys. Res.*, 119, 7099–7122. doi: 10.1002/2014JC010185.

Van der Baaren, A., and Prinsenberg, S. (2000a). Satellite-tracked Ice Drifter Tests for Accuracy and Positioning, 1997–1998. *Can. Tech. Rep. Hydrogr. Ocean. Sci*. 209: vii + 47 p.

Van der Baaren, A., and Prinsenberg, S. (2000b). Labrador Shelf and Gulf of St. Lawrence Sea Ice Program, 1995-1998. *Can. Tech. Rep. Hydrogr. Ocean. Sci*. 207: vii + 213 p.

Van der Baaren, A., and Prinsenberg, S. (2001). Satellite-tracked Ice Drifter Program, 1999- 2001. *Can. Tech. Rep. Hydrogr. Ocean. Sci*. 214: x+ 88 p.

Van der Baaren, A., and Prinsenberg, S. (2006). Wind Forcing of Ice Drift in the Southern Gulf of St. Lawrence: Satellite-tracked Ice Drifter Program 2004. *Can. Tech. Rep. Hydrogr. Ocean. Sci.* 245: xvii + 188 p.

Van der Baaren, A., and Tang, C. L. (2009). Satellite-tracked Surface Drifter Program: Scotian Shelf 2007 and The Gulf of St. Lawrence 2008-2009. *Can. Data Rep. Hydrogr. Ocean Sci.* 183: ix + 80 p.

Vickery, P. J., and Wadhera, D. (2008). Statistical models of Holland pressure profile parameter and radius to maximum winds of hurricanes from flight-level pressure and H*Wind data. *J. Appl Meteorol*., 47, 2497–2517. http://doi.org/10.1175/2008JAMC1837.1.

Walker, N. D., Leben, R. R., and Balasubramanian, S. (2005). Hurricane-forced upwelling and chlorophyll-a enhancement within cold-core cyclones in the Gulf of Mexico. *Geophys. Res. Lett.,* 32, L18610. http:://doi.org/10.1029/2005GL023716.

Wang, P., and Sheng, J. (2016). A comparative study of wave-current interactions over the eastern Canadian shelf under severe weather conditions using a coupled wave-circulation model. *J. Geophys. Res.*, 121, 5252–5281.

Wang, G., Su, J., Ding, Y., and Chen, D. (2007). Tropical cyclone genesis over the south China sea. *J. Mar. Syst.*, 68(3), 318–326. https://doi.org/10.1016/j.jmarsys.2006.12.002.

Wang, P., and Li, Q. (2009). The South China Sea - Paleoceanography and Sedimentology. http://doi.org/10.1007/978-1-4020-9745-4. *Springer, Dordrecht.* pp. 506.

Wang, P., and Sheng, J. (2016). A comparative study of wave-current interactions over the eastern Canadian shelf under severe weather conditions using a coupled wave-circulation model. *J. Geophys. Res.,* 121, 5252-5281, https://doi.org/10.1002/2016JC011758.

Wang, Y., Sheng, J., and Lu, Y. (2022). Examining tidal impacts on seasonal circulation and temperature/salinity variability over the eastern Canadian shelf using a coupled circulation-ice regional model. *Prog. Oceanogr.,* 189, 102448.

Wanninkhof, R. (1992). Relationship between wind speed and gas exchange over the ocean. *J. Geophys. Res. Oceans,* 97(C5), 7373-7382.

Weatherall, P., Marks, K. M., Jakobsson, M., Schmitt, T., Tani, S., Arndt, J. E., Chayes, D., Ferrini, V., and Wigley, R. (2015). A new digital bathymetric model of the world's oceans, *Earth and Space Science,* 2, 331–345, doi:10.1002/2015EA000107.

Williams, G. A. (2010). Evaluating the effects of wastewater treatment on marine sediment chemistry in Halifax Harbour, Nova Scotia. M.A.Sc. *Dalhousie University.* pp. 291.

Wilson, J., Abbound, S., and Beman, J. M. (2017). Primary production, community respiration, and net community production along oxygen and nutrient gradients: environmental controls and biogeochemical feedbacks within and across “marine lakes”. *Frontiers in Marine Science,* 4, 12. doi: https://doi.org/10.3389/fmars.2017.00012.

Wirth, A., and Negretti, M. E. (2022). Intruding gravity currents and their recirculation in a rotating frame: Numerical results. *Ocean Model.*, 173, 101994.

Wu, Y., Chaffey, J., Greenberg, D., Colbo, K., and Smith, P. (2011). Tidally-induced sediment transport patterns in the upper Bay of Fundy: A numerical study, *Cont. Shelf Res.*, 31, 2041-2053. doi:https://doi.org/10.1016/j.csr.2011.10.009.

Wu, Y., Tang, C., and Hannah, C. (2012). The circulation of eastern Canadian seas. *Prog. Oceanogr*., 106, 28–48.

Yang, H., Liu, Q., Liu, Z., Wang, D., and Liu, X. (2002). A general circulation model study of the dynamics of the upper ocean circulation of the South China Sea, *J. Geophys. Res*., 107(C7), 3085. http://doi.org/10.1029/ 2001JC001084.

Yang, B., and Sheng, J. (2008). Process study of coastal circulation on the inner Scotian Shelf using a nested-grid ocean circulation model, during with a special emphasis on the storm-induced circulation during tropical storm Alberto in 2006. *Ocean Dynamics*, 58, 375–396. doi:10.1007/s10236-008-0149-2. https://link.springer.com/article/10.1007/s10236-008-0149-2.

Yankovsky, A. E., Hickey, B. M., and Munchow, A. K. (2001). Impact of variable inflow on the dynamics of a coastal buoyant plume. *J. Geophys. Res*., 106(C9), 19809–19824.

Yu, L., Fennel, K., and Laurent, A. (2015). A modeling study of physical controls on hypoxia generation in the northern Gulf of Mexico. *J. Geophys. Res. Oceans,* 120(7), 5019–5039.

Zhang, H., and Sheng, J. (2013). Estimation of extreme sea levels over the eastern continental shelf of North America. *J. Geophys. Res*: *Oceans*, 118, 6253–6273.

Zhai, L., Sheng, J., and Greatbatch, R. J. (2008). Application of a nested-grid ocean circulation model to Lunenburg Bay of Nova Scotia: Verification against observations. *J. Geophys. Res*: *Oceans*, 113, C02024.

Zhao, X., Zhou, C., Xu, X., Ye, R., and Zhao, W. (2020). Deep circulation in the South China Sea simulated in a regional model. *Ocean Dyn.,* 70, 1461–1473. https://doi.org/10.1007/s10236-020-01411-2.

Zhang, H. (1998). The effects of freshwater inflow on the water quality of Bedford Basin Estuary: A modeling study, M.A.Sc. *Dalhousie University.* pp. 55.

Zhang, H., Chen, D., Zhou, L., Liu, X., Ding, T., and Zhou, B. (2016). Upper ocean response totyphoon Kalmaegi. *J. Geophys. Res. Oceans*. 121, 6520–6535. https://doi.org/10.1002/2016JC012064.

Zheng, G. M., and Tang, D. (2007). Offshore and nearshore chlorophyll increases induced by typhoon winds and subsequent terrestrial rainwater runoff. *Mar. Ecol. Prog. Ser.*, 333, 61–72.

Zuur, E. A. H., and Dietrich, D. E. (1990). The SOMS model and its application to Lake Neuchatel. *Aquat. Sci.,*52. 115–129.